Precise Predictions for Jets and Tracks

Solange Schrijnder van Velzen

Title: Precise Predictions for Jets and Tracks
Printed by: Ridderprint

UNIVERSITEIT VAN AMSTERDAM

This work is supported by the NWO projectruimte 680-91-122.

Precise Predictions for Jets and Tracks

ACADEMISCH PROEFSCHRIFT

ter verkrijging van de graad van doctor
aan de Universiteit van Amsterdam
op gezag van de Rector Magnificus
prof. dr. G.T.M. ten Dam
ten overstaan van een door het College voor Promoties ingestelde
commissie, in het openbaar te verdedigen in de Agnietenkapel
op donderdag 22 september, om 13:00 uur

door

Solange Vivianne Schrijnder van Velzen

geboren te Amsterdam

Promotiecommissie:

Promotor:	dr. W.J. Waalewijn	Universiteit van Amsterdam
Co-promotor:	prof. dr. E.L.M.P. Laenen	Universiteit van Amsterdam
Overige leden:	prof. dr. J. de Boer	Universiteit van Amsterdam
	dr. A. Castro Anich	Universiteit van Amsterdam
	prof. dr. I.B. van Vulpen	Universiteit van Amsterdam
	prof. dr. P.J.G. Mulders	Vrije Universiteit Amsterdam
	dr. M.C. van Beekveld	University of Oxford
	dr. I.J. Moult	Yale University

Faculteit der Natuurwetenschappen, Wiskunde en Informatica

The material presented in this thesis is based on the following publications:

[1] A. Basdew-Sharma, F. Herzog S.V. Schrijnder van Velzen and W.J. Waalewijn, *One-loop jet functions by geometric subtraction*, JHEP 10 (2020) 118

[2] Y. Chien, R. Rahn, S.V. Schrijnder van Velzen, D. Shao, W.J. Waalewijn and B. W, *Recoil-free azimuthal angle for precision boson-jet correlation*, Phys. Lett. B 815 (2021)

[3] Y. Li, I. Moult, S.V. Schrijnder van Velzen, W.J. Waalewijn and H.X. Zhu, *Extending Precision Perturbative QCD with Track Functions*, Phys. Rev. Lett. 128 (2022) 182001

Author contributions:

In Ref. [1], I developed a general method to calculate one-loop jet contributions. I implemented it, resulting in the GOJet program (including documentation and examples). In particular, I used it to calculate the jet function for for angularities with respect to the thrust axis, taking recoil into account. I wrote most of the paper.

In Ref. [2], I worked out the factorization of the cross section. I calculated the jet contribution for linearly polarized gluons, and for general recombination schemes. Furthermore, I worked on the numerical implementation of resummed predictions for the production of a boson in association with a jet in proton-proton collisions.

In Ref. [3], I worked out the evolution of track functions using shift symmetries and explicit calculations, and I rewrote the evolution of track functions in terms of the shift-invariant central moments.

Contents

Introduction

The goal of a particle physicist is to describe the laws of nature at the most fundamental level. Currently our best understanding is summarized by a theory called The Standard Model (SM). This theory describes all the elementary particles we currently know exist and their interactions. It gets extensively tested by experiments conducted at particle colliders, such as the Large Hadron Collider (LHC). The LHC accelerates beams of protons close to the speed of light and lets them collide to search for new fundamental particles or interactions. Even though the data from particle colliders seems to be well described by theory predictions based on the SM, we know that it is not complete: Theoretically, the SM still needs to be unified with gravity. Phenomenologically, the SM does not explain the matter-antimatter asymmetry, the dark matter holding around 85% of the mass in the universe, or dark energy that seems to cause our universe to expand. As we do not know where to look for answers yet, our best chance is to search for deviations between theory en experiment, which might indicate new physics. Current discrepancies between the SM and experiment are at most 4.2σ (muon g-2) or 3.2σ (violation of lepton flavor) [4]. As potential signs of new physics are very small, it becomes unavoidable to resort to *precision physics*. To match the ever increasing precision in experiments, theoretic predictions are required to reach higher accuracy as well. The work presented in this thesis aims to conduct more precise theoretical calculations and develop tools that serve this goal.

In the first chapter we describe the framework which we use to perform precision calculations. It starts in section 1.1 with an introduction of Quantum Chromodynamics (QCD). This is the sector of the SM which is most prominent in collisions at the LHC as it is essential to describe quarks and gluons that the colliding protons consist of. Furthermore, the dynamics of cross sections is highly affected by QCD corrections due to the large size of the coupling between quarks and gluons, which is why QCD is often referred to as the theory of the strong interactions. Although more in-depth discussions can be found in textbooks, we review the concepts necessary for the research in this thesis: renormalization, the energy dependence of the strong coupling constant, the soft and collinear limit, and the appearance of large logarithms

in cross-section calculations. In section 1.2, we introduce Soft Collinear Effective Theory (SCET), an effective field theory that describes the infrared limit of QCD. In the last section of this chapter, we discuss the collimated sprays of particles called jets. These objects are a prominent feature of QCD and are copiously produced at hadron colliders. In particular we will discuss jet algorithms, which make it possible to bridge the gap between theory and experiment.

The three chapters that follow are dedicated to new research: In chapter 2, we use the method of geometric subtraction to automatize the calculation of the one-loop jet functions. We have created the GOJet Mathematica-package: a numerical implementation of this method. In chapter 3, we consider the azimuthal decorrelation between a vector boson and a jet in pp collisions. The success of the work described there rests upon the use of the recoil-free Winner-Take-All jet algorithm. We will discuss the advantages of this particularly neat setup and present results with higher accuracy then previously possible. In chapter 4, we extend our set of tools with track functions. These objects allow us to construct observables for charged particles only, exploiting the higher angular resolution with which these can be measured at the LHC.

1

Theoretical background

The Standard Model (SM) is built on symmetry considerations: it is constructed to be invariant under the $\mathrm{SU}(3)_c \times \mathrm{SU}(2)_L \times \mathrm{U}(1)_Y$ gauge group. The $\mathrm{SU}(3)_c$ sector, corresponding to the invariance under SU(3) gauge transformations, is also known as Quantum Chromodynamics (QCD). QCD describes the behaviour of quarks and gluons. Because QCD is not involved in electroweak symmetry breaking and mixing, it can be seen as a stand alone theory that takes a prominent role in many scattering processes. Due to the large coupling, perturbative corrections that follow from QCD are the most dominant and shall be the focus of this thesis. We will start with a short review on the basic concepts of QCD in section 1.1. As in any Quantum Field Theory we start with the Lagrangian. We will then investigate the ultraviolet and infrared divergences that show up in perturbative calculations and discuss how to deal with them. The infrared behaviour of QCD is essential in determining the perturbative corrections to leading order physics. In section 1.2 we will set up an effective field theory that is particularly good at describing the infrared regime of QCD: Soft Collinear Effective Theory. Finally, in section 1.3 we shall discuss an interesting phenomena that emerges from QCD: jets. Jets arise from final state quarks or gluons that emit radiation in the infrared regime. Jets will play a central role throughout this thesis. This section focusses on the formation of jets and how this understanding leads to the description of jets used in particle physics.

1.1 Quantum Chromodynamics

QCD is the fundamental field theory of the strong interactions between quarks and gluons. This chapter will give a short overview of the main aspects of QCD. We will start with a discussion of the QCD Lagrangian in section 1.1.1. Considering perturbative corrections introduces divergences in both the high

and low energy limit. However, it is clear that processes that involve QCD are not divergent by itself. In section 1.1.2 we setup the renormalization framework to deal with ultraviolet divergences and in section 1.1.3 we describe the implications for the strong coupling constant. Finally, in section 1.1.4 we discuss the infrared limit of QCD. This chapter is based on [5–8].

1.1.1 QCD Lagrangian

QCD describes the dynamics of the fundamental particles: quarks and gluons. The force that governs the interactions between these fields is known as the strong force. The theory is invariant under the non-abelian gauge group SU(3). The internal degree of freedom of the QCD fields that transforms under these transformations is called color. The quarks are described by Dirac spin-1/2 fields $\psi(x)$ that transform under the fundamental representation of SU(3) as

$$\psi(x) \to U(x)\psi(x), \tag{1.1}$$

where $U(x)$ are unitary matrices with unit determinant in SU(3) corresponding to gauge transformations. They can be written as

$$U(x) = \exp\left[\mathrm{i}\phi^a(x)t^a\right], \tag{1.2}$$

where $\phi^a(x)$ is an arbitrary function of the spacetime coordinates and t^a are the generators in the fundamental representation of SU(3). The generators form a basis of traceless hermitian 3×3 matrices. Note that we have adopted the notation where summation over repeated indices is always implied. The non-abelian nature of SU(3) is reflected by the non-zero commutation relation of these generators

$$\left[t^a, t^b\right] = \mathrm{i}f^{abc}t^c, \tag{1.3}$$

where the coefficients f^{abc} go by the name of structure constants. The generators in a general representation r are normalized as

$$\mathrm{Tr}\left[t_r^a t_r^b\right] = T_r\delta^{ab}. \tag{1.4}$$

By convention, the fundamental representation has $T_F = \frac{1}{2}$. The Casimir operator, defined as $t_r^a t_r^a$, commutes with all generators of SU(3) and therefore yields[1]

$$\sum_a ((t_r)^a(t_r)^a)_{ij} = C_r\delta_{ij}, \tag{1.5}$$

[1] As a result of Schur's lemma

The invariants in SU(3) that correspond to the fundamental en adjoint representations are $C_F = \frac{4}{3}$ and $C_A = 3$ respectively.

To describe the dynamics of the quark fields we need a kinetic term. However, such a term would not be gauge invariant due to the appearance of the derivative on the quark field. We therefore define the covariant derivative

$$D_\mu = \partial_\mu - \mathrm{i} g_s A_\mu, \tag{1.6}$$

where g_s is the strong coupling constant that will determine the interaction strength between quarks and gluons. The spin-1 gauge fields $A_\mu(x)$ describe the gluons and transform as

$$A_\mu(x) \to U_{adj}(x) A_\mu(x) = U(x) A_\mu U^\dagger(x) + \frac{\mathrm{i}}{g_s} U(x) \left[\partial_\mu U^\dagger(x)\right], \tag{1.7}$$

where $A_\mu(x)$ are matrices in colorspace that can be decomposed into a linear combination of the generators

$$A_\mu(x) = A^a_\mu(x) t_a, \qquad a = 1, \ldots, 8. \tag{1.8}$$

The kinetic term for the gauge field can be constructed by considering the fieldstrength tensor $G^{\mu\nu}_a$, defined by

$$G^a_{\mu\nu} = \partial_\mu A^a_\nu - \partial_\nu A^a_\mu + g_s f^{abc} A^b_\mu A^c_\nu. \tag{1.9}$$

The final term will lead to interactions between gluon fields, which is specific to non-abelian theories.

The complete QCD Lagrangian, invariant under SU(3) transformations and conserving parity and time-reversal, is found to be [9]

$$\mathcal{L}_{\mathrm{QCD}} = -\frac{1}{4} G^{\mu\nu}_a G^a_{\mu\nu} + \sum_f \bar{\psi}_f \left(\mathrm{i}\gamma^\mu D_\mu - m_f\right) \psi_f + \mathcal{L}_{\mathrm{gf}} + \mathcal{L}_{\mathrm{gh}}, \tag{1.10}$$

where γ are the Dirac matrices, f denotes the quark flavour of the quark and m_f the corresponding quark mass. As far as we know now from experiments there are six flavours, of which 3 are extremely light and often considered massless for practical purposes. The two-point function for the gluons that follows from the QCD Lagrangian contains an ambiguity in terms of a gauge parameter, analogous to the photon propagator in QED. This can be solved by a gauge fixing procedure, which leads to the second to last term in (1.10). One specific choice is the covariant gauge

$$\mathcal{L}_{gf} = -\frac{1}{2\xi} \left(\partial_\mu A^\mu_a\right) \left(\partial^\nu A^a_\nu\right), \tag{1.11}$$

where ξ is a free parameter. In this thesis we use $\xi = 1$, which is known as the Feynman-'t Hooft gauge. Gauge-fixing introduces unphysical gluon states, corresponding to time-like and longitudinally polarized propagation. These degrees of freedom are cancelled by adding ghost and anti-ghost fields, c_a and $\bar{c}_a$ respectively, which are anti-commuting scalar fields transforming in the adjoint representation of SU(3). The ghost fields are unphysical by construction, as they violate the spin–statistics theorem: ghosts are complex scalar fields (spin 0), but they anti-commute. The ghost fields may therefore never appear as external states in matrix elements. Their only role is to cancel the unphysical polarizations of gluons appearing in loop contributions. The ghost dynamics is described by the Fadeev-Popov Lagrangian

$$\mathcal{L}_{\text{gh}} = (\partial^\mu \bar{c}_a) D^{ab}_\mu c_b = (\partial^\mu \bar{c}_a)\big(\delta^{ab}\partial_\mu - g_s f^{abc} A^\mu_c\big) c_b. \tag{1.12}$$

The QCD Lagrangian can now be used to generate Feynman rules in the quantized theory. These can in turn be used to calculate physical observables by considering the different contributions from Feynman diagrams, following the standard QFT techniques. Contributions from loop integrals will suffer from ultraviolet divergences. In the next section we will discuss how to deal, with them with the knowledge that our final prediction should not be divergent.

1.1.2 Renormalization of QCD

Ultraviolet divergences (UV) appear from the momentum integrals in virtual corrections. A renormalization procedure provides a systematic way to remove the UV divergences. In short, this is done by exploiting freedom to (re)define the parameters in the Lagrangian. This is motivated by realizing that the parameters in the Lagrangian differ from physical constants, due to loop corrections. For example, the coefficient m_f does not correspond to the measured fermion mass, as it receives contributions from loop diagrams at higher orders in perturbation theory. It would therefore be more convenient to absorb the divergent part of such corrections by redefining our set of parameters.

To be able to remove the divergences from Feynman diagrams we first need to identify them. There are many ways to make the UV divergences explicit. The most abrupt one being the introduction of an ultraviolet cutoff Λ_c to stop the loop momentum from reaching infinity. The divergences would then show up in the final answer in the limit $\Lambda_c \to \infty$. This method is not very practical as it breaks translation invariance of the integral as well as gauge invariance, since we constrain the partial derivative (in the covariant derivative) but not the gauge field. The most successful scheme is dimensional regularization [10, 11]. The loop integrals are UV divergent in four spacetime dimensions, while

dimensional regularization uses $d = 4 - 2\epsilon$ dimensions to regulate the loop integrals

$$\int \frac{\mathrm{d}^4 p}{(2\pi)^4} \to \int \frac{\mathrm{d}^d p}{(2\pi)^d}. \tag{1.13}$$

The UV divergences will now show up as $1/\epsilon$ poles in the $\epsilon \to 0$ limit, which can explicitly be seen when evaluating the following representative integral in d-dimensions:

$$I(d,2) = \int \frac{\mathrm{d}^d q}{(2\pi)^d} \frac{1}{(q^2+m^2)^2} = \frac{\mathrm{i}}{16\pi^2}\Gamma(\epsilon)\left(\frac{m^2}{4\pi^2}\right)^{-\epsilon}, \tag{1.14}$$

where the i is a result from Wick rotating the q^0 into the complex plane to avoid the poles in the denominator. The series that will make the poles in ϵ appear should maintain the mass dimension $[\text{mass}]^{-2\epsilon}$ of the expression. This is done with the introduction of the renormalization scale μ, a parameter with mass dimension one,

$$\begin{aligned} I(d,2) &= \frac{\mathrm{i}\mu^{-2\epsilon}}{16\pi^2}\Gamma(\epsilon)\left(\frac{m^2}{4\pi^2\mu^2}\right)^{-\epsilon}, \\ &\approx \frac{\mathrm{i}\mu^{-2\epsilon}}{16\pi^2}\left(\frac{1}{\epsilon} - \log\left(\frac{m^2}{4\pi\exp^{-\gamma_E}\mu^2}\right) + \mathcal{O}(\epsilon)\right). \end{aligned} \tag{1.15}$$

It is important to keep in mind that cross sections should not depend on the value of μ, since it is an unphysical parameter.

Dimensional regularization does not only regulate the divergences resulting from high loop momenta, but also divergences resulting from small loop momenta manifest themselves as $1/\epsilon$ poles. When dealing with scaleless integrals the UV and IR poles cancel each other, and therefore scaleless integrals vanish in dimensional regularization. (An integral is considered scaleless when the integrand scales homogeneously under rescaling of the loop momenta.) An example of such an integral is [12]

$$\int \frac{\mathrm{d}^d q}{(2\pi)^d}\frac{1}{q^4} = \frac{\mathrm{i}\mu^{-2\epsilon}}{16\pi^2}\left(\frac{1}{\epsilon_{\mathrm{UV}}} - \frac{1}{\epsilon_{\mathrm{IR}}}\right) = 0. \tag{1.16}$$

Now that the UV divergences manifest themselves as poles, they can be removed by adding a counterterm to the Lagrangian. This counterterm is not unique and can also include finite terms, which is reflected by the possibility to redefine our artificial renormalization scale μ. In this thesis we will use the modified minimal subtraction ($\overline{\mathrm{MS}}$) scheme [13, 14]. Inspired by equation (1.15), μ is rescaled such that

$$\bar{\mu}^2 = 4\pi e^{-\gamma_E}\mu^2, \tag{1.17}$$

subtracting the $\log(4\pi) - \gamma_E$ terms in addition to the $1/\epsilon$ pole.

Even though UV divergences will always cancel in physical observables, it is useful to implement these counterterms at the level of the Lagrangian. This is the procedure known as renormalization, which makes the theory UV finite. The counterterms are absorbed in the parameters and fields. Explicitly, the bare parameters are rescaled in terms of renormalized ones by

$$m_f = m_f^R Z_m, \qquad g_s = \mu^\epsilon g_s^R \sqrt{Z_\alpha}, \tag{1.18}$$

where the superscript R indicates the set of renormalized quantities. The extra factor μ^ϵ had to be introduced to keep the renormalized coupling constant dimensionless. Similar relations can be written down for the fields

$$\psi = \sqrt{Z_\psi}\,\psi^R, \quad A_a^\mu = \sqrt{Z_A}\,A_a^{R\mu}, \quad c_a = \sqrt{Z_c}\,c_a^R. \tag{1.19}$$

These factors of Z can now be fixed order by order by demanding that they produce the counterterms needed to cancel the UV divergences, i.e. they have the following structure

$$Z_k = 1 + \sum_{n=0}^{\infty} \left(\frac{\alpha_s}{4\pi}\right)^n Z_k^n, \tag{1.20}$$

where $\alpha_s \equiv g_s^2/4\pi$ is known as the strong coupling. The gauge fixing parameter is renormalized such that the gauge fixing term (see equation (1.11)) will not produce any counterterms, meaning $\xi = Z_A \xi^R$ (due to renormalization of the gauge fields). At leading order no renormalization is needed, as there are no UV divergences and the bare quantities will indeed correspond to the physical ones. This is reflected by $Z_k = 1$ at $\mathcal{O}(\alpha_s^0)$. Calculating the higher order contributions to the quark self-energy, gluon self-energy and the quark-gluon vertex is enough to fix all renormalization constants at the corresponding order. For example, rewriting the gluon field strength in terms of the renormalized fields, we find

$$\begin{aligned} -\frac{1}{4} G_{\mu\nu} G^{\mu\nu} &= -Z_A \frac{1}{4} G^R_{\mu\nu} G^{R\mu\nu} \\ &= -(1 + \delta_{AA}) \frac{1}{4} G^R_{\mu\nu} G^{R\mu\nu}, \end{aligned} \tag{1.21}$$

where the δ_{AA} denotes the counterterm that cancels the UV divergences in the gluon self-energy. Performing the calculation of the gluon self energy, where we include all one particle irreducible bubble diagrams,

$$\mathrm{i}\delta_{ab}\Pi_{\mu\nu}(p) = \mathrm{i}\delta_{ab}(p^2\eta_{\mu\nu} - p_\mu p_\nu)\Pi(p^2), \tag{1.22}$$

$=$ 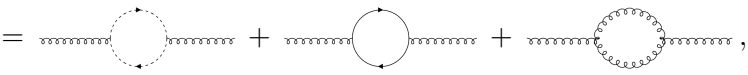 ,

using that the gluon self-energy is transverse, i.e. $\Pi_{\mu\nu}(p)p^\mu = 0$. Performing the loop integrals in $d = 4 - 2\epsilon$ dimensions and expanding around the limit $\epsilon \to 0$, we find [5]

$$\Pi(p^2) = \frac{\alpha_s}{4\pi} e^{-\epsilon L}\left[C_A\left(\frac{\xi}{2}\frac{1}{\epsilon} - \frac{13}{6}\frac{1}{\epsilon} - \frac{9\xi^2+18\xi+97}{36}\right) + n_f T_F\left(-\frac{4}{3}\frac{1}{\epsilon} - \frac{20}{9}\right)\right], \tag{1.23}$$

where $L = \ln\left(\frac{-p^2}{4\pi\mu^2 e^{-\gamma_E}}\right)$. The minimal subtraction, cancelling only the poles, leads to

$$Z_A = 1 + \frac{\alpha_s}{4\pi\epsilon}\left[\left(\frac{13}{6} - \frac{\xi}{2}\right)C_A - \frac{4}{3}n_f T_F\right] + \mathcal{O}(\alpha_s^2). \tag{1.24}$$

The $\overline{\text{MS}}$ scheme is now easily recovered by rewriting μ in terms of $\bar{\mu}$ in the final result. To extract the remaining renormalization constants at $\mathcal{O}(\alpha_s)$ we have to construct counterterms for the quark self-energy and the quark-gluon vertex at one loop

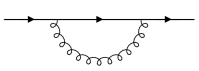

$$\implies \delta_{\psi\psi} = \frac{1}{\epsilon}\frac{\alpha_s}{4\pi} C_F\left(4m - \not{p}\right), \tag{1.25}$$

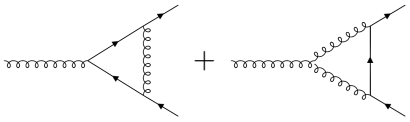

$$\implies \delta_{\psi\bar{\psi}g} = -\frac{1}{\epsilon}\frac{\alpha_s}{4\pi}\left(C_F + \frac{3+\xi}{4}C_A\right).$$

Noting that

$$\delta_{\psi\psi} = (1 - Z_\psi)\not{p} + (1 - Z_\psi Z_m)m, \qquad \delta_{\psi\bar{\psi}g} = 1 - Z_\alpha Z_\psi \sqrt{Z_A}, \tag{1.26}$$

allows us to determine to the renormalization constants. In appendix all Z_i^R are given in $\overline{\text{MS}}$.

The renormalized constants in the Lagrangian can be used to derive physical predictions beyond leading order. The measurable calculations, collectively known as observables O (e.g. cross sections), thus have to be expressed in these renormalized parameters. At this point it is clear that the renormalized quantities will depend on the introduced renormalization scale μ. However, the final predictions may not and thus

$$\mu\frac{\mathrm{d}}{\mathrm{d}\mu}O(\mu, \alpha_s(\mu), m_f(\mu)) = 0, \tag{1.27}$$

up to corrections beyond the order that one is working. This property leads to differential equations that connect these renormalized quantities for different

values of μ. The corresponding evolution is described by an evolution kernel U that connects the observable at different renormalization scales

$$O(\mu, \alpha_s(\mu), m_f(\mu)) = U(\mu, \mu_0) O(\mu, \alpha_s(\mu_0), m_f(\mu_0)), \tag{1.28}$$

where the value at some reference scale μ_0 is extracted from experiment. These kernels depend on the observable O and obey

$$U(\mu_0, \mu_0) = 1, \qquad U(\mu, \mu_1) U(\mu_1, \mu_0) = U(\mu, \mu_0), \tag{1.29}$$

and their action is known as the Renormalization Group (RG). Equation (1.27) is an example of a Renormalization Group Equation (RGE). For a deeper understanding of the RGE's let us consider the gluon n-point function $G_g^{(n)}(p, \alpha_s, m_f)$. Renormalizing this bare Green's function gives

$$G_g^{(n)}(p, \alpha_s, m_f) = Z_A^n(\alpha_s^R)\, G_{g,R}^{(n)}(p, \alpha_s^R(\mu), m_f^R(\mu)), \tag{1.30}$$

where all renormalization factors indirectly depend on μ through $\alpha_s(\mu)$ (see e.g. (1.24)). The RGE for the gluon n-point function then reads

$$\left[\frac{\mu\, \mathrm{d}}{\mathrm{d}\mu} + \frac{\mu\, \mathrm{d}\alpha_s}{\mathrm{d}\mu} \frac{\partial}{\partial \alpha_s} + \frac{\mu\, \mathrm{d}m_f}{\mathrm{d}\mu} \frac{\partial}{\partial m_f} + \frac{n}{2} \frac{\mu\, \mathrm{d} \ln Z_A}{\mathrm{d}\mu} \right] G_g^{(n)}(p, \alpha_s(\mu), m_f(\mu)) = 0, \tag{1.31}$$

where all the constants are renormalized but the index R is dropped for simplicity. The quantities

$$\gamma_A(\alpha_s(\mu)) = \frac{\mathrm{d} \ln Z_A}{\mathrm{d} \ln \mu}, \qquad \gamma_{m_f}(\alpha_s(\mu)) = \frac{\mathrm{d} \ln m_f}{\mathrm{d} \ln \mu}, \tag{1.32}$$

are known as anomalous dimensions. The explicit dependence of the strong coupling constant on μ is described by the beta function

$$\beta(\alpha_s, \epsilon) = \frac{\mu\, \mathrm{d}\alpha_s(\mu)}{\mathrm{d}\mu}. \tag{1.33}$$

The RG has an important role in the calculations of observables in particle physics. In this thesis it will be used to perform resummation, a procedure that will allow us to include large contributions from higher orders. We will e.g. use resummation in section 3.4 for our study of the azimuthal angle between a vector boson and a jet in pp collisions.

1.1.3 Strong coupling constant

The strong coupling constant α_s controls the strength of the interaction between quarks and gluons. It is actually not a constant, but varies due to its dependence on μ, as described by the beta function in equation (1.33). As was true for the renormalization constants themselves, the beta function is calculated order by order. To extract the beta function we use the fact that the bare α_s does not depend on the renormalization scale. Combined with $\alpha_s^{\text{bare}} = \mu^{2\epsilon}\alpha_s Z_\alpha$ (see equation (1.18)), this leads to

$$\mu\frac{\mathrm{d}\alpha_s^{\text{bare}}}{\mathrm{d}\mu} = 0 = \mu^{2\epsilon}Z_\alpha(\alpha_s,\epsilon)\Big(\beta(\alpha_s,\epsilon) + 2\epsilon\alpha_s + \alpha_s\frac{\mathrm{d}\ln Z_\alpha(\alpha_s,\epsilon)}{\mathrm{d}\ln\mu}\Big), \tag{1.34}$$

where the indices R and the explicit dependence on μ are dropped from the renormalized strong coupling constant. Since the renormalization group equation involves finite Green's functions and parameters, it is clear that the beta function should be finite when taking the limit $\epsilon \to 0$. The other $1/\epsilon$ poles in (1.34) must cancel, which we make explicit by writing

$$Z_\alpha(\alpha_s) = 1 + \sum_{\nu=1}^{\infty}\frac{c^{(\nu)}(\alpha_s)}{\epsilon^\nu}, \tag{1.35}$$

where $c^{(\nu)}(\alpha_s)$ are still all order expressions that follow from renormalization. Equation (1.34) now leads to

$$\left(2\epsilon\alpha_s + \sum_{\nu=1}^{\infty}\frac{\alpha_s c^{(\nu)}(\alpha_s)}{\epsilon^\nu} + \beta(\alpha_s,\epsilon) + \beta(\alpha_s,\epsilon)\frac{\mathrm{d}c^{(\nu)}(\alpha_s)}{\mathrm{d}\alpha_s}\frac{1}{\epsilon^\nu}\right) = 0, \tag{1.36}$$

where α_s is the renormalized quantity with implicit μ dependence. The beta function can be determined from the finite terms in this equation by resubstitution. The perturbative form of the beta function is thus

$$\beta(\alpha_s,\epsilon) = -2\epsilon\alpha_s - \frac{\alpha_s^2}{4\pi}\sum_{n=0}\beta_n\left(\frac{\alpha_s}{4\pi}\right)^n. \tag{1.37}$$

The state of the art accuracy for the beta function includes calculations up to five-loops [15]. To find β_0, we can substitute the renormalization factor Z_α (see equation (1.168) in appendix 1.4) in (1.36) to find

$$\beta_0 = \frac{11}{3}C_A - \frac{4}{3}n_f T_F. \tag{1.38}$$

Taking the limit $\epsilon \to 0$, the analytical solution for α_s in terms of β_0 is given by

$$\alpha_s(\mu) = \frac{\alpha_s(\mu_0)}{1 + \frac{\beta_0}{2\pi}\alpha_s(\mu_0)\ln\frac{\mu}{\mu_0}}. \tag{1.39}$$

Because β_0 is positive this shows that the value of α_s is decreasing as μ grows. In the limit $\mu \to \infty$ its strength will eventually go to zero, which is a phenomena called asymptotic freedom. This explains why we can think of quarks and gluons as free particles at sufficiently high energies. At low energies the coupling gets so strong that perturbation theory fails and quarks en gluons experience confinement: They cannot be taken apart and are stuck together in hadrons, the objects we actually collide and detect. The energy scale at which our perturbative understanding of QCD fails completely is known as the Landau pole

$$\mu_{\text{pole}} = \mu_0 \exp\left[-\frac{2\pi}{\beta_0\alpha_s(\mu_0)}\right]. \tag{1.40}$$

At this order, with $n_f = 5$ and $\alpha(M_Z) = 0.1179$, the pole is found at $\mu_{\text{pole}} = 87$ MeV and provides a rough estimate for the scale at which we find confinement[2]. The running of α_s has been tested extensively [16], see figure 1.1. In the calculation of physical quantities, α_s will be evaluated at the typical energy scale Q of the process, which is shown on the horizontal axis in figure 1.1.

1.1.4 Infrared limit of QCD

Apart from the UV divergences, QCD also suffers from divergences in the low-energy regime. These infrared (IR) divergences cannot be removed from the theory at the level of Feynman diagrams. When calculating cross sections the IR divergences arise from the phase-space integrals in real radiation matrix elements, but also from the loop integrals in virtual corrections. Eventually IR divergences cancel in the total cross section order by order in perturbation theory when sufficiently inclusive initial and final states are considered, which is known as the KLN theorem [17–19]. To understand where this cancellation of the IR poles comes from, consider additional final state radiation that does not carry energy or goes exactly in the same direction as the particle it radiates from. As it is impossible to differentiate between final states with or without this extra radiation, we have to include all these energy-degenerate final states. This realization leads to the cancellation of IR poles.

[2]We say 'rough' as it will still receive higher order corrections.

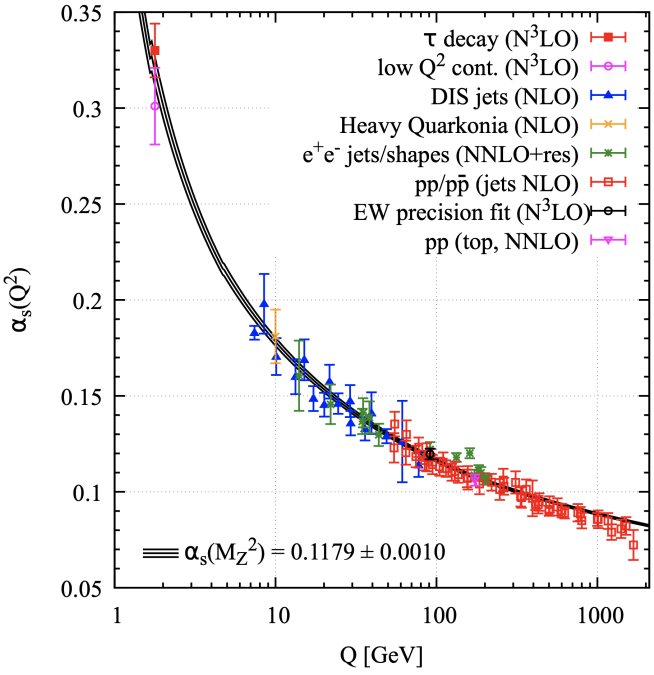

Figure 1.1 Evolution of the strong coupling constant as a function of the energy scale Q. Various experiments (colored errorbars) are included to validate the analytic predictions (black curve). The strong coupling constant becomes large for small energies and small for large energies, corresponding to confined and asymptotically-free quarks at the two ends of the energy spectrum respectively. This figure was taken from the Particle Data Group Collaboration [16].

As a concrete example, consider the cross section for $e^+e^- \to \gamma^* \to$ hadrons. At lowest order there is no extra radiation, see figure 1.2, and IR divergences are absent. At the next order we need to consider the two corrections given in figure 1.3 to include the radiation of a virtual and real gluon.
Calculating the contributions to the cross section we find

$$\sigma^{(1)}_{\text{virtual}} = \sigma^{(0)} \frac{8}{3\Gamma(1-\epsilon)} \left(\frac{4\pi\mu^2}{E_{cm}}\right)^{\epsilon} \left(-\frac{2}{\epsilon^2} - \frac{3}{\epsilon} + \pi^2 - 8 + \mathcal{O}(\epsilon)\right),$$
$$\sigma^{(1)}_{\text{real}} = \sigma^{(0)} \frac{8}{3\Gamma(1-\epsilon)} \left(\frac{4\pi\mu^2}{E_{cm}}\right)^{\epsilon} \left(\frac{2}{\epsilon^2} + \frac{3}{\epsilon} - \pi^2 + \frac{19}{2} + \mathcal{O}(\epsilon)\right), \tag{1.41}$$

where $\sigma^{(0)}$ follows from the born-level diagram,

$$\sigma^{(0)} = \frac{4\pi}{3E_{\text{cm}}} \alpha_s N_c \sum_q e_q^2. \tag{1.42}$$

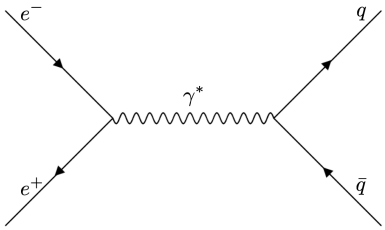

Figure 1.2 The born matrix element for $e^+e^- \to \gamma^* \to q\bar{q}$.

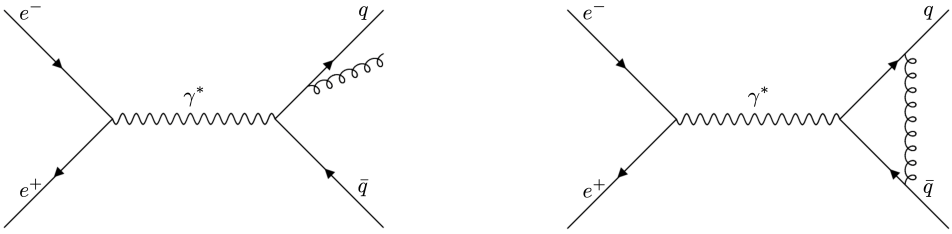

Figure 1.3 The radiative (left) and virtual (right) QCD corrections to the leading order process for $e^+e^- \to \gamma^* \to q\bar{q}$. The diagram with a gluon radiating from the other leg is not shown explicitly, but has to be taken into account in the total cross section.

Here N_c is the number of colors, the sum over q includes all quark flavors with electric charge e_q. The $1/\epsilon$ poles in equation (1.41) are IR divergences, which cancel when summing the virtual and real contribution:

$$\sigma(e^+e^- \to \gamma^* \to \text{hadrons}) = \sigma^{(0)} \left(1 + \frac{\alpha_s}{\pi}\right) + \mathcal{O}(\alpha_s^2). \tag{1.43}$$

The kinematic configurations where these poles arise are described by the collinear and soft emissions. The single poles in $1/\epsilon$ correspond to either a collinear or a soft emission and the double poles arise from kinematic regions where particles become soft and collinear at the same time. To validate this statement, let us consider the radiation of a gluon of one of the quark legs. In a massless theory this gives

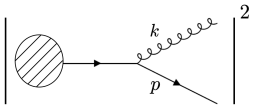

$$\sim \frac{\not{p} + \not{k}}{(k+p)^2} = \frac{\not{p} + \not{k}}{2E_kE_p(1 - cos\theta)}, \tag{1.44}$$

where the striped blob presents the rest of the scattering process. The kinematics of the internal propagator leads to singularities when the emitted gluon carries no energy or propagates in the exact same direction as the quark,

i.e. $E \to 0$ or $\theta \to 0$ respectively[3]. This result is universal, as the appearance of these IR divergences does not depend on the interactions prior to this emission. Note however that for massive particles the collinear singularities are replaced by logarithms of the ratio Q/mass (which still cancel between real and virtual contributions). As there is no suppression of these low-energy emissions, we expect them to dominate scattering processes. This is exactly what we observe in high-energy collisions in the form of collimated sprays of particles called jets. These imprints of the IR limit of QCD will be discussed in section 1.3. Furthermore, the enhancement of soft and collinear radiation allows us to use SCET as an effective field theory to describe their effect in high energy collisions, which shall be discussed in section 1.2.

In this thesis we are particularly interested in proton-proton collisions, as this is studied at high energies at the LHC. Whenever we consider a process with initial protons we cannot describe the initial state with perturbation theory. Instead we perform the perturbative calculation with initial quark and/or gluons. The extraction of a parton from a parent hadron is a non-perturbative process described by the parton distribution function (PDF). An explicit calculation of their partonic counterparts vanishes in dimensional regularization as a result of scaleless integrals, and we conclude that the partonic PDF contains both UV and IR divergences. The KLN theorem cannot guarantee IR finite cross sections when we consider incoming protons, but the remaining IR poles of the partonic calculation cancel exactly against the ones in the PDF. A common perspective is that the IR divergences are absorbed by the PDF such that it has an explicit UV divergence, which can be remedied by renormalization. The PDFs depend on the energy scale of the collision, which is described by the RGE known as the DGLAP equation [20–22]. The PDFs are non-perturbative objects and therefore need to be extracted from experiment.

We saw in equation (1.43) that the cross section $e^+e^- \to \gamma^* \to \text{hadrons}$ was indeed free of IR divergences. Generally, IR poles cancel between real and virtual contributions for inclusive processes. These kind of processes include all possible final state radiation and no cuts on particle properties were introduced. For measurements on the final state, we have to make sure that the cancellation of IR poles remains intact. Observables that do not spoil the convergence due to uncancelled IR poles are called infrared-and-collinear (IRC) safe. This means that the observable is not sensitive to soft emissions or to collinear splittings,

$$\begin{aligned} O(\{p_i\}, k_1, k_2) &= O(\{p_i\}, k_1 + k_2) \quad \text{for} \quad \vec{k}_1 \parallel \vec{k}_2 \\ O(\{p_i\}, k) &= O(\{p_i\}) \quad \text{for} \quad \vec{k} \to 0 \end{aligned} \tag{1.45}$$

[3]It turns out that once the whole interaction is considered, only the limit in which the gluon becomes soft produces a singularity, which is not clear from equation (1.44).

where O represents some measurement on the final state. Examples of IRC safe quantities include event-shapes, e.g. thrust [23], energy-energy correlators [24] and jet cross sections using a well-defined jet algorithm [25]. Jets and jet algorithms shall be discussed in section 1.3.

1.1.5 Appearance of large logarithms

IRC safe observables are free of IR divergences. Generally speaking, cross sections have the following perturbative structure

$$\sigma = \sigma^{(0)} + \frac{\alpha_s}{4\pi}\sigma^{(1)} + \left(\frac{\alpha_s}{4\pi}\right)^2 \sigma^{(2)} + \dots . \tag{1.46}$$

Predictions for the cross section that include all contributions up to some order in α_s are referred to as fixed order (FO) predictions. In particular, predictions that only include $\sigma^{(0)}$ are leading order (LO) predictions, predictions that also include $\sigma^{(1)}$ are called next-to-leading (NLO) predictions, and so on. Terms with a higher power of α_s are increasingly more difficult to calculate, due to the increasing number of diagrams and the complicated divergence structure. Luckily for us, each subsequent term in the perturbative series is less important as long as $\alpha_s \ll 1$.

There is one caveat: The cancellation of the IR poles between real and virtual contributions in IRC safe observables may still introduce large logarithms. These logarithms grow in size in the collinear and/or soft limit, spoiling the convergence of perturbation theory. Scattering processes usually depend on multiple energy scales and the soft and collinear limits of QCD lead to logarithms that depend dimensionless ratios of these energy scales. Consider the dimensionless variable y, the cumulative distributions R is then defined by

$$R = \int_0^y dy' \frac{1}{\sigma_0}\frac{\mathrm{d}\sigma}{\mathrm{d}y} = 1 + \frac{\alpha_s}{4\pi}R_1 + \left(\frac{\alpha_s}{4\pi}\right)^2 R_2 + \dots . \tag{1.47}$$

Each order in α_s is schematically given by

$$R_n = \sum_{m=0}^{2n} c_{n,m} L^m + D(y), \tag{1.48}$$

where c are constants, $L = \ln y$, and $D(y)$ refers to terms that vanish when $y \to 0$. We immediately see the divergence that arises in the $y \to 0$ limit. The perturbative predictions for the cross section therefore become less reliable as y becomes smaller and will eventually break down completely. The regime in which this happens is called the resummation regime. In this regime we may not truncate our prediction at some fixed order. It is however possible to

regain the predictive power by including all order logarithmic contributions. One might be tempted to start by including the largest logs at each order first, then the next-to-largest, and so forth. Even though this method systematically includes contributions with the same scaling, i.e. $\alpha_s \ln^2(y)$ is considered to have the same scaling as $\alpha_s^3 \ln^4(y)$, this is nowadays not the preferred way to include higher order logarithms. As established by the CTTW convention [26, 27], it is convenient to define the accuracy at which logarithms are included in exponentiated form. We therefore write the cumulative cross section R as

$$\begin{aligned} R(y) &= C(\alpha_s) \exp \Sigma + D(\alpha_s, y), \\ &= C(\alpha_s) \exp \Big\{ \frac{\alpha_s}{4\pi} \big[c_{12} L^2 + c_{11} L + c_{10}\big] \\ &\quad + \Big(\frac{\alpha_s}{4\pi}\Big)^2 \big[c_{23} L^3 + c_{22} L^2 + c_{21} L + c_{20}\big] \\ &\quad + \Big(\frac{\alpha_s}{4\pi}\Big)^3 \big[c_{34} L^4 + c_{33} L^3 + c_{32} L^2 + c_{31} L + c_{30}\big] + \dots \Big\} + D(\alpha_s, y), \\ &\qquad\qquad \text{LL} \;+\; \text{NLL} \;+\; \text{N}^2\text{LL} + \text{N}^3\text{LL} + \dots \end{aligned} \tag{1.49}$$

where C is independent of logarithms and can be expanded in α_s,

$$C(\alpha_s) = 1 + \frac{\alpha_s}{4\pi} C_1 + \Big(\frac{\alpha_s}{4\pi}\Big)^2 C_2 + \dots \tag{1.50}$$

Assuming that $L \sim \alpha_s^{-1}$ we see that each column has uniform scaling. The logarithms in the first column are referred to as leading logarithms (LL), the second next-to-leading logarithms (NLL), etc. In this thesis we refer to N^kLL accuracy when including logarithms up to the corresponding column.

The structure in (1.49) is naturally found when we use a separation of scales to calculate the cross section. In chapter 1.2 we will introduce a particular framework in which this factorization of scales is achieved. Concretely, the cross section is written as a product (or convolution) of ingredients involving a single scale. Each element of this factorized cross section has its own RG evolution. The trick is then to evaluate each ingredient at the energy scale where its logarithms vanish and use the RG to evolve all ingredients to a common energy scale (remember we can only choose one μ). This procedure is known as resummation and the potentially large logarithms can then be included at the desired accuracy.

1.2 Soft-Collinear Effective Theory

The most general theory to describe physical phenomena is often very compact, but it can be challenging to use it to make predictions with high precision. In these cases physicists resort to an effective theory, which describes

the dominant physics at the desired energy scale. For example, the elliptic orbits of planets are much easier to calculate in Newtonian gravity than General Relativity. To describe the trajectory of planets while taking all details of general relativity into account is overkill. Newton's law of gravitation had been accepted for more than two hundred years as a valid description of the gravitational force before it was understood as a simplification of the underlying theory of General Relativity. The intuitive idea behind effective theories is thus that you can make reliable predictions without needing the full underlying theory. In a sense we want to think of an effective field theory as the simplest framework that captures the essential physics. In quantum field theory we exploit this idea to construct effective field theories (EFTs). In particular we will use Soft-Collinear effective theory (SCET) to make precise predictions for the effects of QCD radiation in high energy collisions at the LHC.

This chapter will start with a general introduction to effective field theories in section 1.2.1. The rest of the chapter will focus on introducing SCET, the effective theory we will use throughout this thesis to make precise predictions in high energy collisions. First, we will discuss in section 1.2.2 the relevant degrees of freedom. In section 1.2.3 the SCET Lagrangian will be introduced and in section 1.2.4 we explore its symmetries. Lastly will focus on the factorization of the contributing degrees of freedom in section 1.2.5, using an explicit example. This chapter is based on the lecture notes and material in [28–31].

1.2.1 Effective field theories

EFTs are a tool to describe physical phenomena, taking only the relevant degrees of freedom into account. EFTs are constructed in such a way that they exhibit a systematic expansion and a procedure to include higher order corrections. This is done by introducing a small expansion parameter λ that is often defined as the ratio between two energy scales, known as the power counting parameter. Effective field theories are therefore most useful when there is a large separation between the energy scale of interest and the energy scale of the underlying dynamics. In this case effects of the neglected degrees of freedom are small enough to make precise predictions, as λ will be small. The full theory can be expanded in λ up to the desired order of precision. The Lagrangian of the full theory can thus be written as

$$\mathcal{L}_{\text{full}} = \sum_n \mathcal{L}^{(n)}_{\text{EFT}}, \tag{1.51}$$

where n labels the expansion order in the small parameter λ.

The Lagrangian that describes the EFT is constructed in two main steps. First we need to determine the low energy degrees of freedom and write down

all possible operators that respect the symmetries of the full theory. The EFT exhibits the same symmetry properties as the underlying full theory. However, the EFT can have additional symmetries that appear due to expanding. The second step is to determine the coefficients of these operators. If the underlying theory is known, but overly complicated for low-energy calculations, one can employ the top down approach. The coefficients in the EFT Lagrangian are then fixed by a procedure we call matching. This is done by calculating a (simple) observable in both the full theory and EFT, demanding that the low energy limit of the full theory gives the same results as the EFT. On the other hand, if the high-energy theory is not known, the coefficients in the EFT Lagrangian need to be fixed by comparing to experiments (bottom-up approach).

To see how this procedure works, let us consider an illustrative example where the Lagrangian of the full theory is given by

$$\mathcal{L}_{\text{full}} = \frac{1}{2}(\partial\phi)^2 - \frac{1}{2}m\phi^2 + \frac{1}{2}(\partial\rho)^2 - \frac{1}{2}M\rho^2 + g\phi^2\rho, \tag{1.52}$$

where ϕ is a light scalar field with mass m and ρ is a heavy scalar field with mass M. These two fields are coupled by a 3-particle vertex with strength g. In situations where the energy is not high enough to produce heavy particles, we can construct an effective theory that only considers the ϕ as external particles. To construct this EFT we consider only ϕ as a dynamical field (degree of freedom). The Lorentz invariant operators we can write down that obey $\phi \to -\phi$ (a symmetry of equation (1.52)) are

$$\mathcal{L}_{\text{EFT}} = \frac{1}{2}(\partial\phi)^2 - \frac{1}{2}m\phi^2 - \frac{C_4}{4!}\phi^4 + \frac{C_6}{6!M^2}\phi^6 + \dots \tag{1.53}$$

The Wilson coefficients C_n are the dimensionless constants of the corresponding operators with mass dimension n that can be fixed by matching. A priori the 6-dimensional operators that include derivatives $\phi^2\Box\phi$ (e.g. $\phi^2\Box\phi^2, \phi\Box\phi^3$, etc.) must also be included in equation (1.53), but using the equations of motion up to $\mathcal{O}(M^{-4})$ they have all been traded for ϕ^6. The 4-point amplitude in the effective theory is given by

$$\mathrm{i}\mathcal{M}_{\text{EFT}} = -\mathrm{i}C_4. \tag{1.54}$$

The Wilson coefficients C_4 can now be determined by comparing to the calculation of the 4-point correlation in the full theory, expanded in the small

parameter $\lambda = m^2/M^2$.

$$\begin{aligned} \mathrm{i}M_{\text{full}} &= -\mathrm{i}g^2 \left(\frac{1}{s-M^2} + \frac{1}{t-M^2} + \frac{1}{u-M^2} \right), \\ &= \mathrm{i}\frac{g^2}{M^2} \left(3 + \frac{s+t+u}{M^2} + \frac{s^2+t^2+u^2}{M^4} + \cdots \right), \\ &= \mathrm{i}\frac{3g^2}{M^2} + \mathcal{O}(\lambda), \end{aligned} \tag{1.55}$$

where we used that the momenta of the incoming particles are $\sim m^2$ for the energies we are looking at. Matching this expansion to (1.53) sets $C_4 = -3g^2/M^2$. In this example we have $C_n = 0$ for all $n > 4$ Wilson coefficients, since the only interaction in the full theory is $\phi^2\rho$. If one would try to perform the matching for C_6 for example, all the contributions to the 6-ϕ correlation function will be reducible to diagrams with C_4 vertices.

To summarize, let us repeat that the EFTs simplify the calculation by dealing with one scale at a time and including only the relevant interactions. These simplifications allow us to include higher orders in perturbation theory.

1.2.2 SCET degrees of freedom

SCET is the effective theory for infrared (IR) limit of QCD [32–36]. The main difference between SCET and the example in the previous section is the nature of the degrees of freedom of the EFT. The dynamical fields in SCET are the IR degrees of freedom of QCD, while effective interactions describe high-energy QCD (as well as the rest of the SM). SCET is a top-down EFT where off-shell contributions are removed from the full theory, but not fields. As a consequence SCET contains multiple fields that are defined for the same particle, which are required to cleanly separate momentum scales. To construct the SCET Lagrangian we first need to identify and isolate the dominant degrees of freedom (or modes).

Energetic collisions at particle colliders will produce a lot of soft and collinear radiation. This IR radiation plays a crucial role in measurements at the LHC, impacting our understanding of the underlying physics. Both the soft and collinear particles live in the infrared, and are the desired degrees of freedom (or modes) in SCET. The relevant degrees of freedom, effective operators and power counting parameters depend on the process and measurement at hand. Before we proceed, let us introduce light-cone coordinates.

Light-cone coordinates

Light-cone coordinates constitute a natural basis for the four momenta of particles whose energy is much larger than their mass. It is therefore convenient to describe the collinear and soft degrees of freedom that dominate high energy collisions using these coordinates.

The basis of this coordinate system is set by two light-like basis vectors n and $\bar{n}$ that satisfy

$$n^2 = \bar{n}^2 = 0 \qquad \text{and} \qquad n \cdot \bar{n} = 2. \tag{1.56}$$

Obviously this set of auxillary vectors is not unique. An explicit set of light-like vectors that satisfy these equations is given by

$$n^\mu = (1, 0, 0, 1) \qquad \text{and} \qquad \bar{n}^\mu = (1, 0, 0, -1). \tag{1.57}$$

Any 4-vector p^μ can now be represented in light-cone coordinates as

$$p^\mu = \frac{\bar{n}^\mu}{2} p^+ + \frac{n^\mu}{2} p^- + p_\perp^\mu, \tag{1.58}$$

where the plus, minus and perpendicular component are

$$p^+ \equiv n \cdot p = p^0 - p^3, \quad p^- \equiv \bar{n} \cdot p = p^0 + p^3 \quad \text{and} \quad p_\perp^\mu \equiv (0, p^1, p^2, 0). \tag{1.59}$$

To study the degrees of freedom it is useful to introduce the following notation

$$p^\mu = (p^+, p^-, \vec{p}_\perp), \tag{1.60}$$

where the last entry is the two-dimensional Euclidean perpendicular momentum. Using the $(+\,-\,-\,-)$ metric in Minkowski space, the product of two vectors p^μ and q^μ in light-cone coordinates is

$$p \cdot q = \frac{1}{2} \left(p^+ q^- + p^- q^+ \right) - \vec{p}_\perp \cdot \vec{q}_\perp, \tag{1.61}$$

which in particular leads to $p^2 = p^+ p^- - p_\perp^2$.

Modes in SCET

As mentioned before, the degrees of freedom needed to set up SCET depend on the measurement. To illustrate how to choose the appropriate degrees of freedom, let us consider the example of dijet production $e^+e^- \to q\bar{q}$. At lowest order in electroweak corrections this process is mediated by an off-shell photon (or Z-boson) with momenta $q^\mu = (Q, 0, 0, 0)$ in the CM frame. The produced

q and $\bar{q}$ will eventually result in collimated spray of particles that fly in the initial direction of these to partons. These objects are called jets and we will discuss them further in section 1.3. Momentum conservation forces these jets to be back to back at leading order. We choose our light-cone coordinates such that one of the jets points in the n-direction with momentum p_n^μ and the other in the $\bar{n}$-direction with momentum $p_{\bar{n}}^\mu$. Each jet will carry roughly half the energy of the mediating photon. The large momentum component, which will point along the direction of flight, will therefore be of the order of Q, so $p_n^- \sim p_{\bar{n}}^+ \sim Q$. At higher orders the jets are allowed to carry transverse momentum $p_\perp$ due to radiation. To ensure that the jets are indeed a collection of collimated particles, the transverse momentum should be parametrically smaller then the large energy component. Using the on-shell condition and ignoring quark mass effects, we find the scaling of the collinear modes:

$$p_c^\mu \sim Q(\lambda^2, 1, \lambda), \tag{1.62}$$

where $\lambda = \Delta/Q \ll 1$, where Q is referred to as the hard scale and Δ is determined by the measurement. If we want our EFT to work, Δ should be parametrically smaller then Q to retain collinear scaling and larger then Λ_{QCD} to ensure jet formation (otherwise the jet consists of only one or a few hadrons). Simply measuring the invariant mass m_J^2 of the jet would set $\lambda = \sqrt{m_J/Q}$.

We also need to include a soft mode to have all the necessary degrees of freedom, which is homogeneous. Depending on the observable this soft mode can either have soft or ultra-soft scaling:

$$\begin{aligned} p_s^\mu &\sim Q\left(\lambda, \lambda, \lambda\right), \\ p_{us}^\mu &\sim Q\left(\lambda^2, \lambda^2, \lambda^2\right), \end{aligned} \tag{1.63}$$

where the p_{us}^μ and p_s^μ scalings correspond to theories known as $\mathrm{SCET_I}$ and $\mathrm{SCET_{II}}$, respectively. To justify the soft scaling let us return to our $e^+e^- \to q\bar{q}$ example and assume the measurement of the azimuthal decorrelation θ between the two jets (defined such that the back to back situation at leading order has $\theta = 0$). For small angles this is closely related to the relative transverse momentum between the two jets, i.e. $p_\perp \sim \theta Q$. The only way soft radiation can contribute to this offset is when the transverse component of the soft mode has the same scaling as the collinear one. Thus we end up with a $\mathrm{SCET_{II}}$ scaling, where soft modes scale as p_{s}^μ in equation (1.63). Let us now consider the hemisphere mass in $e^+e^- \to q\bar{q}$ instead. The hemisphere mass is defined as the invariant mass of all particles in one (of the two) hemispheres, defined by a half "sphere" centred round the n-direction. Without loss of generality let

us pick n in the direction of q. The hemisphere mass m_n^2 is then defined by

$$m_n^2 = \Big(\sum_i p_i^\mu\Big)^2, \tag{1.64}$$

where the sum on i runs over all particles in the hemisphere. Radiating only a single soft gluon from the quark would lead to

$$m_n^2 = (p_{\rm n}^\mu + p_{us}^\mu)^2 = p_{\rm n}^2 + p_{us}^2 + 2p_{\rm n}\cdot p_{us}. \tag{1.65}$$

Clearly collinear radiation contributes to our measurement as almost all momenta is carried by the jet. The hemisphere mass is therefore of the same order as the jet invariant mass, so $m_n^2 \sim p_{n,\perp}^2 \sim \lambda^2$. The individual terms in equation (1.65) should all contribute at this precision or less. Since the scaling of the collinear radiation is fixed by equation (1.62), $p_{\rm n}\cdot p_{us} = p_{\rm n}^- p_{us}^+ + \ldots$ dominates, leading to the ultrasoft scaling (see p_{us}^μ in equation (1.63)). This is thus an example of $\mathrm{SCET_I}$.

The way soft and/or collinear modes contribute depends on the observable, the details of which determine the relative scaling of the degrees of freedom. The two most used versions of SCET are $\mathrm{SCET_I}$ and $\mathrm{SCET_{II}}$. The former is used when measurements involve the small light-cone momentum component along preferred collinear directions, while the latter is used for observables that include momentum components perpendicular to such directions. These collinear directions are often those of the beams or of outgoing sprays of particles, called jets.

1.2.3 SCET Lagrangian

The detailed derivation of the SCET Lagrangian can be found in [32–35], or in dedicated lecture notes like [30, 37]. Here we will merely show the resulting SCET Lagrangian and briefly describe how to obtain it. We will refer to the $\mathrm{SCET_I}$ Lagrangian as the SCET Lagrangian, as is common in literature. The $\mathrm{SCET_{II}}$ Lagrangian, where the ultrasoft modes are replaced by soft modes, can be found obtained by lowering the virtuality of the collinear modes [38,39]. The big difference is that the ultrasoft fields can interact with all other modes, while the soft fields will at leading power not interact with collinear fields due to its harder scaling. Though we will only discuss the $\mathrm{SCET_I}$ Lagrangian, keep in mind that the $\mathrm{SCET_{II}}$ Lagrangian can still be obtained from the results.

The leading-power SCET Lagrangian is compactly presented by its three sectors:

$$\mathcal{L}^{(0)}_{\rm SCET} = \mathcal{L}^{(0)}_{n\xi} + \mathcal{L}^{(0)}_{ng} + \mathcal{L}^{(0)}_{us}. \tag{1.66}$$

The $\mathcal{L}^{(0)}_{n\xi}$ term describes propagation of collinear quark fields and their interactions with ultrasoft and collinear gluons. The $\mathcal{L}^{(0)}_{ng}$ term describes propagation of the collinear gluon fields and their interactions with the ultrasoft gluons. The sector containing the collinear quarks is obtained from the fermionic QCD Lagrangian, described by interacting Dirac spin-1/2 fields,

$$\mathcal{L}^{\psi}_{\mathrm{QCD}} = \mathrm{i}\bar{\psi}\not{D}\psi. \tag{1.67}$$

We will go through the procedure of building the SCET Lagrangian for this particular sector in steps with some detail. The other two terms in equation (1.66) follow using the same techniques and we therefore only briefly discuss the result.

Step 1: Splitting the fields into their (ultra)soft and collinear parts

The first step is to identify the field components with distinct scaling, which is related to the established modes in the previous section. Let us first split the quark field into a collinear piece and an ultrasoft piece.

$$\psi = \psi_{\mathrm{c}} + \psi_{us}. \tag{1.68}$$

Here we have suppressed the position dependence of the fields for brevity, and will do so throughout this chapter.

As we are deriving the collinear quark part of the SCET Lagrangian, it is convenient to make a preliminary expansion to show that the soft and collinear quarks do not interact with each other and can be dropped. The Lagrangian reads

$$\mathcal{L}_{\psi} = \mathrm{i}\left(\bar{\psi}_{us}\not{D}\psi_{us} + \bar{\psi}_{us}\not{D}\psi_{c} + \bar{\psi}_{c}\not{D}\psi_{us} + \bar{\psi}_{c}\not{D}\psi_{c}\right), \tag{1.69}$$

where we have used equation (1.71) to make the decomposition of the quark field. Ultrasoft and collinear phase space respectively yield λ^{-8} and λ^{-4} scaling; the former compensates for the higher suppression of ultrasoft fields and saves interactions among only such fields. Terms mixing ultrasoft and collinear fields receive the collinear enhancement λ^{-4} and can therefore be dropped from the leading order Lagrangian. The only interesting term besides the purely ultrasoft interactions is

$$\mathcal{L}_{n} = \bar{\psi}_{c}\,\mathrm{i}\not{D}\psi_{c} = \mathrm{i}\bar{\psi}_{c}\left(\frac{\not{n}}{2}\mathrm{i}n\cdot D + \frac{\not{n}}{2}\mathrm{i}\bar{n}\cdot D + \mathrm{i}\not{D}_{\perp}\right)\psi_{c}, \tag{1.70}$$

where we have written the covariant derivative into the light-cone basis for future convenience. The kinetic ultrasoft term is part of $\mathcal{L}^{(0)}_{us}$ and will be discussed later.

Depending on their orientation with respect to the collinear direction, the spin components of collinear fields turn out to scale differently. For this reason we separate the collinear quark field further,

$$\psi_{\mathrm{c}} = (P_n + P_{\bar{n}})\psi_{\mathrm{c}} \equiv \hat{\xi}_n + \phi_{\bar{n}}, \tag{1.71}$$

where we used projection operators defined as

$$P_n = \frac{\not{n}\bar{\not{n}}}{4} \qquad \text{and} \qquad P_{\bar{n}} = \frac{\bar{\not{n}}\not{n}}{4}, \tag{1.72}$$

which obey the relations $P_n^2 = P_n$ and $P_{\bar{n}}^2 = P_{\bar{n}}$. Their effect on the collinear quark field is defined by the identities[4]

$$P_n\hat{\xi}_n = \hat{\xi}_n, \quad P_{\bar{n}}\phi_{\bar{n}} = \phi_{\bar{n}} \quad \text{and} \quad P_n\phi_{\bar{n}} = P_{\bar{n}}\hat{\xi}_n = 0. \tag{1.73}$$

To determine the relative scaling of the constructed constituents of the fermion field we will take a closer look at the two-point functions. Starting with the ultrasoft quark fields we find:

$$\langle 0|\, T\{\psi_{us}(x)\bar{\psi}_{us}(0)\}\,|0\rangle = \int d^4p_{us} e^{-\mathrm{i}p_{us}\cdot x} \frac{\mathrm{i}\not{p}_{us}}{p_{us}^2 + i\epsilon} \sim \lambda^6, \tag{1.74}$$

leading to the scaling $\psi_{us} \sim \lambda^3$. We can do the same for the two components of the collinear quark field.

$$\begin{aligned}
\langle 0|\, T\{\hat{\xi}_n(x)\bar{\hat{\xi}}_n(0)\}\,|0\rangle &= \langle 0|\, T\{P_n\psi_c(x)\bar{\psi}_c(0)P_{\bar{n}}\}\,|0\rangle\,, \\
&= \int \mathrm{d}^4p_c e^{-\mathrm{i}x\cdot p_c} \frac{\mathrm{i}}{p_c^2 + \mathrm{i}\epsilon} \frac{p_c^-\not{n}}{2} \sim \lambda^2, \qquad (1.75) \\
\langle 0|\, T\{\phi_{\bar{n}}(x)\bar{\phi}_{\bar{n}}(0)\}\,|0\rangle &= \langle 0|\, T\{P_{\bar{n}}\psi_c(x)\bar{\psi}_c(0)P_n\}\,|0\rangle\,, \\
&= \int \mathrm{d}^4p_c e^{-\mathrm{i}x\cdot p_c} \frac{\mathrm{i}}{p_c^2 + \mathrm{i}\epsilon} \frac{p_c^+\bar{\not{n}}}{2} \sim \lambda^4, \qquad (1.76)
\end{aligned}$$

where we have used the anti-commutation relation for gamma matrices $\{\gamma^\mu, \gamma^\nu\} = 2\eta^{\mu\nu}$ and the powercounting for momenta in the light-cone basis in equation (1.56) to arrive at the final propagator scaling. The parametric scaling for the collinear quark field components is thus $\hat{\xi}_n \sim \lambda$ and $\phi_n \sim \lambda^2$.

Now that we have separated the spinor components of the fermion field, we still have to do the same for the gauge fields. Again, we split the collinear from the ultrasoft

$$A^\mu = A_n^\mu + A_{us}^\mu. \tag{1.77}$$

[4]The identities for the conjugate fields can be obtained using $\bar{P}_n = P_{\bar{n}}$, e.g. $\bar{\phi}_{\bar{n}}P_{\bar{n}} = 0$.

Here our task of determining the scaling is simpler. The covariant derivative in the Dirac Lagrangian in equation (1.67) dictates that the momenta and the gauge field should scale the same way. We can therefore immediately determine the scaling of the collinear and ultrasoft gluon field by looking at the corresponding modes in equations (1.62) and (1.63):

$$A_n^\mu \sim \left(\lambda^2, 1, \lambda\right), \qquad A_{us}^\mu \sim \left(\lambda^2, \lambda^2, \lambda^2\right). \tag{1.78}$$

Step 2: Integrating out non-dynamical fields

Next, we substitute the decomposition from equation (1.71) in equation (1.70). Note that D still contains both collinear and ultrasoft gluons in this equation. Anti-commutation relations for the gamma matrices and the identities for light-cone basis vectors in equation (1.56) allow us to drop some terms and we find that the collinear Lagrangian reads

$$\mathcal{L}_n = \mathrm{i}\left(\bar{\hat{\xi}}_n \frac{\bar{\not{n}}}{2} n\cdot D \hat{\xi}_n + \bar{\phi}_{\bar{n}} \not{D}_\perp \hat{\xi}_n + \bar{\hat{\xi}}_n \not{D}_\perp \phi_{\bar{n}} + \bar{\phi}_{\bar{n}} \bar{n}\cdot D \phi_{\bar{n}}\right). \tag{1.79}$$

We see that each term in this Lagrangian has the same power counting and we can therefore not use power counting arguments to drop terms in favour of others.

The scaling of the collinear modes in equation (1.62) together with the Dirac equation in light-cone components,

$$\left(\not{n} p_- + \bar{\not{n}} p_+ + \not{p}_\perp\right) u(p) = 0, \tag{1.80}$$

dictate that $\not{n} u(p_n) \sim \lambda$ and $\bar{\not{n}} u(p_n) \sim 1$, where $u(p)$ is the QCD spinor. This means that P_n selects the leading spin component of external fermion states. The spin components of the $\phi_{\bar{n}}$ field are thus suppressed on external, on-shell states. We will therefore not treat $\phi_{\bar{n}}$ as a dynamical field in our Lagrangian and integrate it out, but it still contributes to the Lagrangian via the resulting effective interactions. In practice this is done using the leading order equations of motion for $\phi_{\bar{n}}$,

$$\frac{\delta \mathcal{L}_n}{\delta \phi_{\bar{n}}} - \partial_\mu \frac{\delta \mathcal{L}_n}{\delta \partial_\mu \phi_{\bar{n}}} = 0, \tag{1.81}$$

leading to

$$\phi_{\bar{n}} = \frac{1}{\bar{n}\cdot D} \not{D}_\perp \frac{\not{n}}{2} \hat{\xi}_n. \tag{1.82}$$

Inserting this in the Lagrangian yields

$$\mathcal{L}_{n\xi} = \mathrm{i}\bar{\hat{\xi}}_n \left(n\cdot D + \not{D}_\perp \frac{1}{\bar{n}\cdot D} \not{D}_\perp \right) \frac{\not{n}}{2} \hat{\xi}_n, \tag{1.83}$$

which now only contains dynamical SCET fields. Note that at this point we have separated the ultrasoft from the collinear quark fields and showed that there are no interactions between the two at leading order. No further expansions have been performed yet and the Lagrangian above thus still describes the collinear QCD Lagrangian.

Step 3: Performing a multipole expansion

At this stage, we could use the relative scaling of the fields in position space to start expanding subleading terms away. However, in QFT we prefer to use momentum-space Feynman rules. However, the Fourier transform of the derivative of a collinear field, which appears in the Lagrangian,

$$\int \mathrm{d}^4x \big[\partial^\mu \xi_n(x)\big] e^{ip\cdot x} = \int \mathrm{d}^4x (-\mathrm{i}p_c^\mu) \xi_n(x) e^{\mathrm{i}p_c\cdot x}, \tag{1.84}$$

could reinstate subleading terms through the small momentum components of the collinear momentum p_c. It would therefore be preferable to carry out the expansion step directly in momentum space, such that the need for further expansion is avoided. To serve this purpose we use the so-called label formalism. We start by defining $\tilde{\xi}_n(p)$ as the Fourier transform of $\hat{\xi}_n(x)$

$$\tilde{\xi}_n(p) = \int \mathrm{d}^4x e^{\mathrm{i}p\cdot x} \hat{\xi}_n(x). \tag{1.85}$$

The conventions we use for the Fourier transform are given in appendix A. We now separate the large and small part of the momenta by introducing

$$p^\mu = p_l^\mu + p_r^\mu \qquad \text{with} \qquad p_l \sim (0,1,\lambda), \quad p_r \sim (\lambda^2,\lambda^2,\lambda^2). \tag{1.86}$$

The large label momentum p_l has the small light-cone component in it's scaling set to zero, and the residual momentum describes a perturbation around the large momentum of order λ^2. The residual momenta will be treated as a continuous quantity, whereas the label momenta is discrete[5]. The collinear momenta contain both label en residual components, whereas soft momenta

[5]By combining label and residual momenta, all momenta are continuous in actual calculations.

only consist of a residual component. The phase space integration changes accordingly

$$\text{collinear:} \quad \int \mathrm{d}^4 p_c \to \sum_{p_l \neq 0} \int \mathrm{d}^4 p_r, \tag{1.87}$$

$$\text{ultrasoft:} \quad \int \mathrm{d}^4 p_{us} \to \int \mathrm{d}^4 p_r. \tag{1.88}$$

The ultrasoft momenta have $p_l = 0$ and therefore this is excluded for the integral over the collinear momentum to avoid double counting. It is useful to change notation of our collinear quark to make the discrete nature of the label momentum apparent, i.e.

$$\tilde{\xi}(p) \to \tilde{\xi}_{p_l}(p_r). \tag{1.89}$$

By Fourier transforming only the residual momenta back to position space we create a hybrid field that contains the label momenta in momentum space and the residual momenta in position space

$$\xi_{n,p_l}(x) = \int d^4 p_r e^{-\mathrm{i}p_r \cdot x} \tilde{\xi}_{n,p_l}(p_r). \tag{1.90}$$

The relation to the hatted collinear quark field we introduced in equation (1.71) is given by

$$\hat{\xi}_n(x) = \sum_{p_l \neq 0} e^{-\mathrm{i}p_l \cdot x} \xi_{n,p_l}(x). \tag{1.91}$$

The decomposition into label and residual momenta leads to some statements about label conservation of our hybrid field $\xi_{n,p_l}(x)$: First, interactions with ultrasoft particles do not change the label momenta of collinear fields. Second, interactions between collinear particles will change their label momenta. And last we note that only a hard (external) interaction can couple fields with different collinear directions, such that the collinear label n is preserved. The example in equation (1.84) showed the need for a new procedure when dealing with derivatives. To make derivatives on fields consistent with the label formalism, we define the label momentum operator $\mathcal{P}^\mu$

$$\mathcal{P}^\mu \xi_{n,p_l}(x) = p_l^\mu \xi_{n,p_l}(x) \quad \text{and} \quad \mathcal{P}^\mu \xi^\dagger_{n,p_l}(x) = -p_l^\mu \xi^\dagger_{n,p_l}(x), \tag{1.92}$$

and introduce the notation

$$\mathcal{P}^\mu = \left(0, \bar{\mathcal{P}}, \mathcal{P}_\perp\right), \tag{1.93}$$

where $\bar{\mathcal{P}} = \bar{n}\cdot\mathcal{P} \sim 1$ and $\mathcal{P}_\perp \sim \lambda$. The action of the partial derivative on the hatted collinear field, shown in equation (1.84), is found to

$$\begin{aligned} \mathrm{i}\partial^\mu \xi_n(x) &= \sum_{p_l\neq 0} e^{-\mathrm{i}p_l\cdot x}\left(p_l^\mu \xi_{n,p_l}(x) + \mathrm{i}\partial_r^\mu \xi_{n,p_l}(x)\right), \\ &= e^{-\mathrm{i}\mathcal{P}\cdot x}\sum_{p_l\neq 0}\left(\mathcal{P}^\mu + \mathrm{i}\partial_r^\mu\right)\xi_{n,p_l}(x), \end{aligned} \tag{1.94}$$

where partial derivative ∂_r^μ acting on the hybrid field is now only sensitive to the residual momenta. Finally, we can use the label momentum operator to rewrite $\hat{\xi}_n(x)$ in equation (1.91) a bit further to obtain

$$\hat{\xi}_n(x) = e^{-\mathrm{i}\mathcal{P}\cdot x}\xi_n(x), \tag{1.95}$$

where $\xi_n(x) = \sum_{p_l\neq 0}\xi_{n,p_l}(x)$ is used to simplify the notation. For field products we have

$$\bar{\hat{\xi}}_n(x)\hat{\xi}_n(x) = e^{-\mathrm{i}\mathcal{P}\cdot x}\bar{\xi}_n(x)\xi_n(x), \tag{1.96}$$

where the label operator is understood to act on both fields. Consequently, this phase factor encodes conservation of label momenta.

Step 4: Constructing the leading order Lagrangian

After rewriting our quark and gluon fields in their collinear and ultrasoft counterparts, deriving their distinct scaling, and setting up the label formalism, it is now time to isolate the leading interactions for the collinear quark sector. Using the hybrid fields the Lagrangian is given by

$$\mathcal{L}_{\mathrm{n}}^{(0)} = \mathrm{i}e^{-ix\cdot\mathcal{P}}\bar{\xi}_n\left(\mathrm{i}n\cdot D + i\not{D}_\perp\frac{1}{i\bar{n}\cdot D}\mathrm{i}\not{D}_\perp\right)\frac{\not{\bar{n}}}{2}\xi_n, \tag{1.97}$$

where the derivative operators read

$$\begin{aligned} \mathrm{i}n\cdot D &= \mathrm{i}\partial_r^+ + gA_n^+ + gA_{us}^+, \\ \mathrm{i}\bar{n}\cdot D &= \bar{\mathcal{P}} + \partial_r^- + gA_n^- + gA_{us}^-, \\ \mathrm{i}D_\perp^\mu &= \mathcal{P}_\perp^\mu + \partial_{r,\perp}^\mu + gA_{n\perp}^\mu + gA_{us\perp}^\mu, \end{aligned} \tag{1.98}$$

where we used the notation in equation (1.60) to denote different components of the fields. After expanding the operators up to leading order we arrive at the final result

$$\mathcal{L}_{\mathrm{n}\xi}^{(0)} = ie^{-ix\cdot\mathcal{P}}\bar{\xi}_n\left(in\cdot D_n + i\not{D}_{n\perp}\frac{1}{i\bar{n}\cdot D_n}i\not{D}_{n\perp}\right)\frac{\not{\bar{n}}}{2}\xi_n, \tag{1.99}$$

where we have defined the collinear covariant derivatives in which the $\mathcal{O}(\lambda^2)$ terms are expanded away

$$\begin{aligned} in\cdot D_n &\equiv i\partial_r^+ + gA_n^+ + gA_{us}^+, \\ i\bar{n}\cdot D_n &\equiv \bar{\mathcal{P}} + gA_n^-, \\ iD_{n\perp}^\mu &\equiv \mathcal{P}_\perp^\mu + gA_{n\perp}, \end{aligned} \tag{1.100}$$

where $n\cdot D_n = n\cdot D$ as no terms are expanded out in this case. After these manipulations all terms in $\mathcal{L}^0_{\mathrm{n}\xi}$ now have the same λ^0 scaling. To arrive at the $\mathrm{SCET_{II}}$ Lagrangian the soft gluon fields would be dropped from the collinear covariant derivatives, as the interaction between a soft and two collinear particles would spoil the collinear power counting.

Starting from the gluon QCD Lagrangian, and following the same steps as in the quark case, the leading power collinear gluon $\mathrm{SCET_I}$ Lagrangian is

$$\mathcal{L}^{(0)}_{\mathrm{ng}} = \frac{1}{2g^2}\mathrm{Tr}\Big\{[\mathrm{i}D_n^\mu, \mathrm{i}D_{n\mu}]^2\Big\} + \frac{1}{\xi}\mathrm{Tr}\Big\{[\mathrm{i}D_{us}^\mu, A_{n\mu}]^2\Big\} + 2\mathrm{Tr}\big\{\bar{c}_n[\mathrm{i}D_{us}^\mu, [\mathrm{i}D_{n\mu}, c_n]]\big\}, \tag{1.101}$$

where ξ is the gauge fixing parameter and c are the ghost fields, which find their origin in the covariant gauge in (1.11). The components of the derivative D_n at leading power are given in equation (1.100) and the components of its ultrasoft analogue that only includes ultrasoft gauge fields are

$$\mathrm{i}n\cdot D_{us} = \mathrm{i}\partial_r^+ + gA_{us}^+, \quad \mathrm{i}\bar{n}\cdot D_{us} = \bar{\mathcal{P}} \quad \text{and} \quad D^\mu_{us,\perp} = \mathcal{P}^\mu_\perp. \tag{1.102}$$

The ultrasoft sector of the SCET Lagrangian is simply obtained by a copy of the original QCD Lagrangian where every field is replaced by its ultrasoft counterpart. We already saw that the decomposition of the quark field in equation (1.68) naturally led to the kinetic term for ultrasoft quarks. None of the original terms drop out upon expanding, due to the homogeneous nature of these ultrasoft modes.

$$\mathcal{L}^{(0)}_{us} = \bar{\psi}_{us}\mathrm{i}\not{\mathcal{D}}_{us}\psi_{us} - \frac{1}{4}(G^a_{us,\mu\nu})^2 - \frac{1}{2\xi_{us}}(\partial_r^\mu A^a_{us,\mu})^2 + \partial_r^\mu \bar{c}^a_{us}\mathcal{D}^{ab}_{us,\mu}c^b_{us}, \tag{1.103}$$

where $G^a_{us,\mu\nu}$ is the field strength tensor that only contains ultrasoft gauge fields. The ξ_{us} is the gauge fixing parameter for the soft sector, unless stated otherwise we use $\xi_{us} = 1$. Note that $\mathcal{D}^\mu_{us}$ denotes the unexpanded ultrasoft covariant derivative:

$$\mathcal{D}^\mu_{us} = \partial_r^\mu - igA^\mu_{us}. \tag{1.104}$$

To describe events involving multiple well-separated directions, SCET introduces a different set of dynamical collinear modes for each of those directions. This goes beyond the dijet example we discussed in section 1.2.2, where two back-to-back collinear directions were needed. Interactions between different collinear sectors will have hard scaling. For this reason, these interactions are always integrated out and show up through operators describing the hard scattering with a corresponding hard matching coefficient. Additional collinear sectors are therefore introduced by simply adding a copy of the collinear sector to the Lagrangian, as it also contains the interactions with the ultrasoft gluons.

1.2.4 Symmetries of SCET

In Quantum Field Theories the Lagrangian is often built on underlying symmetries. In this section we will explore the symmetries of the SCET Lagrangian and how we can exploit them to make invariant building blocks, which naturally constrain the effective operators. These effective operators describe the interactions of our dynamical degrees of freedom in SCET with the rest of the SM. The SCET Lagrangian at tree level was directly obtained from QCD at tree level. There are a few symmetries that SCET directly inherited, like parity, and charge conjugation. In addition QCD also has gauge invariance and Lorentz symmetry, however they look somewhat different in SCET. In this section we discuss both, starting with reparametrization invariance, which is related to Lorentz symmetry.

By fixing the reference vectors n and $\bar{n}$ in equation (1.57), the original Lorentz symmetry is broken. However, this freedom is now captured by the reparameterization invariance of these basis vectors. This is known as reparametrization invariance (RPI). There are three types of RPI transformations under which the basis vectors still keep their defining properties in equation (1.56). Each of them takes n and $\bar{n}$ to an equally valid set of light-cone coordinates,

$$I: \begin{cases} n^\mu \to n^\mu + \delta_\perp^\mu \\ \bar{n}^\mu \to \bar{n}^\mu \end{cases} \qquad II: \begin{cases} n^\mu \to n^\mu \\ \bar{n}^\mu \to \bar{n}^\mu + \varepsilon_\perp^\mu \end{cases} \qquad III: \begin{cases} n^\mu \to e^\alpha n^\mu \\ \bar{n}^\mu \to e^{-\alpha} \bar{n}^\mu \end{cases} \tag{1.105}$$

where $\delta_\perp$, $\varepsilon_\perp$ and α are parameters, for which $n \cdot \delta_\perp = \bar{n} \cdot \delta_\perp = n \cdot \varepsilon_\perp = \bar{n} \cdot \varepsilon_\perp = 0$. The scaling of these parameters is such that they do not spoil the power counting: $\delta_\perp \sim \lambda$, $\varepsilon_\perp \sim 1$ and $\alpha \sim 1$. Constructing SCET operators is now constrained by RPI and in particular they can only appear in three combinations

$$(A \cdot n)\,(B \cdot \bar{n})\,, \quad \frac{A \cdot n}{B \cdot n}, \quad \frac{A \cdot \bar{n}}{B \cdot \bar{n}}, \tag{1.106}$$

where A^μ and B^μ are arbitrary operators built from SCET fields. Another reparameterization invariance was introduced with the decomposition into label (p_l) and residual momenta (p_r). We are free to split the total into p_l and p_r in different ways as long as it maintains their relative power counting. This is evident by the invariance under the following transformation

$$\mathcal{P}^\mu \to \mathcal{P}^\mu + \beta^\mu, \quad \partial_r^\mu \to \partial_r^\mu - \beta^\mu, \tag{1.107}$$

where $\beta \sim \lambda^2$. Invariance requires

$$\mathcal{P}^\mu + \mathrm{i}\partial_r, \tag{1.108}$$

to be grouped together for collinear fields. It is important to note that invariance under any of the discussed reparametrizations links different orders in power counting.

The general gauge transformations inherited from QCD mix fields with distinct power counting. In practical terms such a transformation could turn ultrasoft gluons into collinear gluons, which we do not allow in our EFT. The gauge transformations in SCET are found in the same way as we found our Lagrangian: we have to make a decomposition based on power counting. This results in two kinds of gauge transformations: collinear and ultrasoft. They are

$$U_n(x) = \exp[\mathrm{i}\alpha_n^a t_a] \qquad \text{and} \qquad U_{us}(x) = \exp[\mathrm{i}\alpha_{us}^a t_a], \tag{1.109}$$

where α_{us}^a is a real function with $a = 1, \ldots, 8$. They are defined as the subset of gauge transformations where $\partial_\mu U_{us}(x) \sim \lambda^2$ and $\partial_\mu U_n(x) \sim (\lambda^2, 1, \lambda)$. The dynamical SCET fields transform under these gauge transformations according to

$$\text{collinear:} \quad \begin{cases} \xi_n(x) & \to U_n(x)\xi_n(x) \\ A_n^\mu(x) & \to U_n(x)A_n^\mu(x)U_n^\dagger(x) + \frac{\mathrm{i}}{g}U_n(x)D_{us}^\mu U_n^\dagger(x) \\ \psi_{us}(x) & \to \psi_{us}(x) \\ A_{us}^\mu(x) & \to A_{us}^\mu(x) \end{cases} \tag{1.110}$$

and

$$\text{ultrasoft:} \quad \begin{cases} \xi_n(x) & \to U_{us}(x)\xi_n(x) \\ A_n^\mu(x) & \to U_{us}(x)A_n^\mu(x)U_{us}^\dagger(x) \\ \psi_{us}(x) & \to U_{us}(x)\psi_{us}(x) \\ A_{us}^\mu(x) & \to U_{us}(x)A_{us}^\mu(x)U_{us}^\dagger(x) + \frac{\mathrm{i}}{g}U_{us}(x)\partial_r^\mu U_{us}^\dagger(x) \end{cases} \tag{1.111}$$

The collinear gauge transformations do not act on the ultrasoft particles, since these particles cannot resolve the fast local changes induced by $U_n(x)$. Oppositely, the collinear fields are affected by ultrasoft transformations, consistent with their contact term in the collinear Lagrangian. However, these transformations do not include the partial derivative for the collinear gauge field, reflecting the fact that they see it as a smooth change in the background [35]. If we were to introduce more collinear sectors to match the collinear directions of a collision, we have to introduce a separate RPI for each n_i sector. Furthermore, each collinear field will have its own gauge transformation generated by U_{n_i}, which only operate in their own collinear sector.

In order to construct gauge invariant building blocks, we introduce the collinear Wilson line

$$W_n \equiv \mathbf{P} \exp\left\{ \mathrm{i}g \int_{-\infty}^{0} \mathrm{d}s\, \bar{n} \cdot A_n(x + s\bar{n}) \right\}, \tag{1.112}$$

where $\mathbf{P}$ denotes the path ordering. In terms of label momenta, the collinear Wilson line can be defined by

$$\mathrm{i}D_n^- W_n = (\mathcal{P}^- + gA_n^-) W_n = 0, \tag{1.113}$$

which leads to the identities

$$\mathrm{i}D_n^- = W_n \mathcal{P}^- W_n^\dagger \qquad \text{and} \qquad \frac{1}{\mathrm{i}D_n^-} = W_n \frac{1}{\mathcal{P}^-} W_n^\dagger. \tag{1.114}$$

The Wilson line transforms under both ultrasoft and collinear gauge transformations

$$\begin{aligned} W_n(x) &\xrightarrow{\text{collinear}} U_n(x) W_n(x), \\ W_n(x) &\xrightarrow{\text{soft}} U_{us}(x) W_n(x) U_{us}^\dagger(x), \end{aligned} \tag{1.115}$$

where the ultrasoft transformations mirror the ones for a single collinear gluon field and the collinear transformations follow from (1.113).

The collinear Wilson line naturally appears when constructing effective operators. As an example let us go back to dijet production. In full QCD this process would be induced by the current,

$$J_{q\bar{q}}^{\mathrm{QCD},\mu} = \bar{\psi} \Gamma^\mu \psi, \tag{1.116}$$

where Γ^μ describes the EW coupling to a photon or vector boson. In SCET the corresponding current at tree level is

$$J_{q\bar{q}}^{(0),\mu} = \bar{\xi}_n \Gamma_i^\mu \xi_{\bar{n}}. \tag{1.117}$$

Now we can consider the situation where we radiate a gluon from one of the external quarks. Without loss of generality we assume the $\bar{q}$ is radiating. In the SCET language we see that this is reconstructed by attaching a soft, $\bar{n}$-collinear or n-collinear gluon to the $\bar{n}$-collinear quark. The first two are reproduced by the SCET lagrangian. However, attaching a n-collinear gluon to the $\bar{n}$-collinear quark spoils the powercounting of the quark-line and takes the internal quark off-shell. Therefore it is integrated out, leading to the (new) effective operator

$$J^{\mu,1}_{q\bar{q}} = \bar{\xi}_n \left[\frac{-gA^-_n}{q^-}\right] \Gamma^\mu_i \xi_{\bar{n}}. \tag{1.118}$$

We can repeat this process by considering additional gluon radiation, which would introduce a new effective operator at each step. However, it is more convenient to construct an operator that contains all the leading power corrections by default. This is summarized by

$$\langle 0| J^{\mathrm{QCD},\mu}_{q\bar{q}} |0\rangle = C \langle 0| J^\mu_{q\bar{q}} |0\rangle, \tag{1.119}$$

where we take the appropriate limit on the LHS. Iteratively using the result for additional gluon radiation in equation (1.118) and summing over all permutations we find the SCET operator for an arbitrary number of n-collinear gluons

$$J^{(n),\mu}_{q\bar{q}} = \bar{\xi}_n \left[\sum_{\text{perms}} \frac{(-g)^m}{m!} \frac{A^-_n(q_1) \times \ldots A^-_n(q_m)}{q_1^- \left(q_1^- + q_2^-\right) \ldots \left(\sum_{i=1}^m q_i^-\right)}\right] \Gamma^\mu_i \xi_{\bar{n}}, \tag{1.120}$$

where the order m denotes the number of gluons radiated with incoming momentum q_i and each gluon field needs to be understood as $A^-_n = A^{a,-}_n T_a$. The addition of any number of additional collinear gluons is then expressed by $J^\mu_{q\bar{q}} = \sum_{m=0}^\infty J^{(m),\mu}_{q\bar{q}} = \bar{\xi}_n W_n \Gamma^\mu \xi_{\bar{n}}$, where W_n is the collinear Wilson line found in equation (1.112). The same can be argued for the attachment of $\bar{n}$-collinear gluons to the n-collinear quark line, which results in an $\bar{n}$-collinear Wilson line. The resulting current is therefore given by

$$J^\mu_{q\bar{q}} = \sum_{m=0,n=0}^\infty J^{(m),\mu}_{q\bar{q}} = \bar{\xi}_{q,n} W_n \Gamma^\mu W^\dagger_{\bar{n}} \xi_{\bar{q},\bar{n}}. \tag{1.121}$$

The Wilson lines incorporate all possible additions of collinear gluons to the leading order SCET current and restore gauge invariance of the operator. In general, the gauge transformation properties allow us to construct collinear gauge-invariant building blocks,

$$\chi_n = W^\dagger_n \xi_n, \quad B^\mu_{n,\perp} = \frac{1}{g}\left(\frac{1}{\bar{P}} W^\dagger_n \left[D^\mu_{n\perp}, \bar{n}\cdot D_n\right] W_n\right) \quad \text{and} \quad P^\mu_{n\perp}, \tag{1.122}$$

where the $\bar{P}$ only acts inside the outer brackets. The quark jet field χ_n showed up in the derivation of the current above and the gluon jet field $B^\mu_{n,\perp}$ is the gluon analogue. The fields ξ_n and A_n can only appear in hard scattering operators through these gauge invariant building blocks.

1.2.5 Factorization in SCET

The collinear and ultrasoft fields in the SCET Lagrangian are still coupled through the appearance of the ultrasoft covariant derivative appearing in the collinear quark and gluon Lagrangians, given by equation (1.99) and (1.101) respectively. The main power of SCET lies in the possibility to completely separate collinear from ultrasoft fields by making appropriate field redefinitions [40, 41], known as the Bauer-Pirjol-Stewart (BPS) field redefinitions [42]. The factorization of soft and collinear fields at the level of the Lagrangian is an essential ingredient to derive factorization theorems for numerous processes.

Soft-collinear factorization

Let us first introduces the ultrasoft Wilson line Y_n, given by

$$Y_n(x) \equiv \mathbf{P} \exp\left\{ ig \int_{-\infty}^{0} \mathrm{d}s \, n \cdot A_{us}(x + sn) \right\}, \tag{1.123}$$

where $\mathbf{P}$ denotes path ordering. Ulltrasoft Wilson lines are unitary operators and vanish under the ultrasoft covariant derivative, i.e.

$$Y_n^\dagger Y_n = 1 \qquad \text{and} \quad in \cdot D_{us} Y_n(x) = 0. \tag{1.124}$$

In analogy to the collinear Wilson line, the ultrasoft Wilson line includes all possible ultrasoft gluon radiations from a collinear particle. Motivated by the fact that collinear particles will always be accompanied by a haze of soft gluons we transform the SCET fields as

$$\begin{aligned} \xi_{n,p_l} &\to Y_n \xi_{n,p_l} \\ A^\mu_{n,p_l} &\to Y_n A^\mu_{n,p_l} Y_n^\dagger \\ W_n &\to Y_n W_n Y_n^\dagger \\ c_{n,p_l} &\to Y_n c_{n,p_l} Y_n^\dagger \end{aligned} \tag{1.125}$$

which are known as the BPS field redefinitions. Note that the transformation of the collinear Wilson line directly follows from the transformation of the collinear gluon field. The BPS transformation of the ghost field is included for

completeness, as we will only describe the decoupling in the collinear quark sector in detail.

Let us now investigate what happens to the collinear quark Lagrangian when we implement the redefinitions in equation (1.125). We start with the Lagrangian in equation (1.99) and use the first identity in equation (1.114) to rewrite it as

$$\mathcal{L}^{(0)}_{n\xi} = e^{-i\mathcal{P}\cdot x}\bar{\xi}_n \left[iD^+_{us} + gA^+_n + \left(\bar{\mathcal{P}}_\perp + g\bar{\mathcal{A}}_{n\perp}\right) W_n \frac{1}{\mathcal{P}^-} W_n^\dagger \left(\mathcal{P}_\perp + g\mathcal{A}_{n\perp}\right)\right] \frac{\bar{n}\!\!\!/}{2}\xi_n, \tag{1.126}$$

where D_{us} is defined in equation (1.102). Performing the BPS field redefinitions in equation (1.125) dresses the collinear quark and gluon fields with ultrasoft Wilson lines. They cancel everywhere except for the term that includes the ultrasoft derivative. Here we exploit the second identity in equation (1.124), which leads to

$$\mathrm{i}D^+_{us} = Y_n \mathrm{i}\partial^+_r Y_n^\dagger, \tag{1.127}$$

similar to the identity in equation (1.114) for the collinear Wilson line. Combining equation (1.127) with the BPS field redefinition of ξ_{n,p_l} then also for the first term results in the cancellation of the ultrasoft Wilson lines. Summarizing this discussion: performing the BPS field redefinitions and using the identity in equation (1.127), yields

$$\mathcal{L}^{(0)}_{n\xi} \to e^{-\mathrm{i}\mathcal{P}\cdot x}\bar{\xi}_n \left[\mathrm{i}\partial^+_r + gA^+_n + \left(\bar{\mathcal{P}}_\perp + g\bar{\mathcal{A}}_{n\perp}\right) W_n \frac{1}{\mathcal{P}^-} W_n^\dagger \left(\mathcal{P}_\perp + g\mathcal{A}_{n\perp}\right)\right] \frac{\bar{n}\!\!\!/}{2}\xi_n, \tag{1.128}$$

where the ultrasoft gluons completely disappeared. This decoupling is also found in the collinear gluon Lagrangian upon using BPS field redefinitions. Clearly the interactions with the ultrasoft sector did not vanish into thin air. The BPS transformations effectively move the interactions between collinear fields and ultrasoft gluons into the currents describing the hard scattering, as the redefinition of the field has to be implemented everywhere. For the dijet example we discussed previously this results in [35]

$$J^\mu_{q\bar{q}} = \bar{\xi}_n W_n \Gamma^\mu W_n^\dagger \xi_{\bar{n}} \to \underbrace{\left[\bar{\xi}_n W_n\right]}_{\bar{n}\text{-collinear}} \underbrace{\left[Y_n^\dagger Y_{\bar{n}}\right]}_{\text{ultrasoft}} \Gamma^\mu \underbrace{\left[W_{\bar{n}}^\dagger \xi_{\bar{n}}\right]}_{n-\text{collinear}}, \tag{1.129}$$

where we see our first example of factorization at the level of the operator. After the decoupling the operator is decomposed into the product of collinear, ultrasoft and anti-collinear fields.

Hard factorization

We have introduced all necessary degrees of freedom in SCET to describe the infrared behaviour of QCD. The Wilson coefficients of the scattering operators we can construct in SCET contain the residues of the degrees of freedom that were integrated out (see equation (1.119)). In a sense the hard factorization is therefore automatic for SCET, where we match to full QCD through a convolution between the operators and the Wilson coefficient. The Wilson coefficient will depend on the large momenta, as it encodes the high-energy dynamics of QCD. It is therefore constructed from the large component of the label operator $P_{n_i}^-$, where i indicates the inclusion of all collinear directions. As it is an operator by itself in label momentum space, the convolution over new label momenta ω_{n_i} is introduced. The dijet current in equation (1.121), which includes two collinear directions, then gives

$$J_{q\bar{q}}^{\mu} = \int \mathrm{d}\omega_n \mathrm{d}\omega_{\bar{n}} C_{q\bar{q}}(w_n, w_{\bar{n}}) \bar{\chi}_n \delta(\omega_n - \bar{\mathcal{P}}_n^{\dagger}) Y_n^{\dagger} Y_{\bar{n}} \Gamma^{\mu} \delta(\omega_{\bar{n}} - \bar{\mathcal{P}}_{\bar{n}}) \chi_{\bar{n}}, \quad (1.130)$$

where we have used that $\bar{\mathcal{P}}_n = \bar{n} \cdot \mathcal{P}_n$ and $\bar{\mathcal{P}}_{\bar{n}} = n \cdot \mathcal{P}_{\bar{n}}$. In this example there are only two collinear directions. In general, multiple collinear directions can be included by using $\chi_{n_i,\omega_i} = \delta(\omega_i - \bar{\mathcal{P}}_i)\chi_i$.

At this point we have introduced all the tools to completely separated the soft, collinear and hard degrees of freedom. We will now discuss how to factorize the cross section in the example of $e^+e^- \to q\bar{q}$ scattering. The cross section for this process, which is related to the squared transition amplitude by integrating over all intermediate states, is

$$\sigma = \sum_{\vec{n}} \sum_{X}^{\text{dijet}} (2\pi)^4 \delta^4(q - P_X) \sum_{i=v,a} L_{\mu\nu}^{(i)} \langle 0 | J_{i,q\bar{q}}^{\nu\dagger} | X \rangle \langle X | J_{i,q\bar{q}}^{\mu} | 0 \rangle . \quad (1.131)$$

The current $J_{i,q\bar{q}}^{\mu}$ generates a $q\bar{q}$ pair along a specific $\vec{n}$ direction. To calculate the cross section we must therefore sum over all final state (back-to-back) directions. The Dirac delta function ensures momentum conservation, as q^{μ} is the momentum sum of the incoming leptons and P_X^{μ} the momentum sum of the outgoing particles in state X. The sum is restricted to dijet configurations. The leptonic tensor $L_{\mu\nu}^{i}$ describes the production of the intermediate boson (Z^*, γ^*) from the initial e^+e^- pair. To correctly describe the process we need to include both the vector and axial currents, indicated by the sum over i. They are given by equation (1.130), with $\Gamma_v^{\mu} = \gamma^{\mu}$ and $\Gamma_a^{\mu} = \gamma^{\mu}\gamma_5$ for the vector and axial current respectively. The fact that the SCET fields are completely decoupled on the level of the Lagrangian, implies that the Hilbert space is also

factorized. For our example this means

$$\sum_{n_i=n,\bar{n}} \mathcal{L}^{(0)}_{n_i\xi} + \mathcal{L}^{(0)}_{n_i g} + \mathcal{L}^{(0)}_{us} \tag{1.132}$$
$$\Rightarrow \sum_{X}^{\text{dijet}} |X\rangle \langle X| = \sum_{X_n} \sum_{X_{\bar{n}}} \sum_{X_{us}} |X_n\rangle \langle X_n| \otimes |X_{\bar{n}}\rangle \langle X_{\bar{n}}| \otimes |X_{us}\rangle \langle X_{us}| \,.$$

The collinear and ultrasoft fields now only live within their respective sectors and the factorization of operators therefore directly translates to factorization theorems for cross sections:

$$\begin{aligned}
\sigma = & \sum_{\vec{n}} \int \mathrm{d}\omega_n \mathrm{d}\omega_{\bar{n}} \mathrm{d}\omega'_n \mathrm{d}\omega'_{\bar{n}} C(\omega_n, \omega_{\bar{n}}) C^*(\omega'_n, \omega'_{\bar{n}}) L_{\mu\nu} \Gamma^\mu_{ij} \Gamma^\nu_{kl} \\
& \times \sum_{X_n} \sum_{X_{\bar{n}}} \sum_{X_{us}} (2\pi)^4 \delta^4(q - P_{X_n} - P_{X_{\bar{n}}} - P_{X_{us}}) \\
& \times \langle 0| \, \delta(\omega'_n - \bar{\mathcal{P}}_n)(\chi_n)^c_j \, |X_n\rangle \langle X_n| \, (\bar{\chi}_n)^d_k \delta(\omega_n - \bar{\mathcal{P}}^\dagger_n) \, |0\rangle \\
& \times \langle 0| \, (\bar{\chi}_{\bar{n}})^a_i \delta(\omega'_{\bar{n}} - \bar{\mathcal{P}}^\dagger_{\bar{n}}) \, |X_{\bar{n}}\rangle \langle X_{\bar{n}}| \, \delta(\omega_{\bar{n}} - \bar{\mathcal{P}}_{\bar{n}})(\chi_{\bar{n}})^f_l \, |0\rangle \\
& \times \langle 0| \, \bar{T}\{(Y^\dagger_{\bar{n}})_{ab}(Y_n)_{bc} \, |X_{us}\rangle \langle X_{us}| \, T\{(Y^\dagger_n)_{de}(Y_{\bar{n}})_{ef}\} \, |0\rangle \,,
\end{aligned} \tag{1.133}$$

where a, b, c, d, e, f are color indices and i, j, k, l are spin indices and the sum over all of these indices is implicit. The sum over the axial and vector contributions is left implicit through the unspecified Dirac structures Γ, but note that only axial-axial and vector-vector contributions are possible. Color and spin indices are still contracted between different sectors. However, in SCET each sector contribution to the cross-section must separately be a spin and color singlet. We thus need to rearrange the color and spinor indices so that they are fully contracted within each of the n-collinear, $\bar{n}$-collinear, and soft product of matrix elements. The color indices are easily untangled by the restriction that each sector should be a color singlet. This leads to

$$\langle 0| \, (\chi_n)^c_j \, |X_n\rangle \langle X_n| \, (\bar{\chi}_n)^d_k \, |0\rangle = \frac{\delta^{cd}}{N_c} \langle 0| \, (\chi_n)^b_j \, |X_n\rangle \langle X_n| \, (\bar{\chi}_n)^b_k \, |0\rangle \,, \tag{1.134}$$

that will let the ultrasoft Wilson lines contract among themselves, leading to the matrix element

$$\langle 0| \, \mathrm{Tr}\left[\bar{T}\{Y^\dagger_{\bar{n}} Y_n\} T\{Y^\dagger_n Y_{\bar{n}}\}\right] |0\rangle \,. \tag{1.135}$$

The restriction that each sector should be a spin singlet is accomplished by using the spin Fierz identity, which allows us to write any expression of the form

$\bar{\psi}_1 A \psi_2 \bar{\psi}_3 B \psi_4$ as $\bar{\psi}_1 C \psi_4 \bar{\psi} D \psi$ or a sum of such terms, were C, D are matrices from the same basis. Explicitly, for our matrix element this yields

$$\langle 0|\, \bar{\chi}_{\bar{n}} \Gamma^\mu \chi_n \bar{\chi}_n \Gamma^\nu \chi_{\bar{n}} \,|0\rangle = \sum_{A,B} C_{AB}^{\mu\nu} \langle 0|\, \bar{\chi}_n F_A \chi_n \,|0\rangle \langle 0|\, \bar{\chi}_{\bar{n}} F_B \chi_{\bar{n}} \,|0\rangle\,, \tag{1.136}$$

with $C_{AB}^{\mu\nu} = \frac{1}{4}\mathrm{Tr}\left[\Gamma^\mu F_A \Gamma^\nu F_B\right]$. The basis $\{F\}$ is given by the 16 Dirac bilinears expressed in light-cone coordinates. The possible combinations we need are given by the SCET Fierz formula [43, 44],

$$\mathbb{1} \otimes \mathbb{1} = \frac{1}{2}\left[\frac{\bar{n}\!\!\!/}{2} \otimes \frac{n\!\!\!/}{2} + \left(\frac{-\bar{n}\!\!\!/\gamma^5}{2}\right) \otimes \left(\frac{n\!\!\!/\gamma^5}{2}\right) + \left(\frac{-\bar{n}\!\!\!/\gamma_{\perp\alpha}}{2}\right) \otimes \left(\frac{n\!\!\!/\gamma_\perp^\alpha}{2}\right)\right], \tag{1.137}$$

Note that in deriving this formula we started with the complete basis, i.e. including combinations like $\langle 0|\, \bar{\chi}_n \gamma_5 \chi_n \,|0\rangle$ and $\langle 0|\, \bar{\chi}_{\bar{n}} \frac{\bar{n}\!\!\!/}{2} \chi_{\bar{n}} \,|0\rangle$. However, these terms vanish due to the properties in equation (1.56). The only surviving terms are summarized by equation (1.137), which is valid when the identity matrices are inserted so that the $\bar{n}$ terms on the RHS appear between χ_n and $\bar{\chi}_n$ and the n terms between $\chi_{\bar{n}}$ and $\bar{\chi}_{\bar{n}}$. Demanding parity invariance of the collinear matrix elements implies that matrix elements where an extra γ_5 or $\gamma_\perp$ is inserted vanish. It is important to note that the axial vector current has exactly the same decomposition as the vector current, just the constants C_{AB} will differ.

After rearranging both the color and spin indices the collinear matrix elements in (1.133) read

$$\begin{aligned} &\langle 0|\, \frac{\bar{n}\!\!\!/}{4N_c} \left[\delta(\omega_n' - \bar{\mathcal{P}}_n)\chi_n\right] |X_n\rangle \langle X_n|\, \left[\bar{\chi}_n \delta(\omega_n - \bar{\mathcal{P}}_n^\dagger)\right] |0\rangle \\ &\times \langle 0|\, \left[\bar{\chi}_{\bar{n}} \delta(\omega_{\bar{n}}' - \bar{\mathcal{P}}_{\bar{n}}^\dagger)\right] |X_{\bar{n}}\rangle \langle X_{\bar{n}}|\, \frac{n\!\!\!/}{4N_c} \left[\delta(\omega_{\bar{n}} - \bar{\mathcal{P}}_{\bar{n}})\chi_{\bar{n}}\right] |0\rangle\,, \end{aligned} \tag{1.138}$$

where the label operators are understood to work on the fields between the square brackets. We can use momentum conservation to let them work on the state instead

$$\begin{aligned} \delta(\omega_n' + \bar{\mathcal{P}}_n)\ |X_n\rangle &= \delta(\omega_n' + p_{X_n}^-)\, |X_n\rangle\,, \\ \langle X_n|\, \delta(\omega_n + \bar{\mathcal{P}}_n^\dagger) &= \langle X_n|\, \delta(\omega_n + p_{X_n}^-). \end{aligned} \tag{1.139}$$

The product of these delta functions does not contain any operators anymore and can be rearranged as $\delta(\omega_n + \omega_n')\delta(\omega_n + p_{X_n}^-)$. A similar analysis can be done for the $\bar{n}$-collinear sector. The integrals over ω' and $\bar{\omega}'$ now set $\omega' = \omega$ and $\bar{\omega}' = \bar{\omega}$. Applying the color and spin Fierz and rearranging the delta

functions to perform the integrals over de primed variables, we find that the cross section in equation (1.133) now reads [45]

$$\begin{aligned}\sigma = K_0 \sum_{\vec{n}} \int \mathrm{d}\omega_n \mathrm{d}\omega_{\bar{n}} |C(\omega_n, \omega_{\bar{n}})|^2 \sum_{X_n} \sum_{X_{\bar{n}}} \sum_{X_{us}} (2\pi)^4 \delta^4(q - P_{X_n} - P_{X_{\bar{n}}} - P_{X_{us}}) \\ \times \langle 0| \frac{\bar{n}\!\!\!/}{4N_c} \chi_n |X_n\rangle\langle X_n| \, \bar{\chi}_n \delta(\omega_n - \bar{\mathcal{P}}_n^\dagger) |0\rangle \langle 0| \, \bar{\chi}_{\bar{n}} \, |X_{\bar{n}}\rangle\langle X_{\bar{n}}| \, \delta(\omega_{\bar{n}} - \bar{\mathcal{P}}_{\bar{n}}) \frac{n\!\!\!/}{4N_c} \chi_{\bar{n}} \, |0\rangle \\ \times \langle 0| \, \bar{T}\{Y_{\bar{n}}^\dagger Y_n\} \, |X_{us}\rangle\langle X_{us}| \, T\{Y_n^\dagger Y_{\bar{n}}\} \, |0\rangle \, , \end{aligned} \tag{1.140}$$

The constant K_0 is a remnant from the spin Fierz and is given by

$$K_0 = \sum_{i=a,v} L_{\mu\nu}^{(i)} \mathrm{Tr}\Big[\Gamma_i^\mu \frac{\bar{n}}{2} \Gamma_i^\nu \frac{n}{2}\Big] \, . \tag{1.141}$$

To evaluate the integrals in light-cone coordinates the momentum conserving delta functions have to be split accordingly,

$$\begin{aligned}\delta^4(q - P_{X_n} - P_{X_{\bar{n}}} - P_{X_{us}}) &= 2\delta(Q - p_{X_n}^-)\delta(Q - p_{X_{\bar{n}}}^+)\delta^2(p_{X_n}^\perp + p_{X_{\bar{n}}}^\perp), \\ &= 2\delta(Q - \bar{\mathcal{P}}_n)\delta(Q - \bar{\mathcal{P}}_{\bar{n}})\delta^2(\mathcal{P}_n^\perp + \mathcal{P}_{\bar{n}}^\perp), \end{aligned} \tag{1.142}$$

where the extra factor 2 arises when we switch to light-cone coordinates. The combined momentum of the e^+e^- pair in the center of mass frame is $q = (Q, Q, 0)$ when using light-cone coordinates. Note that in this discussion the label and residual momenta have been recombined, leading to continuous integrals and delta functions. Equation (1.140) can be further simplified to

$$\begin{aligned}\sigma = N_c \, K_0 \, |C(Q,Q)|^2 \sum_{\vec{n}} \int \mathrm{d}^2\omega_\perp \\ \times (2\pi)^2 \sum_{X_n}^{\text{dijet}} \langle 0| \frac{\bar{n}\!\!\!/}{4N_c} \chi_n(0) |X_n\rangle\langle X_n| \, \delta^2(\omega_\perp - \mathcal{P}_n^\perp) \bar{\chi}_n(0) \delta(Q - \bar{\mathcal{P}}_n^\dagger) \, |0\rangle \\ \times (2\pi)^2 \sum_{X_{\bar{n}}}^{\text{dijet}} \langle 0| \, \bar{\chi}_{\bar{n}}(0) \, |X_{\bar{n}}\rangle\langle X_{\bar{n}}| \, \delta^2(\omega_\perp + \mathcal{P}_{\bar{n}}^\perp) \delta(Q - \bar{\mathcal{P}}_{\bar{n}}) \frac{n\!\!\!/}{4N_c} \chi_{\bar{n}}(0) \, |0\rangle \\ \times \frac{1}{N_c} \sum_{X_{us}}^{\text{dijet}} \langle 0| \, \bar{T}\{Y_{\bar{n}}^\dagger Y_n\}(0) \, |X_{us}\rangle\langle X_{us}| \, T\{Y_n^\dagger Y_{\bar{n}}\}(0) \, |0\rangle \, , \end{aligned} \tag{1.143}$$

where we explicitly showed the position dependence of the fields and used that

$$\int \mathrm{d}\omega_n \delta(Q - \bar{\mathcal{P}}_n)\delta(\omega_n - \bar{\mathcal{P}}_n) = \int \mathrm{d}\omega_n \delta(Q - \bar{\mathcal{P}}_n)\delta(Q - \omega_n), \tag{1.144}$$

to evaluate the integral over ω_n. A similar manipulation can be done for $\omega_{\bar{n}}$.

The Wilson coefficient in (1.143) needs to be determined by matching to QCD. Due to RPI invariance, the Wilson coefficients can only depend on the specific combination $\omega_n \cdot \omega_{\bar{n}} = Q$. Furthermore, we saw in equation (1.144) that momentum conservation forces ω_n and $\omega_{\bar{n}}$ to be equal to the invariant mass Q of the e^+e^- pair. The Wilson coefficient is independent of the Dirac structure Γ_i, and is given by [46]

$$C_{q\bar{q}}(Q^2,\mu) = 1 + \frac{\alpha_s C_F}{4\pi}\left[-\log^2\left(\frac{-Q^2}{\mu^2}\right) + 3\log^2\left(\frac{-Q^2}{\mu^2}\right) - 8 + \frac{\pi^2}{6}\right] + \mathcal{O}(\alpha_s^2). \tag{1.145}$$

In the next subsection, 1.2.5, the matching procedure leading to the result above is explicitly shown.

The sum over the external states $X_n, X_{\bar{n}}$ and X_{us} in equation (1.144) only includes kinematics that ensures the dijet configuration. This restriction needs to be enforced by the measurement, e.g. of the thrust event shape

$$T = \max_{\hat{t}} \frac{\sum_i \hat{t}\cdot p_i}{Q}. \tag{1.146}$$

This is an observable constructed from the momenta p_i of the final state particles projected on the trust axis $\hat{t}$, chosen in the direction that maximizes the sum of particle momenta projected along $\hat{t}$. In dijet-like events the thrust axis will point along one of the collinear directions as they are back-to-back. Without loss of generality we choose it to be n. It is convenient to define $\tau = 1 - T$, such that $\tau \to 0$ corresponds to the dijet region. For small values of τ, the dijet restriction on the external states is met and the sum over X is unconstrained. The observable is linear and will receive contributions from each sector, which can be made explicit by writing

$$\delta(\tau - \hat{\tau}) = \delta(\tau - \hat{\tau}(X_n) - \hat{\tau}(X_{\bar{n}}) - \hat{\tau}(X_{us})), \tag{1.147}$$

with

$$\begin{aligned}\tau = 1 - T &= \frac{Q - \sum_i |n\cdot p_i|}{Q}, \\ &= \frac{\sum_i^{p_z>0}(p_i^0 - p_i^z) + \sum_i^{p_z<0}(p_i^0 + p_i^z)}{Q}, \\ &= \frac{\sum_i \min(p_i^+, p_i^-)}{Q},\end{aligned} \tag{1.148}$$

where we used that the invariant mass Q is given by the sum over the energies of all final state particles. The soft contributions originate from both hemispheres

set by our choice of reference vector $\vec{n}$. These two hemispheres are half spheres centred around the spatial direction set by $\vec{n}$ and $-\vec{n}$ respectively. The soft contributions in hemisphere a contribute as $p^+_{us,a}$ and from hemisphere b as $p^-_{us,b}$. Equation (1.147) thus becomes:

$$\int \mathrm{d}p_n^+ \mathrm{d}p_{\bar{n}}^- \mathrm{d}l\, \delta(\tau - \frac{p_n^+}{Q} - \frac{p_{\bar{n}}^-}{Q} - \frac{l}{Q})\delta(p_n^+ - P^+_{X_n})\delta(p_{\bar{n}}^- - P^-_{X_{\bar{n}}})\delta(l - p^+_{us,a} - p^-_{us,b}). \tag{1.149}$$

Lastly, as our observable is independent of $\omega_\perp$ we can set $\omega_\perp = 0$ and effectively combining its integral with the sum over $\vec{n}$ leads to

$$\sum_{\vec{n}} \int \omega_\perp = \int \mathrm{d}^2\vec{n}, \tag{1.150}$$

which is an integral over the solid angle of $\vec{n}$ and evaluates to $4\pi^2$. After these manipulations the factorization of the differential cross section is given by

$$\frac{\mathrm{d}\sigma}{\mathrm{d}\tau} = \sigma_0 H_{q\bar{q}}(Q^2,\mu) \int \mathrm{d}l\, \mathrm{d}s_n \mathrm{d}s_{\bar{n}} J_q(s_n,\mu) J_{\bar{q}}(s_{\bar{n}},\mu) S_{q\bar{q}}(l,\mu) \delta\left(\tau - \frac{l}{Q} - \frac{s_n}{Q^2} - \frac{s_{\bar{n}}}{Q^2}\right), \tag{1.151}$$

where $s_n \equiv Qp_n^+$ and $s_{\bar{n}} \equiv Qp_{\bar{n}}^-$. The integration over s_n and $s_{\bar{n}}$ instead of p_n^+ and p_n^- is due to RPI-III invariance. The dependence on the energy scale μ was introduced by renormalizing the operators. The hard function H, jet function J and the soft function S are given by

$$\begin{aligned}
J_q(s_n,\mu) &= (2\pi)^3 \mathrm{Tr}\left[\langle 0| \frac{\bar{n}\!\!\!/}{4N_c} \chi_n(0) \delta(s_n - Q\mathcal{P}_n^+)\delta(Q - \bar{\mathcal{P}}_n)\delta^2(\mathcal{P}_n^\perp)\bar{\chi}_n(0)\,|0\rangle\right], \\
J_{\bar{q}}(s_{\bar{n}},\mu) &= (2\pi)^3 \langle 0|\, \bar{\chi}_n(0) \delta(s_{\bar{n}} - Q\mathcal{P}_{\bar{n}}^+) \frac{n\!\!\!/}{4N_c} \delta(Q - \bar{\mathcal{P}}_{\bar{n}})\delta^2(\mathcal{P}_{\bar{n}}^\perp)\chi_{\bar{n}}(0)\,|0\rangle\,, \\
S_{q\bar{q}}(l,\mu) &= \frac{1}{N_c}\mathrm{Tr}\left[\langle 0|\, \bar{T}\{Y_{\bar{n}}^\dagger Y_n\}\delta(l - p^+_{us,a} - p^-_{us,b}) T\{Y_n^\dagger Y_{\bar{n}}\}\,|0\rangle\right], \\
H_{q\bar{q}}(Q^2,\mu) &= |C_{q\bar{q}}(Q^2,\mu)|^2,
\end{aligned} \tag{1.152}$$

where $C(Q^2,\mu)$ for $e^+e^- \to q\bar{q}$ is given in equation (1.145). For LHC applications, the jet function needs to include constraints from the clustering of the collinear particles into jet and we will discuss this in section 1.3. The factorization formula in equation (1.151) is only valid for small τ.

Deriving a factorization formula for another measurement might include different objects in the final factorization formula. In particular, in proton-proton collisions the initial states also receive QCD corrections and this leads to objects we call beam functions. They describe the evolution of a parton that is

extracted from the proton, as it undergoes collinear splittings before initiating the hard interaction. The beam function can be matched onto the parton distribution functions [47–50]

$$B_i(t,x,\mu) = \sum_j \int_x^1 \frac{\mathrm{d}z}{z} \mathcal{I}_{ij}(t,z,\mu) f_j\Big(\frac{x}{z},\mu\Big) \left[1 + \mathcal{O}\left(\frac{\Lambda^2_{\mathrm{QCD}}}{t}\right)\right], \tag{1.153}$$

where the summation over j includes all possible parton flavors and t can be any variable. The matching coefficients $\mathcal{I}_{ij}$ are perturbative objects that at tree level should be equal to

$$\mathcal{I}_{ij}(t,z,\mu) = \delta_{ij}\delta(1-z)\delta(t), \tag{1.154}$$

in order to reduce the beam function to the standard parton distribution functions at leading order (assuming $t = 0$ at leading order).

Matching for dijet production in e^+e^- collisions

Wilson coefficients are found by calculating simple observables in both the full theory and the EFT. The desired limit of the full theory should then match the direct calculation in the EFT. We have seen this for the example with two scalar fields in 1.2.1. In SCET, matching needs to be performed at each order in perturbation theory. Beyond tree level the matching procedure will include integrals over unconstrained loop momenta. The separation between label and residual momenta complicates this, as label momenta are discrete. The phase space integrals change accordingly

$$I^{LF}_{\mathrm{loop}} = \sum_{p_l} \int \mathrm{d}^d p_r f(p_r^+, p_l^-, p_{l\perp}) - \int \mathrm{d}^d p_r f^{(0)}(p_r^+, 0, 0), \tag{1.155}$$

where LF denotes that this is an integral in label formalism. The final term in this expression goes by the name of zero-bin subtraction, which avoids double counting of $p_l = 0$ that is already described by the ultrasoft momenta [51]. The residual momenta only appears through its p_r^+ component. We can however reintroduce the other components as they describe subleading effects to the label momenta. Specifically $f(p_r^+, p_l^-, p_{l\perp}) = f(p_r^+, p_l^- + p_r^-, p_{l\perp} + p_{r\perp})$ for all values of the residual momenta. Using this substitution, the original splitting into residual and label momentum can be reversed:

$$\begin{aligned} I^{LF}_{loop} &= \sum_{p_l} \int \mathrm{d}^d p_r f(p_r^+, p_l^- + p_r^-, p_{l\perp} + p_{r\perp}) - \int \mathrm{d}^d p_r f^{(0)}(p_r^+, 0, 0), \\ &= \int \mathrm{d}^d p \left(f(p) - f^{(0)}(p)\right). \end{aligned} \tag{1.156}$$

In practice the zero-bin subtraction is achieved by changing the scaling of the label momentum to match the residual scaling ($\mathcal{O}(\lambda^2)$).

We will now consider our dijet example and explicitly perform the matching at $\mathcal{O}(\alpha_s)$. The total amplitude in full QCD is calculated from three Feynman diagrams, resulting from a loop correction to either of the outgoing fermion lines and to the vertex. The combined result, calculated in Feynman gauge, is

$$M_{\text{QCD}} = \frac{\alpha_s C_F}{4\pi}\Big[-2\log^2\left(\frac{p^2}{Q^2}\right) - 4\log\left(\frac{p^2}{Q^2}\right) - \log\left(\frac{-Q^2}{\mu^2}\right) - \frac{2\pi^2}{3}\Big] J^{\text{tree}}_{q\bar{q}}, \tag{1.157}$$

where renormalization has been performed and $p^2 \neq 0$ is the off-shellness of external quarks regulating the IR divergences. In SCET we have more diagrams contributing to the final amplitude. In analogy with the QCD Feynman diagrams there are three diagrams that follow from a loop correction to either of the outgoing collinear fermion lines or the SCET vertex. In addition we have contributions where a collinear gluon, taken from the collinear Wilson line, connects with either of the external collinear fields. Performing the loop integrals in SCET leads to the bare result [32, 33, 46]

$$\begin{aligned} M_{\text{SCET}} = \frac{\alpha_s C_F}{4\pi}\Big[\frac{2}{\epsilon^2} + \frac{3}{\epsilon} - \frac{2}{\epsilon}\log\left(\frac{-Q^2}{\mu^2}\right) - 2\log^2\left(\frac{p^2}{Q^2}\right) + \log^2\left(\frac{-Q^2}{\mu^2}\right) \\ - 4\log^2\left(\frac{p^2}{Q^2}\right) - 4\log^2\left(\frac{-Q^2}{\mu^2}\right) + 8 - \frac{5\pi^2}{6}\Big] J^{\text{tree}}_{q\bar{q}}, \end{aligned} \tag{1.158}$$

where the ϵ poles are UV divergences[6]. Comparing the results in equations (1.157) and (1.158) we see that IR terms overlap. At tree level the matching is trivial, since the tree-level diagrams yield the same result in SCET as in QCD. The bare Wilson coefficient up to $\mathcal{O}(\alpha_s)$ is thus found to be

$$\begin{aligned} C^{\text{bar}}_{q\bar{q}}(Q^2,\epsilon) = 1 + \frac{\alpha_s C_F}{4\pi}\Big[-\frac{2}{\epsilon^2} - \frac{3}{\epsilon} + \frac{2}{\epsilon}\log\left(\frac{-Q^2}{\mu^2}\right) - \log^2\left(\frac{-Q^2}{\mu^2}\right) \\ + 3\log^2\left(\frac{-Q^2}{\mu^2}\right) - 8 + \frac{\pi^2}{6}\Big], \end{aligned} \tag{1.159}$$

which can be normalized by

$$C^{\text{bar}}_{q\bar{q}}(Q^2,\epsilon) = Z_{q\bar{q}}(Q^2,\epsilon,\mu) C_{q\bar{q}}(Q^2,\mu), \tag{1.160}$$

[6] In calculations in dimensional regularization, the zero-bin subtraction effectively converts $\frac{1}{\epsilon_{IR}}$ divergences in SCET into $\frac{1}{\epsilon_{UV}}$ divergences, as it is typically a scaleless integral.

where μ is the renormalization scale and

$$Z_{q\bar{q}}(Q^2,\epsilon,\mu) = 1 + \frac{\alpha_s C_F}{4\pi}\Big[-\frac{2}{\epsilon^2} - \frac{3}{\epsilon} + \frac{2}{\epsilon}\log\left(\frac{-Q^2}{\mu^2}\right)\Big], \tag{1.161}$$

containing all the poles resulting from the introduced counterterms. Finally, the renormalized Wilson coefficient that is determined by matching is given by

$$C_{q\bar{q}}(Q^2,\mu) = 1 + \frac{\alpha_s C_F}{4\pi}\big[-\log^2\left(\frac{-Q^2}{\mu^2}\right) + 3\log^2\left(\frac{-Q^2}{\mu^2}\right) - 8 + \frac{\pi^2}{6}\big] + \mathcal{O}(\alpha_s^2). \tag{1.162}$$

1.3 Jets

Jets are collimated sprays of hadrons that are often found in the detectors at the LHC. They form whenever energetic quarks or gluons are produced in a high-energy collision. Jets enter most LHC analyses as part of the signal or background. The appearance of jets is seen in figure 1.4, which shows the event display of a collision at the LHC. The notion of jets is used throughout this thesis, in particular in chapter 2, where we develop a framework to calculate the contribution of jets to the cross section, including a code that largely automates this calculation.

1.3.1 Jet formation

Before we start working with jets it is important to understand why they form. Jets are an emergent phenomena: they do not appear in the QCD Lagrangian and yet they describe the dynamics we observe at large distances. This means that there are properties specific to QCD that allow jet formation. When an energetic parton is produced in the collision it will start radiating. The strong coupling is at this early stage of event evolution still small enough that we can use a description in terms of quarks and gluons, but large enough that there will be a lot of radiation. This rapid increase of particles through radiation is referred to as the parton shower. There are three main features of QCD that eventually lead to the jet dynamics as we observe it in our detectors: The first is the enhancement of soft and collinear emissions, implying a large probability for particles to be radiated in the direction the initial parton was going. The second is the asymptotic freedom. For the collimation of particles it is important that the strong coupling at short distances is actually small. Too much radiation would repeal the enhancement from collinear emissions, leading to a spherical event (instead of one with jets). The partons radiate more as the energy decreases. At large distances the strong interaction gets so

strong that the behaviour of quarks and gluons is not perturbative anymore, instead they will be confined together through the process of hadronization. This brings us to the third reason for jets, which is the existence of light quarks. In the regime where we have confinement it is energetically unfavourable to have partons placed at a large distance from each other. There would be a huge amount of energy stored in the gluon field lines connecting partons at large distances. The easy transition to a lower energy state by light quark pair creation, such that only neighbouring pairs are connected, allows particles to maintain their direction of flight during hadronization. Jets are therefore a good proxy for the single high-energy partons initiating its formation.

This interplay of QCD dynamics creates the complicated radiation pattern that is referred to as jets. Jets connect the short distance physics, radiating quarks and gluons, to the long distance physics, the hadrons that are eventually detected. While the concept of jets is intuitively clear, a definition is needed for measurements and calculations.

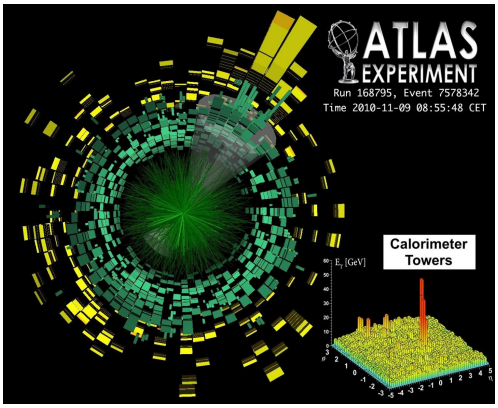

Figure 1.4 Event display of a lead-lead collision at ATLAS. The formation of jets is seen as cones in the main figure (and as a narrow stream of particles on the bottom right of the figure). Source: ATLAS Experiment© 2014 CERN

1.3.2 Jet algorithms

An accurate jet reconstruction is important to study the properties of the partons produced in the hard scattering. These partons are never directly observed and we can only study the hadronized states. The definition of a jet would thus ideally be able to connect the stages of jet formation over the full energy range. This is however not possible, since the partons that initiate the jet carry color whereas the hadrons are color neutral. The jet definition can therefore only describe how particles must be grouped such that

we can call them a jet. Two important aspects that should be taken into consideration are jet size and IRC safety. The jet should be large enough to capture a required amount of non-perturbatively hadronized particles to accurately make the connection to the underlying partons. However, it should not be too large as it will capture an excessive amount of radiation from the underlying event and pile-up, contaminating jet measurements. The statement that the definition must be IRC safe will ensure the validity of perturbative jet calculations. The requirements of a jet definition were established in 1990 [52]: It should be easy to implement in experimental analyses as well as in theoretical calculations. Also, the definition should be valid at each order in perturbation theory and should give a finite cross section. This basically ensures IRC safety of the jet. Lastly, as mentioned before, hadronization should have minimal impact on the jet.

Jet definitions are split in two parts: the jet algorithm and the recombination scheme. The former decides whether particles should be grouped together and the latter dictates how their properties are recombined to determine the properties of the resulting jet. There is a particular class of jet algorithms we will use throughout this thesis. This is the class of sequential recombination algorithms, which try to mimic the parton shower by using pairwise recombination of particles that are 'close' to each other, in the sense that they are products of a kinematically enhanced splitting (collinear/soft). The most used sequential algorithms are the generalized-k_t algorithms. Starting with the list of all particles in the final state of the event, a generalized-k_t algorithm constructs a jet by looping over the following steps:

1. Construct the inter-particle distance d_{ij} for all particle pairs, defined as

$$d_{ij} = \min(p_{T,i}^{2p}, p_{T,j}^{2p}) \frac{\Delta R_{ij}^2}{R^2}, \tag{1.163}$$

   where p is a parameter that defines the different algorithms, R is the chosen jet radius[7] and ΔR_{ij} is the geometric distance given by

$$\Delta R_{ij}^2 = (\eta_i - \eta_j)^2 + (\phi_i - \phi_j)^2 , \tag{1.164}$$

   with η is the pseudorapidity and ϕ the azimuthal angle around the beam axis.

2. Construct the beam distance for each particle, defined as

$$d_{i,B} = p_{T,i}^{2p}. \tag{1.165}$$

[7] At the LHC $R = 0.4$ is often used.

3. Find the smallest distance from the set $\{d_{ij}, d_{i,B}\}$. If the smallest distance is an inter-particle distance, the two objects are merged into a single particle called a 'pseudojet'. If instead the smallest distance is d_{iB}, the corresponding object is removed from the pairwise recombination process and will be considered a jet.

This procedure will come to a stop once all particles are clustered into jets.

There exist many recombination schemes that can be used to cluster two particles into a pseudojet in step 3. The easiest is to simply add the four-momenta of the particles that are being clustered,

$$p_r^\mu = p_i^\mu + p_j^\mu, \tag{1.166}$$

where p_r^μ is the four-momentum of the constructed pseudo particle. Another choice is to add the energies, but let the four-momentum point in the direction of the hardest particle. This is known as the Winner-Takes-All recombination and is used in chapter 3, where we study Azimuthal Decorrelation.

The jet algorithm is used on both the experimental and theoretical side. The freedom to choice the jet radius and algorithm results in many different observables. This is perfectly consistent as long as the same definition is used at both ends. The most common choices that can be made for p in (1.163) are $p = -1, 0, 1$, but note that the value of p is not restricted. Choosing $p = 1$ will lead to the k_t-algorithm [53,54]. This algorithm prefers to cluster soft particles first and as a result is susceptible to the underlying event and pile-up. The clustering with $p = 0$ is known as the Cambridge-Aachen algorithm [55, 56]. The momenta of the particles are completely irrelevant in the clusters, as Cambridge-Aachen selects particles that are close to each other in the $\eta - \phi$ plane for clustering. This algorithm is particularly useful when studying jet substructure, as it organizes particles in an angular-ordered tree, which is convenient for removing sources of contamination from the jet by applying grooming techniques [57–59]. Finally, $p = -1$ results in the anti-k_t algorithm [60]. In this case the inter-particle distance is smallest for particles with high momenta, such that jets form around hard partons. This algorithm produces almost circular jets with radius R, which has advantages when it comes to experimental calibration of jets. Anti-k_t is less sensitive to contamination from pile-up and underlying events.

Finally, let us have a closer look at IRC safety of these sequential algorithms. An additional collinear splitting will produce two particles i and j with $d_{ij} \to 0$. Particles resulting from these kinds of splittings will therefore always be clustered together. An additional soft splitting will either be clustered into the jet or will form a new jet with zero momentum, either way they will not alter the clustering into hard jets. We can therefore conclude that sequential

algorithms are IRC safe by construction, enabling perturbative calculations. It used to be computationally intensive to carry out the pairwise recombination on experimental data, but it became the standard in LHC experiments thanks to the FastJet implementation [61, 62].

IRC safe jet algorithms can safely be used in SCET calculations [63, 64], as they are compatible with powercounting and factorization. The jet function will be of the form

$$J_q(\omega, s, \mu) \tag{1.167}$$
$$= (2\pi)^2 \sum_X \mathrm{Tr}\left[\langle 0| \frac{\bar{n}}{4N_c}\chi_n(0)|X\rangle \langle X| \delta(Q-\bar{\mathcal{P}}_n)\delta^2(\mathcal{P}_n^\perp)\delta(s-\hat{s}_{\mathrm{obs}})\bar{\chi}_n(0)|0\rangle\right],$$

where we have reintroduced the final-state X compared to equation (1.152). The jet function depends on kinematic variables through the measurement $\delta(s - \hat{s}_{\mathrm{obs}})$. In appendix B we provide the techniques to evaluate the jet function.

Appendices

1.4 QCD renormalization factors

The QCD renormalization factors in the $\overline{\mathrm{MS}}$ read

$$\begin{aligned}
\bar{Z}_A &= 1 + \frac{\alpha_s}{4\pi}\Big(\frac{1}{\epsilon} + \ln 4\pi - \gamma_\epsilon\Big)\Big[\Big(\frac{13}{6} - \frac{\chi}{2}\Big)C_A - \frac{4}{3}n_f T_F\Big] + \mathcal{O}(\alpha_s^2),\\
\bar{Z}_\psi &= 1 - \frac{\alpha_s C_F}{4\pi}\Big(\frac{1}{\epsilon} + \ln 4\pi - \gamma_\epsilon\Big) + \mathcal{O}(\alpha_s^2),\\
\bar{Z}_m &= 1 - 3\frac{\alpha_s C_F}{4\pi}\Big(\frac{1}{\epsilon} + \ln 4\pi - \gamma_\epsilon\Big) + \mathcal{O}(\alpha_s^2),\\
\bar{Z}_\alpha &= 1 - \frac{\alpha_s}{4\pi}\frac{1}{2}\Big(\frac{1}{\epsilon} + \ln 4\pi - \gamma_\epsilon\Big)\Big(\frac{11}{3}C_A - \frac{4}{3}n_f T_F\Big) + \mathcal{O}(\alpha_s^2).
\end{aligned} \tag{1.168}$$

The counterterms for the MS scheme can be recovered from these expressions as the counterterms in the $\overline{\mathrm{MS}}$ include an extra $\ln 4\pi - \gamma_\epsilon$ compared to the MS scheme.

2

Jet Functions

2.1 Introduction

In this chapter we focus on calculating one-loop jet functions, which enter in resummed cross sections starting at next-to-leading logarithmic (NLL′) accuracy. Resummation at NLL′ includes the two-loop cusp anomalous dimension and one-loop (non-cusp) anomalous dimensions. Jet functions have been calculated for a wide range of observables, including the invariant mass [65–70], the family of e^+e^- event shapes called angularities with respect to the thrust axis [71–73] or Winner-Take-All axis [74, 75], Sterman-Weinberg jets [76, 77], the cone and the k_T family of jet algorithms for exclusive [64, 77] and inclusive [78, 79] jet production. Jet functions have also been considered for a range of jet substructure observables, such as the jet shape [80–82]. In our calculations we treat quarks as massless and restrict to infrared-safe observables. An example of a massive quark (initiated) jet function is given in refs. [83, 84], and an example of an infrared-unsafe jet observable is the electric charge of the jet [85, 86].

We briefly comment on the other ingredients in the factorization: A general approach to calculating soft functions has been developed in refs. [87–90]. In particular, the SoftSERVE package [90] provides two-loop soft functions for processes with two collinear directions (i.e. two jets in e^+e^- or 0 jets in pp collisions), and an extension to N jets is in progress [91]. Hard functions can be obtained from the IR finite part of helicity amplitudes, as long as the color of the initial (final) particles is not averaged (summed) over, see e.g. ref. [92].

The difficulty in calculating jet functions lies in the phase-space integration, which depends on the observable. When feasible, an analytic approach is superior. However, there are observables for which even the one-loop jet function is highly nontrivial, such as jet broadening [72] and the jet shape [82], for which fully analytic results are difficult to obtain or have not been obtained yet. The numerical approach we develop here offers a promising alternative, address-

ing the collinear and soft divergences in a general way, thereby automating the calculation of one-loop jet functions for a broad range of observables. At minimum, our work provides a valuable cross check for analytic calculations.

The poles in the dimensional regulator are obtained analytically, possibly up to an integral over the azimuthal angle, and depend on the collinear and soft behavior of the observable. This soft behavior is described by a power law, and therefore simply characterized by the exponent and coefficient. Extracting these parameters may require solving non-trivial algebraic equations, and we develop a procedure to simplify this step. The full details/complications of the measurement only enter in the finite term, which can be integrated numerically. We have implemented our approach in a MATHEMATICA package, Geometric One-loop Jet functions (GOJET), which is available online at `https://bitbucket.org/GOJet/gojet/src/master/`. GOJET can handle a large class of infrared-safe observables, including all the observables listed above.

Using GOJET we provide explicit examples of the method for the angularities with respect to the Winner-Take-All axis, the cone and k_T-clustering jet algorithms and the jet shape. Furthermore we calculate for the first time the one-loop jet function for angularities with respect to the thrust axis including recoil. We cross check our result against existing results in the literature for the specific case of jet broadening [72] and for the case of no recoil [71, 93].

The remainder of this chapter is structured as follows: In section 2.2 we discuss how we use geometric subtraction to calculate jet functions, including a simple example. The GOJET package, which provides a MATHEMATICA implementation, is discussed in section 2.3. In section 2.4, we use our package to calculate several one-loop jet functions, and we conclude in section 2.5.

2.2 General Method

In section 2.2.1 we will discuss geometric subtraction and how we apply it to calculate one-loop jet functions. Technical aspects related to the treatment of Heaviside theta functions in our calculation and infrared safety are discussed in secs. 2.2.2 and 2.2.3, respectively. We illustrate our method by calculating the jet function for the e^+e^- angularity event shapes in section 2.2.4, with further examples in section 2.4.

2.2.1 Subtraction scheme

The jet function depends on the flavor $i = q, g$ of the initiating parton and the jet observable, and has a perturbative expansion in α_s

$$\mathcal{J}_{i,\text{obs}} = \sum_n \left(\frac{\alpha_s}{2\pi}\right)^n \mathcal{J}^{(n)}_{i,\text{obs}} \,. \tag{2.1}$$

At tree level the jet consists of a single quark or gluon, and in general $\mathcal{J}^{(0)}_i = 1$ in the appropriate units.[1] The one-loop contribution is given by the collinear limit of two final-state partons

$$\begin{aligned}
\mathcal{J}^{(1)}_{i,\text{obs}} &= \int_0^\pi \mathrm{d}\phi \int_0^\infty \mathrm{d}s \int_0^1 \mathrm{d}z\, Q_i(s,z,\phi)\, M_{\text{obs}}(s,z,\phi)\,, \\
Q_i(s,z,\phi) &= \frac{(\mu^2 e^{\gamma_E})^\epsilon}{\sqrt{\pi}\,\Gamma(\frac{1}{2}-\epsilon)} \left(\frac{\nu}{\omega}\right)^\eta \frac{P_i(z)\,(\sin\phi)^{-2\epsilon}}{z^{\epsilon+\eta}(1-z)^{\epsilon+\eta} s^{1+\epsilon}}, \\
P_q(z) &= C_F \left[\frac{1+z^2}{1-z} - \epsilon(1-z)\right], \\
P_g(z) &= n_f T_R \left[1 - \frac{2z(1-z)}{1-\epsilon}\right] + C_A \left[\frac{z}{1-z} + \frac{1-z}{z} + z(1-z)\right].
\end{aligned} \tag{2.2}$$

Here s denotes the invariant mass of the two partons, and z and $1-z$ the momentum fractions of the partons. The squared matrix element is contained in $Q_i(s,z,\phi)$, with $P_i(z)$ the (sum of) splitting function(s). The calculation is performed in $d = 4-2\epsilon$ dimensions and the $\overline{\text{MS}}$-renormalization scheme with renormalization scale μ is employed. For certain observables an additional rapidity regulator η and corresponding rapidity scale ν are required [49, 50, 94–97], which is included in equation (2.2) for generality. This arises when the collinear and soft functions have the same invariant mass scale μ, with transverse momentum measurements being the typical example. We will use the η regulator defined in [94], but at one loop this is essentially equivalent to almost all other choices. For the extension of equation (2.2) to a two-loop example, see ref. [98].

The measurement in a jet function can often be written as $\delta[\mathcal{O} - f(s,z,\phi)]$. To avoid distributions, we require the user to rewrite the measurement as a Heaviside theta function by integrating, i.e. $\Theta[\mathcal{O} - f(s,z,\phi)]$, where we are now cumulative in $\mathcal{O}$.[2] We therefore assume that the measurement $M_{\text{obs}}(s,z,\phi)$ is a Heaviside theta function, which cuts out a certain region of the collinear phase

[1] An exception is the jet shape, discussed in section 2.4.3, which contains a theta function that sets it to zero if the recoil from soft radiation is too large.

[2] Alternatively, one can consider a conjugate space, as was employed in automated calculations of soft functions [88, 89].

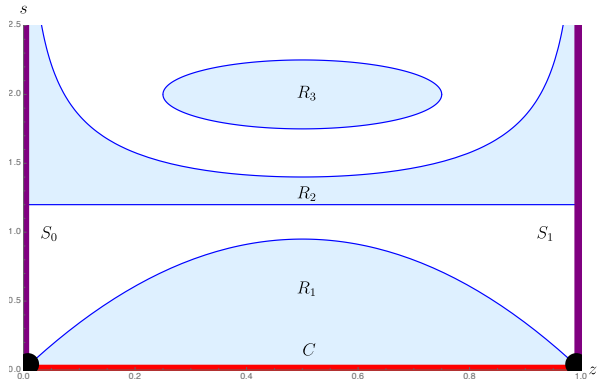

Figure 2.1 For an example of a generic observable the phase space can be constrained to several representative regions (blue). The collinear singularity C (red line), soft singularities S_0 and S_1 (purple lines), and soft-collinear singularities (black dots) are indicated.

space, as illustrated in figure 2.1 (suppressing ϕ dependence). An advantage of cumulative distributions is that they involve logarithms rather than plus distributions:

$$\int_0^{t^c} \mathrm{d}t \left[\frac{\theta(t)\ln^n t}{t}\right]_+ = \frac{1}{n+1}\ln^{n+1} t^c\,. \tag{2.3}$$

In section 2.2.2, a technical point related to rewriting measurement delta functions in terms of theta functions will be discussed. There are also measurements that are naturally theta functions. For example, the k_T-family of jet algorithms requires both particles to be clustered into a jet with radius parameter R, $M_{k_T}(s,z,\phi) = \Theta(s \le z(1-z)p_T^2R^2)$, where p_T is the transverse momentum of the jet. In principle these phase-space constraints M_{obs} can depend on the azimuthal angle ϕ as well, but since there is no singularity associated with the ϕ integration, we will only include ϕ when needed.

The jet function in equation (2.2) has divergences as $s \to 0$ (collinear divergence), and $z \to 0$ and $z \to 1$ (soft divergences), which occur at the phase-space boundaries in figure 2.1. Infrared-safe observables must always either include or exclude the entire collinear divergence (the red line in figure 2.1), as will be discussed more in section 2.2.3. From the point of view of collinear subtraction, one can consider the jet function (as long as it contains the collinear divergence) as a collinear counterterm. Different observables can then be viewed as different schemes, differing in the extent that soft and soft-collinear divergences are included in the observable. For instance, region 1 of the generic observable illustrated in figure 2.1 only contains the collinear and part of the soft-collinear

singularities. By contrast, region 2 only contains part of the soft and none of the collinear divergence. Region 3 does not contain any soft or collinear divergent parts of phase space and does therefore not have to be regulated. Another possibility would be to consider an observable which corresponds to the complement of region 1, which naively causes problems because it develops a logarithmic singularity for $s \to \infty$. However, its one-loop jet function is given by minus the jet function for region 1, because the integral over the full collinear phase space results in a scaleless integral.

To define a general subtraction scheme for calculating jet functions for infrared-safe observables, we follow the approach of geometric subtraction [99]. We would like to define a finite part of the jet function as follows:

$$\text{Finite}(\mathcal{J}^{(1)}_{i,\text{obs}}) = \Big[\int_0^\pi \mathrm{d}\phi \int_{B\mu^2}^\infty \mathrm{d}s \int_A^{1-A} \mathrm{d}z\, Q_{i\to j}(s,z,\phi)\, M_{\text{obs}}(s,z,\phi) \Big]_{A,B\to 0}, \tag{2.4}$$

where we introduced the dimensionless slicing parameters A and B, that remove the soft and collinear divergence, and which we subsequently want to take to zero. The central idea of geometric subtraction rests on the identity:

$$\begin{aligned} \Big[\int_a^1 \mathrm{d}x\, \frac{f(x)}{x} \Big]_{a\to 0} &= \Big[\int_0^1 \mathrm{d}x\, \frac{f(x) - f(x)\Theta(x<a)}{x} \Big]_{a\to 0} \\ &= \int_0^1 \mathrm{d}x\, \frac{f(x) - f(0)\Theta(x<a)}{x}\,, \end{aligned} \tag{2.5}$$

where we exploited that a is small on the second line to replace $f(x)$ by $f(0)$ in the second term. However, the expression on the second line is now regulated for any $0 < a \leq 1$, leading to a duality between slicing and subtraction schemes. To obtain the full jet function from the above finite part, counterterms need to be added to reinstate the part of the integral that is removed by the cuts. The counterterms generated in this way are added back in integrated form, regulated dimensionally and if needed also with a rapidity regulator, and may give a finite contribution to the jet function. While a subtlety arises in general when different limits do not commute, here we do not face this problem as the collinear and soft singularities are factorized. For the small A limit in equation (2.4) we can then straightforwardly apply equation (2.5). However for the parameter B nothing is gained from this procedure, because the jet function is already in the limit of small s and the counterterm generated is the original integral itself.

To obtain a simpler counterterm in the $s < B$ region, we can however use a simpler observable, which we choose to be the jet mass, as a collinear counterterm. (This was also used in the geometric subtraction scheme [99].) Since

the region of the s-z plane corresponding to the jet mass is box-shaped, we will refer to this collinear counterterm as the *box*. A subtlety now appears due to the difference of soft and soft-collinear divergences included in the box counterterm and the given observable $M_{\rm obs}$, which as discussed above may not be the same. To deal with this problem we introduce separate soft counterterms for both the box counterterm and the $M_{\rm obs}$ term in the region $s < B\mu^2$, as discussed in detail below.

These considerations lead us to the following final decomposition of the jet-function into finite and divergent parts:

$$\begin{aligned}
\mathcal{J}^{(1)}_{i,\rm obs} &= G_{i,\rm obs,1} + G_{i,\rm obs,2} + G_{i,\rm obs,3}\,,\\
G_{i,\rm obs,1} &\equiv \int_0^\pi \mathrm{d}\phi \int_0^1 \mathrm{d}z \int_{B\mu^2}^\infty \mathrm{d}s \Big[Q_i M_{\rm obs} - Q_{i,0} M_{\rm obs,0}\Theta(z<A) \\
&\qquad\qquad - Q_{i,1} M_{\rm obs,1}\Theta(1-z<A)\Big] \\
&\quad + \int_0^\pi \mathrm{d}\phi \int_0^1 \mathrm{d}z \int_0^{B\mu^2} \mathrm{d}s \Big[Q_i (M_{\rm obs}-1) - Q_{i,0}(M_{\rm obs,0}-1)\Theta(z<A) \\
&\qquad\qquad - Q_{i,1}(M_{\rm obs,1}-1)\Theta(1-z<A)\Big],\\
G_{i,\rm obs,2} &\equiv \int_0^\pi \mathrm{d}\phi \int_0^1 \mathrm{d}z \int_0^\infty \mathrm{d}s \Big[Q_{i,0} M_{\rm obs,0}\Theta(z<A) + Q_{i,1} M_{\rm obs,1}\Theta(1-z<A)\Big],\\
G_{i,\rm obs,3} &\equiv \int_0^\pi \mathrm{d}\phi \int_0^1 \mathrm{d}z \int_0^{B\mu^2} \mathrm{d}s \Big[Q_i - Q_{i,0}\Theta(z<A) - Q_{i,1}\Theta(1-z<A)\Big],
\end{aligned} \tag{2.6}$$

where the arguments s, z, ϕ are suppressed and A, B are positive real numbers with $A \le 1$. The first term in $G_{i,\rm obs,1}$ corresponds to the finite part defined in equation (2.4), and the other terms correspond to integrated counterterms. The box counterterm $G_{i,obs,3}$ leads to $M_{\rm obs} \to (M_{\rm obs} - 1)$ in the box region $s < B\mu^2$ in $G_{i,\rm obs,1}$. It is straightforward to check that the sum of G_1, G_2 and G_3 is equal to the original one-loop jet function.

The advantage of the above decomposition is that G_3 is observable independent, G_2 only depends on the soft limit of the observable (which can be encoded by a few parameters at one-loop order, see equation (2.8)) and G_1 is finite. In equation (2.6), Q_0 and Q_1 denote the soft $z \to 0$ and $z \to 1$ limit of Q. Explicitly,

$$\begin{aligned}
Q_{q,0}(s,z,\phi) &= Q_q(s,z,\phi)|_{z\to 0} = 0\,,\\
Q_{q,1}(s,z,\phi) &= Q_q(s,z,\phi)|_{z\to 1} = \frac{(\mu^2 e^{\gamma_E})^\epsilon}{\sqrt{\pi}\,\Gamma(\frac{1}{2}-\epsilon)} \Big(\frac{\nu}{\omega}\Big)^\eta \frac{2C_F (\sin\phi)^{-2\epsilon}}{(1-z)^{1+\eta+\epsilon} s^{1+\epsilon}}\,,
\end{aligned}$$

$$Q_{g,1}(s,z,\phi) = \frac{(\mu^2 e^{\gamma_E})^\epsilon}{\sqrt{\pi}\,\Gamma(\frac{1}{2}-\epsilon)}\Big(\frac{\nu}{\omega}\Big)^\eta \frac{C_A(\sin\phi)^{-2\epsilon}}{(1-z)^{1+\eta+\epsilon}s^{1+\epsilon}} = Q_{g,0}(s,1-z,\phi)\,. \quad (2.7)$$

Similarly, $M_{\text{obs},0}$ and $M_{\text{obs},1}$ denote the soft $z \to 0$ and $z \to 1$ limit of the measurement M_{obs}. The soft limit can contain multiple boundary conditions on the phase space, which we account for by writing $M_{\text{obs},0}$ and $M_{\text{obs},1}$ as a sum of Heaviside theta functions that constrain the integration over s as a function of z. Moreover, they will follow a power-law behavior parametrized by

$$\begin{aligned}
M_{\text{obs}}(s,z,\phi)|_{z\to 0} &= \Theta(\Phi)\sum_r M^r_{\text{obs}} \\
&= \Theta(\Phi)\sum_r \Theta\Big(\frac{c^+_{0r}\,\mu^2}{z^{\alpha^+_{0r}}} - s\Big)\Theta\Big(s - \frac{c^-_{0r}\mu^2}{z^{\alpha^-_{0r}}}\Big), \\
M_{\text{obs}}(s,z,\phi)|_{z\to 1} &= \Theta(\Phi)\sum_r M^r_{\text{obs}} \\
&= \Theta(\Phi)\sum_r \Theta\Big(\frac{c^+_{1r}\,\mu^2}{(1-z)^{\alpha^+_{1r}}} - s\Big)\Theta\Big(s - \frac{c^-_{1r}\mu^2}{(1-z)^{\alpha^-_{1r}}}\Big), \quad (2.8)
\end{aligned}$$

where the sum on r is over different regions (see figure 2.1), and the parameters c_i, α_i depend on the observable, and can depend on ϕ as well.[3] We also allow for a constraint Φ on the azimuthal angle, as will be discussed in section 2.2.3. Depending on the observable, each soft boundary condition will therefore follow one out of three distinct behaviors shown in figure 2.1: the upper boundary of R_1 corresponds to $\alpha < 0$, the lower boundary of R_2 to $\alpha = 0$, the upper boundary to $\alpha > 0$ and R_3 does not extend into the soft region. Finding $c_{0,1}$ and $\alpha_{0,1}$ can be nontrivial, and we will discuss a strategy to do so for an involved example in section 2.4.2.

We will now discuss the decomposition in equation (2.6) in more detail, using the graphical representation in figure 2.2 for the k_T algorithm. In order to get a finite G_1 in figure 2.2a, we subtracted the collinear singularity and the soft singularities. The collinear singularity is removed by the box, replacing M_{obs} by $M_{\text{obs}} - 1$ when $s \le B\mu^2$, such that $M_{\text{obs}}(s=0,z,\phi) - 1 = 0$. The soft singularities get accounted for by subtracting the $z \to 0$ and/or $z \to 1$ limits of the integrand. Indeed, one can see that in figure 2.2a the blue plusses and red minuses cancel as $z \to 1$. The resulting integral G_1 is now finite. For general observables, G_1 in equation (2.6) may be hard to calculate analytically, and one has to resort to numerical integration techniques. In the examples in

[3] In general $c_0 = c_1$ and $\alpha_0 = \alpha_1$, but we will show examples where this is no longer true because the observable depends on the azimuthal angle, which differs by π between the two partons.

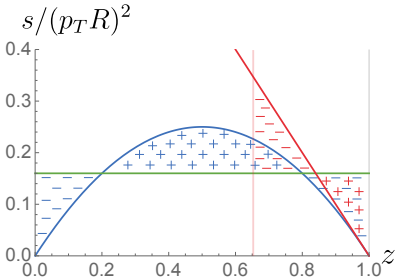

(a) G_1: Numerical contribution

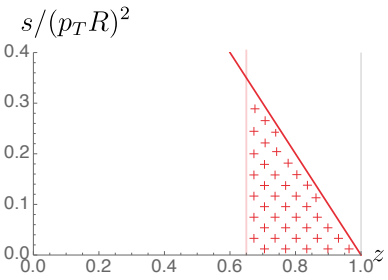

(b) G_2: Soft counterterm

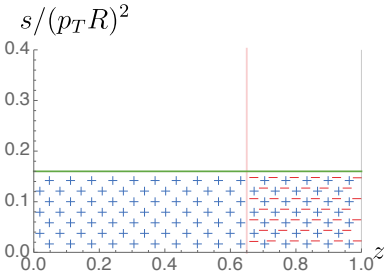

(c) G_3: Box counterterm

Figure 2.2 A graphical representation of our subtraction scheme in equation (2.6). We have only included the soft counterterms for $z \to 1$ for legibility. Shown are the restrictions on the measurement from the observable M_{obs} (blue line), the soft limit of the observable $M_{obs,1}$ (red line), the box $s < B\mu^2$ (green line) and the cut on z arising from A (pink line). Blue plus (minus) areas correspond to positive (negative) contributions of the full integrand Q_i, while red plus (minus) areas correspond to positive (negative) contributions of $Q_{i,1}$.

section section 2.4, we will use the CUBA implementation of VEGAS [100] to perform the integrations. Convergence problems in the numerical integration may arise due to the mismatch of the observable and its soft approximation, which generally can lead to integrable singularities. If these problems are severe it can help to find an explicit remapping of the counterterm, which decreases the mismatch between the observable and its soft limit. We present a method for how this can be achieved with a worked through example in app. 2.B.

Let us now discuss the integrated counterterms. Due to their simplicity, the counterterms can be calculated analytically, which we discuss for a single region r in the sum in equation (2.8). Let us first focus on the soft counterterms, which are contained in G_2 shown in figure 2.2b. The soft limits of the integrand $Q_i M_{\text{obs}}$ are given by $Q_{i,0} M_{\text{obs},0}$ and $Q_{i,1} M_{\text{obs},1}$, see eqs. (2.7) and (2.8). The constants c_i and α_i are user input in our code, see section 2.3. For values

$\alpha \neq 1$, no rapidity regulator is needed and η can be set to 0, leading to the following soft counterterm

$$G_{q,2} = \frac{2C_F}{\epsilon^2} \frac{e^{\gamma_E \epsilon}}{\sqrt{\pi}\,\Gamma(\frac{1}{2}-\epsilon)} \int_0^\pi \mathrm{d}\phi\, \Theta(\Phi)(\sin\phi)^{-2\epsilon} \times \left[\frac{(c_1^+)^{-\epsilon}}{(1-\alpha_1^+)} A^{-\epsilon(1-\alpha_1^+)} - \frac{(c_1^-)^{-\epsilon}}{(1-\alpha_1^-)} A^{-\epsilon(1-\alpha_1^-)} \right], \tag{2.9}$$

$$G_{g,2} = \frac{C_A}{\epsilon^2} \frac{e^{\gamma_E \epsilon}}{\sqrt{\pi}\,\Gamma(\frac{1}{2}-\epsilon)} \int_0^\pi \mathrm{d}\phi\, \Theta(\Phi)(\sin\phi)^{-2\epsilon} \times \left[\frac{(c_0^+)^{-\epsilon}}{(1-\alpha_0^+)} A^{-\epsilon(1-\alpha_0^+)} - \frac{(c_0^-)^{-\epsilon}}{(1-\alpha_0^-)} A^{-\epsilon(1-\alpha_0^-)} + \frac{(c_1^+)^{-\epsilon}}{(1-\alpha_1^+)} A^{-\epsilon(1-\alpha_1^+)} - \frac{(c_1^-)^{-\epsilon}}{(1-\alpha_1^-)} A^{-\epsilon(1-\alpha_1^-)} \right].$$

For $\alpha = 1$ one needs a rapidity regulator and the corresponding expression is given in appendix 2.A. The box counterterm G_3 in figure 2.2c is given by

$$G_{q,3} = C_F\, I(\phi^+, \phi^-; \epsilon)\, \frac{e^{\gamma_E \epsilon} B^{-\epsilon}}{\sqrt{\pi}\,\Gamma(\frac{1}{2}-\epsilon)} \Big(\frac{(4-\epsilon)(1-\epsilon)\Gamma^2[1-\epsilon]}{2\Gamma[2-2\epsilon]} - 2A^{-\epsilon} \Big), \tag{2.10}$$

$$G_{g,3} = I(\phi^+, \phi^-; \epsilon)\, \frac{e^{\gamma_E \epsilon} B^{-\epsilon}}{\sqrt{\pi}\,\Gamma(\frac{1}{2}-\epsilon)} \Big(\Big(\frac{3}{2} C_A (4-3\epsilon) + 2\epsilon n_f T_R \Big) \frac{(1-\epsilon)\Gamma^2[1-\epsilon]}{(3-2\epsilon)\Gamma[2-2\epsilon]} - 2C_A A^{-\epsilon} \Big).$$

The integral over ϕ has been carried out for $\Theta(\Phi) = \Theta(\phi^+ - \phi)\Theta(\phi - \phi^-)$ leading to the function

$$I(a, b; \epsilon) = \int_a^b \mathrm{d}\phi\, \sin^{-2\epsilon}\phi\,. \tag{2.11}$$

The evaluation of this integral and its expansion to order ϵ^2 is presented in app. 2.C.

The chosen subtraction bears fruit in the simplicity of the integrated counterterms. The corresponding Laurent series in ϵ can be expressed solely in terms of the Riemann zeta function at integer values, given that only pure Gamma functions appear. From an analytic point of view, the potentially more complicated pieces are instead captured in the finite part, which depends on the details of the observable and can be calculated numerically to arbitrary high order in ϵ. Notice that the soft counterterm $G_{i,2}$ can give rise to more complicated integrals if the coefficients $c_i^\pm$ depend on the azimuthal angle ϕ. One may be able to carry out this integral analytically in certain cases, but this can certainly not be done in general. This is not a problem, because one can expand in ϵ and η before integrating over ϕ.

2.2.2 Delta and theta functions

In our subtraction scheme we assume that the observables restrict the integration to certain regions of phase space via Heaviside theta functions. However, many observables $\mathcal{O}$ are naturally expressed in terms of Dirac delta functions, requiring one to rewrite it using

$$\delta[\mathcal{O} - f(s,z,\phi)] = \pm\frac{\mathrm{d}}{\mathrm{d}\mathcal{O}}\Theta[\pm(\mathcal{O} - f(s,z,\phi))]\,, \tag{2.12}$$

where f is a function of the kinematics of the collinear splitting, and possibly external parameters. The sign $\pm$ should be chosen such that the theta function does not vanish at tree-level, which ensures that the poles are included in the one-loop jet function. For example, if $\mathcal{O} \geq 0$ and at tree-level $\mathcal{O} = 0$, one needs to choose the plus sign in equation (2.12).

In perturbative QCD one often works with the following convention for the Dirac delta function,

$$g(0) = \int_0^c \mathrm{d}x\; g(x)\delta(x) \qquad \text{for } c > 0\,. \tag{2.13}$$

This differs from the definition given in standard math literature

$$g(0) = \int_b^c \mathrm{d}x\; g(x)\delta(x) \qquad \text{for } c > 0 > b\,, \tag{2.14}$$

where the lower boundary b must be strictly less than zero. If the delta function that encodes the measurement satisfies equation (2.13), this has implications for the definition of the Heaviside function on the right-hand side of equation (2.12). In particular, one must demand then that $\Theta(0) = 0$. To see this, consider a function $g(x)$ with $0 \leq x \leq 1$. From

$$\begin{aligned} g(0) &= \int_0^1 \mathrm{d}x\; g(x)\delta(x) = \int_0^1 \mathrm{d}x\; g(x)\,\frac{\mathrm{d}}{\mathrm{d}x}\Theta(x) = [g(x)\Theta(x)]_0^1 - \int_0^1 \mathrm{d}x\,\frac{\mathrm{d}}{\mathrm{d}x}g(x) \\ &= g(1)\Theta(1) - g(0)\Theta(0) - (g(1) - g(0)) = g(0)(1 - \Theta(0))\,, \end{aligned} \tag{2.15}$$

we conclude that $\Theta(0) = 0$. While this is not of much concern when a theta function is integrated over, there are situations where it must be taken into account. As an example, the jet shape calculation involves a jet function describing the energy fraction z inside a cone, see section 2.4.3. Switching to a cumulant variable for z, we need to choose $\delta(z - \dots) = -\mathrm{d}/\mathrm{d}z[-(z - \dots)]$, because $0 \leq z \leq 1$ and $z = 1$ at tree-level. If we now want to calculate the average momentum fraction from the cumulant tree-level result

$$\begin{aligned} \int_0^1 \mathrm{d}z\, z\,\delta(z-1) = -\int_0^1 \mathrm{d}z\, z\,\frac{\mathrm{d}}{\mathrm{d}z}\,\theta(1-z) &= -z\theta(1-z)|_0^1 + \int_0^1 \mathrm{d}z\,\theta(1-z) \\ &= 1 - \theta(0) = 1\,, \end{aligned} \tag{2.16}$$

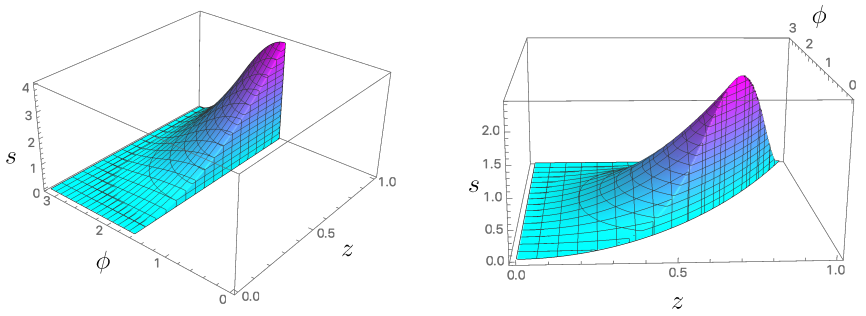

(a) **(b)**

Figure 2.3 IR unsafe observables that our code (a) can and (b) can't handle.

we have to take $\theta(0) = 0$ to find agreement with the direct evaluation using the delta function.

2.2.3 Infrared safety and limitations on the observable

While so far our discussion was mostly based on the s-z plane, there are observables which depend also on the azimuthal angle ϕ. The integration domain is then parametrized by coordinates (s, z, ϕ) and IR safety requires the full $s = 0$ plane to be included or excluded by the observable, i.e. the set of points

$$\{(s, z, \phi)|s = 0\,, 0 \leq z \leq 1\,, 0 \leq \phi \leq \pi\}\,. \tag{2.17}$$

However, our method allows for a special class of IR-unsafe observables, where only subdomains of the collinear plane with the azimuthal angle bounded between constant values are included/excluded by the observable, i.e.

$$\{(s, z, \phi)|s = 0\,, 0 \leq z \leq 1\,, \phi^- \leq \phi \leq \phi^+\}\,, \tag{2.18}$$

with $0 \leq \phi^- < \phi^+ \leq \pi$. This is illustrated in figure 2.3a. An IR-unsafe observable which is not of this form, and currently not supported by GOJet, is illustrated in figure 2.3b. Here $\phi^\pm$ vary as functions of z across the collinear plane in such a way that not the full $s = 0$ plane is included in the integration domain. For $s > 0$ the bounds on ϕ can depend on z. GOJet can also handle IR-unsafe observables that include just $z = 0$ and/or $z = 1$ of the $s = 0$ plane, which only require soft counterterms.

2.2.4 Example: Angularities with the Winner-Take-All axis

We will now illustrate our scheme by considering the family of e^+e^- event shapes called angularities [101]

$$e_b \equiv \frac{1}{Q}\sum_i E_i(\sin\theta_i)^{1-b}(1-|\cos\theta_i|)^b \overset{\theta_i\ll 1}{\approx} \frac{2^{-b}}{Q}\sum_i E_i\theta_i^{b+1}\,, \tag{2.19}$$

parametrized by b[4]. Here Q is the center-of-mass energy, and the sum runs over all particles i in the final state with energy E_i and angle θ_i with respect to some axis. The final expression is only valid in the small-angle limit, which is appropriate for the jet function calculation, highlighting that e_b probes the angular distribution with exponent $1+b>0$. While angles were originally taken with respect to the thrust axis, we will here use the Winner-Take-All axis [74]. For the one-loop jet function this axis is simply along the most energetic particle in the jet, so the only non-zero contribution in the sum on i in equation (2.19) comes from the least energetic particle, with θ_i the angle between the two partons in the jet. Noting that $s = 2p_1\cdot p_2 = \frac{1}{2}z(1-z)(1-\cos\theta)Q^2 \approx \frac{1}{4}z(1-z)\theta^2Q^2$, we obtain the following measurement function for a cut on the angularity $e_b \le e_b^c$,

$$M_b(s,z) = \Theta\Big[z(1-z)\,Q^2\Big(\frac{e_b^c}{\min[z,1-z]}\Big)^{2/(b+1)} - s\Big]. \tag{2.20}$$

For angularity exponent $b<1$, the observable is unbounded from above, similar to the top curve of region 2 in figure 2.1. In the notation of equation (2.8), we see that the soft limit of the observable is characterized by $c_0 = c_1 = Q^2(e_b^c)^{2/(b+1)}/\mu^2$ and $\alpha_0 = \alpha_1 = 2/(1+b)-1$. The one-loop contribution to the jet function is obtained by plugging in these these constants in eqs. (2.9) and (2.10) to calculate G_2, performing the integration over s and z for G_1, and adding these contributions to the box G_3. Performing the integration over s analytically and the integration over z numerically for $b=2$, we obtain using GOJET

$$\mathcal{J}^{(1)}_{q,e_2} = \frac{\alpha_s C_F}{2\pi}\bigg(\frac{\mu^2}{Q^2(e_2^c)^{2/3}}\bigg)^{\epsilon}\Big(\frac{3}{2\epsilon^2}+\frac{3}{2\epsilon}-1.909961286856877\Big), \tag{2.21}$$

where we used $\mu = Q(e_2^c)^{1/3}$ to calculate the constant contribution and re-instated the logarithmic behaviour afterwards. Our result agrees with the expression in refs. [74, 75] up to order 10^{-11}.[5] For $b=0$ the rapidity regulator

[4] Our b is related to the parameter a in ref. [101] by $b = 1-a$.

[5] Refs. [74, 75] both use $\beta = 1+b$ instead of b, and ref. [74] also removes the 2^{-b} from the definition in equation (2.19) and takes Q to be the jet energy.

is required. In that case we find

$$\mathcal{J}^{(1)}_{q,e_0} = \frac{\alpha_s C_F}{2\pi}\left(\frac{2\nu}{Q}\right)^{\eta}\left(\frac{\mu^2}{Q^2(e_0^c)^2}\right)^{\epsilon}\Big(\frac{2}{\epsilon\eta}+\frac{3-4\log 2}{2\epsilon}-1.8693096781349734\Big), \tag{2.22}$$

in agreement with ref. [74].

2.3 GOJET Program

The GOJET MATHEMATICA-package automatically performs the subtraction, given the observable and its soft limit (see equation (2.8)) as input. One can either let MATHEMATICA perform the numerical integration or choose to export the integrand. The latter feature may be useful if `NIntegrate` either has difficulty converging or is not fast enough. In such cases it can be advantageous to use algorithms such as VEGAS, that are faster due to their implementation in C++ or Fortran. A general overview of the various functions included in the package is given in section 2.3.1. A detailed description of their input is given in section 2.3.2, with a worked-out example in section 2.3.3.

2.3.1 Functions

There are a total of 12 different functions, listed in section 2.3.2, which the user can access. As indicated by their names half of these are for calculating gluon jet functions while the other half are for calculating quark jet functions. Restricting to the former, `PolesGluon` returns the pole terms in ϵ and η for the gluon jet function and `GluonJet` returns the integrand of the finite terms, by which we here refer to the $\epsilon^0\eta^0$-term. In addition, `GluonJetN` performs the numerical integration over the cube $0 \leq s, z, \phi \leq 1$ of this integrand. This integration domain is the result of mapping $s \to s/(1-s)$ and $\phi \to \pi\phi$, which also stabilizes the integration over s. Note that `GluonJet` also contains the $\epsilon^0\eta^0$-pieces of the counterterms G_2 and G_3, which are already integrated over analytically. For the convenience of the user these pieces are simply added in integrated form since they are not altered by the trivial numerical integration over the unit cube.

Let us now discuss the arguments of the functions in general terms. The first arguments encode the measurement `O` and its soft limit $\texttt{O}_0$ and $\texttt{O}_1$ corresponding to the limits $z \to 0$ and $z \to 1$, respectively. The observable should generally be IR safe, with some exceptions discussed in section 2.2.3. Furthermore, we require certain restrictions on the form of the soft limits. Specifically, it is not possible to restrict the ϕ-integration boundaries via $\texttt{O}_0$ and $\texttt{O}_1$, whose format

is fixed. It is however possible to apply s, z-independent constraints on the boundaries of the ϕ-integration through the separate argument Φ, which are the same for the finite part as well as the counterterms.

The next set of arguments specify the regularization and IR scheme: the need of a rapidity regulator or collinear regulator is controlled by the switches `rr` and `box`, respectively. The explicit cut for the soft limits and box is specified by `A` and `B` (see equation (2.6)). The independence of the final result on these parameters provides a useful cross-check for the calculation. A specific choice of these parameters can also be used to improve the convergence of the numerical integration. For the gluon jet function, the number of quark flavors is specified through the argument `nf`. The number of colors has been fixed to three, but the full dependence on the Casimirs can be easily reconstructed from the answer. The final set of arguments enables the user to specify the integration method or output format for the integrand.

Finally, we also allow for more complicated observables, where the phase-space restriction due to the measurement breaks up into more than one region. The corresponding functions have "`Regions`" appended to their name, and contain additional arguments specifying possible dependence on external parameters in the regions.

2.3.2 Input format

Here we specify the syntax of each of the functions:

```
GluonJet[O, O0, O1, Φ, rr, box, A, B, s, z, ϕ, nf, format, file]
GluonJetRegions[R, O, R0, O0, R1, O1, Φ, rr, box, A, B, s, z, ϕ, nf,
                format, file]
GluonJetN[O, O0, O1, Φ, rr, box, A, B, s, z, ϕ, nf, method]
GluonJetRegionsN[R, O, R0, O0, R1, O1, Φ, rr, box, A, B, s, z, ϕ, nf,
                 method]
PolesGluon[O0, O1, Φ, rr, box, A, B, ϕ, nf]
PolesGluonRegions[O0, O1, Φ, rr, box, A, B, ϕ, nf]

QuarkJet[O, O0, O1, Φ, rr, box, A, B, s, z, ϕ, format, file]
QuarkJetRegions[R, O, R0, O0, R1, O1, Φ, rr, box, A, B, s, z, ϕ,
                format, file]
QuarkJetN[O, O0, O1, Φ, rr, box, A, B, s, z, ϕ, method]
QuarkJetRegionsN[R, O, R0, O0, R1, O1, Φ, rr, box, A, B, s, z, ϕ,
                 method]
```

`PolesQuark[O0, O1, Φ, rr, box, A, B, ϕ]`
`PolesQuarkRegions[O0, O1, Φ, rr, box, A, B, ϕ]`

The variables used to describe the input are:

- `R`: List of lists which contain arguments of Heaviside theta functions which depend *only* on external parameters for each region. Regions that do not depend on external parameters need {1} as input in their respective position in the list. The number of regions should match with the lists for `O` below.

- `O`: The list of argument(s) of the Heaviside theta function encoding the bounds imposed by the measurement. More specifically, `O` contains the arguments of the Heaviside theta functions M_{obs} in equation (2.2). For the case of a single region, the elements of the list correspond to the arguments of Heaviside theta functions, whose product constrain the region. In the case of multiple regions, `O` is a list of lists. The entries of the outer list correspond to the different regions, each entry is again a list of constraints containing the arguments of the Heaviside theta functions M^r_{obs} constraining the particular region. This allows the user to implement arbitrary sums of products of Heaviside theta functions.

- `R1` (`R0`): List of lists which contain arguments of Heaviside theta functions which depend *only* on external parameters for each region in the limit $z \to 1$ ($z \to 0$). The length of this list is therefore equal to the number of soft regions that emerge in the soft limit. Regions that do not depend on external parameters need {1} as input in their respective position in the list. The number of soft regions can be less than the number of regions, but should match with the lists for `O0` and `O1` below. In particular, regions may merge or disappear in the soft limit. `R1` (`R0`) can also be used in cases with just one region where there is dependence on external parameters in the soft limits.

- `O1` (`O0`): List $\{\{c_1^-, \alpha_1^-\}, \{c_1^+, \alpha_1^+\}\}$ describing the lower and upper boundary of the region in the limit where $z \to 1$ (and similarly for $z \to 0$), see equation (2.8). If there is no lower boundary, c_1^- is just 0. When considering multiple regions, `O1` (`O0`) is a list of lists where each region has an upper and a lower boundary of the aforementioned format.

- Φ: List of arguments of the Heaviside theta functions that impose constraints on the azimuthal angle ϕ, i.e., the input $\{\phi^+ - \phi, \phi - \phi^-\}$ will constrain $\phi^- < \phi < \phi^+$. In the case of multiple regions that contain

collinear and/or soft divergences we require the range on ϕ to be the same for all regions. (Arbitrary constraints on ϕ can of course be encoded in `O`; but these are not allowed to survive singular limits; that is the they should match the boundaries imposed by Φ in these limits; see section 2.2.3 for more details.)

- `rr`: Boolean variable specifying whether a rapidity regulator should be included, which we implemented as

$$(2(1-z)z))^{-\eta} \tag{2.23}$$

  This corresponds to the more conventional factor $(\nu/((1-z)z\ \omega))^{\eta}$, for the scale choice $\nu = \frac{1}{2}\omega$. The user can always reconstruct the full dependence on the scale ν a posteriori, given the knowledge of the $1/\eta$ pole.

- `box`: Boolean controlling whether a box is needed to handle the collinear divergence. It should be included when the region of phase space includes $s = 0$ and not otherwise (in line with the restrictions outlined in section 2.2.3).

- `A`: Real number specifying the region where the soft counterterms are subtracted. Explicitly, the $z \to 0$ ($z \to 1$) counterterms are subtracted in the phase-space region where $z <$ `A` ($1 - z <$ `A`), and therefore $0 <$ `A` ≤ 1.

- `B`: Postive real number specifying the size of the box.

- `s`: Variable used to describe the invariant mass of the parton that initiates the jet. In the code we have made this variable dimensionless by rescaling with the renormalisation scale μ^2, i.e., `s` $= \frac{s}{\mu^2}$.

- `z`: Variable encoding the momentum fraction z of one of the partons in the collinear splitting.

- ϕ: Variable corresponding to the azimuthal angle of the collinear splitting.

- `nf`: Variable specifying the number of (massless) quark flavors. This variable does not need to be set to an integer, but can be left in symbolic form.

- `format`: String specifying the output form of this function. One can choose between “Mathematica", “Fortran" and “C". Note that when performing the numerical integration in Fortran or C, the user needs to

provide a function `HeavisideTheta` that satisfies $\Theta(0) = 0$, as described in section 2.2.2. In addition, for exporting to C, one needs to include the MATHEMATICA header file mdefs.h provided by MATHEMATICA in the directory[6] `$InstallationDirectory`/SystemFiles/IncludeFiles/C.

- `file`: String with the filename to which the integrand will be exported. For an empty string the integrand will be printed to the screen.
- `method`: This string can specify which method `NIntegrate` uses in MATHEMATICA, and we refer the reader to the MATHEMATICA documentation for the available options. For an empty string the default method of `NIntegrate` will be used.

2.3.3 Example: k_T clustering algorithms

To illustrate the use of our code we now calculate the jet function for the family of k_T clustering algorithms. At one-loop order, where there are at most two particles in the final state, they are clustered into a single jet if the angle between them is less than the jet radius parameter R, which for the case of an e^+e^- collider corresponds to a single region[7]

$$s \leq z(1-z)E^2R^2\,, \tag{2.24}$$

where E is the jet energy. The $z \to 0$ and $z \to 1$ limits of equation (2.24) are described by

$$\begin{aligned} z \to 0: &\quad s = zE^2R^2 &&\longrightarrow \quad c_0^+ = E^2R^2/\mu^2, \alpha_0^+ = -1, \\ z \to 1: &\quad s = (1-z)E^2R^2 &&\longrightarrow \quad c_1^+ = E^2R^2/\mu^2, \alpha_1^+ = -1. \end{aligned} \tag{2.25}$$

These are no lower constraints, i.e. $c_i^- = 0$. Calculating this observable requires a box since the $s = 0$ line is inside the domain of integration. Since $\alpha_i \neq 1$, a rapidity regulator is not needed. The constraint in equation (2.24) due to the measurement does not depend on ϕ, and so we take $\Phi = \{\}$.

We now calculate the quark jet function. As equation (2.8) is a relatively simple expression, for which the jet function can be easily calculated analytically, we will use MATHEMATICA to perform the numerical integration over the subtracted integral by using `QuarkJetN` with the the 'LocalAdaptive' integration method. In the following we set $\mu = ER$ for simplicity. Note how

[6] The installation directory can be determined by running `$InstallationDirectory` in MATHEMATICA.

[7] The corresponding result for pp collisions can be obtained by simply replacing the jet energy E by the jet transverse momentum p_T, and R then corresponds to a distance in (η, ϕ) instead of an angle.

this, since the variable `s` corresponds to $\frac{s}{\mu^2}$, cancels the factor E^2R^2 in the obsevable.

```
In[1]:= O = z(1 − z) − s;
        O0 = {{0,0},{1,−1}};
        O1 = {{0,0},{1,−1}};
        method =“LocalAdaptive";
        box = True;
        rr = False;
        A=0.6;
        B=20;

In[2]:= QuarkJetN[O, O0, O1, {}, rr, box, A, B, s, z, phi, method]

Out[2]= −1.2029367022′

In[3]:= PolesQuark[O0, O1, {}, rr, box, A, B, phi]

Out[3]= 4/(3ϵ^2) + 2/ϵ
```

From this answer it is straight forward to reconstruct that the full color-dependence of the regulated one-loop quark jet function is given by:

$$\mathcal{J}_q^{k_T} = C_F\left(\frac{1}{\epsilon^2} + \frac{3}{2\epsilon} - 0.9022033008\right). \tag{2.26}$$

The poles match exactly with the result by [64] and the finite term agrees up to order 10^{-6}. Similar agreement is found for the gluon jet function:

$$\mathcal{J}_g^{k_T} = C_A\left(0.0422426 + \frac{1}{\epsilon^2} + \frac{11}{6\epsilon}\right) - n_f T_R\left(\frac{2}{3\epsilon} + 2.55555\right). \tag{2.27}$$

The accompanying MATHEMATICA notebook contains several hands-on examples to further illustrate the use of the different functions.

2.4 Applications

To validate the method and corresponding code, the jet functions for several known examples have been checked. Some of these were used throughout the paper to explain our approach, namely the k_T family of clustering algorithms (section 2.3.3), and angularities with respect to the WTA axis (section 2.2.4). In addition, we provide results in section 2.4.1 for the cone algorithm and in section 2.4.3 for the jet shape. The latter is more challenging due to its azimuthal-angular dependence, which arises because the jet axis is along the total jet momentum and thus sensitive to recoil of soft radiation. In section 2.4.2 we present, for the first time, the one-loop jet functions for angularities

with respect to the thrust axis, taking into account recoil. Although for $b > 0$ this recoil is formally power-suppressed, it can be numerically large [93].

2.4.1 Cone jet

At one-loop order, the condition that both partons are within a cone jet in an e^+e^- collisions is that their angle with the jet axis is less than R (for pp[7]). Since the jet axis is along the total jet momentum, one simply needs to consider the angle with the parton that initiates the jet, leading to the following condition

$$s \leq E^2 R^2 \min\Big[\frac{1-z}{z}, \frac{z}{1-z}\Big]. \tag{2.28}$$

As we focus on the finite term in the jet function, we fix $\mu = ER$ finding

$$\begin{aligned}
\mathcal{J}_q^{\text{Cone}} &= C_F\Big(1.46711 + \frac{1}{\epsilon^2} + \frac{3}{2\epsilon}\Big), \\
\mathcal{J}_g^{\text{Cone}} &= C_A\Big(2.23477 + \frac{1}{\epsilon^2} + \frac{11}{6\epsilon}\Big) - n_f T_R\Big(\frac{2}{3\epsilon} + 2.20197\Big),
\end{aligned} \tag{2.29}$$

which agrees up to order 10^{-6} with ref. [64].

2.4.2 Angularities with recoil

In this section we determine, for the first time, the one-loop angularity jet function that includes the recoil of the thrust axis due soft radiation. While this recoil is power-suppressed for $b > 0$, ref. [93] noted that it has a numerically large effect and presented a factorization framework to include it. The one-loop jet function we calculate here will start to contribute at NLL$'$ accuracy. This should be contrasted with the calculation in section 2.2.4, where we considered the angularity with respect to the WTA axis. To clearly distinguish these two cases in the notation, we will use τ_n instead of e_b, where n refers to the thrust axis.

The setup underpinning our calculation is illustrated in figure 2.4. Here θ is the angle between the thrust axis $\vec{n}$ and the direction $\vec{n}'$ of the initial collinear parton due to the recoil from soft radiation, which is treated as an external parameter in our calculation. The momenta of the two massless partons in the jet are denoted by $\vec{p_1}$ and $\vec{p_2}$, where we use (un)primed coordinates to denote light-cone components with respect to the $\vec{n}'$ ($\vec{n}$) direction. Explicitly,

$$\begin{aligned}
p_1'^{\mu} &= zQ\,\frac{n'^{\mu}}{2} + \frac{(1-z)s}{Q}\,\frac{\bar{n}'^{\mu}}{2} + p_{1\perp}'^{\mu} \equiv p_1'^{-}\frac{n'^{\mu}}{2} + p_1'^{+}\frac{\bar{n}'^{\mu}}{2} + p_{1\perp}'^{\mu}, \\
p_1^{\mu} &= p_1^{-}\frac{n^{\mu}}{2} + p_1^{+}\frac{\bar{n}^{\mu}}{2} + p_{1\perp}^{\mu}, \qquad p_1^{\pm} = p_1^0 \mp p_1^3\,,
\end{aligned} \tag{2.30}$$

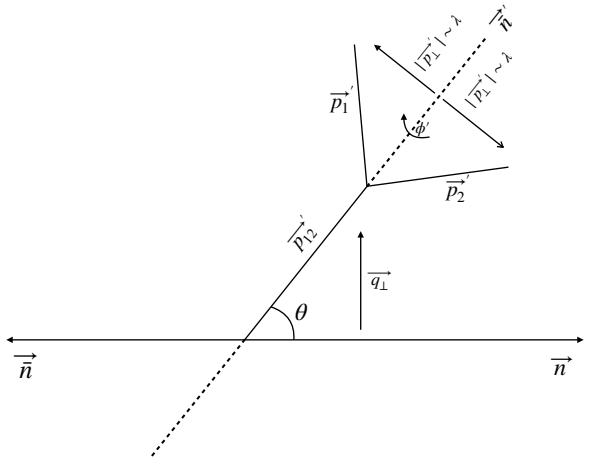

Figure 2.4 The setup of our calculation. The recoil is quantified by θ.

and similarly for p_2. Here we chose $n^\mu = (1,0,0,1)$ and $\bar{n}^\mu = (1,0,0,-1)$, z is the momentum fraction of the parton, s the invariant mass of the jet, and Q the center-of-mass energy of the e^+e^- collision. The expression in the recoiled frame follows from the definition of z and s through $p_1'^- = zQ$ and $s = (p_1' + p_2')^2$, as well as $p_{1\perp}'^\mu = -p_{2\perp}'^\mu$ and the on-shell condition $p_1'^2 = p_2'^2 = 0$. Note that $|p_{i\perp}'|^2 = z(1-z)s$.

The rotation between the two frames is described by

$$\vec{p_1} = \begin{pmatrix} \cos\theta & 0 & -\sin\theta \\ 0 & 1 & 0 \\ \sin\theta & 0 & \cos\theta \end{pmatrix} \vec{p_1}', \tag{2.31}$$

implying $|p_\perp|^2 = |p_\perp'|^2 + \theta^2 (p_1^3)^2 - 2\theta\cos\phi' |p_\perp'||p_1^3|$ in the small θ approximation, where ϕ' is the azimuthal angle around the $\vec{n}'$ axis. The large momentum components are the same in both frames, $p_i^- = p_i'^-$. The expression for the angularity τ_n becomes

$$\begin{aligned} \tau_n &= \frac{1}{Q}\sum_i |p_{i\perp}| \left(\frac{p_i^+}{p_i^-}\right)^{\frac{b}{2}} = \frac{1}{Q}\sum_i \left(\frac{|p_{i\perp}|^{1+b}}{(p_i^-)^b}\right) \\ &= \frac{1}{(2Q)^{1+b}}\, z^{-b} \Big(4z(1-z)s + (\theta Q)^2 z^2 - 4\theta\, Q\cos\phi'\, z^{\frac{3}{2}} \sqrt{(1-z)s}\Big)^{\frac{1+b}{2}} \\ &\quad + \frac{1}{(2Q)^{1+b}} (1-z)^{-b} \Big(4z(1-z)s + (\theta Q)^2 (1-z)^2 + 4\theta Q\cos\phi' (1-z)^{\frac{3}{2}} \sqrt{zs}\Big)^{\frac{1+b}{2}}, \end{aligned} \tag{2.32}$$

where $b > -1$. Using the delta function trick (see section 2.2.2), we switch to a cumulative measurement, writing the observable as

$$M_{\text{obs}} = \Theta[\tau_n^c - \tau_n]\,. \tag{2.33}$$

Unfortunately is it not possible to invert equation (2.33) to obtain an analytic solution for s and subsequently extract the soft limit $z \to 0$. We can, however, use the power-law ansatz in equation (2.8) to find the soft behavior of the observable. Since the equation is symmetric in $z \to 1-z$, we focus on finding the soft behavior in the $z \to 0$ limit. Using

$$s|_{z\to 0} = c_0(\phi) z^{-\alpha_0} \mu^2\,, \tag{2.34}$$

in equation (2.32) and taking the $z \to 0$ soft limit, we find

$$\begin{aligned}\tau_n^c\Big(\frac{2Q}{\mu}\Big)^{1+b} = z^{-b}\Bigg(4\,c_0\,z^{1-\alpha_0} + \Big(\frac{\theta Q}{\mu}\Big)^2 z^2 - 4\sqrt{c_0}\Big(\frac{\theta Q}{\mu}\Big)\cos\phi'\, z^{\frac{3-\alpha_0}{2}}\Bigg)^{\frac{1+b}{2}} \\ + \Bigg(4\,c_0\,z^{1-\alpha_0} + \Big(\frac{\theta Q}{\mu}\Big)^2 + 4\sqrt{c_0}\Big(\frac{\theta Q}{\mu}\Big)\,\cos\phi'(z)^{\frac{1-\alpha_0}{2}}\Bigg)^{\frac{1+b}{2}}.\end{aligned} \tag{2.35}$$

There is a single solution for s in either of the soft limits and therefore this observable only has an upper boundary over the full range of b, i.e. $c_0^- = 0$. The leading terms in equation (2.35) are used to solve for α_0^+ and c_0^+, and differ for $-1 < b < 0$, $b = 0$ and $b > 0$. We will analyze the last case in some detail and only provide the solutions for the others.

Assuming $b > 0$, the leading behavior in the $z \to 0$ limit of equation (2.35) is

$$\tau_n^c\Big(\frac{2Q}{\mu}\Big)^{1+b} = c_0^{\frac{1+b}{2}}\, z^{-b+(1-\alpha_0)(1+b)/2} + \Big(\frac{\theta\, Q}{2\,\mu}\Big)^{1+b}, \tag{2.36}$$

and from this we infer

$$c_0^+ = \frac{Q^2(\tau_n^c)^{2/(1+b)}}{\mu^2}\big(1-k^{1+b}\big)^{\frac{2}{1+b}}\,, \qquad \alpha_0^+ = \frac{1-b}{1+b}\,, \tag{2.37}$$

where

$$k \equiv \tfrac{1}{2}\theta\,(\tau_n^c)^{-1/(1+b)}\,. \tag{2.38}$$

Similarly, for $b = 0$ we obtain

$$c_0^+ = \frac{Q^2(\tau_n^c)^{2/(1+b)}}{\mu^2}\frac{1-k^2}{(2+2k\cos\phi)^2}\,, \qquad \alpha_0^+ = 1\,. \tag{2.39}$$

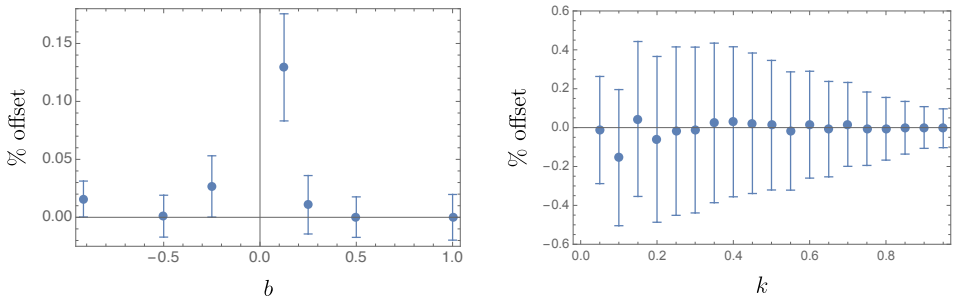

(a) **(b)**

Figure 2.5 The offset between our results for (a) different values of b with $\theta = 0$ and (b) different values of the recoil parameter k with $b = 0$ and the known results from the literature is shown.

For $-1 < b < 0$ the solution is a bit more difficult and reads

$$c_0^+ = \frac{Q^2(\tau_n^c)^{2/(1+b)}}{\mu^2}\left[1 + k^2\,\cos 2\phi - 2k|\cos\phi|\sqrt{1-k^2\sin^2\phi}\right)\Bigg],$$
$$\alpha_0^+ = 1\,. \tag{2.40}$$

In order to use GOJET, we rescale s and choose an energy scale μ. To be able to smoothly turn off the recoil, we choose μ in terms of the angularity, $\mu = Q\,(\tau_n^c)^{1/(1+b)}$. The only independent variable left is then given by k in equation (2.38). To be complete we also give the resulting observable input for GOJET:

$$\begin{aligned}0 = 1 - z^{-b}&\left(z(1-z)s + k^2z^2 - 2k\cos\phi'\,z^{\frac{3}{2}}\sqrt{(1-z)s}\right)^{\frac{1+b}{2}}\\ &- (1-z)^{-b}\left(z(1-z)s + k^2(1-z)^2 + 2k\cos\phi'(1-z)^{\frac{3}{2}}\sqrt{zs}\right)^{\frac{1+b}{2}}.\end{aligned} \tag{2.41}$$

The jet function for $\theta = 0$ (without recoil) was calculated analytically in refs. [71, 93] and we obtain the same results as can be seen in figure 2.5a. The error bars indicate the uncertainty from our numerical integration. Ref. [93] includes a zero-bin subtraction [51] to avoid double counting with the soft function in their factorization, which we do not include. The zero-bin subtraction depends on the details of the factorization theorem (indeed it vanishes in ref. [71]), so we do not offer this as a standard functionality of GOJET. The numerical integration for small values of b is particularly challenging (as can be seen for $b = \frac{1}{8}$), because the sub-leading terms with respect to the leading

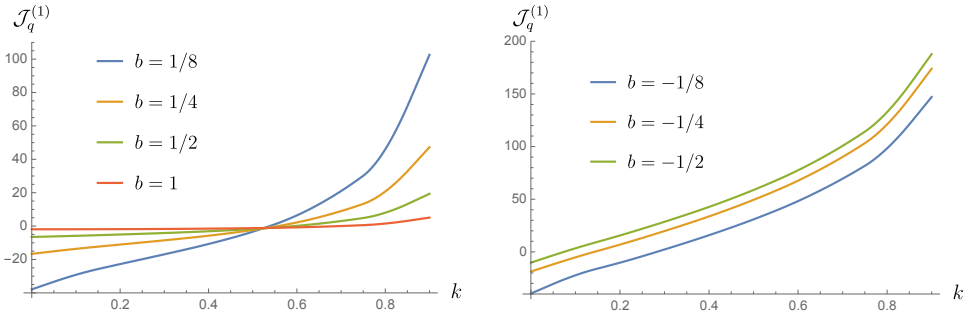

Figure 2.6 The results for the finite part of $\mathcal{J}_q^1$ for different values of b as a function of k.

soft behavior of the observable in equation (2.37) are particularly large in this case. A more detailed discussion of this issue and a method to cope with it is presented in app. 2.B. In figure 2.5b we reproduce the known results for $b = 0$ (broadening) and general recoil [97]. Our new results for general b including the effect of recoil, are shown in figure 2.6. The error bars are not shown in this plot as they are negligibly small.

2.4.3 Jet shape

As another nontrivial example, we calculate the jet function for the classic jet shape observable, reproducing the one-loop result of ref. [82]. The jet shape describes the average energy fraction z_r inside a cone of angular size r around the jet axis. As in section 2.4.2, recoil from soft radiation displaces the jet axis from the initial parton by an angle θ. This breaks the azimuthal symmetry, requiring one to integrate over ϕ. We have checked that our poles match exactly with the poles in [82] for all values of θ and r. The difference between the finite term is always below 0.5%. This has been illustrated in figure 2.7a for gluon jets and figure 2.7b for quark jets. We note that run time is not an issue, as less precision is needed in phenomenological results and the distribution can be interpolated. Our calculation represents the second independent calculation of this observable and thereby delivers a useful cross check of the results of ref. [82].

2.5 Conclusions

In this chapter we described our automated approach for calculating one-loop jet functions, and provide an implementation in the accompanying MATHE-

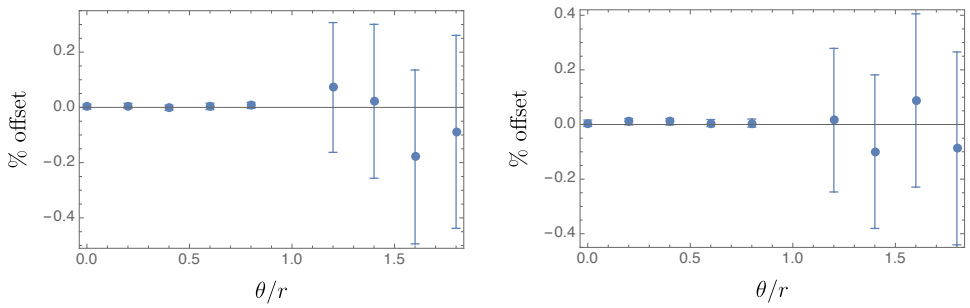

Figure 2.7 The offset between our finite result of the (a) gluon and (b) quark jet function and [82] for several values of $\frac{\theta}{r}$.

MATICA package called GOJET. We use geometric subtraction [99] to isolate the soft and collinear singularities. The collinear counterterm does not depend on the details of the observable, except that certain observables do not require it. We find that the soft counterterm depends on the behavior of the observable in the soft limits, which can be described by a power law. While the user must provide GOJET with this power law as input, we present a strategy to extract this in a highly nontrivial example. We employed cumulative distributions, such that observables correspond to integrating over certain regions of phase space, and thereby avoiding plus distributions. We have demonstrated our approach by reproducing the known one-loop jet function for a range of observables, and calculating, for the first time, the jet function for angularities including recoil. For broadening ($b = 0$ in our conventions) the effect of recoil must be kept [72], while for $b > 0$ it is formally power suppressed but can be numerically large [93]. For b close to 0, we encountered numerical convergence issues, due to an integrable divergence. We addressed this problem by substantially improving the counterterm through a remapping.

Our approach focuses on IR-safe observables, and we did not address the IR-unsafe case. Jet functions containing IR divergences are sensitive to nonperturbative physics, and our purely partonic calculation must be supplemented by a (universal) nonperturbative function that subtracts these divergences. A prime example is initial-state jets, which are described by beam functions [102]. Beam functions contain infrared divergences, which are removed by matching onto parton distribution functions, leaving finite matching coefficients.

The automated approach and code presented here provides a very useful tool, calculating jet functions at one-loop order. Very few two-loop jet functions are known, and an automated approach would allow many resummation calculations to be extended to NNLL′ or $\mathrm{N^3LL}$ accuracy. At this order the

singular limits become more complicated, the order of subtractions matter, and the parametrization of the observable in these limits will no longer be a simple power law, complicating the counterterms.

Appendices

2.A G_2 Subtraction Term for Rapidity Divergences

When the soft limit of the observable scales as $1/z$, we need a rapidity regulator to control the singularities. The resulting expressions for G_2 with rapidity regulator are given by

$$\begin{aligned}
G_{q,2} = {} & \frac{2C_F}{\epsilon} \frac{e^{\gamma_E \epsilon}}{\sqrt{\pi}\,\Gamma(\frac{1}{2}-\epsilon)} \left(\frac{\nu}{\omega}\right)^{\eta} \int_0^{\pi} \mathrm{d}\phi\, \Theta(\Phi) (\sin\phi)^{-2\epsilon} \\
& \left[\frac{(c_1^+)^{-\epsilon}}{\eta + \epsilon(1-\alpha_1^+)} A^{-\eta-\epsilon(1-\alpha_1^+)} - \frac{(c_1^-)^{-\epsilon}}{\eta + \epsilon(1-\alpha_1^-)} A^{-\eta-\epsilon(1-\alpha_1^-)} \right], \\
G_{g,2} = {} & \frac{C_A}{\epsilon} \frac{e^{\gamma_E \epsilon}}{\sqrt{\pi}\,\Gamma(\frac{1}{2}-\epsilon)} \left(\frac{\nu}{\omega}\right)^{\eta} \int_0^{\pi} \mathrm{d}\phi\, \Theta(\Phi) (\sin\phi)^{-2\epsilon} \\
& \left[\frac{(c_0^+)^{-\epsilon}}{\eta + \epsilon(1-\alpha_0^+)} A^{-\eta-\epsilon(1-\alpha_0^+)} - \frac{(c_0^-)^{-\epsilon}}{\eta + \epsilon(1-\alpha_0^-)} A^{-\eta-\epsilon(1-\alpha_0^-)} \right. \\
& \left. + \frac{(c_1^+)^{-\epsilon}}{\eta + \epsilon(1-\alpha_1^+)} A^{-\eta-\epsilon(1-\alpha_1^+)} - \frac{(c_1^-)^{-\epsilon}}{\eta + \epsilon(1-\alpha_1^-)} A^{-\eta-\epsilon(1-\alpha_1^-)} \right]. \qquad (2.42)
\end{aligned}$$

2.B Counterterm Mapping

In this appendix we discuss how to improve the convergence of the soft subtraction through a mapping. For simplicity, we consider only the soft singularity at $z = 0$, for which the finite term generated by the geometric subtraction is of the form:

$$\int_0^1 \mathrm{d}z \left[\frac{f(z)\Theta(O(z)) - f(0)\Theta(O_0(z))}{z} \right]. \qquad (2.43)$$

Here we suppressed the dependence (and integrals) over s and ϕ, extracting the $1/z$ singularity from the integrand Q, i.e. $f = zQ$. While this integrand is by construction integrable, poor numerical convergence may be caused by mismatch of the observable O and its soft limit O_0. This problem can become particularly severe if $O(z)$ has a fractional power series in z, as we illustrate below.

To improve the convergence of the integral, we apply the following mapping

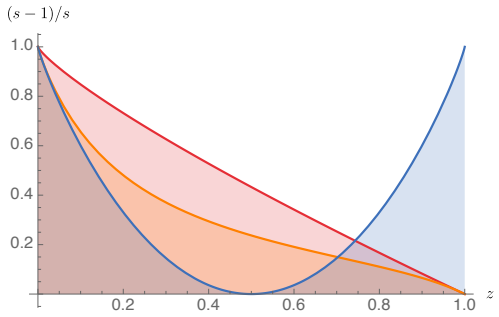

Figure 2.8 The plot shows the observable (blue), its soft approximation in equation (2.49) (red) and the remapped soft approximation in equation (2.50) (orange).

(to the counterterm only):

$$G\colon z \to \frac{z + g(z)}{1 + g(z)}\,. \tag{2.44}$$

This maps the interval $0 \leq z \leq 1$ onto itself, as long as $z + g(z) > 0$, and the subtracted integral will remain the same as long as the function $g(z)$ decreases faster near $z = 0$ than z itself, i.e., it satisfies

$$\lim_{z\to 0} \frac{g(z)}{z} = 0\,. \tag{2.45}$$

Applying this map, we can replace equation (2.43) with:

$$\int_0^1 \mathrm{d}z \left[\frac{f(z)\Theta(O(z))}{z} - \frac{f(0)\Theta(O_0(G(z)))}{G(z)}\left|\frac{\partial G(z)}{\partial z}\right|\right]. \tag{2.46}$$

One can now construct the function $g(z)$ to map $O_0(G(z))$ closer to $O(z)$ in the region $z \to 0$.

For the angularities with recoil in section 2.4.2, we encounter the following instructive example

$$O(z) = 1/s - \frac{(z(1-z))^{\frac{b-1}{b+1}}}{(z^b + (1-z)^b)^{\frac{2}{1+b}}}\,, \tag{2.47}$$

which has poor convergence for small positive values of b. Already $b = 1/10$ yields a sufficiently challenging scenario, for which the power series around

$z = 0$ is given by:

$$\begin{aligned} O(z) = 1/s - z^{\frac{9}{11}} + \frac{20}{11} z^{\frac{101}{110}} + \frac{90}{121} z^{\frac{56}{55}} - \frac{60}{1331} z^{\frac{123}{110}} + \frac{195}{14641} z^{\frac{67}{55}} - \frac{936}{161051} z^{\frac{29}{22}} \\ + \frac{5460}{1771561} z^{\frac{78}{55}} - \frac{35880}{19487171} z^{\frac{167}{110}} + \frac{255645}{214358881} z^{\frac{89}{55}} - \frac{1931540}{2357947691} z^{\frac{189}{110}} \\ - \frac{25922165435}{25937424601} z^{\frac{20}{11}} - \frac{5136983395938}{3138428376721} z^{\frac{211}{110}} + \mathcal{O}(z^2) \,. \end{aligned} \tag{2.48}$$

It is thus apparent that the leading term approximation

$$O_0(s, z, \phi) = 1/s - z^{\frac{9}{11}} \tag{2.49}$$

gives only a poor approximation of the full result. Substituting $z = G(z)$ with

$$g(z) = z \sum_{i=1}^{11} c_i \, z^{\frac{i}{10}} \tag{2.50}$$

into equation (2.49) we can match equation (2.48) by iteratively solving for the constants c_i. This procedure yields:

$$\begin{aligned} &c_1 = \frac{20}{9}, \quad c_2 = \frac{110}{81}, \quad c_3 = \frac{220}{2187}, \quad c_4 = -\frac{385}{19683}, \quad c_5 = \frac{1232}{177147}, \\ &c_6 = -\frac{15400}{4782969}, \quad c_7 = \frac{74800}{43046721}, \quad c_8 = -\frac{402050}{387420489}, \quad c_9 = \frac{20906600}{31381059609}, \\ &c_{10} = -\frac{345319185959}{282429536481}, \quad c_{11} = -\frac{6338162484818}{2541865828329} \,. \end{aligned} \tag{2.51}$$

The resulting curves are plotted in figure 2.8, highlighting the improvement due to the remapping. A VEGAS run using $5 \cdot 10^9$ points for the finite part of the quark jet function of this observable yields $-48.63(2)$ without the mapping, while we obtain $-48.745(9)$ after the mapping. The true value is -48.7731, indicating that the remapped counterterm yields a result significantly closer to the true value. In both cases it becomes clear that the offset is not completely covered by the uncertainty. While the remapping may thus improve convergence, it may not completely solve the issue.

2.C Azimuthal Integral

In this appendix we evaluate the integral

$$I(a, b; \epsilon) = \int_a^b \mathrm{d}\phi \, (\sin\phi)^{-2\epsilon} \,. \tag{2.52}$$

One can convert this integral into a Gauss-type hypergeometric integral using the transformation $\cos\phi = 1 - 2x$. However this leads to square roots in

the denominator which do not naively lead to a polylogarithmic expression. Instead, one can rewrite the integral as a contour integral in the complex plane using the transformation $z = e^{i\phi}$, such that

$$\sin\phi = \frac{z^2 - 1}{2\mathrm{i}z}\,, \tag{2.53}$$

leading to the following representation

$$I(a, b; \epsilon) = -\mathrm{i}\int_{e^{\mathrm{i}a}}^{e^{\mathrm{i}b}} \frac{\mathrm{d}z}{z}\Big(\frac{z^2 - 1}{2\mathrm{i}z}\Big)^{-2\epsilon}\,. \tag{2.54}$$

The integrand can be chosen to have branch cuts on the real axis for $z < 0$ and for $z > 1$. For $0 < a, b < \pi$, which is the range of physical interest, no branch cuts are ever crossed.

It is convenient to perform the integral on a contour along the real axis from $0 < z < A$ with $0 < A < 1$, i.e.,

$$F(A; \epsilon) = -\mathrm{i}2^{2\epsilon}e^{-\mathrm{i}\pi\epsilon}\int_0^A \frac{\mathrm{d}z}{z}\Big(\frac{1 - z^2}{z}\Big)^{-2\epsilon}. \tag{2.55}$$

The result can be analytically continued to the case of interest with $A = e^{\mathrm{i}a}$. We then obtain (in essence via the residue theorem)

$$I(a, b; \epsilon) = F(e^{ia}; \epsilon) - F(e^{ib}; \epsilon)\,. \tag{2.56}$$

While the divergence at $z = 0$ requires careful treatment, this drops out in the difference of the two terms in equation (2.56). We performed the integral using the Maple package Hyperint [103], finding that the integral can performed order by order in ϵ in terms of harmonic polylogarithms. This is to be expected, given that its singularities are located at $z = 0, -1, 1$. Up to order ϵ^2 we can express the result in terms of the classical polylogarithms:

$$I(a, b; \epsilon) = \sum_{n=0}^{\infty} I^{(n)}(a, b)\epsilon^n \tag{2.57}$$

with

$$
\begin{aligned}
I^{(0)}(a,b) &= b-a\,,\\
I^{(1)}(a,b) &= 2\mathrm{i}\,\mathrm{Li}_2(e^{\mathrm{i}a}) - 2\mathrm{i}\,\mathrm{Li}_2(e^{\mathrm{i}b}) + 2\mathrm{i}\,\mathrm{Li}_2(-e^{\mathrm{i}a}) - 2\mathrm{i}\,\mathrm{Li}_2(-e^{\mathrm{i}b}) + \mathrm{i}(a-b)(-a+\pi-b)\\
&\quad + (-2a+2b)\ln 2\,,\\
I^{(2)}(a,b) &= -\tfrac{2}{3}\mathrm{i}\ln^3(e^{\mathrm{i}b}+1) - 2\mathrm{i}\ln^2(e^{\mathrm{i}b}+1)\ln(1-e^{\mathrm{i}b}) - 4b\ln(e^{\mathrm{i}b}+1)\ln(1-e^{\mathrm{i}b})\\
&\quad + 2\mathrm{i}\ln^2(e^{\mathrm{i}a}+1)\ln(1-e^{\mathrm{i}a}) + 4a\ln(e^{\mathrm{i}a}+1)\ln(1-e^{\mathrm{i}a}) - 2\mathrm{i}\ln(e^{\mathrm{i}b}+1)\ln^2 2\\
&\quad - 2\mathrm{i}\ln(1-e^{\mathrm{i}b})\ln^2 2 + 2\mathrm{i}\ln(e^{\mathrm{i}a}+1)\ln^2 2 + 2\mathrm{i}\ln(1-e^{\mathrm{i}a})\ln^2 2 - 4\mathrm{i}\,\mathrm{Li}_3(e^{\mathrm{i}a})\\
&\quad + 4\mathrm{i}\,\mathrm{Li}_3[-(-1+e^{\mathrm{i}a})/(e^{\mathrm{i}a}+1)] - 4\mathrm{i}\,\mathrm{Li}_3[-(-1+e^{\mathrm{i}b})/(e^{\mathrm{i}b}+1)] + 2a\ln^2(e^{\mathrm{i}a}+1)\\
&\quad - 2b\ln^2(1-e^{\mathrm{i}b}) - 2b\ln^2(e^{\mathrm{i}b}+1) + 4\mathrm{i}\,\mathrm{Li}_3(\tfrac{1}{2}+\tfrac{1}{2}e^{\mathrm{i}a}) - 8\mathrm{i}\,\mathrm{Li}_3[1/(e^{\mathrm{i}a}+1)]\\
&\quad + 4\mathrm{i}\,\mathrm{Li}_3(\tfrac{1}{2}-\tfrac{1}{2}e^{\mathrm{i}a}) - 8\mathrm{i}\,\mathrm{Li}_3(1-e^{\mathrm{i}a}) + 4\mathrm{i}\,\mathrm{Li}_3(e^{\mathrm{i}b}) - 4\mathrm{i}\,\mathrm{Li}_3(\tfrac{1}{2}-\tfrac{1}{2}e^{\mathrm{i}b})\\
&\quad + 8\mathrm{i}\,\mathrm{Li}_3(1-e^{\mathrm{i}b}) + 4\mathrm{i}\,\mathrm{Li}_3(-e^{\mathrm{i}b}) + 8\mathrm{i}\,\mathrm{Li}_3(1/(e^{\mathrm{i}b}+1)) - 4\mathrm{i}\,\mathrm{Li}_3(\tfrac{1}{2}+\tfrac{1}{2}e^{\mathrm{i}b})\\
&\quad + 2(b-a)\ln^2 2 + 2\mathrm{i}(a-b)(-a+\pi-b)\ln 2 - 4\mathrm{i}\ln(e^{\mathrm{i}a}+1)\ln(1-e^{\mathrm{i}a})\ln 2\\
&\quad + (2\pi-4a)\mathrm{Li}_2(-e^{\mathrm{i}a}) + \tfrac{1}{3}\mathrm{i}\pi^2\ln(1-e^{\mathrm{i}a}) + 4\mathrm{i}\ln 2\,\mathrm{Li}_2(-e^{\mathrm{i}a})\\
&\quad - 4\mathrm{i}\ln 2\,\mathrm{Li}_2(e^{\mathrm{i}b}) + 4\mathrm{i}\ln(e^{\mathrm{i}b}+1)\mathrm{Li}_2(e^{\mathrm{i}b}) + 4\mathrm{i}\ln(1-e^{\mathrm{i}b})\mathrm{Li}_2(e^{\mathrm{i}b})\\
&\quad - 4\mathrm{i}\ln(e^{\mathrm{i}a}+1)\mathrm{Li}_2(e^{\mathrm{i}a}) - 4\mathrm{i}\ln(1-e^{\mathrm{i}a})\mathrm{Li}_2(e^{\mathrm{i}a}) + 4\mathrm{i}\ln 2\,\mathrm{Li}_2(e^{\mathrm{i}a})\\
&\quad + \tfrac{1}{6}(a-b)(3\pi^2-6\pi a-6\pi b+4a^2+4ab+4b^2) + \tfrac{2}{3}\mathrm{i}\ln^3(e^{\mathrm{i}a}+1)\\
&\quad + (-2\pi+4b)\mathrm{Li}_2(e^{\mathrm{i}b}) + (2\pi-4a)\mathrm{Li}_2(e^{\mathrm{i}a}) - \tfrac{1}{3}\mathrm{i}\pi^2\ln(1-e^{\mathrm{i}b})\\
&\quad + 4\mathrm{i}\ln(e^{\mathrm{i}b}+1)\ln(1-e^{\mathrm{i}b})\ln 2 + 4\mathrm{i}\ln(e^{\mathrm{i}b}+1)\mathrm{Li}_2(-e^{\mathrm{i}b})\\
&\quad + 4\mathrm{i}\ln(1-e^{\mathrm{i}b})\mathrm{Li}_2(-e^{\mathrm{i}b}) - 4\mathrm{i}\ln 2\,\mathrm{Li}_2(-e^{\mathrm{i}b}) + \mathrm{i}\pi^2\ln(e^{\mathrm{i}b}+1)\\
&\quad - \mathrm{i}\pi^2\ln(e^{\mathrm{i}a}+1) - 4\mathrm{i}\ln(e^{\mathrm{i}a}+1)\mathrm{Li}_2(-e^{\mathrm{i}a}) - 4\mathrm{i}\ln(1-e^{\mathrm{i}a})\mathrm{Li}_2(-e^{\mathrm{i}a})\\
&\quad + 2a\ln^2(1-e^{\mathrm{i}a}) - 4\mathrm{i}\,\mathrm{Li}_3(-e^{\mathrm{i}a}) + (-2\pi+4b)\mathrm{Li}_2(-e^{\mathrm{i}b})\,. \qquad (2.58)
\end{aligned}
$$

After this article was posted, we were informed that the azimuthal integral in app. 2.C was evaluated before in terms of so-called Log-sine functions, which were introduced and studied in [104,105] and have been implemented in a C++ library in [106]. Relations can also be found in these references to convert them into Nielsen polylogarithms, although not directly into classical polylogarithms (which is only possible up to order ϵ^2).

3

Azimuthal Decorrelation

3.1 Introduction

The production of a vector boson (V) in association with a jet is a crucial process in pp and heavy ion collisions. It is an important background in the study of Standard Model processes (e.g. to control b-tagging for $t\bar{t}$ measurements [107]) and the search for physics beyond the Standard Model (see [108] for a recent review), and a prime channel to study the effects of the quark-gluon plasma produced in heavy-ion collisions [109–111]. The precise theoretical prediction for such processes relies on advances in both fixed-order calculations and all-order resummation of large (Sudakov) logarithms. In pp collisions, the fixed-order calculations of such processes have reached next-to-next-to-leading order in QCD [112–117], while in the back-to-back limit the Sudakov logarithms in the total transverse-momentum distribution of V+jet have only been resummed up to next-to-leading logarithmic (NLL) accuracy [118–120]. The relatively large uncertainties in the resummed result at NLL accuracy (see the discussion in [120]) is one of the main obstacles to a precise prediction for processes involving the V+jet channel. In order to match to high-accuracy fixed-order calculations, one has to extend these resummation techniques to higher order. Progression to higher order resummation is however difficult due to intrinsic limitations, such as the presence of non-global logarithms [121]. In [122] a factorization formula was derived for the azimuthal angle between the boson and jet using the standard energy recombination scheme (see equation (1.166)). In that case, the recombination procedure is sensitive to recoil from soft radiation enclosed within the jet boundary. This leads to non-global contributions to the factorization of the cross section, as soft radiation inside and outside the jet contributes differently to the measurement.

In this chapter we show how to overcome these limitations using two main ingredients. First, a recoil-free jet axis, obtained using the Winner-Takes-All (WTA) recombination scheme [123, 124]. This specific choice of jet axis will

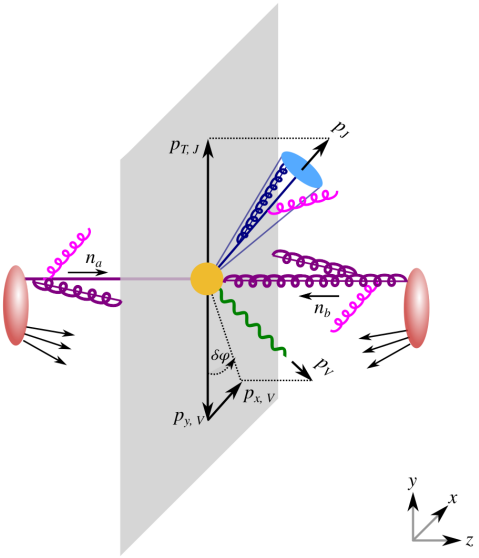

Figure 3.1 The azimuthal angle between the vector boson (green) and WTA jet axis (blue) is related to the momentum of the vector boson $p_{x,V}$ transverse to the colliding protons (red) and jet. Collinear initial (purple) and final-state (blue) radiation and soft radiation (pink) contribute to this measurement.

be discussed in more detail in section 3.1.1. And second, factorization-based methods from Soft-Collinear Effective Theory (SCET) [33–36, 125]. We show how these tools allow us to obtain extremely precise predictions by explicitly calculating the angular decorrelation of Z+jet production [110, 126–128] in the back-to-back limit up to next-to-next-to-leading logarithms (NNLL). We find that predictions for this observable include linearly-polarized gluon transverse-momentum-distributions (TMD's) in the initial *and* final state. It is the first time that these contributions need to be taken into account for the final state. For the initial state this polarization effect arises from spin interference for a single gluon [129]. In Higgs production there is a similar contribution from linear polarized gluons, but there it arises from spin interference between multiple initial-state gluons instead [130].

The outline of this chapter is as follows. In this remaining part of this introductory section we will introduce the recoil-free Winner-Takes-All axis, describe the angular decorrelation measurement in detail and discuss the advantages of angular versus radial decorrelation. In section 3.2 the SCET factorization formula is presented. In particular, we discuss the appearance of the linearly polarized gluon beam- and jet function. Then we focus on calculating the jet function in section 3.3 for the Winner-Takes-All algorithm. We consider

the more general recoil-free p_T^n scheme during calculation, which produces the Winner-Takes-All jet function as $n \to \infty$. In section 3.4 we explain how we can use resummation to improve our predictions in the kinematic region of small azimuthal decorrelation. In section 3.5, we describe the implementation of the theoretic framework used to make predictions. Here, we also discuss the relative contributions of the fixed order and resummed cross section. Finally, in section 3.6 we will present numerical results and compare with results from the PYTHIA parton shower.

3.1.1 Winner-Takes-All jet axis

The recoil-free axis is the prime driver of success for our work. Its unique ability to separate the effects of soft and collinear radiation reduces the impact of soft recoil [74]. In general, complications arise when we have to discriminate between soft radiation inside the jet versus outside the jet boundary. This will lead to logarithms we refer to as 'non-global'. These non-global logarithms have the potential to spoil the predictive power of the resummation, as they involve the same logarithms. Employing a recoil-free axis ensures that the otherwise problematic non-global logarithms are absent. This allows us to make predictions for very small angular deviations from - at leading order - the back-to-back case (see fig. 3.1). The reduced soft sensitivity of this measurement is also crucial in environments with a lot of contamination, such as heavy ion collisions. The use of a recoil-free axis in lepton-ion collisions was proposed in [131]. In this chapter we use a specific recoil free axis, employing the the Winner-Takes-All (WTA) recombination scheme [123, 124].

In section 1.3 we introduced the jet definition, which includes a jet algorithm and recombination scheme. The recombination scheme dictates how the momenta of the particles are combined into the jet momentum. Using the energy scheme, see equation (1.166), one simply adds the four-vectors in a pair-wise recombination ($p_r^\mu = p_1^\mu + p_2^\mu$). As a result the jet axis is aligned with the jet momenta. The vector sum of the momenta of all clustered particles thus directly leads to the jet axis. This is an example of a recoil-sensitive jet algorithm: soft radiation in the jet effects the direction of the jet axis. Let us now consider the WTA recombination scheme, for which the pair-wise recombination gives massless pseudojets with

$$\begin{aligned} p_{T,r} &= p_{T,1} + p_{T,2}, \\ \hat{n}_r &= \begin{cases} \vec{p}_1/|\vec{p}_1| & \text{if} \quad p_{T,1} > p_{T,2} \\ \vec{p}_2/|\vec{p}_2| & \text{if} \quad p_{T,2} > p_{T,1} \end{cases} . \end{aligned} \tag{3.1}$$

The T indicates momenta transverse to the beam direction and p_1^μ and p_2^μ are

the momenta of the clustered particles (or pseudojets). The summed four-momenta of the jet constituents and the jet axis will typically not be aligned when employing the WTA recombination scheme, since the process of pairwise clustering always aligns the jet axis with the more energetic pseudojet. The soft emissions are not relevant to the jets constructed with the WTA scheme, as they do not affect the jet direction and only alter the jet momentum a little. Soft radiation can therefore only contribute a total recoil to the observable (because of momentum conservation).

The measurement of the azimuthal angle can for small values be expressed in terms of the transverse momentum of the jet with respect to the jet axis. Using the coordinate system in figure 3.1, we only need the x-component of the transverse momentum of the jet with respect to the jet axis, q_x. This variable describes the offset between the jet axis and the jet momentum. Considering a single one-to-two splitting in the jet, we find for the WTA algorithm

$$\hat{q}_x = \begin{cases} -\frac{p_x}{1-z} & \text{if} \quad \frac{1}{2} > z > 0 \\ \frac{p_x}{z} & \text{if} \quad 1 > z > \frac{1}{2} \end{cases} \tag{3.2}$$

where z and $1-z$ are the respective energy fractions of the two particles compared to the total energy. The two particles must have vanishing total transverse momentum due to momentum conservation, yielding $p_{x,1} = -p_{x,2}$ in the current axis setup. The WTA algorithm is not the only way to construct recoil-free jet axis. In setion 3.3 we will employ a more general recombination scheme. It turns out that this only changes the finite part of the jet function, and at the end of this section we give explicit results for the WTA case.

3.1.2 Observable definition

The $pp \to V + \text{jet}$ scattering is illustrated in figure 3.1. The coordinate system is chosen such that the y-axis is aligned with the transverse component of the reconstructed jet axis. The azimuthal angle $\Delta\phi$ denotes the opening between the vector boson (V) and the jet (J) in the plane perpendicular to the colliding beams (labelled a, b), i.e. the x-y plane in our setup. The observable of interest is the azimuthal decorrelation $\delta\phi$, which is related to the azimuthal angle by

$$\pi - \Delta\phi \equiv \delta\phi = \arcsin\left(\frac{|p_{x,V}|}{|\vec{p}_{T,V}|}\right) \approx \frac{|p_{x,V}|}{|\vec{p}_{T,V}|}, \tag{3.3}$$

such that the back-to-back limit corresponds to $\delta\phi \to 0$. The azimuthal angle is thus directly related to the offset q_x between vector boson and the reconstructed jet momentum. Although the azimuthal decorrelation is the observable of interest for this chapter, it is very insightful to contrast it with the

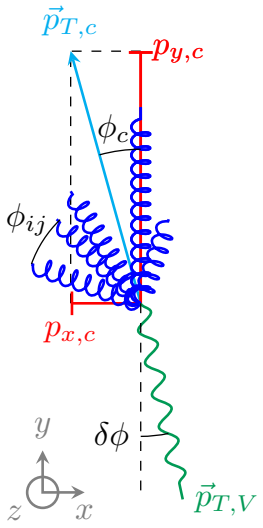

Figure 3.2 Sketch of the geometry in the transverse plane for the $pp \to V+$jet scattering. The angle in between the WTA axis and total collinear momentum is denoted by ϕ_c, where alignment of the two means $\phi_c = 0$. The angle between two generic collinear emissions i and j is denoted with ϕ_{ij}. Lastly, the angle $\delta\phi$ denotes our observable of interest: azimuthal decorrelation between boson and jet. Figure taken from [132].

radial decorrelation. The radial decorrelation is defined as the y component of the offset between V and J, that is q_y, and has a more complicated factorization structure (even for the WTA axis). In what follows we will use the comparison between q_x and q_y to emphasize the simplicity of the azimuthal decorrelation. For this reason we define the dimensionful offset between V and J as

$$\vec{q}_T = \vec{p}_{T,V} + \vec{p}_{T,J} \tag{3.4}$$

where $\vec{p}_{T,V}$ and $\vec{p}_{T,J}$ are the momenta transverse to the beam direction of V and J respectively.

Momentum conservation in the x-y plane requires the total transverse momentum to vanish, as the beams are directed along the z-direction. This leads to

$$\vec{p}_{T,a} + \vec{p}_{T,b} + \vec{p}_{T,c} + \vec{p}_{T,S} + \vec{p}_{T,V} = 0 \tag{3.5}$$

with $\vec{p}_{T,V}$ indicates the contribution from the vector boson, $\vec{p}_{T,a}$ and $\vec{p}_{T,b}$ the collinear radiation off the beams, $\vec{p}_{T,S}$ the overall soft radiation and $\vec{p}_{T,c}$ the

collective contributions from collinear splittings inside the jet. Even though we have aligned the y-axis with the jet axes such that $p_{x,J} = 0$, we can still have a non-zero contribution $\partial_{x,c}$ from collinear radiation inside the jet. As we saw in the previous section this is because the WTA algorithm does not align the jet momentum with the collective momentum of the collinear emissions inside the jet. Using the momentum conservation (3.5), the two components of $\vec{q}_T$ are written as

$$\begin{aligned} q_x &= p_{V,x} & q_y &= p_{J,y} + p_{V,y}. \\ &= -p_{x,a} - p_{x,b} - p_{x,c} - p_{x,S} & &= p_{J,y} - p_{y,a} - p_{y,b} - p_{y,c} - p_{y,S} \end{aligned} \tag{3.6}$$

The large cancellation between the boson and jet momenta in the radial decorrelation leads to complications in the factorization compared to the azimuthal version. To see this explicitly, let us start with the relation between the jet momentum ($p_{T,J}$) and the total collinear momentum of the particles in the jet ($p_{T,c}$). The components of $\vec{p}_{T,c}$ are given by

$$\begin{aligned} p_{x,c} &= |\vec{p}_{T,c}| \sin\phi_c & p_{y,c} &= |\vec{p}_{T,c}| \cos\phi_c \\ &= |\vec{p}_{T,c}|\phi_c + \mathcal{O}(\phi^3) & &= |\vec{p}_{T,c}|\Big(1 - \frac{\phi_c^2}{2}\Big) + \mathcal{O}(\phi^3), \end{aligned} \tag{3.7}$$

where ϕ_c is the angle between WTA jet axis and $\vec{p}_{T,c}$, as illustrated by figure 3.2. The collinear radiation is energetic, and the component transverse to the beam direction therefore scales as $\vec{p}_{T,c} \sim Q$, where Q is the partonic center-of-mass energy. Considering now the components of $p_{T,J}$, we find that $p_{x,J}$ is zero in our reference system and $p_{y,J}$ is the scalar sum of all particle momenta inside the jet. For a jet radius $R \gg \phi_c$ the collinear radiation as well as soft radiation that ends up inside the jet contributes to the jet momentum in the y-direction. Summarized, we find:

$$p_{x,J} = 0 \qquad \text{and} \qquad |p_{y,J}| = \Big|\vec{p}_{T,J}\Big| = \sum_{i\in(s\in J)} |\vec{p}_{T,i}| + \sum_{i\in c} |\vec{p}_{T,i}| \tag{3.8}$$

To make the large cancellation for the radial decorrelation explicit, we relate the vector and scalar sum over the collinear radiation, appearing in in $p_{x,c}$ and $p_{x,J}$ respectively. The absolute value squared is different for the scalar and vector sum, as the vector sum depends on the opening angles ϕ_{ij} between pairwise collinear emissions i and j. They are explicitly given by

$$\Big(\sum_{i\in c}\Big|\vec{p}_{T,i}\Big|\Big)^2 = \sum_{i\in c} |\vec{p}_{T,i}|^2 + 2\sum_{i,j} |\vec{p}_{T,i}|\,|\vec{p}_{T,j}| \tag{3.9}$$

and

$$|\vec{p}_{T,c}|^2 = \Big|\sum_{i\in c}\vec{p}_{T,i}\Big|^2 = \sum_{i\in c}|\vec{p}_{T,i}|^2 + 2\sum_{i,j}|\vec{p}_{T,i}|\,|\vec{p}_{T,j}|\cos\phi_{ij} \tag{3.10}$$

which yields

$$\Big|\sum_{i\in c}\vec{p}_{T,i}\Big| = \sum_{i\in c}|\vec{p}_{T,i}|\cdot\sqrt{1-\frac{2\sum_{i<j}|\vec{p}_{T,i}||\vec{p}_{T,j}|(1-\cos\phi_{ij})}{(\sum_{i\in c}|\vec{p}_{T,i}|)^2}}. \tag{3.11}$$

We are only summing over pairs of collinear particles labelled by i and j. They are collinear to the same direction and therefore have $\phi_{ij} \ll 1$. Expanding in these small angles yields

$$\Big|\sum_{i\in c}\vec{p}_{T,i}\Big| = \sum_{i\in c}|\vec{p}_{T,i}| - \frac{\sum_{i<j}|\vec{p}_{T,i}||\vec{p}_{T,j}|\phi_{ij}^2}{2\sum_{i\in c}|\vec{p}_{T,i}|} + \mathcal{O}(\phi_{ij}^4). \tag{3.12}$$

We can now revisit equation (3.6). We first focus on the x-direction, for which momentum conservation dictates that

$$q_x = -p_{x,a} - p_{x,b} - p_{x,S} - |\vec{p}_{T,c}|\,\phi_c + \mathcal{O}(\phi^2) \tag{3.13}$$

For our SCET setup we need to determine the scaling of the included modes. As was already clear from the contributions to $\vec{q}_T$, there are three collinear modes and a soft mode. The relative scaling of these modes was discussed in section 1.2.2. The modes need to contribute equally to our observable and we therefore find that contributing modes for the azimuthal decorrelation scale as

$$\begin{aligned} p_a &\sim Q(1,\phi_c^2,\phi_c), & p_b &\sim Q(\phi_c^2,1,\phi_c),\\ p_S &\sim Q(\phi_c,\phi_c,\phi_c), & p_c &\sim Q(1,\phi_c^2,\phi_c)_J, \end{aligned} \tag{3.14}$$

where the subscript J refers to a scaling compared to the jet direction, i.e. $p^\mu = (\bar{n}_J\cdot p, n_J\cdot p, p_\perp)_J$ with n_J pointing in the direction of the jet axis. The relative scaling of the modes corresponds to a $\mathrm{SCET_{II}}$ situation. This could be expected as a transverse momentum measurement is a known $\mathrm{SCET_{II}}$ observable. We will now focus on the y component of $\vec{q}_T$. As we are looking at the same process, the radial decorrelation also receives contributions from three collinear modes and a soft mode. Their contributions to q_y are given by

$$q_y = \underbrace{-p_{y,a}-p_{y,b}}_{\text{beam functions}} + \underbrace{\sum_{i\in(s\in J)}|p_{T,i}| - p_{y,S}}_{\text{soft function}} + \underbrace{\sum_{i\in c}|\vec{p}_{T,i}|\frac{\phi_c^2}{2} + \frac{\sum_{(i<j)\in c}|\vec{p}_{T,i}||\vec{p}_{T,j}|\phi_{ij}^2}{2\sum_{i\in c}|\vec{p}_{T,i}|}}_{\text{jet function}}, \tag{3.15}$$

We first note that the power counting of the collinear mode is the same as for the azimuthal decorrelation. It is determined by the component transverse to the jet axis, which scales as $\mathcal{O}(\phi_c)$. The difference however lies in the scaling of the remaining modes. Equation (3.15) shows that in order to have an equal contribution to the radial decorrelation as the collinear jet mode, the transverse components $p_{y,a}$, $p_{y,b}$ and $p_{y,S}$ must scale as $\mathcal{O}(Q\phi_c^2)$. The scaling of the modes for the radial decorrelation is thus given by

$$\begin{aligned} p_a &\sim Q(1, \phi_c^4, \phi_c^2), & p_b &\sim Q(\phi_c^4, 1, \phi_c^2), \\ p_S &\sim Q(\phi_c^2, \phi_c^2, \phi_c^2), & p_J &\sim Q(1, \phi_c^2, \phi_c)_J. \end{aligned} \tag{3.16}$$

This is a non-trivial combination of $\mathrm{SCET_I}$ and $\mathrm{SCET_{II}}$. Looking at p_a, p_b and p_S we would expect a $\mathrm{SCET_{II}}$ situation, but the relative scaling between the jet and the soft modes indicates a $\mathrm{SCET_I}$ situation. Another observation we can make is that the radial decorrelation requires us to differentiate between soft radiation inside and outside the jet, as can be seen in equation (3.15). This reintroduces non-global logarithms.

The azimuthal decorrelation is our preferred observable as it is much simpler: the non-global logarithms are absent and the relative scaling of the necessary modes leads to an observable with $\mathrm{SCET_{II}}$ characteristics only. Having determined the contributing modes and their scaling in equation (3.14), we will now discuss the factorization of the azimuthal decorrelation.

3.2 Factorization

The Born cross section has three partonic channels (see figure 3.3). At NLO we need to consider QCD corrections for each of them. Corrections that involve initial or final state radiation are described by soft and collinear modes in SCET. Hard radiation, producing an extra jet, is not allowed since $\delta\phi \ll 0$. Hard virtual corrections to the born cross section are included in fthe matching to QCD.

3.2.1 Factorization formula

The factorization formula we present in this section is valid for $\delta\phi \ll 1$. We furthermore assume $\delta\phi \ll R$ such that collinear radiation will always end up inside the jet. We will use the WTA recombination scheme to reconstruct the jet axis, ensuring the absence of non-global logarithms.

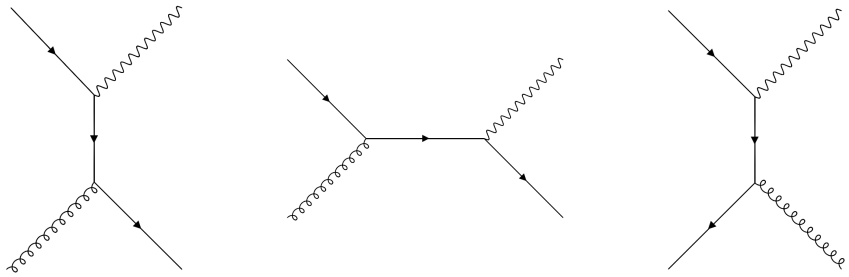

Figure 3.3 Partonnic channels that contribute to the V + jet production at leading order for proton-proton collisions. Note that one also has to include the diagrams where quarks are replaced by anti-quarks and vice versa (i.e. reverse the arrow).

The factorization formula can be derived using the procedure outlined in section 1.2.5 using the measurement in equation (3.13). The result is

$$\begin{aligned}
&\frac{\mathrm{d}\sigma}{\mathrm{d}q_x\,\mathrm{d}p_{T,J}\,\mathrm{d}y_V\,\mathrm{d}\eta_J} \\
&= \int \mathrm{d}p_{x,a}\,\mathrm{d}p_{x,b}\,\mathrm{d}p_{x,c}\,\mathrm{d}p_{x,S}\,\delta\big(q_x + p_{x,a} + p_{x,b} + p_{x,c} + p_{x,S}\big) \\
&\quad\times \sum_{ijk} \mathcal{H}_{ij\to Vk}(p_{T,J}, y_V - \eta_J)\tilde{B}_i(x_a, p_{x,a})\tilde{B}_j(x_b, p_{x,b})\,\tilde{\mathscr{J}}_k(p_{x,c})\tilde{S}_{ijk}(p_{x,S}, \eta_J),
\end{aligned} \tag{3.17}$$

where the dependence on the renormalization scale is suppressed. The variables $p_{T,V}$ and y_V are the transverse momentum and rapidity of the boson, respectively. The pseudo-rapidity of the jet is denoted by η_J. The sum over i, j, k run over the partonic channels that produce a energetic vector boson and jet in the hard scattering processes (see figure 3.3). The hard kinematics is encoded in the hard function $\mathcal{H}$. Collinear radiation of the initial and final state contribute to the q_x measurement through the beam functions $\tilde{B}$ and jet function $\tilde{\mathscr{J}}$ respectively. The $\tilde{B}$ are standard transverse-momentum-dependent beam functions, where we measure only one component. The $\tilde{\mathscr{J}}$ will explicitly be calculated in section 3.3 and it is the first time that also linear polarizations appear for the final state. Contribution from soft radiation is described by the soft function $\tilde{S}$. The tilde on top of these functions is added to indicate the dependence on momentum variables (instead of the Fourier conjugate variable we use later). The Bjorken variables x_a and x_b are determined by the boson and jet kinematics,

$$x_a = \frac{1}{\sqrt{s}}\big(e^{\eta_J} p_{T,V} + e^{y_V}\sqrt{p_{T,V}^2 + m_V^2}\big),$$

$$x_b = \frac{1}{\sqrt{s}}\big(e^{-\eta_J} p_{T,V} + e^{-y_V}\sqrt{p_{T,V}^2 + m_V^2}\big). \tag{3.18}$$

At this point it is important to discuss some differences to the factorization for thrust in equation (1.151). To obtain any factorization theorem Fierz identities are needed to disentangle the color and spin contractions between the different sectors. In the example for thrust in 3.2 we were only dealing with quarks. However, in this factorization gluons also participate. Disentangling the spin contractions leads to a so-called linearly-polarized contribution from gluon beams and jets. The linear polarizations for gluons are accompanied by a corresponding change to the hard function $\mathcal{H}$. The contributions from linear gluon polarizations will be discussed in section 3.2.2.

We can eliminate the convolution in the above factorization formula by switching to the impact parameter variable b_x, which is the Fourier conjugate of q_x,

$$\begin{aligned}&\frac{\mathrm{d}\sigma}{\mathrm{d}q_x\,\mathrm{d}p_{T,J}\,\mathrm{d}y_V\,\mathrm{d}\eta_J} \\ &= \int \frac{\mathrm{d}b_x}{2\pi} e^{ib_x q_x} \sum_{ijk} \mathcal{H}_{ij\to Vk}(p_{T,V}, y_V - \eta_J) B_i(x_a, b_x) B_j(x_b, b_x)\, \mathscr{J}_k(b_x) S_{ijk}(b_x, \eta_J)\end{aligned} \tag{3.19}$$

The factorization formula in impact parameter space thus has a product form. In general, the factorization in b-space leads to logarithms that depend on the renormalization scale(s). It is therefore easy to determine the natural scale of the factorization ingredients. In momentum space the natural scales need to be determined from for distributions, which is much harder [133]. We will therefore proceed with the calculation in impact parameter space and only at the end perform the Fourier transformation back to momentum space.

3.2.2 Contribution of linear gluon polarization

The broken rotational symmetry around the beam axis forces us to include linearly polarized beam and jet functions in the factorization theorem at NLO when producing electroweak vector bosons with non-zero virtuality. Interestingly, the linearly-polarized contributions enter the cross section already at NLO, instead of NNLO for Higgs production [130, 134–136]. Furthermore, it is to our knowledge the first time a linearly-polarized jet function appears.

If the partonic cross section includes a final state gluon the initial Lorentz contractions between the jet- and beam function can be disentangled using projection operators. Specifically, we can write

$$H_{\mu\nu}\,\mathscr{J}^{\mu\nu} = H_L\,\mathscr{J}_L + H_\perp\,\mathscr{J}_\perp \tag{3.20}$$

where we used the (orthogonal) projection operators

$$P_\perp^{\mu\nu} = -\frac{1}{d-2} g_\perp^{\mu\nu} = -\frac{1}{d-2}\left[g^{\mu\nu} - \frac{1}{2}(n_J^\mu \bar{n}_J^\nu + n_J^\nu \bar{n}_J^\mu)\right],$$
$$P_L^{\mu\nu} = \frac{1}{(d-2)(d-3)}\left(g_\perp^{\mu\nu} - \frac{b_\perp^\mu b_\perp^\nu}{|b_\perp|^2}(d-2)\right), \tag{3.21}$$

to define

$$H_L = (d-2)(d-3) P_L^{\mu\nu} H_{\mu\nu}, \qquad \mathscr{J}_L = P_L^{\mu\nu}\mathscr{J}_{\mu\nu},$$
$$H_\perp = (d-2) P_\perp^{\mu\nu} H_{\mu\nu}, \qquad \mathscr{J}_\perp = P_\perp^{\mu\nu}\mathscr{J}_{\mu\nu}. \tag{3.22}$$

The measurement of the transverse component b_x (or q_x) thus allows for this linear polarization. A similar decomposition holds for initial state gluons, for which the projection operators read

$$P_T^{\mu\nu} = -\frac{1}{d-2} g_\perp^{\mu\nu} = -\frac{1}{d-2}\left[g^{\mu\nu} - \frac{1}{2}(n^\mu \bar{n}^\nu + n^\nu \bar{n}^\mu)\right],$$
$$P_L^{\mu\nu} = \frac{1}{(d-2)(d-3)}\left(g_\perp^{\mu\nu} - \frac{b_T^\mu b_T^\nu}{|b_T|^2}(d-2)\right), \tag{3.23}$$

where b_T is perpendicular to the beam axis (and $b_\perp$ perpendicular to the jet axis).

3.3 Jet function for general recoil-free axis

The jet function that appears in the factorization formula in equation (3.19) can be calculated in perturbation theory.

$$\mathscr{J}_i = \mathscr{J}_i^{(0)} + \frac{\alpha_s}{4\pi}\mathscr{J}_i^{(1)} + \dots, \tag{3.24}$$

with $\mathscr{J}_i^{(0)}(b_x) = \mathbb{1}$. The NLO jet function $\mathscr{J}_i^{(1)}$ is given by

$$\mathscr{J}_q^{(1)}(b_x) = 8\pi\left(\frac{\mu^2 e^{\gamma_E}}{4\pi}\right)^\epsilon \int_0^1 \mathrm{d}x \int \frac{\mathrm{d}^{d-2}p_\perp}{(2\pi)^{d-2}} \frac{1}{|p_\perp|^2} P_q(x) e^{-ib_x \hat{q}_x}, \tag{3.25}$$

for quarks, and

$$\mathscr{J}_g^{\mu\nu(1)}(b_x) = 8\pi\left(\frac{\mu^2 e^{\gamma_E}}{4\pi}\right)^\epsilon \int_0^1 \mathrm{d}x \int \frac{\mathrm{d}^{d-2}p_\perp}{(2\pi)^{d-2}} \frac{1}{|p_\perp|^2} P_g^{\mu\nu}(x) e^{-ib_x \hat{q}_x}, \tag{3.26}$$

for gluons. The curly $\mathscr{J}$ indicates that we assumed $\delta\phi \ll R$, and therefore did not need to impose the jet boundary as a constraint. These jet definitions are

obtained by evaluating the jet function matrix elements, which for the quark case is given in equation (1.167). The detailed calculation is given in appendix B. For the gluon case in particular there are two polarizations possible, since we are measuring transverse momenta. As was already discussed in the previous section, the gluon jet function decomposes as

$$\mathscr{J}_g^{\mu\nu}(b_\perp,\mu) = (d-2)P_L^{\mu\nu}J_g^L(b_\perp,\mu) + (d-3)(d-2)P_\perp^{\mu\nu}J_g^\perp(b_\perp,\mu), \quad (3.27)$$

The transverse and linearly projection projectors $P_\perp^{\mu\nu}$ and $P_L^{\mu\nu}$ are given in equation (3.21), and $J_g^L(b_\perp,\mu)$ and $J_g^\perp(b_\perp,\mu)$ are defined in equation (3.22). The $\hat{q}_x$ in equations (3.25) and (3.26) is understood as the operator that picks out the x-component of the transverse momentum for final state radiation, after clustering. For the WTA $\hat{q}_x$ is given by equation (3.2). In this section we will calculate the jet function for the more general recoil-free p_T^n scheme. The clustering of two particles (or pseudojets) with momenta p_i and p_j are recombined into p_r as follows

$$\begin{aligned} p_{T,r} &= p_{T,i} + p_{T,j}, \\ \phi_r &= (p_{T,i}^n\phi_i + p_{T,j}^n\phi_j)/(p_{T,i}^n + p_{T,j}^n), \\ y_r &= (p_{T,i}^n y_i + p_{T,j}^n y_j)/(p_{T,i}^n + p_{T,j}^n), \end{aligned} \quad (3.28)$$

where p_T is the transverse momentum with respect to the beam axis, ϕ the azimuthal angle around the beam and y the rapidity. For $n \geq 1$, the recombined direction will be closer to the harder particle, due to the factors $p_{T,i}^n$. In particular, for values bigger then one the effects of soft radiation are power suppressed. Due to this recoil safety the factorization theorem provided in section 3.2.1 is valid for all $n > 1$. It should be mentioned at this point that changing n will therefore not alter the pole structure of the jet function: renormalization leads to a finite cross section and as the other ingredients in the factorization do not depend on n, changing it can only change the finite part of the jet function. We will revisit this point during the calculation. Note that equation (3.28) produces the WTA recombination in (3.1) in the limit $n \to \infty$.

In order to implement the recoil-free p_T^n recombination in the calculation for the jet function, we have to know the constraints it imposes on the measurement. Restricting ourselves to the limit $\delta\phi \ll R$ we know that two collinear particles are well inside the jet. The azimuthal angle ϕ is related to the offset of the jet in the x direction. We have chosen our coordinate system in such a way that the x-direction is perpendicular to the beams and jet. The total momentum in the x direction is zero by momentum conservation: $p_x = p_{x,i} = -p_{x,j}$. For small angles we can write $\phi_i = \frac{p_{x,i}}{p_{T,i}}$, where $p_{T,i}$ is the momentum transverse to the beam. The jet is a boost invariant object (as are the other constituents

in the factorization theorem). For this reason we carry out the calculation for $\eta_J = 0$, in which situation the transverse momentum $p_{T,i}$ can be related to the energy of the particle $p_i^-/2$, which is constructed using the light-like four vector n_J, yielding

$$\phi_i = \frac{p_{x,i}}{p_{T,i}} = \frac{2p_{x,i}}{p_i^-}. \tag{3.29}$$

We have now expressed ϕ using momentum components in the jet coordinate system. The total transverse momentum in the x-direction is given by

$$p_{x,r} = \phi_r p_{T,J} \tag{3.30}$$

The recombination of the azimuthal angle in equation (3.28) now dictates that

$$\begin{aligned} p_{x,r} &= \frac{(p_{T,1})^n \frac{p_{x,1}}{p_{T,1}} + (p_{T,2})^n \frac{p_{x,2}}{p_{T,2}}}{p_{T,1}^n + p_{T,2}^n} p_{T,J} \\ &\overset{\eta_J \to 0}{=} \frac{\left(\frac{p_1^-}{2}\right)^n \frac{2p_x}{p_1^-} - \left(\frac{p_2^-}{2}\right)^n \frac{2p_x}{p_2^-}}{\left(\frac{p_1^-}{2}\right)^n + \left(\frac{p_2^-}{2}\right)^n} \frac{p_J^-}{2} \\ &= \frac{x^{n-1} - (1-x)^{n-1}}{x^n + (1-x)^n} p_x, \end{aligned} \tag{3.31}$$

where in the last step we used that $p_1^- = x p_J^-$, $p_2^- = (1-x)p_J^-$ and $p_{T,J} = p_J^-/2$. The measurement q_x exactly picks up the recombined momentum and we write

$$\hat{q}_x = \tilde{x} p_x, \tag{3.32}$$

where we conveniently introduced

$$\tilde{x} = \frac{x^{n-1} - (1-x)^{n-1}}{x^n + (1-x)^n}. \tag{3.33}$$

We are now ready to start the jet function calculation. Starting from equation (3.25) we find

$$\mathscr{J}_i^{(1)} = 8\pi \left(\frac{\mu^2 e^{\gamma_E}}{4\pi}\right)^{\epsilon} \int_0^1 \mathrm{d}x \int \frac{\mathrm{d}^{d-2} p_\perp}{(2\pi)^{d-2}} \frac{1}{|p_\perp|^2} P_i(x) e^{-i\tilde{x} b_x p_x}, \tag{3.34}$$

where i is the initiating parton (note that it can also be a linearly polarized gluon). To evaluation of $\mathscr{J}_i^{(1)}$ involves the two integrals

$$\begin{aligned} I_1(\tilde{x} b_x) &\equiv \int \frac{\mathrm{d}^{d-2} p_\perp}{(2\pi)^{d-2}} \frac{e^{\mathrm{i}\tilde{x}\, b_x p_x}}{|p_\perp|^2} = \frac{1}{4\pi} (\pi \tilde{x}^2\, b_x^2)^{\epsilon} \Gamma(-\epsilon), \\ I_2(\tilde{x} b_x) &\equiv \int \frac{\mathrm{d}^{d-2} p_\perp}{(2\pi)^{d-2}} \frac{p_x^2 e^{\mathrm{i}\tilde{x}\, b_x p_x}}{(|p_\perp|^2)^2} = \frac{1}{8\pi} (2\epsilon + 1)(\pi \tilde{x}^2\, b_x^2)^{\epsilon} \Gamma(-\epsilon). \end{aligned} \tag{3.35}$$

This leads to

$$\begin{aligned}\mathscr{J}_q^{(1)} &= 2\left(\frac{\mu^2 b_x^2 e^{\gamma_E}}{4}\right)^{\epsilon}\Gamma(-\epsilon)\int_0^1 \mathrm{d}x P_q(x)\tilde{x}^{2\epsilon},\\ \mathscr{J}_g^{T(1)} &= 2\left(\frac{\mu^2 b_x^2 e^{\gamma_E}}{4}\right)^{\epsilon}\Gamma(-\epsilon)\int_0^1 \mathrm{d}x P_g(x)\tilde{x}^{2\epsilon},\end{aligned} \tag{3.36}$$

for the quark and transverse polzarized gluon jet. The splitting functions $P_i(x)$ are given in equation (2.2). These integrals cannot be evaluated analytically for general n, but one can however find analytic results for specific values of n. The linear gluon polarization gives[1]

$$\begin{aligned}\mathscr{J}_g^{L(1)} =& 4\pi\left(\frac{\mu^2 b_x^2 e^{\gamma_E}}{4}\right)^{\epsilon}\frac{2(4T_F n_f-(d-2)C_A)}{(d-2)(d-3)}\\ &\times\int \mathrm{d}x\, x(1-x)\big(I_1(\tilde{x}b_x)-(d-2)I_2(\tilde{x}b_x)\big)\end{aligned} \tag{3.37}$$

which is finite at this order since

$$\big(I_1(\tilde{x}b_x)-(d-2)I_2(\tilde{x}b_x)\big) = \frac{1}{4\pi}+\mathcal{O}(\epsilon). \tag{3.38}$$

This was expected, as the tree level contribution vanishes for the linear polarization. We find that $\mathscr{J}_g^{L(1)}$ does not depend on n. Using $d=4-2\epsilon$ and expanding in ϵ, it evaluates to

$$\mathscr{J}_g^{L(1)} = -\frac{1}{3}C_A+\frac{2}{3}n_f T_F. \tag{3.39}$$

Let us now revisit the integrals in equation (3.36). First, we focus on the pole structure. The integrals in equation (3.36) leads to poles for $x\to 1$ and $x\to 0$. For $n>1$ we find that $\tilde{x}$ is finite in these limits,

$$\lim_{x\to 1}\tilde{x}=1 \qquad \text{and} \qquad \lim_{x\to 0}\tilde{x}=-1 \tag{3.40}$$

and will therefore not alter the pole structure by its presence. The jet function renormalization and the anomalous dimensions are thus valid for any value of $n>1$, and can be calculated once. For $n\leq 1$ the jet is no longer recoil-free. These cases have a the different pole structure and the factorization will therefore be different as well. The only pole in ϵ comes from $\Gamma(-\epsilon)$ and does not depend on x. We may therefore first expand in ϵ before evaluating the integration over x.

$$\left(\frac{\mu^2 b_x^2 e^{\gamma_E}}{4}\right)^{\epsilon}\Gamma(-\epsilon)\tilde{x}^{2\epsilon} = -\left(\frac{1}{\epsilon}+L_b+2\log(|\tilde{x}|)\right)+\mathcal{O}(\epsilon). \tag{3.41}$$

[1] See appendix B for more details, here we used $b_\perp=(b_x,0)$.

where $L_b = \log(\mu^2 b_x^2 e^{2\gamma_E}/4)$. This leaves us with the following two integrals

$$I_i^A = \int_0^1 \mathrm{d}x P_i(x) = \int_{\frac{1}{2}}^1 \mathrm{d}x (P_i(x) + P_i(1-x)),$$
$$I_i^B = \int_0^1 \mathrm{d}x P_i(x) \log(|\tilde{x}|), \tag{3.42}$$

for $i = q, g_\perp$, such that

$$\mathscr{J}_i^{(1)} = -2\left(\frac{1}{\epsilon} + L_b\right) I_i^A - 4 I_i^B. \tag{3.43}$$

In I_i^B all divergences are regulated (as long as $n > 1$) by the addition $\log(\tilde{x})$, hence this is a finite contribution dependent on n. In the integral I_i^A however, not all divergences are regulated, and we are forced to introduce a rapidity regulator. We choose the η regulator [50, 94]

$$\left(\frac{\nu}{\omega_J}\right) \frac{1}{(1-x)^\eta} \tag{3.44}$$

with $\omega_J = 2p_{T,J}$. This shall eventually give $1/\eta$ poles for $\eta \to 0$, replacing the pole at $x \to 1$. Focussing on the pole structure first, I_q^A and $I_{g_\perp}^A$ evaluate to

$$I_q^A = C_F \left(1 + L_b \left(3 + 4\log\frac{\nu}{\omega_J}\right) + \frac{4L_b}{\eta} + \frac{4}{\eta\epsilon} + \frac{3 + 4\log\frac{\nu}{\omega_J}}{\epsilon}\right),$$
$$I_{g_\perp}^A = C_A \left(L_b \left(\frac{11}{3} + 4\log\frac{\nu}{\omega_J}\right) + \frac{4L_b}{\eta} + \frac{4}{\eta\epsilon} + \frac{\frac{11}{3} + 4\log\frac{\nu}{\omega_J}}{\epsilon}\right)$$
$$+ n_f T_F \left(\frac{2}{3} - \frac{4}{3}L_b - \frac{4}{3\epsilon}\right). \tag{3.45}$$

The poles give us direct access to the jet renormalization factors. They read

$$Z_q = 1 + \frac{\alpha_s}{4\pi} C_F \left(\frac{4L_b}{\eta} + \frac{4}{\eta\epsilon} + \frac{3 + 4\log\frac{\nu}{\omega_J}}{\epsilon}\right), \tag{3.46}$$
$$Z_{g_\perp} = 1 + \frac{\alpha_s}{4\pi}\left(\frac{1}{\eta} C_A \left(4L_b + \frac{4}{\epsilon}\right) + \frac{1}{\epsilon} C_A \left(\frac{11}{3} + 4\log\frac{\nu}{\omega_J}\right) - n_F T_F \frac{4}{3\epsilon}\right).$$

The finite contributions to the jet function depend on n through I_i^B and are given by

$$\mathscr{J}_q^{(1)}|_{\text{finite}} = C_F \left(1 + L_b \left(3 + 4\log\frac{\nu}{\omega_J}\right)\right) - 4 I_q^B = C_F \mathscr{J}_{C_F}|_{\text{finite}}. \tag{3.47}$$

for the quark-initiated jet and

$$\mathscr{J}_g^{\perp(1)}|_{\text{finite}} = C_A L_b \left(\frac{11}{3} + 4\log\frac{\nu}{\omega_J}\right) + n_f T_F \left(\frac{2}{3} - \frac{4}{3}L_b\right) - 4I^B_{g_\perp}$$
$$= CA\,\mathscr{J}_{C_A}|_{\text{finite}} + n_f T_F\,\mathscr{J}_{T_F}|_{\text{finite}} \tag{3.48}$$

for the gluon-initiated jet with transverse polarization. We are particularly interested in finite contributions for the WTA recombination, which yield

$$\mathscr{J}_{C_F}|_{\text{finite,WTA}} = 7 - \frac{2}{3}\pi^2 - 6\log 2,$$
$$\mathscr{J}_{C_A}|_{\text{finite,WTA}} = \frac{131}{18} - \frac{2}{3}\pi^2 - \frac{22}{3}\log 2 + L_b\left(\frac{11}{3} + 4\log\frac{\nu}{\omega_J}\right),$$
$$\mathscr{J}_{T_F}|_{\text{finite,WTA}} = -\frac{17}{9} + \frac{8}{3}\log 2 - \frac{4}{3}L_b. \tag{3.49}$$

The results for the numerical evaluation of the jet constants in equation (3.39),(3.47) and (3.48) are shown as a function of n in figure 3.4.

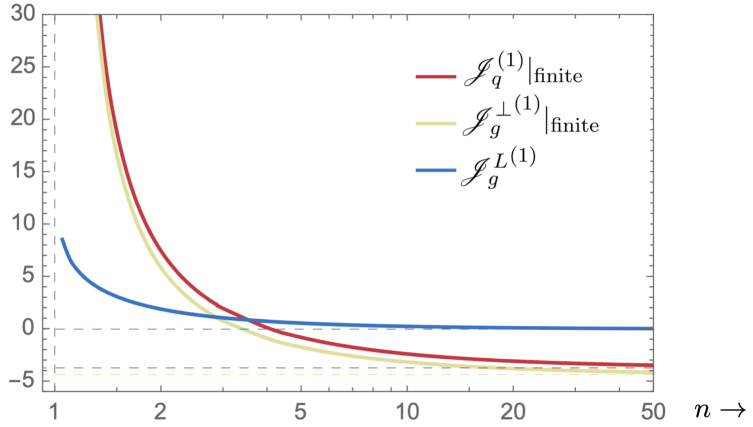

Figure 3.4 The finite contributions $\mathscr{J}|_{\text{finite}}$ at $L_b = 0$ to the linearly polarized gluon (blue), transversely polarized gluon (yellow) quark (red) jet function are shown as a function of n. The dashed line in the same color represents the WTA limit. The vertical dashed line at $n = 1$ shows a singularity: the point at which the jet function is no longer recoil free (and needs a different renormalization).

3.4 Resummation

The factorization theorem in (3.19) enables the resummation of large logarithms by separating the physics at different scales. We evaluate each ingredient at its natural scale, such that they don't involve large logarithms, and

use the ingredients' RG equations to evolve them to a common scale, thereby resumming the logarithms of $\delta\phi$. The collinear (beam and jet) and soft ingredients in equation (3.19) have the same virtuality and are only separated in rapidity. This requires a rapidity regulator, for which we have adopted the η-regulator [50,94], leading to rapidity divergences of $1/\eta$ and a corresponding evolution in the rapidity renormalization scale ν that sums (large) rapidity logarithms. The natural for the ingredients in (3.19) are:

$$\begin{aligned} &\mu_H \sim \nu_B \sim \nu_J \sim p_{T,V} \sim m_V\,, \\ &\mu_B \sim \mu_J \sim \mu_S \sim \nu_S \sim 1/|b_x|\,. \end{aligned} \tag{3.50}$$

Generally, the RG equations for a function F are given by

$$\frac{\mathrm{d}}{\mathrm{d}\ln\mu}F(\mu) = \Gamma^F_\mu F(\mu), \quad \frac{\mathrm{d}}{\mathrm{d}\ln\nu}F(\nu) = \Gamma^F_\nu F(\nu) \tag{3.51}$$

where Γ is known as the anomalous dimension. This multiplicative form of the RG equation only holds in impact parameter space for our factorization ingredients, and the anomalous dimensions for the beam, jet and soft function will depend on b_x. The anomalous dimension is often split in a cusp and a non-cusp contribution:

$$\frac{\mathrm{d}}{\mathrm{d}\ln\mu}F(Q^2,\mu) = \Gamma^{\mathrm{cusp}}_F \log\frac{Q^2}{\mu^2} + \gamma_F \tag{3.52}$$

where the Q can in general be any kinematic variable. The cusp anomalous dimension shows up due to the appearance of double poles in the calculations of the bare ingredients. The anomalous dimensions can be extracted from these direct calculations, as renormalization removes the poles. For example, in section 3.3 we calculated the quark jet function, which led to the pole structure given in equation (3.46). Up to two loops, the anomalous dimension of the jet function is given by

$$\begin{aligned} \Gamma^{\mathscr{J}_i}_\mu &= 2C_i\Gamma_{\mathrm{cusp}}(\alpha_s)\log\frac{\nu}{\omega_J} + \gamma^{\mathscr{J}_i}_\mu, \\ \Gamma^{\mathscr{J}_i}_\nu &= C_i\Gamma_{\mathrm{cusp}}(\alpha_s)L_b + \left(\frac{\alpha_s}{4\pi}\right)^2\left[\frac{\beta_0}{2}C_i\Gamma^{\mathrm{cusp}}_0 L_b^2 - C_i\frac{\gamma^\nu_1}{2}\right] + \mathcal{O}(\alpha_s^3), \end{aligned} \tag{3.53}$$

where the color factor C_i for parton i is C_F for a quark or antiquark and C_A for a gluon (independent of its polarization). From Z_q we can read off that $\Gamma^{\mathrm{cusp}}_q = 4\alpha_s/(4\pi)$, $\gamma^\mu_q = 6\alpha_s C_F/(4\pi)$ and $\gamma^\nu_1 = 0$ at $\mathcal{O}(\alpha_s)$[2]. The anomalous dimensions

[2]The values of γ^ν_1 and Γ^{cusp} in (3.53) do not require knowledge of the initiating parton, which is reflected by the extraction of the color factor C_i.

(cusp and non-cusp) for the other partons are included in appendix 3.A. The anomalous dimensions for the gluon jet are independent of the polarization. This can be argued as follows: the anomalous dimensions of the hard Wilson coefficients are independent of the gluon spin degrees of freedom. At leading power, the same is true for the soft anomalous dimension. Consistency then implies that the anomalous dimensions of the gluon jet are the same, i.e. also independent of spin.

We will now summarize the anomalous dimensions for the other ingredients in our factorization. Note that all values for the cusp and non-cusp anomalous dimensions are summarized in appendix 3.A for convenience. Starting with the hard function it does not depend on ν and the the μ anomalous dimension is given by

$$\Gamma_\mu^{\mathcal{H}_{ij\to Vk}} = \Gamma^{\text{cusp}}(\alpha_s)\left(C_i \ln\frac{\hat{u}^2}{p_{T,V}^2\mu^2} + C_j \ln\frac{\hat{t}^2}{p_{T,V}^2\mu^2} + C_k \ln\frac{p_{T,V}^2}{\mu^2}\right) + 2\big(\gamma^g(\alpha_s) + 2\gamma^q(\alpha_s)\big) + \mathcal{O}(\alpha_s^3)\,, \tag{3.54}$$

where we have conveniently used that there are always two (anti-)quarks and one gluon contributing to the process. The mandelstam variables $\hat{s}, \hat{t}$ and $\hat{u}$ depend on kinematic quantities and are given in equation (3.63). The anomalous dimension of the beam function is the same as for the jet function in (3.53), with the replacement by $\omega_i = \bar{n}_i \cdot p_i$ (see equation (3.67)). The natural rapidity scales of the jet and beam function are $\nu_i = \omega_i$, with $i = a, b, J$. Note that the anomalous dimensions of the gluon beam function are spin independent, by the same reasoning we followed for jets below equation (3.53). Lastly, the soft anomalous dimensions up to two-loop level are

$$\begin{aligned}\Gamma_\mu^{S_{ijk}}(\alpha_s) &= \Gamma^{\text{cusp}}(\alpha_s)\bigg[(C_i+C_j+C_k)\ln\frac{\mu^2}{\nu^2} - C_i\ln\frac{\alpha_{ji}\alpha_{ik}}{\alpha_{jk}} - C_j\ln\frac{\alpha_{ij}\alpha_{jk}}{\alpha_{ik}} \\ &\qquad - C_k\ln\frac{\alpha_{ik}\alpha_{kj}}{\alpha_{ij}}\bigg] + (C_i+C_j+C_k)\gamma^S(\alpha_s) + \mathcal{O}(\alpha_s^3), \\ \Gamma_\nu^{S_{ijk}}(\alpha_s) &= -(C_i+C_j+C_k)\Big(\Gamma^{\text{cusp}}(\alpha_s)L_b + \Big(\frac{\alpha_s}{4\pi}\Big)^2\Big[\frac{\beta_0}{2}\Gamma_0^{\text{cusp}}L_b^2 - \frac{\gamma_1^\nu}{2}\Big]\Big) + \mathcal{O}(\alpha_s^3),\end{aligned} \tag{3.55}$$

with $\alpha_{ij} = (n_i \cdot n_j)/2$.

The all-order resummation formula can be written as

$$\frac{\mathrm{d}\sigma_{\text{resum}}}{\mathrm{d}q_x\,\mathrm{d}p_{T,V}\mathrm{d}y_V} = \sum_{ijk}\int_0^\infty \frac{\mathrm{d}b_x}{\pi}\,\cos(b_x q_x)\prod_{a=ijk}\Big(\frac{\nu_S}{\nu_a}\Big)^{\Gamma_\nu^{B_a}(\mu_B)}\exp\bigg(\int_{\mu_H}^{\mu_B}\frac{\mathrm{d}\mu}{\mu}\Gamma_\mu^{\mathcal{H}_{ij}\to Vk}(\alpha_s)\bigg)$$

$$\times \mathcal{H}_{ij\to kV}(p_{T,V}, y_V - \eta_J, \mu_H) B_i(x_1, b_x, \mu_B, \nu_i) B_j(x_2, b_x, \mu_B, \nu_j)$$
$$\times \mathscr{J}_k(b_x, \mu_B, \nu_k) S_{ijk}(b_x, \mu_B, \nu_S)\,, \tag{3.56}$$

which describes the evolution of all ingredients from their natural scales to a common scale, effectively predicting large logarithmic contributions at higher orders in α_s.

3.5 Implementation

In the next section we will show results for the cross section at NNLL accuracy. This requires the ingredients in equation (3.19) at one-loop order, their anomalous dimensions at two-loop order [137–142], the cusp anomalous dimension at three-loop order [137, 143] and the beta function at three-loop order [144, 145]. Furthermore, most of the ingredients for N^{3}LL resummation are available. The only missing ingredients to extend the precision to this order are the one-loop linearly polarized hard function and the linearly polarized jet function at two-loop order.

In this section we first provide the one-loop ingredients for resummation. Then we introduce the b^* prescription to avoid the Landau singularity in the Fourier transformation back to momentum space. Finally we discuss the matching to MCFM to correctly describe the cross section in the region where $\delta\phi$ becomes large.

3.5.1 One-loop ingredients

For our NNLL predictions we need the hard function at one-loop order [146, 147], and a new contribution multiplying the *linearly-polarized* gluon beam [148] and jet functions. The hard function for the process $ij \to kV$ is given by

$$\mathcal{H}_{ij\to kV} = \frac{p_T^2}{8\pi s^2 \zeta_1 \zeta_2} |\overline{\mathcal{M}}_{ij\to kV}|^2 \tag{3.57}$$

with the Born level matrix elements as

$$|\overline{M}_{q\bar{q}\to gV}|^2 = \frac{16\pi^2 \alpha_s \alpha_{em} e_f^2 \left(N_c^2 - 1\right)}{N_c^2} \frac{\hat{t}^2 + \hat{u}^2 + 2\hat{s} m_V^2}{\hat{t}\hat{u}} \tag{3.58}$$

$$|\overline{M}_{qg\to qV}|^2 = -\frac{16\pi^2 \alpha_s \alpha_{em} e_f^2}{N_c} \frac{\hat{s}^2 + \hat{t}^2 + 2\hat{u} m_V^2}{\hat{s}\hat{t}}, \tag{3.59}$$

$$|\overline{\mathcal{M}}_{qg_L\to qV}|^2 = \frac{32\pi^2 \alpha_{em} \alpha_s e_f^2}{N_c} \frac{\hat{u} m_V^2}{\hat{s}\hat{t}}, \tag{3.60}$$

$$|\overline{\mathcal{M}}_{q\bar{q}\to g_L V}|^2 = -\frac{32\pi^2 \alpha_{em} \alpha_s e_f^2 (N_c^2 - 1)}{N_c^2} \frac{\hat{s} m_V^2}{\hat{u}\hat{t}} \tag{3.61}$$

Here $\hat{s}, \hat{t}, \hat{u}$ are the partonic Mandelstam variables, m_V^2 is the off-shellness of the photon, α_{em} is the electromagnetic coupling constant and e_f is the electric charge of a quark with flavor f. For the Z boson we can use the usual replacement

$$e_f^2 \to \frac{\left(1 - 2\left|e_f\right| \sin^2\theta_W\right)^2 + 4e_f^2 \sin^4\theta_W}{8 \sin^2\theta_W \cos^2\theta_W}. \tag{3.62}$$

The Mandelstam variables in the hard function can be expressed in terms of kinematic variables as

$$\begin{aligned}
\hat{s} &= m_V^2 + 2p_{T,V}^2 + 2p_{T,V}\sqrt{m_V^2 + p_{T,V}^2}\cosh(\eta_J - y_V)\,, \\
\hat{t} &= -p_{T,V}^2 - p_{T,V}\sqrt{m_V^2 + p_{T,V}^2}\exp(\eta_J - y_V)\,, \\
\hat{u} &= -p_{T,V}^2 - p_{T,V}\sqrt{m_V^2 + p_{T,V}^2}\exp(y_V - \eta_J)\,.
\end{aligned} \tag{3.63}$$

The corresponding expressions for the one-loop corrections can be found in the appendix of [147], where in our case we use $b_T = (0, 1, 0, 0)$. As described in (3.20), $\mathcal{H}^L$ gets accompanied by one linearly-polarized gluon beam or jet function. Since these start at order α_s, we only need the LO results for $\mathcal{H}^L$.

Up to order α_s^2, the soft function S_{ijk} can be determined from the standard TMD soft function S [141,142,149]. Similar to [150], our observable is perpendicular to the boost, so only the rapidity regulator is affected by such a boost (see e.g. [87]), yielding

$$\begin{aligned}
S_{ijk}^{(1)}(b_x, \eta_J, \mu, \nu) &= -\sum_{i<j} \mathbf{T}_i\cdot\mathbf{T}_j S^{(1)}\Big(b_x, \mu, \nu\sqrt{n_i\cdot n_j/2}\Big), \\
S_{ijk}^{(2)}(b_x, \eta_J, \mu, \nu) &= -\sum_{i<j} \mathbf{T}_i\cdot\mathbf{T}_j S^{(2)}\Big(b_x, \mu, \nu\sqrt{n_i\cdot n_j/2}\Big) + \frac{1}{2}\Big[S_{ijk}^{[1]}(b_x, \eta_J, \mu, \nu)\Big]^2,
\end{aligned} \tag{3.64}$$

where $S = 1 + \alpha_s/(4\pi)S^{(1)} + \ldots$ with

$$S^{(1)}(b_x, \mu, \nu) = -2L_b^2 + 8L_b \ln\frac{\mu}{\nu} - \frac{\pi^2}{3}\,, \tag{3.65}$$

with $L_b = \ln(\mu^2 b_x^2 e^{2\gamma_E}/4)$. The color factors are $\mathbf{T}_q\cdot\mathbf{T}_{\bar{q}} = \frac{1}{6}$ and $\mathbf{T}_q\cdot\mathbf{T}_g = \mathbf{T}_{\bar{q}}\cdot\mathbf{T}_g = -\frac{3}{2}$, and $n_a\cdot n_b = 2$, $n_{a,b}\cdot n_J = 1 \mp \tanh\eta_J$. The contribution involving exchanges between three Wilson lines vanishes due to color conservation [151].

The beam functions describe the transverse momentum of the colliding hard parton with respect to the beam axis due to collinear initial-state radiation.

Its definition was given in (1.153) of the introduction. They have a perturbative matching onto PDFs, and the matching coefficients $\mathcal{I}_{ij}$ are known at two-loop [135, 140, 142, 152–156] and three-loop order [157–159]. In equation (3.19), we only probe the x-component of the transverse momentum. As azimuthal symmetry is broken, we get a linearly-polarized contribution, which encodes the effect of a spin-superposition of the gluon extracted from the proton. This linear polarization was not taken into account in previous studies of the azimuthal angular decorrelation and is an NLO effect, as the linearly polarized beam functions start at $\mathcal{O}(\alpha_s)$. The matching coefficients, including the linearly polarized one, are given by

$$\begin{aligned}
\mathcal{I}_{qq}(z, b_x, \mu, \nu) &= \delta(1-z) + \frac{\alpha_s}{4\pi}\Big[C_F L_b \left(3 + 4\ln\frac{\nu}{\omega}\right)\delta(1-z) - 2p_{qq}(z)L_b \\
&\quad + 2C_F(1-z)\Big] + \mathcal{O}(\alpha_s^2), \\
\mathcal{I}^T_{gg}(z, b_x, \mu, \nu) &= \delta(1-z) + \frac{\alpha_s}{4\pi}\left[L_b\left(\beta_0 + 4C_A\ln\frac{\nu}{\omega}\right)\delta(1-z) - 2p_{gg}(z)L_b\right] \\
&\quad + \mathcal{O}(\alpha_s^2), \\
\mathcal{I}_{qg}(z, b_x, \mu, \nu) &= \frac{\alpha_s}{4\pi}\left[-2p_{qg}(z)L_b + 4T_F z(1-z)\right] + \mathcal{O}(\alpha_s^2), \\
\mathcal{I}^T_{gq}(z, b_x, \mu, \nu) &= \frac{\alpha_s}{4\pi}\left[-2p_{gq}(z)L_b + 2C_F z\right] + \mathcal{O}(\alpha_s^2), \\
\mathcal{I}^L_{gg}(z, b_x, \mu, \nu) &= -\frac{\alpha_s}{4\pi}C_A\frac{4(1-z)}{z} + \mathcal{O}(\alpha_s^2), \\
\mathcal{I}^L_{gq}(z, b_x, \mu, \nu) &= -\frac{\alpha_s}{4\pi}C_F\frac{4(1-z)}{z} + \mathcal{O}(\alpha_s^2),
\end{aligned} \tag{3.66}$$

with

$$\omega_i = \bar{n}_i \cdot p_i = x_i E_{\mathrm{cm}}\,, \tag{3.67}$$

and the splitting functions p_{ij} are the regularized splitting functions, which enter in the DGLAP equation for parton distribution functions.

The jet function describes the offset of the WTA axis with respect to the jet momentum. The advantage of this recoil-free axis was discussed in section 3.1.1. We recalculated the jet functions [160, 161] using the η-regulator and extended it to general recoil free axis. We used $\delta\phi \ll R$, which removes all dependence on the jet radius. In this limit the momentum of the initial parton is contained in the jet, which simplifies its expression. The calculation was shown in section 3.3, with a first calculation of the gluon jet function with linear polarization. Writing $\mathcal{J}_i = 1 + \alpha_s/(4\pi)\mathcal{J}_i^{[1]} + \ldots$, the one-loop contributions are given by equation (3.39), (3.47), (3.48) and here summarized

for convenience

$$\begin{aligned}
\mathcal{J}_q^{(1)}(b_x,\mu,\nu) &= C_F\Big[L_b\Big(3+4\ln\frac{\nu}{\omega_J}\Big)+7-\frac{2\pi^2}{3}-6\ln 2\Big]\,,\\
\mathcal{J}_g^{(1)}(b_x,\mu,\nu) &= C_A\Big[L_b\Big(\frac{11}{3}+4\ln\frac{\nu}{\omega_J}\Big)+\frac{131}{18}-\frac{2\pi^2}{3}-\frac{22}{3}\ln 2\Big]\\
&\quad + T_F n_f\Big[-\frac{4}{3}L_b-\frac{17}{9}+\frac{8}{3}\ln 2\Big]\,,\\
\mathscr{J}_g^{L(1)}(b_x,\mu,\nu) &= -\frac{1}{3}C_A+\frac{2}{3}n_f T_F.
\end{aligned} \tag{3.68}$$

with $\omega_J = 2p_{T,J}$.

3.5.2 b^* prescription

We choose to eventually evaluate our prediction for $\mu = \mu_B$. However, at very large values of b_x (corresponding to small $p_{T,V}$) the scale μ_B hits the Landau pole, see equation (1.40). To avoid this unphysical behaviour we apply the b^* prescription [48]

$$b^* = |b_x|/\sqrt{1+b_x^2/b_{\max}^2}\,, \tag{3.69}$$

with $b_{\max} = 1.51/\mathrm{GeV}$. The natural scales are then chosen as

$$\mu_H = \sqrt{m_V^2+p_{T,V}^2}\,,\quad \mu_B = \nu_S = 2e^{-\gamma_E}/b^*,\quad \nu_a = \omega_a = \bar{n}_a\cdot p_a\,, \tag{3.70}$$

and evolved to the common scale (μ_B,ν_s) using the resummation formula in equation (3.56). This setup allows us to transform back to momentum space, avoiding the Landau pole.

3.5.3 Large $\delta\phi$ limit

The resummation formula we provided in section 3.4 describes the back-to-back region where $\delta\phi$ is small. It will however fail to produce the correct result at the other end of the spectrum. If $\delta\phi$ is not small, the factorization formula receives large corrections of powers $\delta\phi$. A correct prediction for large $\delta\phi$ is provided by fixed-order calculations, that do include these power corrections. Note that in this regime one has to worry less about large logarithmic contributions $\sim \ln\delta\phi$. We use MCFM [162, 163] to calculate the NLO results for $qq \to V + \text{jet}$.

We employ the so-called additive matching scheme $\sigma_{\rm A}$ together with a transition function $t(\delta\phi)$. The differential cross section is then given by

$$\mathrm{d}\sigma\,(\mathrm{NLO}+\mathrm{NNLL}) = [1-t(\delta\phi)]\,\mathrm{d}\sigma_{\rm A}(\mathrm{NLO}+\mathrm{NNLL}) + t(\Delta\phi)\mathrm{d}\sigma(\mathrm{NLO}), \quad (3.71)$$

where $\sigma_{\rm A}$ has an additive construction given by

$$\mathrm{d}\sigma_{\rm A}(\mathrm{NLO}+\mathrm{NNLL}) = \mathrm{d}\sigma(\mathrm{NNLL}) + \underbrace{\mathrm{d}\sigma(\mathrm{NLO}) - \mathrm{d}\sigma(\mathrm{NLO\,singular})}_{\mathrm{d}\sigma(\mathrm{NLO\ non-singular})}. \quad (3.72)$$

where $\mathrm{d}\sigma(\mathrm{NNLL})$ is exactly given by (3.56), the NLO singular refers to the $\mathcal{O}(\alpha_s)$ contribution of the resummed prediction and $\mathrm{d}\sigma(\mathrm{NLO})$ refers to the fixed order calculation in QCD. The NLO non-singular distribution is given by the difference between NLO and NLO singular results. It should be clear that this contribution goes to zero for small $\delta\phi$. In some sense $\sigma_{\rm A}$ already accomplishes the transition from the resummation to the fixed order regime by itself, as equation (3.72) reduces to the fixed order calculation in the large $\delta\phi$ limit. However, the highly oscillating Fourier transform makes the prediction $\sigma_{\rm A}$ by itself unstable. These numerical problems are solved with the introduction of a transition function $t(\delta\phi)$ with $t(0) = 0$ and $t(\pi) = 1$ [164]. The transformation function reduces and eventually stops resummation for increasing $\delta\phi$. In this region the resummed prediction is then simply replaced by the NLO prediction, as can be seen in the last term of equation (3.71). The MCFM NLO prediction is calculated directly in momentum space, and does not suffer the same numerical instabilities as our factorized prediction.

3.6 Results

Linearly-polarized contributions are not visible in the *fixed-order* cross section differential in $\delta\phi$. The linearly polarized contributions are constant, as can be seen for the jet in equation (3.39). The Fourier transformation to momentum space will therefore only contribute at $q_x = 0$. We provide evidence for contributions from linearly-polarized gluon beam and jet functions in Fig. 3.5, by showing the difference between the cumulative cross section obtained using our factorization in (3.19) and MCFM at NLO [162, 163], with a cut $\delta\phi < \delta\phi^{\rm cut}$. This difference should vanish in the limit $\delta\phi^{\rm cut} \to 0$, but only does so when the linearly-polarized gluon beam and jet functions are included. The left panel shows the contribution involving qq PDFs, which only involves linearly-polarized beam functions, and in the right panel we focus on the n_f-dependent contribution from $q\bar{q}$ PDFs, to provide evidence for a nonzero contribution from linearly-polarized jet functions.

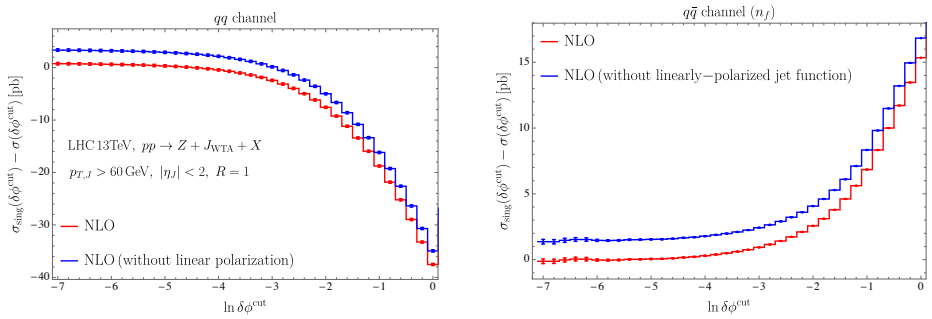

Figure 3.5 Difference between the singular cross section in equation (3.19) and the cross section from MCFM at NLO with a cut $\delta\phi < \delta\phi^{\text{cut}}$. Shown are the contribution from qq (left) and $q\bar{q}$ (right) PDF flavors. Jets are identified using the anti-k_T algorithm with $R = 1$ and the leading jet fulfills $p_{T,J} > 60\,\text{GeV}$ and $|\eta_J| < 2$. In the right plot we only consider NLO corrections proportional to n_f. The difference between the singular and full NLO only vanishes if linear polarizations are included.

We obtain predictions for the LHC with $\sqrt{s} = 13$ TeV, using the factorization formula in equation (3.19). Jets are identified by the anti-k_T clustering algorithm with $R = 0.5$ and the WTA recombination scheme. We use the CT14nlo parton distribution functions [165]. We show our resummed predictions in figure 3.6 at NLL+NLO and NNLL+NLO order, and compare to the NLO cross section obtained from MCFM. In the figure we use $\Delta\phi = 180° - \delta\phi$. For our central curve we take the natural scales in equation (3.70). We estimate the perturbative uncertainty by varying μ_B and μ_H by a factor two around their central values, taking the envelope of the scale variations. The uncertainty bands of the NLL and NNLL predictions overlap, and are substantially reduced for the NNLL result in the resummation region $\Delta\phi \gtrsim 170°$. While the resummed predictions approaches a constant in the back-to-back limit (far right of the plot), the NLO prediction becomes unreliable due to unresummed logarithms. On the other hand, for $\delta\phi \gtrsim 140°$ the fixed-order corrections are important and (3.19) fails to deliver a correct prediction (towards the left of the plot). We therefore included the NLO fixed order through additive matching scheme σ_{add} together with a transition function $t(\delta\phi)$, details of which can be found in section 3.5.3. Our prediction does not show a Sudakov peak, which one might expect for a transverse measurement. However, since we are probing only one component of the transverse momentum it is absent. In figure 3.6 we also compare to Pythia [166], which is a parton shower Monte Carlo that simulates collisions with LL accuracy. The simulation includes some power

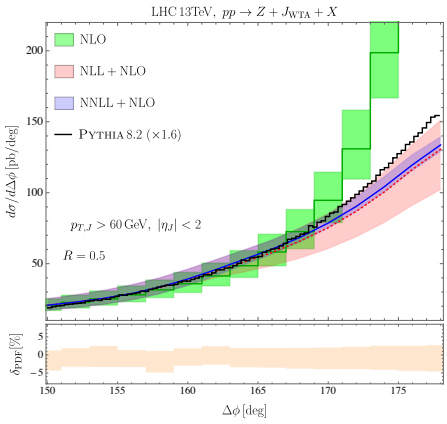

Figure 3.6 Our resummed prediction for the cross section differential in the azimuthal angle at NLL+NLO (red) and NNLL+NLO (blue), compared to the NLO cross section from MCFM (green) and PYTHIA at hadron level (black). We used $\Delta\phi = 180^\circ - \delta\phi$. The lower panel shows the PDF uncertainty.

corrections, hadronization effects and multi-parton interactions. We can include the $\mathcal{O}(\alpha_s)$ corrections from the fixed-order by an overall normalization factor, refered to as K-factor. In the comparison in figure 3.6 we used the NLO K-factor of 1.6. The difference in shape for $\Delta\phi \gtrsim 170^\circ$ is not significant, given the size of the NLL uncertainty band (a reasonable proxy for the PYTHIA uncertainty). We have verified that this is not due to multiparton interactions or hadronization effects, which have a minimal effect on this observable.

3.7 Conclusions

We studied the back-to-back configuration in V+jet production, by including QCD corrections from the dominant contributions due soft and collinear radiation. The azimuthal angle in combination with the WTA axis ensures non-global logarithms are absent at leading power, allowing us to obtain resummed predictions at NNLL accuracy. Many ingredients that go into the (resummed) factorization formula are already available for an analysis at N^{3}LL. This factorization is checked at NLO by comparing to MCFM, verifying the necessity of including linearly-polarized gluon beam and jet functions.

The choice of recoil-free axis ensures insensitivity of the observable to soft recoil effects, hadronization, and the underlying event. This makes the observable attractive experimentally. Our work also serves as a baseline for pinning down the inner-working of the QCD medium produced in heavy-ion collisions,

where the use of a recoil-free axis will be even more important to suppress effects from the huge underlying event background.

In the final chapter of this thesis, section 4.4.2, we shall show from first principles that the same measurement with solely charged particles in the final state has an almost identical distribution, implemented using track functions [167,168]. This makes it possible to exploit the superior angular resolution of the tracking system (compared to calorimetry). As we shall see, the usage of a recoil-free jet definition also significantly simplifies the transition to tracks.

Appendices

3.A Anomalous dimensions

This appendix summarizes all the anomalous dimensions needed for this chapter. We start with the beta function, which describes the RG evolution for the strong coupling constant,

$$\frac{\mathrm{d}\alpha_s(\mu)}{\mathrm{d}\ln\mu} = -2\varepsilon\alpha_s + \beta(\alpha_s), \quad \beta(\alpha_s) = -2\alpha_s \sum_{n=0}^{\infty} \beta_n \left(\frac{\alpha_s}{4\pi}\right)^{n+1}. \tag{3.73}$$

The first three loop orders are given by [144, 145]

$$\begin{aligned}
\beta_0 &= \frac{11}{3}C_A - \frac{4}{3}T_F n_f\,, \\
\beta_1 &= \frac{34}{3}C_A^2 - \frac{20}{3}C_A T_F n_f - 4C_F T_F n_f\,, \\
\beta_2 &= \frac{2857}{54}C_A^3 + \Big(2C_F^2 - \frac{205}{9}C_F C_A - \frac{1415}{27}C_A^2\Big)T_F n_f + \Big(\frac{44}{9}C_F + \frac{158}{27}C_A\Big)T_F^2 n_f^2\,.
\end{aligned} \tag{3.74}$$

The cusp, non-cusp, and rapidity anomalous dimensions are perturbative functions, and we write their expansion in α_s as

$$\Gamma_{\text{cusp}} = \sum_{n=0}^{\infty} \left(\frac{\alpha_s}{4\pi}\right)^{n+1} \Gamma_n\,, \quad \gamma_\mu^i = \sum_{n=0}^{\infty} \left(\frac{\alpha_s}{4\pi}\right)^{n+1} \gamma_n^i\,, \quad \gamma_\nu = \sum_{n=0}^{\infty} \left(\frac{\alpha_s}{4\pi}\right)^{n+1} \gamma_n^\nu. \tag{3.75}$$

The cusp anomalous dimension is, up to three loops, given by [143, 169]

$$\begin{aligned}
\Gamma_0^{\text{cusp}} &= 4\,,\\
\Gamma_1^{\text{cusp}} &= \left(\frac{268}{9}-\frac{4\pi^2}{3}\right)C_A-\frac{80}{9}\,T_F n_f\,,\\
\Gamma_2^{\text{cusp}} &= C_A^2\left(\frac{490}{3}-\frac{536\pi^2}{27}+\frac{44\pi^4}{45}+\frac{88}{3}\,\zeta_3\right)+C_F T_F n_f\left(-\frac{220}{3}+64\zeta_3\right)\\
&\quad + C_A T_F n_f\left(-\frac{1672}{27}+\frac{160\pi^2}{27}-\frac{224}{3}\,\zeta_3\right)-\frac{64}{27}\,T_F^2 n_f^2.
\end{aligned} \tag{3.76}$$

The non-cusp rapidity anomalous dimension is given by [142]

$$\gamma_1^\nu = 0\,,\qquad \gamma_1^\nu = -C_A\left(\frac{128}{9}-56\,\zeta_3\right)-\beta_0\frac{112}{9}, \tag{3.77}$$

where we have made use of its universality, i.e. it is the same for each ingredient and the color dependence has been extracted.
The other non-cusp anomalous dimension are however different for each factorization ingredient. For the hard function they are given by [137, 170–172]

$$\begin{aligned}
\gamma_0^q &= -6C_F, \qquad (3.78)\\
\gamma_1^q &= C_F^2\left(-3+4\pi^2-48\zeta_3\right)+C_F C_A\left(-\frac{961}{27}-\frac{11\pi^2}{3}+52\zeta_3\right)\\
&\quad + C_F T_F n_f\left(\frac{260}{27}+\frac{4\pi^2}{3}\right),\\
\gamma_0^g &= -2\beta_0 = -\frac{22}{3}\,C_A+\frac{8}{3}\,T_F n_f\,,\\
\gamma_1^g &= C_A^2\left(-\frac{1384}{27}+\frac{11\pi^2}{9}+4\zeta_3\right)+C_A T_F n_f\left(\frac{512}{27}-\frac{4\pi^2}{9}\right)+8C_F T_F n_f.
\end{aligned}$$

The non-cusp anomalous dimensions for the beam and jet function are given by [142]

$$\begin{aligned}
\gamma_0^{B_q} &= 6C_F\,,\\
\gamma_1^{B_q} &= C_F^2\big(3-4\pi^2+48\zeta_3\big)+C_F C_A\big(\frac{17}{3}+\frac{44\pi^2}{9}-24\zeta_3\big)+C_F T_F n_f\left(-\frac{4}{3}-\frac{16\pi^2}{9}\right),\\
\gamma_0^{B_g} &= 2\beta_0\,,\\
\gamma_1^{B_g} &= C_A^2\left(\frac{64}{3}+24\zeta_3\right)-\frac{32}{3}C_A T_F n_f-8C_F T_F n_f\,.
\end{aligned} \tag{3.79}$$

For the soft function they are [142]

$$\gamma_0^S = 0\,,\qquad \gamma_1^S = C_A\left(\frac{64}{9}-28\,\zeta_3\right)+\beta_0\left(\frac{56}{9}-\frac{\pi^2}{3}\right). \tag{3.80}$$

4

Track Functions

In particle physics we want to test the Standard Model and search for new physics by comparing experiment with data. We therefore aim to extend the level of precision on both sides. On the theory side, we accomplish this by performing higher order calculations and using resummation in regions of phase space where large logarithms spoil the perturbative nature. On the experimental side, we are constrained by the limits of our detectors. The precision at which we can measure angles at the LHC is for example limited by the size of the calorimeter cells. Especially in the collinear limit, where particles tend to end up in the same cell, this leads to large uncertainties. The way to improve the accuracy of such measurements is by using data from the tracking system. The tracking system is a layer in the detector with the principle task to provide efficient reconstruction of charged-particle tracks, from which one can determine the momenta of charged particles, and has superior angular resolution. It is clear that a theory description to make predictions with only charged particles in the final state is highly desirable. In this chapter we will show that we can reach state-of-the-art precision for observables defined on charged particles only.

Track-based calculations are IRC unsafe and therefore require nonperturbative track functions, which we will introduce in 4.1. In this section we will discuss the importance of track functions, their properties and how they can be used to capture the effects of non-perturbative physics of track-based measurements. In section 4.2.1 we will identify the symmetries inherent to track functions to organize the evolution structure. Using the pure Yang-Mills theory as a toy model, we will show in section 4.2.2 how this symmetry alone fully fixes the evolution of the track function up to the sixth moment in terms of the (known) DGLAP splitting kernels. In section 4.2.3 we will present the full result for the evolution of track functions in a theory where all quarks have the same track function, where again the structure of the evolution is highly constrained by symmetry relations. The remaining constants that cannot be

completely fixed by symmetry will be calculated in section 4.3. We will use two independent methods, which provides a good check on the validity. Lastly, in section 4.4 we will obtain results for the Energy-Energy-Correlelator and the azimuthal decorrelation in $pp \to Z + \text{jet}$ with tracks. This shows the consistency of track functions beyond the leading order through an explicit $\mathcal{O}(\alpha_s^2)$ calculation.

4.1 Introduction to track functions

The tracking system has a superior angular resolution compared to the calorimeter. We can exploit this advantage if we focus on observables that are defined by using only charged particles. The angular resolution is most important when looking at jet substructure [173–175], for which interest has been increasing ever since the LHC was built. Jet substructure aims to study the internal kinematic properties of high-P_t jets and search for new physics. The complex radiation pattern inside jets contains valuable information that can be used to enhance our understanding of QCD. Since jets describe a collimated spray of particles, the angular resolution is of utmost importance when studying its substructure. A second advantage of using tracking is that the tracking system is closest to the interaction point and its data can be used to accurately reconstruct the primary interaction vertex and secondary vertices from particle decays. This effectively removes contamination from pile up effects, which are additional proton-proton collisions that take place in the same bunch crossing. Increasing the luminosity is therefore less of a problem for track-based measurements. Many jet substructure measurements are performed on charged hadrons [176–180]

This sounds great and we can even ask the question: "why consider calculations with data from calorimetry at all?". However, uncharged particles do not leave any tracks and will only show up in the calorimeter cells. Restricting to the tracking data is therefore only possible if we consider solely charged particles in our study. In the literature there has been a lot of work on IRC safe observables and theoretical predictions can be made using factorization, e.g. for jet substructure [181]. However, whenever the measurement includes just a subset of the final state particles, the cross section will have left-over IR divergences at the partonic level [182, 183] and this theoretical framework falls apart. Track functions solve this issue of uncancelled divergences, such that the observable is theoretically well defined and we can make precise predictions to be tested at the LHC.

Track functions are non-perturbative objects by construction. Originally they were introduced to describe the measurements involving *all* charged hadrons [167,

168]. They have been successfully applied in a number of calculations in perturbative QCD [2,167,168,184]. One can generalize this notion to other subsets of hadrons specified by their quantum numbers, e.g. flavor. The formal definition of a track function for quarks (in light-cone gauge) as a function of the momentum fraction x transferred into charged particles, $T_q(x)$, is given by

$$T_q(x) = \int \mathrm{d}y^+ \mathrm{d}^2 y_\perp e^{ik^- y^+/2} \frac{1}{2N_c} \sum_{R,\bar{R}} \delta\left(x - \frac{P_R^-}{k^-}\right) \times \mathrm{tr}\left[\frac{\gamma^-}{2} \langle 0|\psi(y^+, 0, y_\perp)|R\bar{R}\rangle\langle R\bar{R}|\bar{\psi}(0)|0\rangle\right], \tag{4.1}$$

and similarly for gluons. Here R denotes the hadrons in the final state belonging to the subset, $\bar{R}$ denotes all other hadrons (the complement), and P_R^- is the large light-cone momentum component of R. Despite the fact that we allow R to be a more general subset of hadrons, we continue to refer to the object in equation (4.1) as a track function. The hadronization process, for which our understanding is limited, describes the transition from the highly energetic partons that exit the hard collision to the lower energic hadrons and makes sure that we end up with a finite cross section. The track functions model this hadronization and remove the uncancelled IR divergences at the partonic level.

Another feature of track functions is that they are independent of the hard process. This universality can be used to extract track functions once from some measurement, and use them to make predictions for other observables defined on tracks. Furthermore, we know that the track functions are normalized such that the integral over all momentum fractions gives one, as expected by probability conservation,

$$\int_0^1 T_i(x)\mathrm{d}x = 1. \tag{4.2}$$

To obtain the track function evolution we can treat the intermediate states in (4.1) partonically, obtaining the bare track functions. In pure dimensional regularization all radiative corrections are scaleless and vanish. We therefore conclude that the bare track function is just a constant to all orders. More specifically, we know that the bare track function is the renormalized track function at zeroth order, $T_{i,\mathrm{bare}} = T_i^{(0)}$. Another conclusion we can draw from these scaleless radiative corrections is that the renormalized track functions beyond leading order only has IR poles. The renormalized track function has been studied before [167, 168] and $T_{i,\mathrm{bare}}^{(1)}$ in pure dimensional regularization

with $d = 4 - 2\epsilon$ is given by

$$T^{(1)}_{i,\text{bare}}(x,\mu) = \frac{1}{2}\sum_{j,k}\int \mathrm{d}z \left[\frac{\alpha_s(\mu)}{2\pi}\left(\frac{1}{\epsilon_{\text{UV}}} - \frac{1}{\epsilon_{\text{IR}}}\right) P_{i\to jk}(z)\right] \times \int \mathrm{d}x_1 \mathrm{d}x_2 T^{(0)}_j(x_1) T^{(0)}_k(x_2) \delta\big(x - z x_1 - (1-z)x_2\big), \quad (4.3)$$

where $P_{i\to jk}(z)$ are the DGLAP splitting functions [20–22]. From this one can immediately extract the evolution of track functions. In general we expect that contributions to the RGE at order N are of the form

$$\frac{\mathrm{d}}{\mathrm{d}\log\mu^2} T_i(x,\mu) = \sum_{i_1,i_2,\ldots,i_N} \int (\Pi_{m=1}^N \mathrm{d}x_m \mathrm{d}z_m) \tilde{\gamma}_{i\to i_1\ldots i_N}(z_1,\ldots,z_N) \prod_{m=1}^N T_{i_m}(x_m) \times \delta(1 - z_1 - \ldots - z_N)\delta(x - x_1 z_1 - \ldots - x_N z_N), \quad (4.4)$$

with i the flavour of the initial parton, x the final momentum fraction that is converted into tracks, x_m the momentum fraction that is transferred into tracks for each branch m in the splitting, and i_m the flavour and z_m the momentum fraction of the corresponding branch. The $\tilde{\gamma}_{i\to i_1\ldots i_N}(z_1,\ldots z_N)$ are general objects that describe the splitting in terms of energy fractions, but are for the moment left unspecified. As we will see in section 4.1.3, by taking moments of these objects they can be related to the DGLAP splitting functions.

Although the definition of track functions given in (4.1) is similar to the better understood case of fragmentation, which describes the energy fraction of a single hadron, the fact that R is the set of *all* hadrons of a given property leads to crucial differences. Concretely, if R consists of all pions in the final state, a final-state with two pions with momentum fractions x_1 and x_2 would give a contribution $\sim \delta(x - x_1 - x_2)$ to the track function, while it would give a contribution $\sim \delta(x - x_1) + \delta(x - x_2)$ to the pion fragmentation function. Objects similar to track functions have been studied in the context of jet charge [85,86] and fractal observables [185]. Due to the fact that they encode correlations between arbitrary numbers of hadrons, the track functions satisfy complicated non-linear evolution equations, generated by multiparton splittings. Nothing is known about the structure of these equations beyond the leading order. Exploring this will be the subject of this chapter.

Now we know how track functions are defined and where they can be applied. We will discuss the theoretical implementation of track functions in calculations of cross sections in section 4.1.1. We will introduce a certain class of observables (energy correlators) that will only use moments of track functions when restricting the final state to charged particles. Therefore the focus of the remaining part of this chapter will shift to moments of track functions.

How these moments are defined will be discussed in detail in section 4.1.2. In the last part, section 4.1.3, we will make the comparison to the more often studied case of fragmentation, as a reference for readers that are familiar with them, but also to make the first statements about the renormalization group equations for track functions.

4.1.1 How to use track functions

The partonic cross section for an IRC safe observable e is

$$\frac{\mathrm{d}\sigma}{\mathrm{d}e} = \sum_N \int \mathrm{d}\Pi_N \frac{\mathrm{d}\sigma_N}{\mathrm{d}\Pi_N} \delta\left(e - \hat{e}(p_i^\mu)\right), \tag{4.5}$$

where we use $\mathrm{d}\sigma_N$ to denote the N-body differential cross section, and $\mathrm{d}\Pi_N$ the N-body Lorentz invariant phase space measure. Here we consider all particles. As explained in section 4.1, if we would like to select the charged particles that will be detected by the tracking system at the LHC, we need to use the track functions. To convert a perturbative calculation to a calculation on tracks, one must simply attach a track function onto each parton. The observable defined on tracks is then given by

$$\frac{\mathrm{d}\sigma}{\mathrm{d}e} = \sum_N \int \mathrm{d}\Pi_N \frac{\mathrm{d}\bar{\sigma}_N}{\mathrm{d}\Pi_N} \int \prod_{i=1}^{N} \mathrm{d}x_i T_i(x_i) \delta\left(e - \hat{e}(x_i p_i^\mu)\right), \tag{4.6}$$

where the $\bar{\sigma}_N$ now denotes the cross section from which the IR divergences are subtracted. These IR divergences are absorbed by the track functions.

Let us illustrate this for the partonic cross section in $e^+e^- \to$ hadrons at $\mathcal{O}(\alpha_s)$, measured on tracks. The partonic cross section $e^+e^- \to q\bar{q}g$ will have uncancelled IR divergences in the limit where the gluon is collinear to the final state quark or anti-quark. The convolutions with the LO track functions are trivial since at the at the partonic level these are just delta functions. However, $e^+e^- \to q\bar{q}$ involves an NLO track function, containing all the IR poles. This matching procedure is schematically shown in figure 4.1, where the cross section defined on tracks is matched onto track functions.

Until now we have only considered observables which constrain the final state through a delta function measurement. As seen from (4.6), the constraint operator $\hat{e}$ depends on x_i when we consider only tracked particles. As a result the full functional form of the track function is needed for the calculation.

There is another class of observables where one applies an energy weighting to the final state, called energy correlators [186–193]. They represent an infinite family of experimentally convenient observables, each of which can be

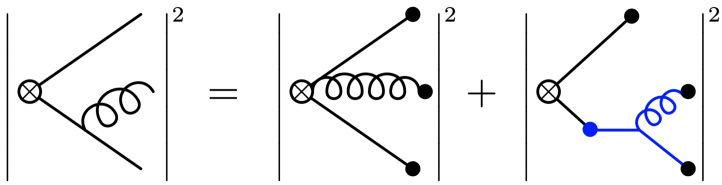

Figure 4.1 In this figure we show the correspondence between the three body partonic matrix element σ_3 and the matching coefficient $\bar{\sigma}_3$ for $e^+e^- \to q\bar{q}g$. The dots represents the track functions at tree-level (black) and $\mathcal{O}(\alpha_s)$ (blue). The diagrams where the gluon is emitted from the other leg are not shown for simplicity. Note that the leading order matching, which is not shown here, is trivial and leads to $\sigma_2 = \bar{\sigma}_2$. This figure was taken from [167].

expressed in terms of a finite number of energy flow operators. These energy flow operators are defined as

$$\mathcal{E}(\vec{n}) = \int_0^\infty \mathrm{d}t \lim_{r\to\infty} r^2 n^i T_{0i}(t, \vec{r}n), \tag{4.7}$$

where unit vector $\vec{n}$ sets the direction and T denotes the energy-momentum tensor. When these operators act on a final state X, they 'weight' the final state by the energy of all particles going into direction $\vec{n}$,

$$\mathcal{E}(\vec{n})\,|X\rangle = \sum_i E_i \delta(\Omega_{\vec{p}_i} - \Omega_{\vec{n}_i})\,|X\rangle\,, \tag{4.8}$$

where i runs over all particles in the final state and Ω is the solid angle. The delta function thus makes sure that the energy of particles is only considered when they travel in a certain direction $\hat{n}$. Experimentally this means that we restrict to particles that hit a specific calorimeter cell. The cross sections constructed with these energy correlators are weighted cross sections and read

$$\sigma = \int_0^\infty \mathrm{d}^4x e^{iq\cdot x}\,\langle 0|\,\mathcal{O}(x)\mathcal{E}(\vec{n}_1)\cdots\mathcal{E}(\vec{n}_N)\mathcal{O}(0)\,|0\rangle\,, \tag{4.9}$$

where N denotes the number of energy deposits we are correlating. The $\mathcal{O}$ are the source operators in QCD which prepare the initial state, e.g. the electromagnetic current $\bar{\psi}\gamma^\mu\psi$ in $e^+e^- \to$ hadrons. These correlations can be computed in perturbation theory, and are known explicitly for the two [192, 194–198] and three-point correlator [199]. They have recently received extensive theoretical interest from a variety of communities [150, 184, 190–193, 198–204, 204–214].

One of the key benefits of energy correlators is that they enable a simple incorporation of tracks in perturbative calculations. Let us discuss this with the relatively simple case where we look at the correlation between two energy flow operators. This observable is referred to as the Energy-Energy-Correlator (EEC). The cross section for the EEC as a function of the angular separation reads

$$\frac{\mathrm{d}\sigma}{\mathrm{d}\chi} = \sum_{i,j} \int \mathrm{d}\Pi_N \frac{\mathrm{d}\sigma_N}{\mathrm{d}\Pi_N} \frac{E_i E_j}{Q^2} \delta(\chi - \chi_{ij}), \tag{4.10}$$

where E_i and E_j are the energies of final-state partons i and j with angular separation χ_{ij}. The modification to only include tracks is achieved by

$$E_i \to \int \mathrm{d}x_i x_i T_i(x_i) E_i = T_i(1) E_i, \tag{4.11}$$

where x_i is the energy fraction that is transferred into charged particles. The $T_i(1)$ is the first moment of the track function, for which the definition can be found in equation (4.15). The weights for the track EEC are the weights in the EEC multiplied with the first moment of the corresponding track function. If we stay away from the collinear limit, i.e. $\chi > 0$, the cross section for the track EEC as a function of the angular separation reads

$$\frac{\mathrm{d}\sigma}{\mathrm{d}\chi} = \sum_{i,j} \int \Pi_N \frac{\mathrm{d}\sigma_N}{\mathrm{d}\Pi_N} \frac{E_i E_j}{Q^2} T_i(1) T_j(1) \delta(\chi - \chi_{ij}). \tag{4.12}$$

Higher moments of the track functions appear when multiple energy flow operators are placed at the same parton. These so-called contact terms are necessary for describing collinear limits. So for the track EEC, the contact term will have both correlators on the same parton, hence $z = 0$. This will result in

$$E_i^2 \to \int \mathrm{d}x_i x_i^2 T_i(x_i) E_i^2 = T_i(2) E_i^2. \tag{4.13}$$

This statement can be generalized to an N-point correlator, for which one must consider up to N correlators placed on a single parton. If all correlators are placed on the same parton, we get the N-th moment of the track function. We conclude that describing track-based weighted cross sections of N-point correlators only requires integer moments $\leq N$ of track functions. As a result, the resummation of track correlators only requires the renormalization of these integer moments, which we will focus on. We will see in the following sections that the renormalization group equations for moments of track functions are non-linear. However, they are largely fixed by symmetry and can be completely

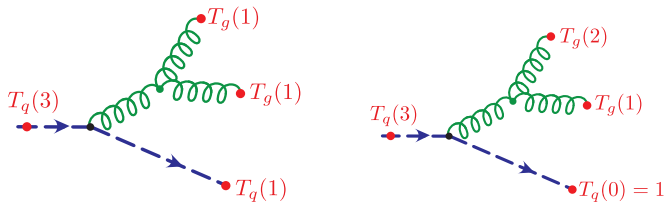

Figure 4.2 Triple collinear splittings contributing to the evolution of the track function moment $T_q(3)$ at next-to-leading order: (a) $T_g(1)T_g(1)T_q(1)$ and (b) $T_g(2)T_g(1)$. Note that $T_q(0) = 1$ by normalization.

fixed by looking at the singular behaviour of track cross sections. This will allow us to perform perturbative calculations involving track information at high order.

The standard observables, for which the cross section was given in (4.5), involve the knowledge of an infinite number of energy correlators. The operator valued δ-function observables can be related to moments after an expansion:

$$\delta(e - \hat{e}) = \delta(e) + \hat{e}\delta^{(1)}(e) + \cdots + \frac{\hat{e}^n}{n!}\delta^{(n)}(e), \tag{4.14}$$

where $\delta^{(n)}(e)$ is the n-th derivative of the delta function. This relation suggests that the weighted observables are the simpler building blocks for the more traditional δ-function type observables, since any observable that is defined by specifying its value on the final state involves an infinite number of moments to define it. It is therefore very natural to study moments of track functions, before one even considers the full functional form.

4.1.2 Moments of track functions

As discussed in 4.1.1, energy correlators only involve moments of track functions when restricting the final set of hadrons. For this class of observables it is therefore sufficient to know the evolution equations for moments of the track functions. To organize the structure of these evolution equations, we note that track functions measure the energy fraction in all hadrons of a given type. The more branches are involved, the more non-linear the structure will be. Taking moments will turn the complicated functional convolution structure in (4.4) into a product of moments of track functions, which are just numbers. In figure 4.2 we illustrate this non-linearity by the fact that there is a $T_i(m)$ on each branch.

Before we continue, let us define the n-th moment of the track function as

$$T_i(n,\mu) = \int_0^1 \mathrm{d}x\; x^n\; T_i(x,\mu)\,. \tag{4.15}$$

The track function is normalized such that $T_i(0,\mu) = 1$. In the following we often suppress the argument μ for brevity. Taking the n-th moment of the general form of the evolution of the track function function, as shown in (4.4), we find

$$\begin{aligned}
&\frac{\mathrm{d}}{\mathrm{d}\log\mu^2} T_i(n) \\
&= \sum_{i_1,\ldots,i_N} \left(\int \prod_{m=1}^{N} \mathrm{d}x_m \mathrm{d}z_m T_{i_m}(x_m) \right) \tilde{\gamma}_{i\to i_1\ldots i_o}(\{z_m\}) \delta\Big(1-\sum_r z_r\Big) \left(\sum_{l=1}^{N} x_l z_l\right)^n, \\
&= \sum_{i_1,\ldots,i_N} \sum_{l_1+l_2+..=n} \tilde{\gamma}_{i\to i_1\ldots i_N}(n;\{l_j\}) \prod_{m=1}^{N} T_{i_m}(l_m),
\end{aligned} \tag{4.16}$$

where

$$\tilde{\gamma}_{i\to i_1\ldots i_N}(n;\{l_j\}) = \binom{n}{l_1\ldots l_N} \left(\int \prod_{m=1}^{N} \mathrm{d}z_m z_m^{l_m} \right) \tilde{\gamma}_{i\to i_1\ldots i_N}(\{z_m\}) \delta\Big(1-\sum_m z_m\Big). \tag{4.17}$$

At NLO we are dealing with at most three branches, so we can have at most a product of three track functions on the right-hand side of (4.16).

The diagonal terms in the evolution of the moments of track functions only involve a single track function of moment n. This linearity is the same as one encounters for fragmentation functions, which will be discussed in section 4.1.3. We will see there that the diagonal terms are given by moments of splitting functions,

$$\frac{\mathrm{d}}{\mathrm{d}\log\mu^2} T_i(n) = -\sum_{jk=q,\bar{q},g} \gamma_{jk}(n+1) T_j(n) + \text{non-diagonal terms}, \tag{4.18}$$

where

$$\gamma_{ij}(n+1) = -\int P_{ij}(x) x^n \mathrm{d}x, \tag{4.19}$$

with $P_{ij}(x)$ the DGLAP splitting functions[1]. The terms that we call non-diagonal involve multiple track functions for which the sum of their moments is equal to n. Appendix 4.C provides a list of these γ_{ij}.

[1] This is a different notation than in equation (4.3), but it denotes the same object: $P_{i\to jk}(x) = P_{ki}(x)$.

Before we continue our discussion about track functions, we will discuss the better known fragmentation functions [47, 215], which describe the energy distribution of *single* hadrons, in the next section. They have a long history in QCD and have been used in precision studies.

4.1.3 Fragmentation functions

Fragmentation functions measure the energy fraction of a single hadron fragmenting from a quark or gluon. Since they have been studied in much detail, we can compare them to the track functions to see how (if at all) the evolution relates. While fragmentation functions have been well tested in higher-order calculations, track functions have only been investigated at leading logarithmic order. In order to firmly establish the track function formalism, we will compute their renormalization group evolution beyond the leading order in the coming sections, and furthermore show that these objects absorb the IR divergences appearing in perturbative calculations at $\mathcal{O}(\alpha_s^2)$.

Let us first construct the evolution of the fragmentation function in the same manner as we did for tracks in (4.4). The difference now is that the evolution is linear. In other words, the evolution of fragmentation only includes terms with a single fragmentation function, regardless of the order in perturbation theory:

$$\frac{\mathrm{d}}{\mathrm{d}\log\mu^2} D_i(z,\mu) = \int \prod_{m=1}^{N} \mathrm{d}z_m \delta\Big(1 - \sum_r z_r\Big) \sum_{i_1,i_2,..i_N} \tilde{\gamma}_{i\to i_1\ldots i_N}(\{z\}) \times \sum_{l=1}^{N} \int \mathrm{d}x D_{i_l}(x,\mu)\delta\left(z - x z_l\right), \tag{4.20}$$

where N is the order in perturbation theory and the indices $i_1 \ldots i_N$ denote flavor. The objects that describe the splitting in terms of the energy fraction, $\gamma_{i\to i_1\ldots i_o}(\{z\})$, are the same as we encountered in (4.4) for track functions. However the renormalization group equation of the fragmentation function is well known and reads

$$\frac{\mathrm{d}}{\mathrm{d}\log\mu^2} D_i(z,\mu) = \sum_j P_{ji}(z) \otimes D_j(z,\mu). \tag{4.21}$$

This is an all-order expression, where $P_{ji}(z)$ is the DGLAP splitting function. We can now take the n-th moment of (4.21), to transforms the convolution into a product in moment space:

$$\frac{\mathrm{d}}{\mathrm{d}\log\mu^2} D_i(n) = -\sum_j \gamma_{ji}(n+1) D_j(n). \tag{4.22}$$

Comparing this to the n-th moment of (4.20), we see that the moments of splitting functions can be related to $\gamma_{i\to i_1\ldots i_o}(\{z\})$ as

$$P_{ji}(n) = \int \prod_{m=1}^{o} \mathrm{d}z_m \delta\Big(1 - \sum_r z_r\Big) \sum_{i_1,i_2,..i_o} \tilde{\gamma}_{i\to i_1\ldots i_o}(\{z\}) \sum_m^o z_m^n \delta_{j,i_m}, \quad (4.23)$$

$$\text{where} \quad P_{ji}(n) \equiv \int dz z^n P_{ji}(z).$$

Now that we have this relation between $\tilde{\gamma}$ and the splitting kernels P, we can investigate the evolution of tracks a little more. Let us start by looking at the evolution of the first moment, as shown in (4.18). Here we see a direct relation with the first moment of fragmentation functions. We conclude that the evolution of the first moment of track functions is completely determined by moments of splitting functions:

$$\frac{\mathrm{d}}{\mathrm{d}\log\mu^2} T_i(1) = -\sum_j T_j(1)\gamma_{ji}(2). \quad (4.24)$$

For higher moments the non-linearity kicks in and we cannot express all anomalous dimensions in terms of moments of splitting functions $\gamma_{ij}(n)$. However, if we only consider diagonal contributions, as we wrote in (4.16), we see that they are directly related to the moments of splitting functions:

$$\frac{\mathrm{d}}{\mathrm{d}\log\mu^2} T_i(n) = -\sum_j T_j(n)\gamma_{ji}(n+1) + \text{non-diagonal terms}. \quad (4.25)$$

It is now clear that the diagonal terms in the evolution, one term for each flavour, are given by the corresponding moment of the splitting function. This is an all order statement as well, but keep in mind that for low orders some of these terms are zero because some flavours cannot yet be produced at that order.

Lastly, we note that the n-th moment of track functions encodes correlations between n final state hadrons. Concretely, $T_i(n)$ is related to the n-hadron fragmentation function [216–218]. This is discussed for $n = 2$ in [86].

Comparing to the better known fragmentation function we established that the diagonal terms in the evolution of moments of the track functions are given by moments splitting functions. For the first moment in particular the evolution is completely determined by the first moment of splitting functions to all orders. In the next sections we will focus on the anomalous dimensions that are not fixed by the comparison to fragmentation. We will start by looking at the symmetries of the evolution of the track functions to organize their structure.

4.2 Symmetries of the track function evolution

The track functions satisfy complicated non-linear evolution equations, generated by multi-parton splittings, see figure 4.2. This is due to the fact that they encode correlations between arbitrary numbers of hadrons. Nothing is known about the structure of these equations beyond the leading order. To organize their structure, we will identify and use symmetries that the track function evolution obeys.

If we take a step back and look at fragmentation functions we notice that their evolution is invariant under scaling, $x_i \to a x_i$ with a an arbitrary parameter. This is a result of the possibility to rescale the energy fractions of the partons z_i, since they are integrated over (see (4.20). Whenever scaling comes out to play one can restrict to homogeneous relations. For fragmentation functions we know that the evolution is even linear, see (4.21), so the Mellin transformation diagonalizes the evolution. Track functions did not inherit this scale invariance. However, in (4.16) we have already seen that the evolution of $T(n)$ only involves terms $\prod_i T(n_i)$ with $\sum_i n_i = n$. This feature constrains the evolution of jet functions quite a bit. To further constrain the evolution of track functions we can use a symmetry they do exhibit: shift symmetry. We will discuss this in section 4.2.1. In 4.2.2 we will look at the implications on the evolution of moments of track functions in a simple example with only gluons. In that section we will define a convenient basis of building blocks which are invariant under this symmetry. In the section 4.2.3, we will make our setup more realistic by adding quarks, but still keep the track function the same for all quark flavours. The completely general expressions are given in appendix 4.E.

4.2.1 Shift symmetry

The fact that track functions measure the energy fraction of all hadrons of a given type (e.g. charged hadrons) implies that the evolution of track functions exhibits a symmetry corresponding to energy conservation: it is invariant under shifts, $x \to x+b$. The energy fraction that is converted into hadrons of a given type is given by $x = \sum z_i x_i$, where i runs over the final state partons and $\sum z_i = 1$ by energy conservation. The delta function that appears in the evolution of the track function therefore satisfies the shift invariance:

$$\begin{aligned}\delta\Big(x - \sum_i x_i z_i\Big) \to \delta\Big(x + b - \sum_i (x_i + b) z_i\Big) &= \delta\Big(x + b - \sum_i x_i z_i - b \sum_i z_i\Big), \\ &= \delta\Big(x - \sum_i x_i z_i\Big). \end{aligned} \tag{4.26}$$

We can now relate moments of track functions to each other by utilizing this shift symmetry.

$$\begin{aligned} T(n) = \langle x^n \rangle &= \int dx\, x^n\, T(x) \\ &\to \int dx\, x^n\, T(x+b) \\ &= \int dx'(x'-b)^n\, T(x') \\ &= \sum_m \binom{n}{m} (-1)^{n-m} b^{n-m} T(m), \end{aligned} \tag{4.27}$$

where we suppressed the flavor indices for simplicity. In moment space, this corresponds to an infinite set of polynomial shift symmetries,

$$\begin{aligned} &T(0) \to 1, \\ &T(1) \to T(1) - b, \\ &T(2) \to T(2) - 2bT(1) + b^2, \\ &T(3) \to T(3) - 3bT(2) + 3b^2 T(1) - b^3, \\ &T(4) \to T_i(4) - 4bT_i(3) + 6b^2 T_i(2) - 4b^3 T_i(1) + b^4, \\ &\text{etc.} \end{aligned} \tag{4.28}$$

which severely constrain the form of the evolution. The shift symmetry suggests changing to a basis of *central moments* $\sigma(n)$, which are shift invariant by construction. These are defined as

$$\sigma(n) = \langle (x - \langle x \rangle)^n \rangle, \tag{4.29}$$

where the notation $\langle x^n \rangle = T(n)$ is defined in (4.27). To see that this definition is indeed shift invariant we now perform the shift $x \to x + b$ in (4.29). Noting that $\langle x + b \rangle$ is just the same as $\langle x \rangle + b$, as we showed in (4.30), we see that the shifts cancel:

$$\langle (x - \langle x \rangle)^n \rangle \to \langle (x + b - \langle x + b \rangle)^n \rangle = \langle (x \cancel{+ b} - \langle x \rangle \cancel{- b})^n \rangle = \langle (x - \langle x \rangle)^n \rangle\,. \tag{4.30}$$

To write the central moments in terms of track functions we use the binomial expansion in (4.29). This leads to

$$\sigma(n) = \sum_{m<n} (-1)^{n-m} \binom{n}{m} T(m) T(1)^{n-m}, \tag{4.31}$$

with $n \geq 2$. For the first five moments, this results in

$$\begin{aligned}
\sigma(2) &= T(2) - T(1)^2, \\
\sigma(3) &= T(3) - 3T(2)(1) + 2T(1)^3, \\
\sigma(4) &= T(4) - 4T(3)T(1) + 6T(2)T(1)^2 - 3T(1)^4, \\
\sigma(5) &= T(5) - 5T(4)T(1) + 10T_i(3)T(1) - 10T(2)T(1)^2 + 4T(1)^4.
\end{aligned} \tag{4.32}$$

For the first moment we cannot construct an invariant this way. We would need a theory with different flavours to define an object that is shift invariant by taking the difference between two track functions, such that the shift is cancelled between them. In the next section, we will demonstrate the implications of this shift symmetry for a theory that only includes gluons.

4.2.2 Evolution of track functions in a pure gluon theory

We will restrict ourselves to the simplified case with solely gluons. In this case, the shift symmetry fully predicts the evolution up to the third moment at all orders. At order α_s^2 the evolution is even predicted up to the sixth moment.

Since we will be exploiting the shift invariance, it is convenient to write the evolution in terms of the central moments. The evolution is then found by following a simple algorithm. The evolution of the first moment is directly related to the moment of the corresponding splitting function, as we already discussed in the comparison with fragmentation functions in (4.24). In a theory with only gluons this implies $\frac{\mathrm{d}}{\mathrm{d}\ln\mu^2} T_g(1) = 0$, as there can only appear shift invariant objects in the evolution. The evolution of the higher moments will be expressed in terms of the central moments. The total number of moments of each term in the evolution should be equal by construction. As there is no object at first moment that is invariant under shifts (this is specific to the pure gluon case), nothing interesting happens for the evolution of the first three moments. At the fourth moment we can have contributions from both $\sigma_g(4)$ and $\sigma_g(2)^2$, which gives us:

$$\begin{aligned}
&\frac{\mathrm{d}}{\mathrm{d}\ln\mu^2} T_g(1) = 0, \\
&\frac{\mathrm{d}}{\mathrm{d}\ln\mu^2} \sigma_g(2) = -\gamma_{gg}(3)\sigma_g(2), \\
&\frac{\mathrm{d}}{\mathrm{d}\ln\mu^2} \sigma_g(3) = -\gamma_{gg}(4)\sigma_g(3), \\
&\frac{\mathrm{d}}{\mathrm{d}\ln\mu^2} \sigma_g(4) = -\gamma_{gg}(5)\sigma_g(4) + \sum_{i_3 \ldots i_N} \tilde{\gamma}_{g\to g g i_3 \ldots i_N}(4; 2, 2, 0 \ldots 0)\sigma_g(2)^2.
\end{aligned} \tag{4.33}$$

where N is the order of perturbation theory.

When you restrict to NLO, terms involving more than three track functions are not allowed, since there is a maximum of three branches at this order. This constraints anomalous dimensions in equation (4.33) and the evolution can be completely fixed up to the sixth moment. In particular, when looking at the fourth moment we see that $\sigma_g(2)^2$ includes a term $T_g(1)^4$. Inserting the definition of $\sigma_g(4)$ and subsequently the known evolution equations for the first three moments, we can solve for the constant by requiring that all the terms including more than three T's cancel out. Similar manipulations can be done to completely fix the evolution at the fifth moment. From the sixth moment and higher the extra constraints are not enough to completely fix the evolution. The evolution equations for a pure gluon theory at NLO for the sixth moment has one unknown constant:

$$\begin{aligned}
\frac{\mathrm{d}}{\mathrm{d}\ln\mu^2}\sigma_g(4) &= -\gamma_{gg}(5)\sigma_g(4)+(-6\gamma_{gg}(3)+8\gamma_{gg}(4)-3\gamma_{gg}(5))\sigma_g(2)^2, \qquad (4.34)\\
\frac{\mathrm{d}}{\mathrm{d}\ln\mu^2}\sigma_g(5) &= -\gamma_{gg}(6)\sigma_g(5)-2\sigma_g(2)\sigma_g(3)(5\gamma_{gg}(3)-5\gamma_{gg}(4)+\gamma_{gg}(6)),\\
\frac{\mathrm{d}}{\mathrm{d}\ln\mu^2}\sigma_g(6) &= -\gamma_{gg}(7)\sigma_g(6)+\tilde{\gamma}_{g\to ggg}(6;2,2,2)(-\sigma_g(2)^3-\sigma_g(3)^2+\sigma_g(2)\sigma_g(4))\\
&\quad +\sigma_g(2)^3(-15\gamma_{gg}(3)+40\gamma_{gg}(4)-60\gamma_{gg}(5)+48\gamma_{gg}(6)-15\gamma_{gg}(7))\\
&\quad +\sigma_g(3)^2(-15\gamma_{gg}(3)+20\gamma_{gg}(4)-15\gamma_{gg}(5)+12\gamma_{gg}(6)-5\gamma_{gg}(7)).
\end{aligned}$$

As we saw for the pure gluon theory, and will be true in general, the shift symmetry alone is not enough to determine all the coefficients in the evolution. In section 4.3.1, we will focus on the missing pieces.

4.2.3 Evolution for quarks and gluons

In the previous section we discussed the general form of evolution equations for a pure gluon theory. To make the setup more realistic we will now add quarks, but take the same track functions for all quark flavours. The shift symmetry implies that the evolution equations can be expressed in terms of shift-invariant *central moments* $\sigma_g(n)$ and $\sigma_q(n)$, as well as a first moment invariant: $\Delta = T_q(1) - T_g(1)$. The fact we now have an invariant for the first moment, makes the evolution equations less restrictive. Let us first summarize how to find the evolution of track functions in terms of central moments now that we can define an invariant for the first moment. The first step is to define $p(n)$ that gives the partitions of n. We can then write the general form of the

evolution in terms of the central moments as

$$\frac{\mathrm{d}}{\mathrm{d}\ln\mu^2}\sigma_i(n) = \prod_{m=1}^{p(n)} c_m \prod_{k_m} \sigma_i(k_m), \tag{4.35}$$

where k_m a parameter that runs over the values of the particular partition m and σ_i can only denote shift invariant objects, which includes Δ for the first moment. The relation between c and $\tilde{\gamma}$ is found by using the definition of the central moments in terms of track functions, see (4.32). Let us take $n = 4$ as an example, for which the number of partitions, $p(4)$, is 5. The possible partitions are (4), (3,1), (2,2), (2,1,1) and (1,1,1,1). Using equation 4.35 we then find

$$\begin{aligned}\frac{\mathrm{d}}{\mathrm{d}\ln\mu^2}\sigma_i(4) = \sum_j &- \gamma_{ij}(5)\sigma_j(4) + c_{ij}(3,1)\sigma_j(3)\Delta + c_{ijk}(2,2)\sigma_j(2)\sigma_k(2) \\ &+ c_{ij}(2,1,1)\sigma_j(2)\Delta^2 + c_i(1,1,1,1)\Delta^4.\end{aligned} \tag{4.36}$$

The diagonal piece, $\sum_j -\gamma_{ij}(5)\sigma_j(4)$, is a result from the LO comparison to fragmentation functions. In the final step one can impose extra constraints when restricting to a specific order. Meaning, if we constrain to NLO, terms involving 4 (or more) track functions need to cancel, if we constrain to NNLO, terms involving 5 (or more) track functions need to cancel, and so forth. As we saw for the pure gluon theory, and will be true in general, the shift symmetry alone is not enough to determine all the coefficients in the evolution.

For charged particles we can make use of the fact that $T_q = T_{\bar{q}}$. To simplify the notation, we will define $\vec{\sigma}(n) = (\sigma_q(n), \sigma_g(n))$. Using the shift symmetry in section 4.2.1, combined with a comparison to the fragmentation function limit, we obtain

$$\begin{aligned}\frac{\mathrm{d}}{\mathrm{d}\ln\mu^2}\Delta &= -(\gamma_{qq}(2) + \gamma_{gg}(2))\Delta\,, \\ \frac{\mathrm{d}}{\mathrm{d}\ln\mu^2}\vec{\sigma}(2) &= -\hat{\gamma}(3)\vec{\sigma}(2) + \vec{c}_{\Delta^2}\Delta^2\,, \\ \frac{\mathrm{d}}{\mathrm{d}\ln\mu^2}\vec{\sigma}(3) &= -\hat{\gamma}(4)\vec{\sigma}(3) + \hat{c}_{\sigma_2\Delta}\vec{\sigma}(2)\Delta + \vec{c}_{\Delta^3}\Delta^3\,, \\ \frac{\mathrm{d}}{\mathrm{d}\ln\mu^2}\vec{\sigma}(4) &= -\hat{\gamma}(5)\vec{\sigma}(4) + \hat{c}_{\sigma_2\sigma_2} \otimes (\vec{\sigma}(2)\cdot\vec{\sigma}(2)^T) \\ &\quad + \hat{c}_{\sigma_3\Delta}\vec{\sigma}(3)\Delta + \hat{c}_{\sigma_2\Delta^2}\vec{\sigma}(2)\Delta^2 + \vec{c}_{\Delta^4}\Delta^4\,,\end{aligned} \tag{4.37}$$

and similarly for the higher central moments. Note that the $\otimes$ in the evolution of the fourth moment should be read as $\hat{c}_{\sigma_2\sigma_2} \otimes (\vec{\sigma}(2)\cdot\vec{\sigma}(2)^T)_i =$

$\sum_{j,k} c_{ijk}\sigma(2)_j\sigma(2)_k$, where i is the index of $\vec{\sigma}(n)$ on the LHS. We emphasize that since this structure is derived from symmetry, it holds to all orders in perturbation theory. It is remarkably simple compared to the most general form of the non-linear evolution, emphasizing the important role the shift symmetry plays in constraining the evolution. Remarkably, despite the non-linearity of the equations, shift invariance, combined with the uniqueness of the first three central moments, forces the evolution of the first three *central moments* of the track functions to be the standard DGLAP evolution [20–22, 219], since (at least for charged hadrons) $\Delta = T_q(1) - T_g(1)$ is suppressed. On the other hand, unlike the central moments, the moments themselves, $T_i(n)$, exhibit complicated non-linear evolution. The first genuine unsupressed non-linearities in the evolution of the central moments occur at the fourth moment due to mixings between $\vec{\sigma}(4)$ and $(\vec{\sigma}(2) \cdot \vec{\sigma}(2)^T)$, and similarly at higher moments.

This form of the evolution admits a particularly pleasing interpretation. In a unitary field theory, the eigenvalues of the $\hat{\gamma}(n)$ are positive, and monotonically increasing with n [220, 221]. This implies that all central moments (with the exception of the mean) of the track functions vanish as the energy is taken to infinity, as does Δ. Furthermore higher central moments vanish more rapidly. Therefore the track functions converge to the UV fixed point $T_i(x, \mu) \to \delta(x - x_0)$. To what extent this limit is relevant for phenomenology may depend on the subset of hadrons considered, e.g. for charged hadrons Δ is already small at rather low scales, as are higher central moments, but $\sigma_i(2)$ remains relatively large for $\mu = 1$ TeV [167].

4.3 Evolution of track functions

Having understood the structure of the evolution equations for the moments of the track functions, in this section we explicitly compute the remaining anomalous dimensions for the first three moments at next-to-leading order. This allows us to to describe three-point correlation functions of energy flow with only charged particles in the final state, which matches the current state of the art calculations [199]. In section 4.3.1 we will compute the RGEs of the track functions by integrating the collinear splitting functions [222–224] to obtain a jet function for the nth moment of charged particles, differential in the invariant mass of all particles [98]. This is illustrated in figure 4.2. After the renormalization of this jet function (which is the same as the renormalization of the invariant mass jet function [66, 68]), the track function evolution can be inferred from the remaining IR poles. We will see that the shift symmetry of the track function evolution equations significantly reduces the required calculations. In section 4.3.2, we compute all mixing terms separately, as an

additional check on our calculation, and verified that they respect the shift symmetry. In section 4.4.1 we then calculate the two-point energy correlation analytically at order $\mathcal{O}(\alpha_s^2)$. The IR poles from the partonic correlator give an independent calculation of the evolution equations, providing a strong check on the track function formalism at $\mathcal{O}(\alpha_s^2)$.

4.3.1 Full Track Function Evolution at Next-to-Leading Order

As discussed in section 4.1, calculating the track function directly will result in scaleless integrals, and will therefore not give us the desired evolution. We will therefore instead calculate a jet function $J(s, x)$ differential in the total invariant mass s of the jet and the track fraction x. In this section we will go through the steps for the quark track function in detail. For the gluon track function the calculation is similar and can be performed by following the analogue of the steps discussed here. We will focus on the first three moments, but it is straightforward to extend the procedure to arbitrary moments. We will work at NLO accuracy to match state of the art calculations.

Track functions are constructed in such a way that they remove any IR divergences that may appear by not including the full subset of particles on the partonic level. In our track jet function, we therefore expect that the track functions cancel any left over IR divergences after renormalization. In this subsection we will focus on extracting the evolution for the quark track function.

To extract the evolution of the quark track function, we start with the quark track jet function, which can be calculated order by order,

$$J_q(s, x) = J_q^{(0)}(s, x) + \frac{\alpha_s}{4\pi} J_q^{(1)}(s, x) + \left(\frac{\alpha_s}{4\pi}\right)^2 J_q^{(2)}(s, x) + \mathcal{O}(\alpha_s^3), \tag{4.38}$$

where the dependence on the renormalization scale μ is left implicit. At lowest order the calculation is fairly simple since there are no divergences

$$J_q^{(0)}(s, x) = T_q^{(0)}(x)\delta(s). \tag{4.39}$$

If we go to the first order we see that including only a subset of particles in the final state results in divergences on the partonic level, which will be captured by the track function.

$$\begin{aligned} J_q^{(1)}(s, x) = & T_q^{(1)}(x, \mu)\delta(s) + \sum_{ij} \int \mathrm{d}x_1 \mathrm{d}x_2 \mathrm{d}z_1 \mathrm{d}z_2 \mathcal{J}_{q\to ij}^{(1)}(s, z_1, z_2) \\ & \times T_i^{(0)}(x_1) T_j^{(0)}(x_2) \delta\left(x - z_1 x_1 - z_2 x_2\right), \end{aligned} \tag{4.40}$$

where $\mathcal{J}^{(1)}_{qi}$ is a one loop matching coefficient, which is finite by construction. Since the second term in this expression is finite, the one loop track function therefore contains all the poles. We can now continue to $\mathcal{O}(\alpha_s^2)$

$$\begin{aligned} J_q^{(2)}(s,x) =& T_q^{(2)}(x)\delta(s) + \sum_{ij}\int \mathrm{d}z_1\mathrm{d}z_2\mathrm{d}x_1\mathrm{d}x_2 \mathcal{J}^{(1)}_{q\to ij}(s,z_1,z_2) \\ &\times T_i^{(1)}(x_1)T_j^{(0)}(x_2)\delta(x-z_1x_1-z_2x_2) \\ &+ \sum_{ijk}\int \mathrm{d}z_1\mathrm{d}z_2\mathrm{d}z_3\mathrm{d}x_1\mathrm{d}x_2\mathrm{d}x_3 \mathcal{J}^{(2)}_{q\to ijk}(s,z_1,z_2,z_3) \\ &\times T_i^{(0)}(x_1)T_j^{(0)}(x_2)T_k^{(0)}(x_2)\delta(x-z_1x_1-z_2x_2-z_3x_3). \end{aligned} \tag{4.41}$$

Again the matching coefficients are finite, so the last term in the expression above does not contain any poles. We can therefore neglect this last term in our quest to extract the second order quark track function, which only consist of poles. We calculate the renormalized $J_q^{(2)}$ and subtract the $\mathcal{J}^{(1)}T^{(1)}$ terms. The IR poles that are left over give us the $\mathcal{O}(\alpha_s^2)$ evolution of $T_q^{(2)}$. In the rest of this section we will focus on calculating the evolution for the first three moments at $\mathcal{O}(\alpha_s^2)$. We will do this by calculating the renormalized jet function up to $\mathcal{O}(\alpha_s^2)$ and then proceed moment by moment to extract the evolution of the track function.

The bare jet function at $\mathcal{O}(\alpha_s)$ was introduced in chapter 1.2.5. We now include tracks by including a $T_i^{(0)}$ for resulting each particle after splitting, where i matches the flavour. Using the definition in 2.2 and taking the n-th moment we find

$$\begin{aligned} J^{(1)}_{q,\mathrm{bare}}(s,n) =& \frac{-2C_F\mu^{2\epsilon}}{s^{1+\epsilon}}\int_0^1 \mathrm{d}z \left(\frac{1+z^2}{1-z} - \epsilon(1-z)\right)\frac{e^{\epsilon\gamma_E}(1-z)^{-\epsilon}}{\Gamma(1-\epsilon)} \\ &\times \sum_{k+m=n}(1-z)^k z^m T_q^{(0)}(k)T_g^{(0)}(m), \end{aligned} \tag{4.42}$$

where z $(1-z)$ is the energy fraction of the quark (gluon) after the splitting. In (4.40) we see that the renormalized track functions we want to extract always come with a $\delta(s)$. We can therefore use the expansion in ϵ and only consider the $\delta(s)$ terms when we want to extract $T_q^{(1)2}$. For the first moment we see that there are only two possibilities for k and m, namely a first moment of the quark ($k=1$ and $m=0$) or gluon ($k=0$ and $m=1$) track function. We

[2]The series in ϵ will also give a plus distribution, however this does not contribute a pole.

therefore have

$$J^{(1)}_{q,\text{bare}}(s,1)|_{\delta(s)} = T_q^{(0)}(1)\Big(\frac{\gamma_{qq}^{(0)}(2)}{\epsilon} + j_{qq}(1) + \epsilon\, p_{qq}(1)\Big) + T_g^{(0)}(1)\Big(\frac{\gamma_{gq}^{(0)}(2)}{\epsilon} + j_{gq}(1) + \epsilon\, p_{gq}(1)\Big), \tag{4.43}$$

where the $\gamma_{ij}(n)$ are the moments of splitting functions defined in (4.19) and the constants $j_{ij}(n)$ and $p_{ij}(n)$ are listed in appendix 4.D. Similar expressions can be found for higher moments. The bare jet function at first order for the second and third moment can be found in appendix 4.D. The first thing to note is that the ϵ^{-1} pole is the n-th moment of the time-like splitting function ($\gamma(n+1)$ by convention). Second, we see that contributions with three track functions are absent at LO, because we have at most two partons in the final state.

Equations (4.40) and (4.41) hold for the renormalized track jet function and the renormalized track function captures all the IR divergences that are left after renormalization . We remove UV divergences with the modified minimal subtraction scheme ($\overline{\text{MS}}$). The renormalization of the track jet function is the same as for the normal jet function. This is due to the fact that in the factorization only the jet function contributes to the measurement of x. RGE consistency then tells us that the UV structure should therefore be unchanged [98] and the renormalization is given by

$$J_q(s,x,\mu) = \int_0^\infty \mathrm{d}s'\, Z_{J_q}(s',\mu) J_{q,\text{bare}}(s-s',x)\,, \tag{4.44}$$

$$\begin{aligned}
&Z_{J_q}(s',\mu) = \\
&\delta(s') + \frac{\alpha_s C_F}{4\pi}\left[\frac{4}{\epsilon}\frac{1}{\mu^2}\mathcal{L}_0\left(\frac{s'}{\mu^2}\right) - \delta(s')\left(\frac{4}{\epsilon^2}+\frac{3}{\epsilon}\right)\right] \\
&+ \frac{\alpha_s^2 C_F}{(4\pi)^2}\Bigg[\Bigg[\frac{1}{\mu^2}\mathcal{L}_1\Big(\frac{s'}{\mu^2}\Big)\frac{16}{\epsilon^2} + \frac{1}{\mu^2}\mathcal{L}_0\Big(\frac{s'}{\mu^2}\Big)\Big(-\frac{16}{\epsilon^3}-\frac{12}{\epsilon^2}\Big) \\
&\qquad + \delta(s')\Big(\frac{8}{\epsilon^4}+\frac{12}{\epsilon^3}+\frac{1}{\epsilon^2}\Big(\frac{9}{2}-\frac{4}{3}\pi^2\Big)+\frac{1}{\epsilon}\Big(-\frac{3}{4}+\pi^2-12\zeta_3\Big)\Big)\Bigg] \\
&\quad + C_A\Bigg[\frac{1}{\mu^2}\mathcal{L}_0\Big(\frac{s'}{\mu^2}\Big)\Big(-\frac{22}{3}\frac{1}{\epsilon^2}+\frac{1}{\epsilon}\Big(\frac{134}{9}-\frac{2}{3}\pi^2\Big)\Big) \\
&\qquad + \delta(s')\Big(\frac{11}{\epsilon^3}+\frac{1}{\epsilon^2}\Big(-\frac{35}{18}+\frac{\pi^2}{3}\Big)+\frac{1}{\epsilon}\Big(-\frac{1769}{108}-\frac{11}{18}\pi^2+20\zeta_3\Big)\Big)\Bigg] \\
&\quad + T_F n_f\Bigg[\frac{1}{\mu^2}\mathcal{L}_0\Big(\frac{s'}{\mu^2}\Big)\Big(\frac{8}{3}\frac{1}{\epsilon^2}-\frac{40}{9}\frac{1}{\epsilon}\Big)
\end{aligned}$$

$$+\,\delta(s')\Big(-\frac{4}{\epsilon^3}+\frac{2}{9}\frac{1}{\epsilon^2}+\frac{1}{\epsilon}\Big(\frac{121}{27}+\frac{2}{9}\pi^2\Big)\Big)\Big]$$
$$+\,\mathcal{O}(\alpha_s^3)\,.$$

Furthermore, we need to renormalize the strong coupling constant with

$$Z_\alpha = 1-\frac{\alpha_s}{4\pi}\frac{\beta_0}{\epsilon}+\mathcal{O}(\alpha_s^3), \tag{4.45}$$

with

$$\beta_0 = -\frac{11}{3}C_A+\frac{4}{3}T_F n_f. \tag{4.46}$$

Now we use a neat trick: we know that the bare track function is zero beyond leading order, since it consists of scaleless integrals. We can therefore write $T_i^{(0)} = T_{i,\text{bare}}$. Then, by renormalizing the bare jet function, all the left over IR divergences in the renormalized jet function will cancel. In this way we automatically obtain the right-hand side (RHS) of (4.40) and (4.41). The renormalization factor we introduce for this track function should thus cancel all divergences. It is exactly this feature that we will use to fix the missing pieces in the evolution equation. In practice we substitute the following expression for the first moment

$$\begin{aligned}T_{q,\text{bare}}(1) =& T_q(1)+\frac{\alpha_s}{4\pi}\frac{1}{\epsilon}\Big(R_{qq}^{(1)}(1)T_q(1)+R_{qq}^{(1)}(1)T_g(1)\Big)\\ &+\frac{1}{2}\frac{\alpha_s^2}{(4\pi)^2}\Big(\frac{1}{\epsilon}\big(R_{qq}^{(2)}(1)T_q(1)+R_{\bar{q}q}^{(2)}(1)T_{\bar{q}}(1)+R_{gq}^{(2)}(1)T_g(1)\\ &\qquad+R_{Qq}^{(2)}(1)T_Q(1)+R_{\bar{Q}q}^{(2)}(1)T_{\bar{Q}}(1)\big)\\ &\qquad+\frac{1}{\epsilon^2}(\cdots)\Big)\\ &+\mathcal{O}(\alpha_s^3),\end{aligned} \tag{4.47}$$

where all the track functions on the rhs are renormalized track functions and the $R_{ij}^{(m)}(n)$ represent the renormalization factors at order m. The $1/\epsilon^2$ poles in (4.47) at $\mathcal{O}(\alpha_s^2)$ are completely fixed by the $\mathcal{O}(\alpha_s)$ evolution factors $R_{ij}^{(1)}(1)$, and they only function as a check on the procedure, so we will leave them out for now. The expressions for the second and third moment are similar, but include mixing terms in alignment with (4.16).

The contribution to the track jet function at order $\mathcal{O}(\alpha_s^2)$ consists of contributions from purely virtual corrections, real-virtual corrections and corrections with two real emissions. This calculation can be done analytically, as we will

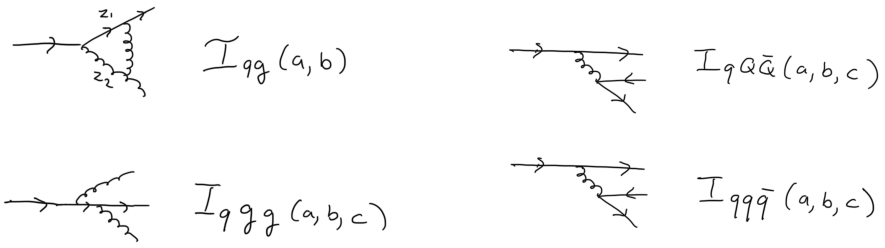

Figure 4.3 The NLO splittings contributing to the two loop jet function. The integrals I schematically denote the integration over the momentum fractions z_1, z_2 and z_3 with weight $z_1^a z_2^b z_3^c$. Note that the I integrals only represent the $\delta(s)$ contributions, since these are of interest when extracting the evolution of track functions from the track jet function.

see in section 4.3.2. In this section, however, there is no need to perform the calculation in detail, since the evolution of the track functions can be fully extracted from consistency. It is sufficient to write the contributions to the jet function at order $\mathcal{O}(\alpha_s^2)$ in integral form. As one can see in figure 4.3 there are four diagrams that contribute to the quark initiated jets, from which one of them is a real virtual contribution. Instead of performing the calculation we will introduce variables that denote the integrals that show up, which are also introduced in figure 4.3. After the integration over the invariant masses has been performed, as will become more clear in when we peform the full calculation in in section 4.3.2, the dependency on s is an overall factor $\frac{-1}{\epsilon} s^{-1-2\epsilon}$. As explained before we are only interested in the $\delta(s)$ terms and the integrals I will therefore only include these pieces. The variables of the integrals a, b, c represent the weighting by the momentum fractions. For example $I_{qgg}[a,b,c]$ represents the integrated splitting from a quark in a quark and two gluons, where the splitting amplitude is weighted by the momentum of the quark z_1 and both gluons z_2 and z_3 as $z_1^a z_2^b z_3^c$,

$$I_{qgg}(a,b,c) = \int \mathrm{d}\Phi_3^c \Theta(\mu^2 - s_{123}) P_{q\to qgg}(\{s\}, z_1, z_2, z_3) z_1^a z_2^b z_3^c. \tag{4.48}$$

The collinear phase space $\mathrm{d}\Phi_3^c$ is given in (4.57) and the NLO splitting function in appendix 4.B.

Another feature specific to each integral is its color structure. The real virtual contribution I_{qg} has two color structures, namely C_F^2 and $C_F C_A$. The same color structures show up for the integrated splitting amplitude in the $q \to qgg$ process. In $n_f I_{qQ\bar{Q}}$ there is a single color structure $n_f C_F T_f$. Lastly, in $I_{qq\bar{q}}$ we have the $C_F T_F$ and $C_F C_A/2$. It is convenient to split the integrals

such that

$$I_{qq\bar{q}} = I_{qQ\bar{Q}} + I_{q\text{int}}. \tag{4.49}$$

Now it is also clear why we have chosen to extract the color structures with n_f from the integrals in figure 4.3. It enables us to split the calculation in an n_f part and one without. The same could be done for other color structures, but since in our case it sufficient to only keep track of the n_f pieces, we avoid introducing unnecessary notation.

If we now construct the track quark jet function in terms of these integrals at order $\mathcal{O}(\alpha_s^2)$ we find for the first moment

$$\begin{aligned} J^{(2)}_{q,bare}(1) = {} & T_q(1)\big(I_{qg}(1,0)+I_{qgg}(1,0,0)+(1+n_f)I_{qQ\bar{Q}}(1,0,0)+2I_{qq\bar{q}}(1,0,0)\big) \\ & + T_{\bar{q}}(1)\big(I_{qQ\bar{Q}}(0,1,0)+I_{qq\bar{q}}(0,0,1)\big)+n_f\big(T_Q(1)+T_{\bar{Q}}(1)\big)I_{qQ\bar{Q}}(0,1,0) \\ & + T_g(1)\big(I_{qg}(0,1)+2I_{qgg}(0,0,1)\big), \end{aligned} \tag{4.50}$$

where the track functions are all bare track functions. The expressions for the second and third moment can be found in the appendix.

After renormalization we thus have a system of equations which we can solve for these renormalization factors R order by order, starting with the first moment. As expected we find that after renormalization the IR poles at order α_s cancel for each moment independently. This just tells us that the general form of the evolution that we took in equation (4.4) is indeed correct.

As we have seen in (4.24), the evolution of the first moment is completely fixed by symmetries. However, we can still extract information from the cancellation of poles. Namely, instead of calculating the integral expressions in (4.50), we can infer them from the cancellation of poles. For first moment we have 5 terms: $T_q(1), T_{\bar{q}}(1), T_Q(1), T_{\bar{Q}}(1)$ and $T_g(1)$. The equations for $T_Q(1)$ and $T_{\bar{Q}}(1)$ provide the same information, as these quarks are interchangeable. By looking at all terms that are tagged with renormalized quark track function of a different flavor than the initiating quark, $T_Q(1)$, we can infer the integral $I_{qQ\bar{Q}}(0,1,0)$. We find that

$$I_{qQ\bar{Q}}(0,1,0) = \frac{118}{27} T_F C_F. \tag{4.51}$$

In the next section we calculate this integral and similar integrals directly, to check our procedure. Looking at the first moment of the renormalized track jet function thus only gives us integral expressions of weight 1, meaning is that the integrals are weighted with either z_1, z_2 or z_3.

Let us now discuss what happens when we go to the second moment. In (4.37) we see the coefficient $\vec{\gamma}_{\delta^2}$ is not known yet. After a basis change to the

evolution of track functions, this transforms into several unknown constants in the evolution of the quark and gluon jet functions. From the pole structure in the diagonal terms of the renormalized track jet function, i.e. terms that come with $T_i(2)$, we can obtain the expressions for integrals weighted with either z_1^2, z_2^2 or z_3^2. From the non-diagonal terms, e.g. $T_q(1)T_g(1)$, we can extract the missing constants. We will elaborate a bit on this procedure for the particular case of $R^{(2)}_{Q\bar{Q}q}(2)$. We thus first collect all the $\frac{1}{\epsilon}$-terms that are tagged with $T_Q T_{\bar{Q}}$. This gives us

$$\begin{aligned} R^{(2)}_{Q\bar{Q}q}(2) &= -4\left(I_{qQ\bar{Q}}(0,1,1) + j_{gq}(2)\left(\gamma^{(1)}_{qg}(2) - \gamma^{(1)}_{qg}(1)\right)\right) \\ &= -\frac{17}{100} C_F T_F. \end{aligned} \tag{4.52}$$

In order to obtain the answer we had to calculate $I_{qQ\bar{Q}}(0,1,1)$, which is an integral of weight 2 that we did not infer from the diagonal pieces. However, we can use symmetry to rewrite this integral in terms of ones we do know. This particular integral is weighted with $z_2 z_3$. Momentum conservation allows us to use the identity

$$z_2 z_3 = \frac{1}{2}(-(z_1 - z_1^2) + (z_2 - z_2^2) + (z_3 - z_3^2)). \tag{4.53}$$

in order to write the weighted integral $I_{qQ\bar{Q}}(0,1,1)$ in terms of integrals that are weighted by a single momentum fraction

$$\begin{aligned} I_{qQ\bar{Q}}(0,1,1) = \frac{1}{2}\big((I_{qQ\bar{Q}}(1,0,0) - I_{qQ\bar{Q}}(2,0,0)) - (I_{qQ\bar{Q}}(0,1,0) - I_{qQ\bar{Q}}(0,2,0)), \\ + (I_{qQ\bar{Q}}(0,0,1) - I_{qQ\bar{Q}}(0,0,2)\big) \\ = \frac{197}{72} C_F T_F. \end{aligned} \tag{4.54}$$

This procedure, of extracting $R^{(2)}_{Q\bar{Q}q}(2)$, can be repeated to completely determine all unknown coefficients for the evolution of the second moment of the quark track function.

Going to the third moment there is nothing conceptually different compared to the evolution at second moment. In particular, the diagonal terms provide expressions for integrals weighted by a single momentum fraction of weight 3. Then again we can use momentum conservation to find all integrals of weight 3. Finally we look at the different diagonal structures and solve for the unknown coefficients such that the $1/\epsilon$ terms cancel.

We did not go to higher moments, because for the energy correlator low moments suffice, but in principle we can proceed systematically to higher moments. Also, this same procedure is used to fix the evolution of moments of the gluon track function.

We have now built a procedure to systematically fix the evolution of the quark track function, without having to calculate any integrals for the track jet function at $\mathcal{O}(\alpha_s^2)$ for the first three moments. We have also performed the direct calculation of these integrals to check our methods. In the next section we will explain how this was done.

4.3.2 Direct calculation of the $\mathcal{O}(\alpha_s^2)$ track jet function

In chapter 1.2.5 we already introduced the jet function. At first order the jet function is calculated in dimensional regularization by integrating the collinear matrix element over the two particle phase space [225], see (2.2).

At two-loop order the jet function has contributions from a virtual correction, a real-virtual correction and two real emissions. The virtual correction is a scaleless integral and vanishes in dimensional regularization. The contributions with a real-virtual correction has the same two body phase as in the NLO jet function, given by

$$\mathrm{d}\Phi_2^{\mathrm{c}}(s,z) = \mathrm{d}s\,\mathrm{d}z\,\frac{[z(1-z)s]^{-\epsilon}}{(4\pi)^{2-\epsilon}\Gamma(1-\epsilon)}\,. \tag{4.55}$$

The collinear matrix element has a correction to the splitting function $P_{qg}^{(0)}$, namely [226]

$$\begin{aligned} P_{qg}^{(1)} =& \Big(\frac{\mu^2 e^{\gamma_E}}{s}\Big)^{\epsilon}\frac{2g^2}{(4\pi)^2}\frac{\pi\,\Gamma(1-\epsilon)}{\epsilon\tan(\pi\epsilon)\Gamma(1-2\epsilon)}\,C_F\Big\{(C_F-C_A)\frac{z(1+z)}{1-z}\frac{\epsilon^2}{1-2\epsilon} \\ &+\Big[\frac{1+z^2}{1-z}-\epsilon(1-z)\Big]\Big[(C_F-C_A)\Big(1-\frac{\epsilon^2}{1-2\epsilon}\Big)+C_F \\ &-C_A\,{}_2F_1\Big(1,-\epsilon;1-\epsilon;\frac{z}{z-1}\Big)+(C_A-2C_F)\,{}_2F_1\Big(1,-\epsilon;1-\epsilon;\frac{z-1}{z}\Big)\Big]\Big\}, \end{aligned} \tag{4.56}$$

For the contributions from two real emissions we need to consider a three particle phase space. The collinear phase space for non-identical particles is given by [227]

$$\begin{aligned} \mathrm{d}\Phi_3^{\mathrm{c}} =& \,\mathrm{d}s_{123}\,\mathrm{d}s_{12}\,\mathrm{d}s_{13}\,\mathrm{d}s_{23}\,\delta(s_{123}-s_{12}-s_{13}-s_{23}) \\ &\times \mathrm{d}z_1\,\mathrm{d}z_2\,\mathrm{d}z_3\,\delta(1-z_1-z_2-z_3) \\ &\times \frac{4\Theta(-\Delta)(-\Delta)^{-\frac{1}{2}-\epsilon}}{(4\pi)^{5-2\epsilon}\Gamma(1-2\epsilon)}. \end{aligned} \tag{4.57}$$

Here,

$$\Delta = (z_3 s_{12} - z_1 s_{23} - z_2 s_{13})^2 - 4 z_1 z_2 s_{13} s_{23}\,, \tag{4.58}$$

with the total invariant mass given by $s_{123} \geq 0$, the invariant mass of partons i and j by $s_{ij} \geq 0$ and the momentum fraction of parton i is denoted by $0 \leq z_i \leq 1$. The collinear matrix element is given by

$$\sigma^{\mathrm{c}}_{3,ijk} = \Big(\frac{\mu^2 e^{\gamma_E}}{4\pi}\Big)^{2\epsilon} \frac{4g^4}{s^2_{123}} P_{ijk}\,, \tag{4.59}$$

where the LO splitting functions for $q \to ijk$ are given in (4.65) of appendix 4.B.

Going back to the track jet function we see that at $\mathcal{O}(\alpha_s^2)$ we have contributions where integrals are weighted by momentum fractions. It is exactly this weighting that makes the integrals easier to compute. Due to the presence of extra momentum fraction factors, soft divergences are (mostly) eliminated.

The integration over the double unresolved invariant masses can be performed using appendix A in [224].

4.4 Applications

Now that we have expressions for the track function evolution we can start putting it into practise. We will first calculate the cross section for the two-point energy correlation using only charged particles in the final state. The two-point energy correlation (EEC) measurement was already introduced in (4.10) and describes the correlation between two energy deposits. We saw that for an energy correlator it is trivial to incorporate tracking information, since this just rescales the weight function. The collinear limit, where the angle between the two detectors approaches zero, is of particular interest for describing the substructure of jets produced at hadron colliders. Furthermore, we will describe in 4.4.2 how track functions can improve the experimental accuracy for the azimuthal decorrelation between a vector boson and a jet in pp collisions. Due to consistency of the factorization theorem derived in 3.2.1, switching to charged particles will only change the jet function by a finite amount.

4.4.1 Two-Point Correlations at Next-to-Leading Order.

Having calculated the evolution of track functions at next-to-leading order, we will now illustrate the consistency of track functions beyond the leading order. We analytically compute the two-point energy correlation [24,194,195] at order $\mathcal{O}(\alpha_s^2)$, with a generic restriction on hadrons. The two-point energy correlator is characterized by a single angle between the two calorimeter cells, called χ (see (4.10)). This calculation also illustrates how track functions seamlessly

mesh with perturbative calculations, as this calculation matches the highest order available analytically for the two-point energy correlator on all partons.

The two-point energy correlator has been computed analytically at NLO for both e^+e^- collisions [196] and Higgs decays [197, 228]. When computed on all final state particles it is infrared finite to all orders in perturbation theory. However, when computed in dimensional regularization with $d = 4 - 2\epsilon$, the partonic two-point correlator in (4.12) has infrared poles in ϵ which must be absorbed into the track function. These poles are uniquely fixed in terms of the renormalization group evolution of the track function. Since the RG of the n-th moment of the track function involve mixing with products of all lower moments, it is convenient to write their RG in an abstract form

$$\frac{\mathrm{d}}{\mathrm{d}\ln\mu^2}\vec{\mathbf{T}}_n = \widehat{R}_n\ \vec{\mathbf{T}}_n\,, \tag{4.60}$$

where $\vec{\mathbf{T}}_n$ is a vector of all possible products of moments of track functions that have total weight n (e.g. for $n = 2$, $\vec{\mathbf{T}}_2 = \{T_g(2), T_q(2), T_q(1)T_q(1), T_g(1)T_q(1), T_g(1)T_g(1)\}$), and $\widehat{R}_n$ is a matrix, whose perturbative expansion is $\widehat{R}_n = \sum a_s^j \widehat{R}_n^{(j)}$. The IR divergences of the partonic energy correlators follow from the UV divergences of track functions, which we saw for quarks specifically in equation (4.47), and in general reads

$$\begin{aligned}\vec{\mathbf{T}}_{n,\mathrm{bare}} =& \vec{\mathbf{T}}_n(\mu) + a_s\frac{\widehat{R}^{(1)}}{\epsilon}\vec{\mathbf{T}}_n(\mu) \\ &+\frac{1}{2}a_s^2\left(\frac{\widehat{R}_n^{(2)}}{\epsilon}+\frac{\widehat{R}_n^{(1)}\widehat{R}_n^{(1)}-\beta_0\widehat{R}_n^{(1)}}{\epsilon^2}\right)\vec{\mathbf{T}}_n(\mu)+\mathcal{O}(a_s^3).\end{aligned} \tag{4.61}$$

The $1/\epsilon^2$ poles at two loops are completely predicted from the one-loop renormalization, while the $1/\epsilon$ provide an independent calculation of the NLO RG evolution, and the universality of the track functions.

To compute the EEC on tracks requires the calculation of the general partonic correlators in equation (4.12), extending the calculation of the EEC in [196]. To perform this calculation we follow the approach of [196], and use reverse unitarity [229] to express the phase space integrals for the EEC in terms of multiloop integrals. These integrals are reduced to master integrals using `LiteRed` [230, 231] and `FIRE6` [232]. The master integrals are found to be the same as for the standard EEC, and are evaluated by differential equations, using `CANONICA` [233] to obtain their canonical form [234]. Master integrals for the contact terms ($\delta(\chi)$) are the same as those for cut bubble integrals, and can be extracted from [235] and [236]. The final results are written in terms of classical polylogarithms using `HPL` [237], and complete analytic results will be

presented elsewhere. We again emphasize that this perturbative calculation on tracks matches the state of the art for analytic perturbative calculations of energy flow observables. This clearly illustrates how important the factorization property of energy correlator observables in equation (4.12) is for simplifying the perturbative component of calculations interfaced with tracks.

Extracting the IR poles from the calculation of the partonic correlators, we find that they exactly match with those predicted by equation (4.61), providing a strong check on the track function formalism at $\mathcal{O}(\alpha_s^2)$. Absorbing these poles into the renormalized track functions, gives an IR finite result for the EEC computed on any subset of final state hadrons at NLO. In figure 4.4 we show our results for the EEC on all particles, charged particles, and positively charged particles, along with a comparison to Pythia [166]. Here we have used track functions extracted from Pythia [167, 168]. In figure 4.5 we compare our LO and NLO results with DELPHI data [238] for the EEC asymmetry (AEEC), defined as $\text{AEEC}(\cos(\chi)) = \text{EEC}(\cos(\chi)) - \text{EEC}(-\cos(\chi))$, finding remarkably good agreement at NLO. The disagreement in the region $\cos(\chi) \to -1$ is due to the fact that we have not incorporated resummation. Such resummation could be included with next-to-next-to-leading logarithm precision using the factorization of [239] and results reported here, but is beyond the scope of our current analysis. Although we find this agreement promising, it will be important to better understand the details of the experimental analysis of [238] for a more detailed interpretation of the comparison. This is the first $\mathcal{O}(\alpha_s^2)$ calculation of a track-based observable, and we hope that the reduced experimental uncertainty for track-based observables can enable improved extractions of the strong coupling constant from event shapes.

4.4.2 Azimuthal decorrelation

In chapter 3 we discussed the azimuthal decorrelation for $pp \to Z + \text{jet}$. Before we start discussing the details that lead to a track-based prediction, let us address a subtlety concernig the factorization theorem in (3.19). At first one might expect that we could have chosen to keep the cross section differential in $p_{T,J}$, instead of $p_{T,V}$. The recombined jet momentum $p_{T,J}$ will however change when we restrict ourselves to charged particles. It loses the connection to the hard kinematics as the neutral particles will not be clustered and therefore impose a mismatch compared to the hard kinematics. The $p_{T,V}$ will however not be affected, which makes it the preferred choice.

To exploit the better angular resolution of the inner detectors' tracking system, compared to the calorimetry based jet reconstruction, we switch to a track-based measurement. Here we identify another advantage of the WTA axis: since the effect of soft radiation on the jet algorithm is power suppressed,

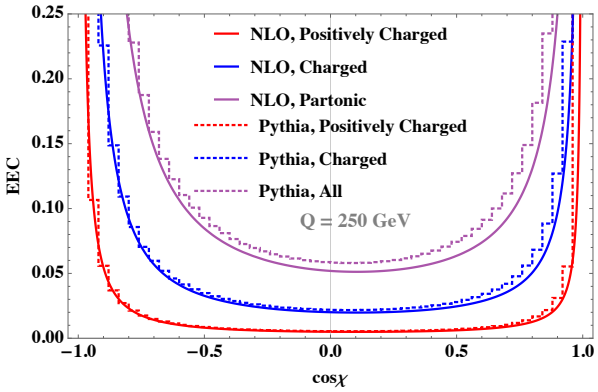

Figure 4.4 An illustration of the track function formalism for different subsets of final state hadrons. Here we show the EEC at NLO as computed on all particles, on charged particles, and on positively charged particles, as well as a comparison with the Pythia parton shower.

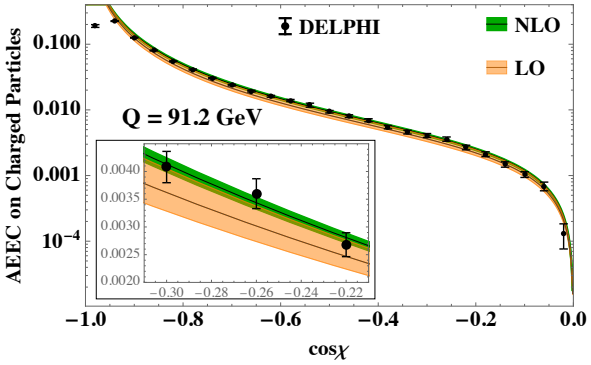

Figure 4.5 The EEC Asymmetry (AEEC) on charged particles at LO and NLO, compared with DELPHI data. Excellent agreement is observed, except in the region $\cos(\chi) \to -1$, where resummation is required.

switching to a track-based measurement only modifies the jet function. (Note that η_J does not require a fine angular resolution and is therefore measured on the full jet.) Consistency of the factorization formula then implies that this track-based jet function $\bar{\mathcal{J}}$ has the same anomalous dimension as $\mathcal{J}$. We reach the same conclusion by a direct calculation using track functions [167, 168]. Explicitly, the difference in the one-loop constant for the quark jet function is

$$\bar{\mathcal{J}}_q^{(1)} = \mathcal{J}_q^{(1)} + 4C_F \int_0^1 \mathrm{d}z_1 \int_0^1 \mathrm{d}z_2\, T_q(z_1,\mu) T_g(z_2,\mu) \int_0^1 \mathrm{d}x\, \ln\frac{x}{1-x}$$

$$\times \frac{1+x^2}{1-x}\big(\theta(z_1 x - z_2(1-x)) - \theta(x-\tfrac{1}{2})\big)\,, \tag{4.62}$$

in terms of the track functions $T_i(z,\mu)$. The change reflects the possibility of a hadronization mismatch in the WTA recombination: A losing (in WTA sense) parton may hadronize into the winning track. The expression for the gluon jet function involves the appropriate replacement of the splitting functions,

$$\begin{aligned}\bar{\mathcal{J}}_g^{(1)} = \mathcal{J}_g^{(1)} &+ 4C_A \int_0^1 \mathrm{d}z_1 \int_0^1 \mathrm{d}z_2\, T_g(z_1,\mu) T_g(z_2,\mu) \int_0^1 \mathrm{d}x\, \ln\frac{x}{1-x} \\ &\times \Big(\frac{x}{1-x} + \frac{1-x}{x} + x(1-x)\Big)\big(\theta(z_1 x - z_2(1-x)) - \theta(x-\tfrac{1}{2})\big) \\ &+ 4n_f T_F \int_0^1 \mathrm{d}z_1 \int_0^1 \mathrm{d}z_2\, T_q(z_1,\mu) T_{\bar{q}}(z_2,\mu) \int_0^1 \mathrm{d}x\, \ln\frac{x}{1-x} \\ &\times \Big(1 - 2x(1-x)\Big)\big(\theta(z_1 x - z_2(1-x)) - \theta(x-\tfrac{1}{2})\big)\,, \end{aligned} \tag{4.63}$$

and there is no modification to the linearly-polarized gluon jet function at order α_s. We have verified using Pythia 8.2 [166] that using tracks only has a minimal effect on this measurement, see fig. 4.6. For the standard jet axis, this difference is larger [240]. The conclusions reached here also apply to other angular measurements, such as in [150, 160, 161].

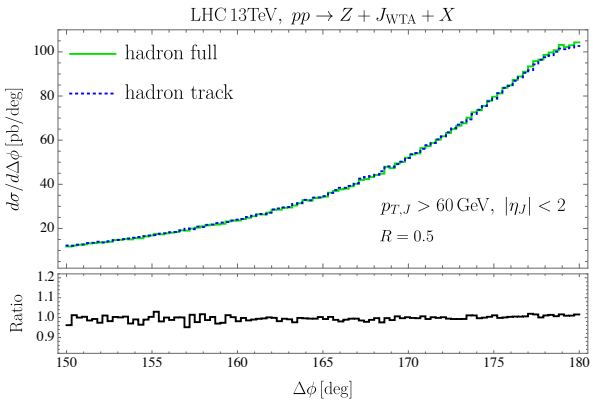

Figure 4.6 Predictions from Pythia for the azimuthal angle between the vector boson and jet, using all particles (green) or only charged particles (blue dotted).

4.5 Conclusion

We have presented a method for computing the next-to-leading order renormalization group equations (RGEs) for moments of track functions, and include explicit results for the first few moments. The structure of these evolution equations is highly constrained due to invariance under shift symmetry and the evolution can be compactly written in terms of shift-invariant combinations of track functions. Even tough shift symmetry does not completely fix all anomalous dimensions, we presented a method where we consider the track jet function to completely fix the evolution at NLO.

We have shown that track functions can be applied to make predictions for the EEC and Azimuthal angle on tracks. Although track functions were originally introduced to describe the energy fraction of charged final state particles, they can be used for any other quantum number as well (as long as the measurement including all final state particles of that observable has a valid factorization theorem). This opens the door to a wide variety of new calculations and enables powerful perturbative calculations to also be applied to obtain predications for certain non-perturbative measurements.

To extend what is done in this thesis, one could go beyond moments by exploring the full x dependence, which will require plus distributions to handle soft limits. Furthermore, since $\mathcal{O}(\alpha_s^2)$ calculations are more and more automatized, it will be important to develop a scheme to implement track functions in these calculations to extend these predictions to measurements using only charged particles.

Appendices

4.A Notation

In this chapter we introduced some notation. As a reference we summarize it here:

- P_{ji}: DGLAP splitting function, appearing in the evolution of fragmentation functions as in (4.20). These do not contain any poles.
- γ: introduced to describe the (diagonal) anomalous dimensions in the evolution of moments of track functions that are moments of DGLAP splitting functions, see (4.19).
- $P_{i\to jkl}$: Splitting function in d-dimensions, from the collinear factorization of the squared amplitude. It is used to calculate the jet function at $\mathcal{O}(\alpha_s^2)$, showing up in (4.59).

- $\tilde{\gamma}$: Symbols that are used to schematically denote anomalous dimensions, as introduced in (4.4). This variable is also used in the moment space version of the evolution for which one uses the relation in (4.17).
- c: Explicit anomalous dimensions that are not (necessarily) the splitting functions, used in (4.35).

4.B Splitting Functions

The LO splitting functions for $q \to ij$ and $g \to ij$ are [219, 225]

$$\begin{aligned} P_{qg}(z) &= C_F\left[\frac{1+z^2}{1-z} - \epsilon(1-z)\right], \\ P_{gg}(z) &= 2C_A\left[\frac{z}{1-z} + \frac{1-z}{z} + z(1-z)\right], \\ P_{q\bar{q}}(z) &= n_f T_R\left[1 - \frac{2z(1-z)}{1-\epsilon}\right]. \end{aligned} \tag{4.64}$$

The LO splitting functions for $q \to ijk$ are [222, 223]

$$\begin{aligned} P_{\bar{q}'q'q} =& C_F T_F \frac{s_{123}}{2s_{12}}\left[-\frac{[z_1(s_{12}+2s_{23}) - z_2(s_{12}+2s_{13})]^2}{(z_1+z_2)^2 s_{12} s_{123}} + \frac{4z_3+(z_1-z_2)^2}{z_1+z_2}\right. \\ &\left. +(1-2\epsilon)\left(z_1+z_2-\frac{s_{12}}{s_{123}}\right)\right], \\ P_{\bar{q}qq} =& (P_{\bar{q}'q'q}+2\leftrightarrow 3)+P^{(\mathrm{id})}_{\bar{q}qq}, \\ P^{(\mathrm{id})}_{\bar{q}qq} =& C_F\left(C_F-\frac{1}{2}C_A\right)\left\{(1-\epsilon)\left(\frac{2s_{23}}{s_{12}}-\epsilon\right)+\frac{s_{123}}{s_{12}}\left[\frac{1+z_1^2}{1-z_2}-\frac{2z_2}{1-z_3}\right.\right. \\ &\left. -\epsilon\left(\frac{(1-z_3)^2}{1-z_2}+1+z_1-\frac{2z_2}{1-z_3}\right)-\epsilon^2(1-z_3)\right] \\ &\left. -\frac{s_{123}^2}{2s_{12}s_{13}}z_1\left[\frac{1+z_1^2}{(1-z_2)(1-z_3)}-\epsilon\left(1+2\frac{1-z_2}{1-z_3}\right)-\epsilon^2\right]\right\}+(2\leftrightarrow 3), \\ P_{ggq} =& C_F^2\left\{\frac{s_{123}^2}{2s_{13}s_{23}}z_3\left[\frac{1+z_3^2}{z_1z_2}-\epsilon\frac{z_1^2+z_2^2}{z_1z_2}-\epsilon(1+\epsilon)\right]+(1-\epsilon)\left[\epsilon-(1-\epsilon)\frac{s_{23}}{s_{13}}\right]\right. \\ &\left. +\frac{s_{123}}{s_{13}}\left[\frac{z_3(1-z_1)+(1-z_2)^3}{z_1z_2}-\epsilon(z_1^2+z_1z_2+z_2^2)\frac{1-z_2}{z_1z_2}+\epsilon^2(1+z_3)\right]\right\} \\ &+C_FC_A\left\{(1-\epsilon)\left(\frac{[z_1(s_{12}+2s_{23})-z_2(s_{12}+2s_{13})]^2}{4(z_1+z_2)^2s_{12}^2}+\frac{1}{4}-\frac{\epsilon}{2}\right)\right. \\ &\left. +\frac{s_{123}^2}{2s_{12}s_{13}}\left[\frac{2z_3+(1-\epsilon)(1-z_3)^2}{z_2}+\frac{2(1-z_2)+(1-\epsilon)z_2^2}{1-z_3}\right]\right. \end{aligned}$$

$$
\begin{aligned}
&-\frac{s_{123}^2}{4s_{13}s_{23}}z_3\left[\frac{2z_3+(1-\epsilon)(1-z_3)^2}{z_1z_2}+\epsilon(1-\epsilon)\right]\\
&+\frac{s_{123}}{2s_{12}}\left[(1-\epsilon)\frac{z_1(2-2z_1+z_1^2)-z_2(6-6z_2+z_2^2)}{z_2(1-z_3)}+2\epsilon\frac{z_3(z_1-\!-2z_2)-z_2}{z_2(1-z_3)}\right]\\
&+\frac{s_{123}}{2s_{13}}\left[(1-\epsilon)\frac{(1-z_2)^3+z_3^2-z_2}{z_2(1-z_3)}-\epsilon\left(\frac{2(1-z_2)(z_2-z_3)}{z_2(1-z_3)}-z_1+z_2\right)\right.\\
&\left.-\frac{z_3(1-z_1)+(1-z_2)^3}{z_1z_2}+\epsilon(1-z_2)\left(\frac{z_1^2+z_2^2}{z_1z_2}-\epsilon\right)\right]\Bigg\}+(1\leftrightarrow 2). \qquad (4.65)
\end{aligned}
$$

The LO splitting functions for $g \to ijk$ can be found in [223]. The virtual correction to the LO splitting function for $q \to qg$, that is needed for NLO jet function calculations, is given in (4.56).

4.C Moments of splitting functions

The moments of the timelike splitting functions in appendix 4.B are defined in equation (4.19) and here repeated for convenience:

$$\gamma_{ij}(n+1) = -\int P_{ij}(x)x^n \mathrm{d}x. \qquad (4.66)$$

These are perturbative objects

$$\gamma_{ij}(n+1) = \sum_{L=0}^{\infty}\left(\frac{\alpha_s}{4\pi}\right)^{(L+1)}\gamma_{ij}^{(L)}(n+1). \qquad (4.67)$$

Explicit calculation yields the NLO results:

$$
\begin{aligned}
\gamma_{gg}^{(1)}(2) =& n_f T_F\left(\left(\frac{200}{27}-\frac{16\pi^2}{9}\right)C_A+\frac{260}{27}C_F\right),\\
\gamma_{gq}^{(1)}(2) =& \left(\frac{32\pi^2}{9}-\frac{568}{27}\right)C_F^2-\frac{376}{27}C_AC_F,\\
\gamma_{qg}^{(1)}(2) =& T_F\left(\left(\frac{8\pi^2}{9}-\frac{100}{27}\right)C_A-\frac{130}{27}C_F\right),\\
\gamma_{qq}^{(1)}(2) =& C_AC_F\left(4\zeta_3+\frac{1495}{54}-\frac{17\pi^2}{9}\right)+C_F^2\left(-8\zeta_3-\frac{175}{27}+\frac{2\pi^2}{9}\right)\\
&-\frac{128}{27}C_Fn_fT_F+\frac{64}{27}C_FT_F,\\
\gamma_{\bar{q}q}^{(1)}(2) =& C_AC_F\left(-4\zeta_3-\frac{743}{54}+\frac{17\pi^2}{9}\right)+C_F^2\left(8\zeta_3+\frac{743}{27}-\frac{34\pi^2}{9}\right)\\
&+\frac{64}{27}C_FT_F,
\end{aligned}
$$

$$
\begin{aligned}
\gamma^{(1)}_{q'q}(2) =& \frac{64}{27} C_F T_F, \\
\gamma^{(1)}_{\bar{q}'q}(2) =& \frac{64}{27} C_F T_F, \\
\gamma^{(1)}_{gg}(3) =& C_A^2 \Big(-8\zeta_3 + \frac{2158}{675} + \frac{26\pi^2}{45}\Big) + n n_f T_F \Big(\Big(\frac{3803}{675} - \frac{16\pi^2}{9} \Big) C_A \\
& + \frac{12839}{2700} C_F \Big), \\
\gamma^{(1)}_{gq}(3) =& \Big(-\frac{39451}{5400} - \frac{7\pi^2}{9} \Big) C_A C_F + \Big(\frac{14\pi^2}{9} - \frac{2977}{432} \Big) C_F^2, \\
\gamma^{(1)}_{qq}(3) =& T_F \Big(\Big(\frac{619}{2700} + \frac{14\pi^2}{45} \Big) C_A - \frac{833}{216} C_F \Big) - \frac{8}{25} n_f T_F^2, \\
\gamma^{(1)}_{qq}(3) =& C_A C_F \Big(4\zeta_3 \frac{16673}{432} - \frac{43\pi^2}{18} \Big) + C_F^2 \Big(-8\zeta_3 + \frac{989}{432} - \frac{7\pi^2}{9} \Big) \\
& - \frac{415}{54} C_F n_f T_F + \frac{4391}{5400} C_F T_F, \\
\gamma^{(1)}_{\bar{q}q}(3) =& C_A C_F \Big(4\zeta_3 + \frac{8113}{432} - \frac{43\pi^2}{18} \Big) + C_F^2 \Big(-8\zeta_3 - \frac{8113}{216} + \frac{43\pi^2}{9} \Big) \\
& + \frac{4391}{5400} C_F T_F, \\
\gamma^{(1)}_{q'q}(3) =& \frac{4391}{5400} C_F T_F, \\
\gamma^{(1)}_{\bar{q}'q}(3) =& \frac{4391}{5400} C_F T_F,
\end{aligned}
\tag{4.68}
$$

4.D Moments of track jet functions

In this appendix we give the expressions for moments of track functions up to $\mathcal{O}(\alpha_s^2)$. We present only the quark case, as the gluon jet function has a very similar structure. The bare quark jet function is given by

$$
J_{q,\mathrm{bare}}(n) = T_{q,\mathrm{bare}}(n) + \alpha_s J^{(1)}_{q,\mathrm{bare}}(n) + \alpha_s^2 J^{(2)}_{q,\mathrm{bare}}(n) + \mathcal{O}(\alpha_s^3). \tag{4.69}
$$

At order α_s the first three moments are

$$
\begin{aligned}
J^{(1)}_{q,\mathrm{bare}}(1) =& T_q(1) \Big(\frac{\gamma^{(0)}_{qq}(2)}{\epsilon} + j_{qq}(1) + \epsilon\, p_{qq}(1) \Big) + T_g(1) \Big(\frac{\gamma^{(0)}_{gq}(2)}{\epsilon} + j_{gq}(1) + \epsilon\, p_{gq}(1) \Big), \\
J^{(1)}_{q,\mathrm{bare}}(2) =& T_q(2) \Big(\frac{\gamma^{(0)}_{qq}(3)}{\epsilon} + j_{qq}(2) + \epsilon\, p_{qq}(2) \Big) + T_g(2) \Big(\frac{\gamma^{(0)}_{gq}(3)}{\epsilon} + j_{gq}(2) + \epsilon\, p_{gq}(2) \Big), \\
& + T_q(1) T_g(1) \Big(\frac{\gamma^{(0)}_{qq}(2) - \gamma^{(0)}_{qq}(3)}{\epsilon} + j_{qq}(1) - j_{qq}(2) + \epsilon \left(p_{qq}(1) - p_{qq}(2) \right) \Big) \\
J^{(1)}_{q,\mathrm{bare}}(3) =& T_q(3) \Big(\frac{\gamma^{(0)}_{qq}(4)}{\epsilon} + j_{qq}(3) + \epsilon\, p_{qq}(3) \Big) + T_g(3) \Big(\frac{\gamma^{(0)}_{gq}(4)}{\epsilon} + j_{gq}(3) + \epsilon\, p_{gq}(3) \Big),
\end{aligned}
$$

$$+T_q(2)T_g(1)\Big(\frac{\gamma_{qq}^{(0)}(3)-\gamma_{qq}^{(0)}(4)}{\epsilon}+j_{qq}(2)-j_{qq}(3)+\epsilon\,(p_{qq}(2)-p_{qq}(3))\Big)$$
$$+T_q(1)T_g(2)\Big(\frac{\gamma_{gq}^{(0)}(3)-\gamma_{gq}^{(0)}(4)}{\epsilon}+j_{gq}(2)-j_{gq}(3)+\epsilon\,(p_{gq}(2)-p_{gq}(3))\Big), \tag{4.70}$$

with γ_{ij} given in appendix 4.C, and

$$\begin{aligned}
j_{qq}(1) &= \left(\frac{106}{9}-\pi^2\right)C_F, & p_{qq}(1) &= \left(\frac{635}{27}-\frac{17\pi^2}{12}-\frac{28\zeta_3}{3}\right)C_F,\\
j_{gq}(1) &= -\frac{43}{9}C_F, & p_{gq}(1) &= \left(-\frac{257}{27}+\frac{2\pi^2}{3}\right)C_F,\\
j_{qq}(2) &= \left(\frac{133}{9}-\pi^2\right)C_F, & p_{qq}(2) &= \left(\frac{1603}{54}-\frac{43\pi^2}{24}-\frac{28\zeta_3}{3}\right)C_F\\
j_{gq}(2) &= -\frac{16}{9}C_F, & p_{gq}(2) &= \left(-\frac{181}{54}+\frac{7\pi^2}{24}\right)C_F,\\
j_{qq}(3) &= \left(\frac{7717}{450}-\pi^2\right)C_F, & p_{qq}(3) &= \left(\frac{233977}{6750}-\frac{247\pi^2}{120}-\frac{28\zeta_3}{3}\right)C_F\\
j_{gq}(3) &= -\frac{517}{450}C_F, & p_{gq}(3) &= \left(-\frac{7301}{3375}+\frac{11\pi^2}{60}\right)C_F.
\end{aligned} \tag{4.71}$$

At order α_s^2 the first three moments are

$$\begin{aligned}
J^{(2)}_{q,\mathrm{bare}}(1) =& T_q(1)(I_{qg}(1,0)+I_{qgg}(1,0,0)+(1+n_f)C_FT_FI_{qQ\bar{Q}}(1,0,0)\\
&+2I_{qq\bar{q}}(1,0,0))+T_{\bar{q}}(1)(T_FC_FI_{qQ\bar{Q}}(0,1,0)+I_{qq\bar{q}}(0,0,1))\\
&+n_fT_FC_F(T_Q(1)+T_{\bar{Q}}(1))I_{qQ\bar{Q}}(0,1,0)\\
&+T_g(1)(I_{qg}(0,1)+2I_{qgg}(0,0,1)),\\
J^{(2)}_{q,\mathrm{bare}}(2) =& T_g(2)\big(I_{qg}(0,2)+2I_{qgg}(0,0,2)\big)\\
&+T_q(2)\big(I_{qg}(2,0)+I_{qgg}(2,0,0)+(1+n_f)C_FT_FI_{qQQ}(2,0,0)\\
&\qquad+2I_{q\mathrm{int}}(2,0,0))\\
&+T_{\bar{q}}(2)(T_FC_FI_{qQQ}(0,2,0)+I_{q\mathrm{int}}(0,0,2))\\
&+(T_Q(2)+T_{\bar{Q}}(2))(n_fT_FC_FI_{qQQ}(0,2,0))\\
&+2T_g(1)T_q(1)(I_{qg}(1,1)+2I_{qgg}(1,0,1))+2T_g(1)T_g(1)I_{qgg}(0,1,1)\\
&+2T_q(1)T_{\bar{Q}}(1)(C_FT_F(I_{qQ\bar{Q}}(1,0,1)+I_{qQ\bar{Q}}(0,1,1))+2I_{q\mathrm{int}}(1,0,1))\\
&+2T_q(1)(T_Q(1)+T_{\bar{Q}}(1))(n_fT_FC_FI_{qQ\bar{Q}}(1,1,0))\\
&+2T_q(1)T_q(1)(C_FT_FI_{qQ\bar{Q}}(1,1,0)+I_{q\mathrm{int}}(1,1,0))\\
&+2T_Q(1)T_{\bar{Q}}(1)(n_fC_FT_FI_{qQ\bar{Q}}(0,1,1)),
\end{aligned}$$

$$
\begin{aligned}
J^{(2)}_{q,\mathrm{bare}}(3) = {} & T_g(3)(I_{qg}(0,3) + 2I_{qgg}(0,0,3)) \\
& + T_q(3)(I_{qg}(3,0) + I_{qgg}(3,0,0) + (1+n_f)C_F T_F I_{qQ\bar{Q}}(3,0,0) \\
& \quad + 2I_{q\mathrm{int}}(3,0,0)) \\
& + (T_Q(3) + T_{\bar{Q}}(3))(n_f T_F C_F I_{qQ\bar{Q}}(0,3,0)) \\
& + T_{\bar{q}}(3)(T_F C_F I_{qQ\bar{Q}}(0,3,0) + I_{q\mathrm{int}}(0,0,3)) \\
& + 3T_g(2)T_q(1)(I_{qg}(1,2) + 2I_{qgg}(1,0,2)) \\
& + 3T_g(1)T_q(2)(I_{qg}(2,1) + 2I_{qgg}(2,0,1)) \\
& + 3T_q(2)T_{\bar{q}}(1)(C_F T_F(I_{qQ\bar{Q}}(2,0,1) + I_{qQ\bar{Q}}(0,2,1)) + 2I_{q\mathrm{int}}(2,0,1)) \\
& + 3T_q(1)T_{\bar{q}}(2)(C_F T_F(I_{qQ\bar{Q}}(1,0,2) + I_{qQ\bar{Q}}(0,1,2)) + 2I_{q\mathrm{int}}(1,0,2)) \\
& + 3T_q(2)(T_Q(1) + T_{\bar{Q}}(1))(n_f T_F C_F I_{qQ\bar{Q}}(2,1,0)) \\
& + 3T_q(1)(T_Q(2) + T_{\bar{Q}}(2))(n_f T_F C_F I_{qQ\bar{Q}}(1,2,0)) \\
& + 3T_q(2)T_q(1)(C_F T_F(I_{qQ\bar{Q}}(2,1,0) + I_{qQ\bar{Q}}(1,2,0)) + 2I_{q\mathrm{int}}(1,1,0)) \\
& + 3T_Q(2)T_{\bar{Q}}(1)(n_f C_F T_F I_{qQ\bar{Q}}(0,2,1)) \\
& + 3T_Q(1)T_{\bar{Q}}(2)(n_f C_F T_F I_{qQ\bar{Q}}(0,1,2)) \\
& + 6T_Q(1)T_{\bar{Q}}(1)T_q(1)(n_f T_F C_F I_{qQ\bar{Q}}(1,1,1)) \\
& + 6T_q(1)^2 T_{\bar{q}}(1)(C_F T_F I_{qQ\bar{Q}}(1,1,1) + 2I_{q\mathrm{int}}(1,1,1)) \\
& + 6T_g(1)^2 T_q(1) I_{qgg}(1,1,1). \qquad (4.72)
\end{aligned}
$$

The constants in $J^{(1)}_{q,\mathrm{bare}}(n)$ can be obtained from direct calculation and are given by

$$uitdrukkingen \qquad (4.73)$$

4.E Evolution of track functions

In this thesis, we presented the results for the NLO evolution of the first three moments of the track functions under the simplified assumption that $T_q = T_{\bar{q}}$, and that the track functions are equal for all quark flavors. This simplified case was sufficient to illustrate the structure of the equations, without excessive notation. In this appendix, we present the complete results in several different forms. These different forms may be useful for different users, depending on their particular application.

Although the results can be drastically simplified by working in terms of shift-invariant central moments, we begin by presenting the results for the evolution of the standard moments of the track functions. For gluons, we find that the NLO contribution to the evolution for the first three moments is given

by

$$\frac{\mathrm{d}\,T_g(1)}{\mathrm{d}\ln\mu^2} = -\gamma_{gg}^{(1)}(2)T_g(1) - \sum_i \gamma_{qg}^{(1)}(2)\left(T_{q_i}(1)+T_{\bar{q}_i}(1)\right), \tag{4.74}$$

$$\begin{aligned}\frac{\mathrm{d}\,T_g(2)}{\mathrm{d}\ln\mu^2} &= -\gamma_{gg}^{(1)}(3)T_g(2) - \sum_i \gamma_{qg}^{(1)}(3)\left(T_{q_i}(2)+T_{\bar{q}_i}(2)\right) \\ &\quad + \left[C_A^2\left(-8\zeta_3+\frac{26}{45}\pi^2+\frac{2158}{675}\right)-\frac{4}{9}C_A n_f T_F\right] T_g(1)T_g(1) \\ &\quad + \sum_i \left[T_F\left(-\frac{299}{225}C_A-\frac{4387}{900}C_F\right)\right] T_g(1)\left(T_{q_i}(1)+T_{\bar{q}_i}(1)\right) \\ &\quad + \sum_i T_F\left[\left(\frac{12413}{1350}-\frac{52}{45}\pi^2\right)C_A+\frac{1528}{225}C_F-\frac{16}{25}n_f T_F\right] T_{q_i}(1)T_{\bar{q}_i}(1),\end{aligned} \tag{4.75}$$

$$\begin{aligned}\frac{\mathrm{d}\,T_g(3)}{\mathrm{d}\ln\mu^2} &= -\gamma_{gg}^{(1)}(4)T_g(3) - \sum_i \gamma_{qg}^{(1)}(4)\left(T_{q_i}(3)+T_{\bar{q}_i}(3)\right) \\ &\quad + \left[C_A^2\left(24\zeta_3-\frac{278}{15}\pi^2+\frac{767263}{4500}\right)-\frac{2}{3}C_A n_f T_F\right] T_g(2)T_g(1) \\ &\quad + \sum_i \left[T_F\left(-\frac{46}{15}C_A-\frac{1727}{2250}C_F\right)\right] T_g(2)\left(T_{q_i}(1)+T_{\bar{q}_i}(1)\right) \\ &\quad + \sum_i T_F\left[\left(\frac{14}{15}\pi^2-\frac{10318}{1125}\right)C_A-\frac{4544}{1125}C_F\right] \left(T_{q_i}(2)+T_{\bar{q}_i}(2)\right)T_g(1) \\ &\quad + \sum_i T_F\left[\left(\frac{5321}{3000}-\frac{2}{5}\pi^2\right)C_A+\frac{1523}{240}C_F-\frac{12}{25}n_f T_F\right] \\ &\qquad\qquad \times \left(T_{q_i}(2)T_{\bar{q}_i}(1)+T_{q_i}(1)T_{\bar{q}_i}(2)\right) \\ &\quad + C_A^2\left(-\frac{248561}{2250}+\frac{194}{15}\pi^2-24\zeta_3\right)T_g(1)T_g(1)T_g(1) \\ &\quad + \sum_i \left[C_A T_f\left(\frac{23051}{1125}-\frac{28}{15}\pi^2\right)-C_F T_f\frac{501}{100}\right] T_g(1)T_{q_i}(1)T_{\bar{q}_i}(1)\,.\end{aligned} \tag{4.76}$$

The results for quarks are slightly more complicated due to the presence of identical quark contributions. At NLO we find

$$\begin{aligned}\frac{\mathrm{d}\,T_q(1)}{\mathrm{d}\ln\mu^2} &= -\gamma_{gq}^{(1)}(2)T_g(1) - \gamma_{qq}^{(1)}(2)T_q(1) - \gamma_{\bar{q}q}^{(1)}(2)T_{\bar{q}}(1) \\ &\quad - \sum_i \gamma_{Qq}^{(1)}(2)\left(T_{Q_i}(1)+T_{\bar{Q}_i}(1)\right),\end{aligned} \tag{4.77}$$

$$\frac{\mathrm{d}\,T_q(2)}{\mathrm{d}\ln\mu^2} = -\gamma_{gq}^{(1)}(3)T_g(2) - \gamma_{qq}^{(1)}(3)T_q(2) - \gamma_{\bar{q}q}^{(1)}(3)T_{\bar{q}}(2) \tag{4.78}$$

$$
\begin{aligned}
&-\sum_i \gamma_{Qq}^{(1)}(3)\big(T_{Q_i}(2)+T_{\bar{Q}_i}(2)\big)\\
&+\Big[\Big(\frac{1399}{5400}-\frac{7}{9}\pi^2\Big)C_AC_F-\frac{67}{18}C_F^2\Big]T_g(1)T_g(1)\\
&+\Big[\Big(-\frac{3023}{108}+\frac{34}{9}\pi^2-8\zeta_3\Big)C_AC_F+\Big(\frac{3023}{54}-\frac{68}{9}\pi^2+16\zeta_3\Big)C_F^2\\
&\quad-\frac{53}{18}C_FT_F\Big]T_q(1)T_q(1)\\
&+\Big[\Big(\frac{14057}{216}-\frac{77}{9}\pi^2+16\zeta_3\Big)C_AC_F+\Big(-\frac{14057}{108}+\frac{154}{9}\pi^2-32\zeta_3\Big)C_F^2\\
&\quad-\frac{2803}{900}C_FT_F\Big]T_q(1)T_{\bar{q}}(1)\\
&+\Big[\frac{229}{18}C_AC_F+\Big(\frac{2573}{72}-4\pi^2\Big)\Big]T_g(1)T_q(1)-\sum_i\frac{17}{100}C_FT_FT_{Q_i}(1)T_{\bar{Q}_i}(1)\\
&-\sum_i\Big[\frac{53}{18}C_FT_F\Big]T_q(1)\big(T_{Q_i}(1)+T_{\bar{Q}_i}(1)\big),
\end{aligned}
$$

$$
\begin{aligned}
\frac{\mathrm{d}\,T_q(3)}{\mathrm{d}\ln\mu^2} &= -\gamma_{gq}^{(1)}(4)T_g(3)-\gamma_{qq}^{(1)}(4)T_q(3)-\gamma_{\bar{q}q}^{(1)}(4)T(3)_{\bar{q}} \qquad (4.79)\\
&-\sum_i\gamma_{Qq}^{(1)}(4)\big(T_{Q_i}(3)+T_{\bar{Q}_i}(3)\big)+\Big[-\frac{3787}{750}C_AC_F-\frac{249}{50}C_F^2\Big]T_g(2)T_g(1)\\
&+\Big[\Big(\frac{7}{3}\pi^2-\frac{14161}{3000}\Big)C_AC_F+\Big(\frac{84329}{6000}-\frac{26}{15}\pi^2\Big)C_F^2\Big]T_g(2)T_q(1)\\
&+\Big[\frac{2327}{180}C_AC_F+\Big(\frac{10189}{250}-\frac{64}{15}\pi^2\Big)C_F^2\Big]T_g(1)T_q(2)\\
&+\sum_i\Big[-\frac{1448}{450}C_FT_F\Big]T_q^{(2)}\big(T_{Q_i}(1)+T_{\bar{Q}_i}(1)\big)\\
&+\sum_i\Big[-\frac{9557}{9000}C_FT_F\Big]T_q(1)\big(T_{Q_i}(2)+T_{\bar{Q}_i}(2)\big)\\
&+\sum_i\Big[-\frac{59}{1000}C_FT_F\Big]\big(T_{Q_i}(2)T_{\bar{Q}_i}(1)+T_{Q_i}(1)T_{\bar{Q}_i}(2)\big)\\
&+\Big[\Big(-\frac{353801}{3600}+\frac{77}{6}\pi^2-24\zeta_3\Big)C_AC_F+\Big(\frac{353801}{1800}-\frac{77}{3}\pi^2+48\zeta_3\Big)C_F^2\\
&\quad-\frac{12839}{3000}C_FT_F\Big]T_q(2)T_q(1)\\
&+\Big[\Big(-\frac{369503}{3000}+\frac{77}{5}\pi^2-24\zeta_3\Big)C_AC_F+\Big(\frac{369503}{1500}-\frac{154}{5}\pi^2+48\zeta_3\Big)C_F^2\\
&\quad-\frac{1261}{1125}C_FT_F\Big]T_{\bar{q}}(2)T_q(1)
\end{aligned}
$$

$$
\begin{aligned}
&+\Big[\Big(\frac{649211}{6000}-\frac{139}{10}\pi^2+24\zeta_3\Big)C_AC_F+\Big(-\frac{649211}{3000}+\frac{139}{5}\pi^2-48\zeta_3\Big)C_F^2\\
&\quad-\frac{29491}{9000}C_FT_F\Big]T_{\bar q}(1)T_q(2)\\
&+\Big[\Big(\frac{202651}{1800}-\frac{43}{3}\pi^2+24\zeta_3\Big)C_AC_F+\Big(-\frac{202651}{900}+\frac{86}{3}\pi^2-48\zeta_3\Big)C_F^2\\
&\quad-\frac{137}{500}C_FT_F\Big]T_q(1)T_q(1)T_{\bar q}(1)\\
&+\Big[\Big(\frac{97883}{9000}-\frac{7}{3}\pi^2\Big)C_AC_F-\frac{181}{150}C_F^2\Big]T_q(1)T_g(1)T_g(1)\\
&+\sum_i\Big[-\frac{137}{500}C_FT_F\Big]T_q(1)T_{Q_i}(1)T_{\bar Q_i}(1).
\end{aligned}
$$

The expressions for anti-quarks can be obtained by charge conjugation. Here, $\gamma_{ij}^{(1)}(n)$ are the NLO moments of the timelike splitting function (given in appendix 4.C), and $Q\neq q$ is used to denote the distinct quark flavors. The expressions for anti-quarks can be obtained by charge conjugation.

As described in section 4.2.1, when written in terms of standard moments these equations are highly redundant, due to the presence of the underlying shift symmetry. When we include all quark flavors we can construct a first moment invariant for each flavor, $\Delta_i=T_{q_i}(1)-T_g(1)$. The evolution of the first three central gluon moments can be written as

$$
\begin{aligned}
\frac{\mathrm{d}\,\sigma_g(2)}{\mathrm{d}\ln\mu^2}&=-\gamma_{gg}^{(1)}(3)\sigma_g(2)+\sum_i\Big\{-\gamma_{qg}^{(1)}(3)(\sigma_{q_i}(2)+\sigma_{\bar q_i}(2)+\Delta_{q_i}^2+\Delta_{\bar q_i}^2)\\
&\quad+T_F\Big[\Big(\frac{12413}{1350}-\frac{52}{45}\pi^2\Big)C_A+\frac{1528}{225}C_F-\frac{16}{25}n_fT_F\Big]\Delta_{q_i}\Delta_{\bar q_i}\Big\},
\end{aligned}
\tag{4.80}
$$

$$
\begin{aligned}
\frac{\mathrm{d}\,\sigma_g(3)}{\mathrm{d}\ln\mu^2}&=-\gamma_{gg}^{(1)}(4)\sigma_g(3)\\
&\quad+\sum_i\Big\{-\gamma_{qg}^{(1)}(4)(\sigma_{q_i}(3)+\sigma_{\bar q_i}(3)+3\sigma_{q_i}(2)\Delta_{q_i}+3\sigma_{\bar q_i}(2)\Delta_{\bar q_i}+\Delta_{q_i}^3+\Delta_{\bar q_i}^3)\\
&\qquad+T_F\Big[\Big(-\frac{638}{45}+\frac{8}{3}\pi^2\Big)C_A-\frac{3803}{250}C_F\Big]\sigma_g(2)(\Delta_{q_i}+\Delta_{\bar q_i})\\
&\qquad+T_F\Big[\Big(\frac{5321}{3000}-\frac{2}{5}\pi^2\Big)C_A+\frac{1523}{240}C_F-\frac{12}{25}n_fT_F\Big]\\
&\qquad\quad\times(\sigma_{q_i}(2)\Delta_{\bar q_i}+\sigma_{\bar q_i}(2)\Delta_{q_i}+\Delta_{q_i}^2\Delta_{\bar q_i}+\Delta_{\bar q_i}^2\Delta_{q_i})\Big\}.
\end{aligned}
\tag{4.81}
$$

This form emphasizes the large redundancy present in the expressions given in equation (4.74). We emphasize that while it is true that the mixing into $\sigma_{q_i}(2)$ and $\sigma_{q_i}(3)$ is governed to all loop order by $\gamma_{qg}^{(1)}$, the fact that the mixing

into the products $\sigma_{q_i}(2)\Delta_{q_i}$, $\Delta^2_{q_i}$, and $\Delta^3_{q_i}$ are also governed by these same anomalous dimensions is a coincidence at this order in perturbation theory.

Finally, for the evolution of the quark track functions in terms of shift-invariant central moments, we have

$$\begin{aligned}
\frac{\mathrm{d}\,\sigma_{q_i}(2)}{\mathrm{d}\ln\mu^2} =& -\gamma^{(1)}_{gq}(3)\,\sigma_g(2) - \gamma^{(1)}_{qq}(3)\left(\sigma_{q_i}(2)+\Delta^2_{q_i}\right) \\
&- \sum_j \frac{17}{100} C_F T_F \Delta_{Q_j}\Delta_{\bar{Q}_j} - \sum_j \gamma^{(1)}_{Qq}(3)\left(\sigma_{Q_j}(2)+\sigma_{\bar{Q}_j}(2)+\Delta^2_{Q_j}+\Delta^2_{\bar{Q}_j}\right) \\
&- \gamma^{(1)}_{\bar{q}q}\left(\sigma_{\bar{q}_i}(2)+\Delta^2_{\bar{q}_i}-2\Delta_{q_i}\Delta_{\bar{q}_i}\right) + \frac{97}{54} C_F T_F \sum_j \Delta_{q_i}\left(\Delta_{Q_j}+\Delta_{\bar{Q}_j}\right) \\
&+ \left[\frac{2957}{108} C_A C_F + \left(\frac{2323}{54} - \frac{64\pi^2}{9}\right) C_F^2 + \left(\frac{97}{54} - \frac{256}{27} n_f\right) C_F T_F\right] \Delta^2_{q_i}
\end{aligned} \tag{4.82}$$

$$\begin{aligned}
\frac{\mathrm{d}\,\sigma_{q_i}(3)}{\mathrm{d}\ln\mu^2} =& -\gamma^{(1)}_{gq}(4)\left(\sigma_g(3) - 2\sigma_g(2)\Delta_{q_i}\right) \\
&- \gamma^{(1)}_{qq}(4)\left(\sigma_{q_i}(3) - 2\sigma_g(2)\Delta_{q_i} + 3\sigma_q(2)\Delta_{q_i} - 2\Delta^3_{q_i}\right) \\
&- \gamma^{(1)}_{\bar{q}q}(4)\left(\sigma_{\bar{q}_i}(3) + \sigma_g(2)\Delta_{q_i} + 3\sigma_{\bar{q}_i}(2)\Delta_{\bar{q}_i} + 3\sigma_{q_i}(2)\Delta_{\bar{q}_i} - 3\sigma_{\bar{q}_i}(2)\Delta_{q_i}\right. \\
&\qquad \left. + 3\Delta^2_{q_i}\Delta_{\bar{q}_i} - 3\Delta_{q_i}\Delta^2_{\bar{q}_i} + \Delta^3_{\bar{q}_i}\right) \\
&- \gamma^{(1)}_{Qq}(4) \sum_{j\neq i} \left(\sigma_{Q_j}(3) + \sigma_{\bar{Q}_j}(3) - \sigma_g(2)\Delta_{q_i} + 3\sigma_{Q_j}(2)\Delta_{Q_j}\right. \\
&\qquad + 3\sigma_{\bar{Q}_j}(2)\Delta_{\bar{Q}_j} - 3(\sigma_{Q_j}(2) + \sigma_{\bar{Q}_j}(2))\Delta_{q_i} \\
&\qquad \left. + \Delta^3_{Q_j} + \Delta^3_{\bar{Q}_j} - 3\Delta_{q_i}(\Delta^2_{Q_j} + \Delta^2_{\bar{Q}_j} - \Delta_{Q_j}\Delta_{\bar{Q}_j})\right) \\
&- \frac{59}{1000} C_F T_F \sum_j \left(\sigma_{Q_j}(2)\Delta_{\bar{Q}_j} + \sigma_{\bar{Q}_j}(2)\Delta_{Q_j} - (\sigma_{\bar{Q}_j}(2) + \sigma_{Q_j}(2))\Delta_{q_i}\right. \\
&\qquad \left. + \Delta^2_{Q_j}\Delta_{\bar{Q}_j} + \Delta_{Q_j}\Delta^2_{\bar{Q}_j} - \Delta_{q_i}(\Delta^2_{\bar{Q}_j} + \Delta^2_{Q_j}) + \Delta_{Q_j}\Delta_{\bar{Q}_j}\right) \\
&+ \frac{292}{75} C_F T_F \sum_j \left(\sigma_{q_i}(2)(\Delta_{Q_j}+\Delta_{\bar{Q}_j}) + \Delta^2_{q_i}(\Delta_{Q_j}+\Delta_{\bar{Q}_j})\right. \\
&\qquad \left. - \Delta_{q_i}\Delta_{Q_j}\Delta_{\bar{Q}_j}\right) \\
&- \frac{97}{18} C_F T_F \sum_j \left(\Delta^2_{q_i}(\Delta_{Q_j} + \Delta_{\bar{Q}_j}) - \Delta_{q_i}\Delta_{Q_j}\Delta_{\bar{Q}_j}\right) \\
&- \frac{12929}{9000}(n_f - 1) C_F T_F\, \sigma_g(2)\Delta_{q_i} \\
&+ \left[\frac{29}{300} C_A C_F - \frac{29}{150} C_F^2 + \frac{5797}{1125} C_F T_F\right] \sigma_{q_i}(2)\Delta_{\bar{q}_i}
\end{aligned} \tag{4.83}$$

$$
\begin{aligned}
&+\left[\left(-\frac{12929}{9000}C_F+\frac{4648}{225}C_F n_f\right)T_F+\left(\frac{81443}{3000}-\frac{23}{15}\pi^2+24\zeta_3\right)C_F^2\right.\\
&\quad\left.+\left(-\frac{2163833}{18000}+\frac{247}{30}\pi^2-12\zeta_3\right)C_A C_F\right](\sigma_g(2)\Delta_{q_i}+\Delta_{q_i}^3)\\
&+\left[\frac{45253}{450}C_A C_F+C_F^2\left(\frac{662327}{3600}-\frac{82}{3}\pi^2\right)\right.\\
&\quad\left.+\left(\frac{23719}{4500}C_F-\frac{671}{18}C_F n_f\right)T_F\right]\sigma_q(2)\Delta_q.
\end{aligned}
$$

This case is notationally more cumbersome than for the gluon evolution due to the contributions from different quark flavors. As with equation (4.80), this results exhibits a number of coincidences in the evolution, that will not persist beyond NLO.

5

Conclusions

The research described in this thesis contributes to the ongoing improvement in precision for predictions at particle colliders. It uses Soft-Collinear effective theory (SCET), which provides a framework to derive factorization theorems for observables, separating soft and collinear radiation effects from the hard interaction and accounting for their dominant effects at higher orders in the coupling.

Final-state collinear radiation manifests itself by the existence of jets, which are collimated sprays of particles. In SCET the contribution of collinear final-state radiation is described by jet functions. These objects are widely used and the automation of jet function calculations is a crucial step forward. In chapter 2, geometric subtraction is used to isolate the soft and collinear singularities that complicate the direct evaluation of the corresponding integrals. Defining simple counterterms to subtract the soft and collinear poles from the calculation allows us to define the finite subtracted jet function. This object can be evaluated numerically, whereas the divergences are known analytically. Together they describe the complete jet function. A MATHEMATICA implementation called GOJET is readily available to calculate one-loop jet functions for IR-safe observables. Few two-loop jet functions are known, and extending GOJET to this order would allow for direct increase in accuracy for resummed predictions of many observables. The difficulties that need to be overcome arise from the order of subtraction of the collinear and soft singularities, but also in the parametrization of the observable constraints in these limits (as they will no longer have a simple power law behaviour).

In chapter 3 we studied the azimuthal decorrelation between a vector boson and a jet in pp collisions. Factorization for processes with jets at the LHC generally involve non-global logarithms, that arise from the varying sensitivity to soft radiation in different regions of phase space. We employ the recoil-free winner-takes-all jet algorithm to remove the effects of soft recoil on the jet axis, eliminating the non-global logarithms: the soft radiation does not perceive the

jet boundary and so there is no need to differentiate between soft emissions in- or outside the jet. Experimentally, the recoil-free jet definition reduces the effects of contamination inside the jet, especially from the underlying event. The predictions for azimuthal decorrelation include contributions from linearly-polarized gluons in the initial and final state. We show that these polarizations are necessary by comparing to MCFM NLO predictions. Using the methods of SCET we then obtain results for the differential cross section in the back-to-back limit at NNLL accuracy. The robustness of this observable makes it an excellent candidate to study the dynamics of the QCD medium produced in heavy-ion collisions, as the WTA axis reduces the effect of underlying events. Furthermore, the accuracy of this calculation can be extended to $\mathrm{N^3LL}$ once the one-loop linearly polarized hard function and the two-loop linearly porized jet function are calculated.

As the precision of theoretical predictions is rapidly increasing, it is important to reduce the uncertainties in data analysis as well. To exploit the superior angular resolution of the tracking system (compared to the calorimeter) one must switch to observables defined on charged particles only. However, these track-based observables are collinear unsafe. In chapter 4 we use non-perturbative track functions to absorb the uncancelled IR divergences, much like parton distribution functions do for initial-state radiation. Focussing on weighted cross sections, the inclusion of tracks only requires moments of track functions. The evolution for moments of track functions at order α_s^2 is fixed by symmetry considerations up to the sixth moment and we validated these results by direct calculation. We explicitly showed that track functions can be applied by obtaining predictions for the EEC and the azimuthal angle on tracks, allowing for more accurate experimental extractions. These examples imply the utilization of track functions for other known observables, to reduce the uncertainty of experimental analysis. Until now, track functions were explicitly used to describe the energy fraction of charged particles. However, their applications can be extended to a wide variety of new non-perturbative measurements to include only final state particles with certain quantum numbers, as long as there exists a valid factorization theorem for the case where all final state particles are included. For example, measurements on flavored (e.g. strange) hadrons allow flavor tagging for nucleon structure studies. This indicates the bright future of track functions at particle colliders.

A

Fourier transform

The Fourier transform and its inverse can be used to switch between momentum and impact parameter space. In this thesis the following conventions are used

$$F(x) = \int d^d k \tilde{F}(k) e^{-ik\cdot x},$$
$$\tilde{F}(x) = \int \frac{d^d x}{(2\pi)^d} F(x) e^{ik\cdot x}, \tag{A.1}$$

such that

$$\delta^d(x) = \int \frac{d^d k}{(2\pi)^d} e^{-ik\cdot x},$$
$$\delta^d(k) = \int \frac{d^d x}{(2\pi)^d} e^{ik\cdot x}. \tag{A.2}$$

B

Calculation of jet functions

This section provides the techniques to evaluate the jet function given in equation (1.167). For convenience we summarize the definition for the jet function for both quark and gluon initiated jets:

$$J_q(\omega_J, s, \mu) \tag{B.1}$$
$$= 2(2\pi)^{d-1}\mathrm{Tr}\left[\langle 0|\,\frac{\bar{n}\!\!\!/}{4N_c}\chi_n(0)\delta(\omega_J-\bar{\mathcal{P}}_n)\delta^{(d-2)}(\mathcal{P}_n^\perp)\delta_M\bar{\chi}_n(0)|0\rangle\right],$$
$$\mathscr{J}_g^{\mu\nu}(\omega_J, s, \mu) \tag{B.2}$$
$$= \frac{2(2\pi)^{d-1}}{N_c^2-1}\omega_J\langle 0|\mathcal{B}_{n\perp}^{a\mu}(0)\delta(p_\perp\delta(\omega_J-\bar{\mathcal{P}}_n)\delta^{(d-2)}(\mathcal{P}_n^\perp)\delta_M\mathcal{B}_{n\perp}^{a\nu}(0)|0\rangle,$$

where $\omega_J = \bar{n}\cdot p_J$. The recombination scheme dependence which determines how final state partons are clustered is implicit in the measurement δ_M. The matrix elements above can be evaluated at order α_s to yield an integration over energy fraction x and invariant mass s, which is the form we employ in chapter 2.

In this appendix we will explicitly show how to calculate the jet function, starting from the matrix definition above. The jet function can be calculated order by order

$$J_i = J_i^{(0)} + \frac{\alpha_s}{4\pi}J_i^{(1)} + \dots. \tag{B.3}$$

At leading order the parton does not radiate. Indeed, the tree level diagram yields

$$J_i^{(0)} = \delta_{M,0}. \tag{B.4}$$

where $\delta_{M,0}$ is the measurement on a jet of a single parton. To obtain the jet function at $\mathcal{O}(\alpha_s)$ we have to evaluate all SCET diagrams that contribute at this order. The three SCET diagrams that lead to the quark jet function are

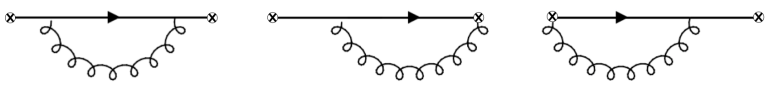

where all the lines are collinear. The crosses on the end of the quark line indicate the SCET jet fields χ_n, which means that gluon fields that exit from these crosses are in fact attached to the Wilson line W_n. Evaluating these diagrams requires summing over all possible cuts. Due to scaleless loop integrals, the only non-vanishing contributions are the ones where we cut through the loop. The SCET feynman rule we need for a gluon taken from a Wilson line, which becomes apparent upon expanding in g, is given by

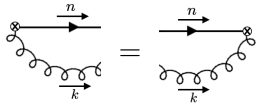

$$= -g\frac{\bar{n}^\mu t^a}{\bar{n}\cdot k}. \tag{B.5}$$

We start by evaluating the diagram on the left. The cut through the loop introduces the integration over final (on-shell) states and the contraction with external polarizations and/or spinors. Furthermore we are required to sum over all spin and color indices.

$$A = 2(2\pi)^{(d-1)}\mathrm{tr}\left[\frac{\bar{n}\!\!\!/}{4N_c}\right. \tag{B.6}$$

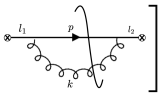

$$\left.\right],$$

$$\begin{aligned}
&= -2g^2(2\pi)^{(d-1)}\sum_{s,s',\lambda,\lambda',c}\int\frac{\mathrm{d}^dk}{(2\pi)^{d-1}}\delta(k^2)\int\frac{\mathrm{d}^dp}{(2\pi)^{d-1}}\delta(p^2)\\
&\quad\times\int\mathrm{d}^dl_1\delta^d(l_1-k-p)\int\mathrm{d}^dl_2\,\delta^d(l_2-k-p)\delta(Q-l_1^-)\delta^{(d-2)}(l_{1,\perp})\\
&\quad\times\mathrm{tr}[t^at^a]\mathrm{tr}\left[\frac{\bar{n}\!\!\!/}{4N_c}\frac{l\!\!\!/_2}{l_2^2}\gamma^\mu\bar{v}^s(p)v^{s'}(p)\gamma_\nu\frac{l\!\!\!/_1}{l_1^2}\right]\varepsilon_\lambda^\mu(k)\varepsilon_{\lambda'}^{\nu\,*}(k)\delta_M.
\end{aligned}$$

The trace over generators simply gives a factor N_c, the sum over color yields a factor C_F, the sum over spins can evaluated using the completeness relations for spinors and polarization vectors. The integral over k is evaluated by replacing $k = l_1 - p$ and the integral over l_2 then sets $l_2 = l_1$. This leads to

$$\begin{aligned}
A = &-2g^2\int\frac{\mathrm{d}^dp}{(2\pi)^{d-1}}\delta((l_1-p)^2)\delta(p^2)\int\mathrm{d}^dl_1\delta(Q-l_1^-)\delta^{(d-2)}(l_{1,\perp})\\
&\times\frac{1}{l_1^4}\mathrm{tr}\left[\frac{\bar{n}\!\!\!/}{4}l\!\!\!/_1\gamma^\mu p\!\!\!/\gamma_\mu l\!\!\!/_1\right]\delta_M,
\end{aligned}$$

where we have used the momentum conserving delta functions to get rid of the integration over l_2 and k. We can evaluate the trace:

$$\begin{aligned}\mathrm{tr}\left[\frac{\not{\bar{n}}}{4}\not{l}_1\gamma^\mu\not{p}\gamma_\mu\not{l}_1\right] &= -\frac{d-2}{4}\mathrm{tr}\left[\not{\bar{n}}\not{l}_1\not{p}\not{l}_1\right] = -(d-2)(2l_1^- p\cdot l_1 - p^- l_1^2),\\ &= -(d-2)(l_1^-)^2 p^+, \end{aligned} \tag{B.7}$$

where we already used that the perpendicular component of l_1 is zero to avoid unnecessary terms. We now find

$$\begin{aligned}A =& 2(d-2)g^2 C_F \int \frac{\mathrm{d}^d p}{(2\pi)^{d-1}}\delta(p^2)\int\frac{\mathrm{d}^d l_1}{l_1^4}\delta((l_1-p)^2)\delta(Q-l_1^-)\delta^{(d-2)}(l_{1,\perp})\delta_M\\ &\times (l_1^-)^2 p^+. \end{aligned} \tag{B.8}$$

For the two remaining integrals we wish to switch to light-cone coordinates. We therefore rewrite the phase space measure as

$$\mathrm{d}^d p = \frac{1}{2}\mathrm{d}p^+\mathrm{d}p^-\mathrm{d}^{d-2}p_\perp, \tag{B.9}$$

and similarly for l_1. The delta functions then fix l_1^- and $l_{1,\perp}$ and the resulting expression reads.

$$A = 2(d-2)g^2 C_F \int\frac{\mathrm{d}p^+\mathrm{d}p^-}{(4\pi)}\int\frac{\mathrm{d}^{d-2}p_\perp}{(2\pi)^{d-2}}\delta(p^+p^- - p_\perp^2)\int\frac{\mathrm{d}l_1^+}{2}\delta((l_1-p)^2)\frac{p^+}{l^+}\delta_M. \tag{B.10}$$

Integration over p^+ and l_1^+ now yields

$$A = \alpha_s C_F(d-2)\int\mathrm{d}p^-\int\frac{\mathrm{d}^{d-2}p_\perp}{(2\pi)^{d-2}}\frac{1}{|p_\perp|^2}\frac{1}{(Q-p^-)(1+\frac{p^-}{Q-p^-})^2}\,\delta_M. \tag{B.11}$$

To proceed, we change variables $p^- = xQ$, where x represents the momentum fraction of the quark after the splitting

$$A = \alpha_s C_F(d-2)\int\mathrm{d}x\int\frac{\mathrm{d}^{d-2}p_\perp}{(2\pi)^{d-2}}\frac{1}{|p_\perp|^2}(1-x)\,\delta_M. \tag{B.12}$$

At this point it is useful to evaluate the contributions from the other two diagrams in the same fashion, before we continue. We find that both diagrams

give the same contribution due to cyclicity of the trace.

$$B+C = 2(2\pi)^{d-1}\mathrm{tr}\left[\frac{\not{n}}{4N_c}\left(\quad +\quad\right)\right], \tag{B.13}$$

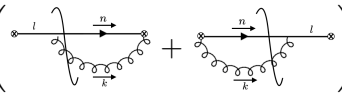

$$\begin{aligned}
&= 4g^2C_F(2\pi)^{d-1}\int\frac{\mathrm{d}^dk}{(2\pi)^{d-1}}\delta(k^2)\int\frac{\mathrm{d}^dp}{(2\pi)^{d-1}}\delta(p^2)\int\mathrm{d}^dl\,\delta^d(l-k-p)\\
&\quad\times\delta(Q-l^-)\delta^{(d-2)}(l_\perp)\delta_M\mathrm{tr}\left[\frac{\not{n}}{4}\frac{\not{l}}{l^2}\frac{\not{n}}{k^-}\not{p}\right],
\end{aligned}$$

where we have already evaluated the sum over final state configurations. The trace can be evaluated to

$$\mathrm{tr}\left[\frac{\not{n}}{4}\frac{\not{l}}{l^2}\frac{\not{n}}{k^-}\not{p}\right] = \frac{2l^-p^-}{l^2k^-} = \frac{2p^-}{l^+k^-}. \tag{B.14}$$

Performing the integration over p sets all components of p to $l-k$. and we find

$$\begin{aligned}
&B+C\\
&= 4g^2C_F\int\frac{\mathrm{d}^dk}{(2\pi)^{d-1}}\int\mathrm{d}^dl\,\delta(k^2)\delta((l-k)^2)\delta(Q-l^-)\delta^{(d-2)}(l_\perp)\frac{2(l^--k^-)}{l^+k^-}\delta_M.
\end{aligned} \tag{B.15}$$

Switching again to lightcone coordinates (which yields a total jacobian of $\frac{1}{4}$) we continue with

$$\begin{aligned}
&B+C\\
&= 4g^2C_F\int\frac{\mathrm{d}k^+\mathrm{d}k^-}{4\pi}\int\frac{\mathrm{d}^{d-2}k_\perp}{(2\pi)^{d-2}}\int\frac{\mathrm{d}l^+}{2}\,\delta(k^+k^- - k_\perp^2)\delta((l-k)^2)\frac{2(Q-k^-)}{l^+k^-}\delta_M,\\
&= 2g^2C_F\int\frac{\mathrm{d}k^-}{4\pi}\int\frac{\mathrm{d}^{d-2}k_\perp}{(2\pi)^{d-2}}\int\mathrm{d}l^+\,\delta((Q-k^-)(l^+-k^+) - |k_\perp|^2)\frac{2(Q-k^-)}{l^+(k^-)^2}\delta_M,\\
&= 2\alpha_sC_F\int\mathrm{d}k^-\int\frac{\mathrm{d}^{d-2}k_\perp}{(2\pi)^{d-2}}\frac{1}{|k_\perp|^2}\frac{2(Q-k^-)}{Qk^-}\delta_M.
\end{aligned} \tag{B.16}$$

Making the replacement $k^- = Q(1-x)$, as k is the momentum of the gluon which carries a fraction $1-x$ of the total jet energy, gives

$$B+C = \alpha_sC_F\int\mathrm{d}x\int\frac{\mathrm{d}^{d-2}k_\perp}{(2\pi)^{d-2}}\frac{1}{|k_\perp|^2}\frac{4x}{1-x}\delta_M. \tag{B.17}$$

Let us now merge the contributions from the three diagrams before we proceed. Adding equation (B.12) and (B.17) we get

$$\frac{4x}{1-x} + (d-2)(1-x) = 2\left(\frac{1+x^2}{1-x} - \epsilon(1-x)\right) = 2P_q(x), \tag{B.18}$$

where we have used $d = 4-2\epsilon$, and find

$$J_q(\{M\},\mu) = 2\alpha_s(\mu)\bar{\mu}^{2\epsilon}C_F \int \mathrm{d}x \int \frac{\mathrm{d}^{d-2}k_\perp}{(2\pi)^{d-2}} \frac{1}{|k_\perp|^2} P_q(x)\delta_M, \tag{B.19}$$

where we have renormalized the expression using the $\overline{\mathrm{MS}}$ scheme by changing $\alpha_s \to \alpha_s(\mu)\tilde{\mu}^{2\epsilon}$[1], with $\tilde{\mu}^{2\epsilon} = \left(\mu^2\gamma_E/4\pi\right)^\epsilon$. Note that the strong coupling constant now depends on μ, i.e. $\alpha_s(\mu)$. This result will be used as the starting point for jet calculation in chapter 3. In chapter 2 we specifically constrain ourselves to scalar quantities, for which the constraint δ_M can be written as $\delta(s-s_{\mathrm{obs}})$. In this case can simplify the expression even more. The integration over $d-2$ components of $k_\perp$ is split into an angular integration over $d-3$ angles $\theta_1,\ldots,\theta_{d-3}$ and an integration over the radius $|k_\perp|$.

$$\begin{aligned}
\int \frac{\mathrm{d}^{d-2}k_\perp}{(2\pi)^{d-2}} &= \frac{1}{(2\pi)^{d-2}} \int \mathrm{d}|k_\perp||k_\perp|^{d-3} \int_0^{2\pi} d\theta_1 \cdots \int_0^{\pi} \mathrm{d}\theta_{d-3} \sin^{d-4}(\theta_{d-3}), \\
&= \frac{1}{(2\pi)^{2-2\epsilon}} \int \mathrm{d}|k_\perp||k_\perp|^{1-2\epsilon} (2\pi) \frac{(\sqrt{\pi})^{d-4}}{\Gamma(1+\frac{1}{2}(d-4))}, \\
&= \frac{1}{(2\pi)(4\pi)^{-\epsilon}\,\Gamma(1-\epsilon)} \int \mathrm{d}|k_\perp||k_\perp|^{1-2\epsilon},
\end{aligned} \tag{B.20}$$

using again $d = 4-2\epsilon$. The collinear limit of a two particle final state gives the invariant mass $s = |k_\perp|^2 x(1-x)$. Switching to the integration over s thus gives

$$\begin{aligned}
J_q(\{M\},\mu) &= \frac{\alpha_s\tilde{\mu}^{2\epsilon}C_F}{(2\pi)(4\pi)^{-\epsilon}\,\Gamma(1-\epsilon)} \int \frac{\mathrm{d}x}{(1-x)^\epsilon x^\epsilon} \int \frac{\mathrm{d}s}{s^{1+\epsilon}} P_q(x)\delta(s-\hat{s}_{\mathrm{obs}}(M)), \\
&= \left(\frac{\alpha_s}{4\pi}\right) 2C_F \frac{\left(\mu^2\gamma_E\right)^\epsilon}{\Gamma(1-\epsilon)} \int \frac{\mathrm{d}x}{(1-x)^\epsilon x^\epsilon} \int \frac{\mathrm{d}s}{s^{1+\epsilon}} P_q(x)\delta(s-\hat{s}_{\mathrm{obs}}(M)),
\end{aligned} \tag{B.21}$$

where we inserted $\tilde{\mu}^{2\epsilon} = \left(\mu^2\gamma_E/4\pi\right)^\epsilon$. As a final step we reintroduce the ϕ dependence through

$$\int \mathrm{d}\phi \sin(\phi)^{-2\epsilon} = \frac{\Gamma(\frac{1}{2}-\epsilon)}{\Gamma(1-\epsilon)}\sqrt{\pi}, \tag{B.22}$$

[1] This replacement is valid at $\mathcal{O}(\alpha_s)$. At higher orders one should use the all order replacement, $alpha_s \to Z_\alpha\alpha_s(\mu)\tilde{\mu}^{2\epsilon}$. The renormalization constant Z_α is given in appendix 1.4.

as some observables impose constraints that break azimuthal symmetry.

$$J_q(\{M\},\mu) = \Big(\frac{\alpha_s}{2\pi}\Big)\frac{4C_F\left(\mu^2\gamma_E\right)^\epsilon}{\Gamma(\frac{1}{2}-\epsilon)\sqrt{\pi}}\int_0^\pi \mathrm{d}\phi\int_0^1\mathrm{d}x\int_0^\infty \mathrm{d}s \\ \times \frac{P_q(x)\sin(\phi)^{-2\epsilon}}{s^{1+\epsilon}(1-x)^\epsilon x^\epsilon}\delta(s-\hat{s}_{\mathrm{obs}}(M)). \tag{B.23}$$

This is the jet function used in chapter 2.

The gluon jet function can be obtained by following similar steps as outlined above. The Lorentz structure of the gluon jet function, as it appears in (B.2), should be maintained. After calculating the contributing Feynamn diagrams we find that the complete gluon jet function is described by

$$J_g^{\mu\nu}(\{M\},\mu) = 4\alpha_s(\mu)\tilde{\mu}^{2\epsilon}\int \mathrm{d}x\int\frac{\mathrm{d}^{d-2}k_\perp}{(2\pi)^{d-2}}\frac{1}{|k_\perp|^2}P_g^{\mu\nu}(x)\delta_M \tag{B.24}$$

where

$$P_g^{\mu\nu}(x,k_\perp) = \hat{P}_{gg}^{\mu\nu}(x,k_T;\epsilon) + 2n_f\hat{P}_{q\bar{q}}^{\mu\nu}(x,k_\perp;\epsilon) \tag{B.25}$$

with [223]

$$\hat{P}_{gg}^{\mu\nu}(x,k_\perp;\epsilon) = 2C_A\left[-g^{\mu\nu}\Big(\frac{x}{1-x}+\frac{1-x}{x}\Big) - 2(1-\epsilon)x(1-x)\frac{k_\perp^\mu k_\perp^\nu}{\vec{k}_\perp^2}\right], \\ \hat{P}_{q\bar{q}}^{\mu\nu}(x,k_\perp;\epsilon) = T_F\left[-g^{\mu\nu}+4x(1-x)\frac{k_\perp^\mu k_\perp^\nu}{\vec{k}_\perp^2}\right] \tag{B.26}$$

When the measurement δ_M does not depend on the transverse momentum there is only one Lorentz structure that can describe the free indices, namely $g_\perp^{\mu\nu}$. To obtain the contribution we use the$d$-dimensional average over the polarizations of the gluon, which is obtained using the transverse projector:

$$P_\perp^{\mu\nu} = -\frac{1}{d-2}g_\perp^{\mu\nu} = -\frac{1}{d-2}\left[g^{\mu\nu}-\frac{1}{2}(n_J^\mu\bar{n}_J^\nu+n_J^\nu\bar{n}_J^\mu)\right]. \tag{B.27}$$

Averaging over polarizations then yields

$$J_g(\{M\},\mu) = 4\alpha_s(\mu)\tilde{\mu}^{2\epsilon}\int \mathrm{d}x\int\frac{\mathrm{d}^{d-2}k_\perp}{(2\pi)^{d-2}}\frac{1}{|k_\perp|^2}P_g(x)\delta_M \tag{B.28}$$

with

$$P_g(x) = 2C_A\left(\frac{x}{1-x}+\frac{1-x}{x}+x(1-x)\right)+2T_Fn_f\left(1-\frac{2}{1-\epsilon}(1-x)x\right). \tag{B.29}$$

If the measurement does however involve (one or more components of) the transverse momentum there is an extra contribution, resulting from the linear polarization. For this reason it is convenient to Fourier transform the gluon jet function to impact parameter space

$$J_g^{\mu\nu}(b_\perp,\mu) = \int \mathrm{d}^{d-2}p_\perp J_g^{\mu\nu}(\omega,p_\perp,\mu)e^{-\mathrm{i}p_\perp\cdot b_\perp} \tag{B.30}$$

and write it in terms of polarizations as

$$J_g^{\mu\nu}(b_\perp,\mu) = (d-2)P_L^{\mu\nu}J_g^L(b_\perp,\mu) + (d-3)(d-2)P_\perp^{\mu\nu}J_g^\perp(b_\perp,\mu), \tag{B.31}$$

where

$$P_L^{\mu\nu} = \frac{1}{(d-2)(d-3)}\left(g_\perp^{\mu\nu} - \frac{b_\perp^\mu b_\perp^\nu}{|b_\perp|^2}(d-2)\right). \tag{B.32}$$

The projectors are defined to be orthogonal, i.e.

$$P_\perp^{\mu\nu}P_{L\mu\nu} = 0, \tag{B.33}$$

and are normalized such that

$$P_\perp^{\mu\nu}P_{\perp\mu\nu} = \frac{1}{d-2} \qquad \text{and} \qquad P_L^{\mu\nu}P_{L\mu\nu} = 1 = \frac{1}{(d-2)(d-3)}. \tag{B.34}$$

The projection operators can be used to extract the contribution of the two Lorentz structures in the following way

$$\begin{aligned} J_g^\perp &= P_\perp^{\mu\nu}J_{g\mu\nu} = 1 + \mathcal{O}(\alpha_s), \\ J_g^L &= P_L^{\mu\nu}J_{g\mu\nu} = \mathcal{O}(\alpha_s). \end{aligned} \tag{B.35}$$

The linear polarization exists because the collinear gluon splitting is intrinsically polarized. In most cases however the linear polarization is absent, as it contributes at a higher accuracy. The linear polarized jet function starts at $\mathcal{O}(\alpha_s)$, as shown in equation (B.35), since a non-zero transverse momentum is needed to have a non-zero contribution from linear polarization. At leading order there is no transverse momentum and hence the linear contribution vanishes. In chapter 3 we calculate the azimuthal angle, which is closely related to the transverse momentum. Here the linear gluon polarization will in fact contribute at the level of accuracy we are working (in both jet and beam). It is useful to already perform the projections to obtain the contributions. The

transverse contribution was already performed in momentum space, see equation (B.28). To perform the projection onto the linear contributions, we first investigate the effect of the polarization on a general structure

$$P_L^{\mu\nu}\left(Ag^{\mu\nu}+B\frac{k_\perp^\mu k_\perp^\nu}{|k_\perp|^2}\right) = \frac{1}{(d-2)(d-3)}\left(g_\perp^{\mu\nu}-\frac{b_\perp^\mu b_\perp^\nu}{|b_\perp|^2}(d-2)\right)\left(Ag^{\mu\nu}+B\frac{k_\perp^\mu k_\perp^\nu}{|k_\perp|^2}\right),$$
$$= \frac{B}{(d-2)(d-3)}\left(1-(d-2)\frac{(b_\perp\cdot k_\perp)^2}{|k_\perp|^2|b_\perp|^2}\right). \tag{B.36}$$

Projecting out the linear contributions of the gluon splitting function in equation (B.25) then yields

$$J_g^L(b_\perp,\mu) = 4\,\alpha_s(\mu)\tilde{\mu}^{2\epsilon}\frac{2(4T_F n_f-(d-2)C_A)}{(d-2)(d-3)}\int \mathrm{d}x\, x(1-x) \tag{B.37}$$
$$\times\int\frac{\mathrm{d}^{d-2}k_\perp}{(2\pi)^{d-2}}\left(1-(d-2)\frac{(b_\perp\cdot k_\perp)^2}{|k_\perp|^2|b_\perp|^2}\right)\int \mathrm{d}^{d-2}p_\perp\delta_M(p_\perp)e^{-\mathrm{i}p_\perp\cdot b_\perp}.$$

A concrete example that includes linear gluon polarizations is discussed in chapter 3.

Summary

The research described in this thesis contributes to progress made in the field of theoretical particle physics. This is an area of physics that aims to understand the behaviour of the most elementary building blocks of our universe. As curiosity is something inherent to human kind, this summary is written for the general audience that may wonder about this topic.

Particle Physics and the Standard Model

For hundreds of years people have understood that matter was built from tiny building blocks. The Greek philosopher Democritus dared to introduce the concept of an atom, postulating that there should be an infinite number of objects, which differ in shape and size. Nowadays we know matter is indeed made out of atoms. However, these are not the smallest building blocks of matter. Atoms themselves are made up of a positively charged nucleus surrounded by a cloud of negatively charged electrons. The electron seem to be point-like, meaning that it is a fundamental particle. The nucleus is in turn composed of protons and neutrons. As the name suggests the neutrons do not carry charge, whereas protons are responsible for the positive charge of the nucleus. The total charge of an atom is zero, meaning that there are as many protons as neutrons. Even though this seems complicated enough, the protons and neutrons can be pictured as a soup of the fundamental particles called quarks and gluons.

The field of particle physics dedicates itself to unravel the fundamental building blocks and their interactions. Its greatest accomplishment thus far is encompassed by the theory we call the Standard Model (SM). It describes all fundamental particles and their mutual interactions, except gravity. The particles described by the SM are summarized in figure 1. Ordinary matter is made of fermions: the quarks, electrons and neutrinos. There are six quark flavors and six leptons, which can be grouped into three generations. The first generation includes the up- and down-quark, the electron and the electron neutrino. The second generation includes the strange-quark, charm-quark, muon and muon neutrino. The third and last generation includes the bottom-quark,

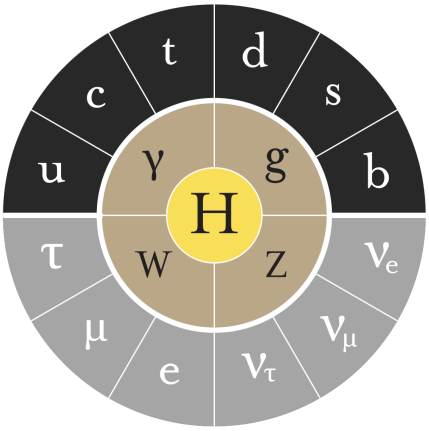

Figure 1 All the fundamental particles in the SM are represented by this picture. The outer circle includes the twelve elementary particles that make up matter. These are the leptons and quarks, represented by the black and grey boxes respectively. There are 6 quark flavors: up (u), down (d), strange (s), charm (c), bottom (b) and top (t). There are also 6 leptons: electron (e), muon (μ), tau (τ) and the corresponding neutrino's ((ν_e, ν_μ, ν_τ). The four fundamental force carriers are included in the middle ring. The electromagnetic force is carried by the photon (γ), the weak force is carried by the Z- and W-bosons and the strong force is carried by the gluon (g). The center of this figure is reserved for the Higgs particle. The particles that interact with the Higgs particle acquire mass. The photon and gluon do not interact with the Higgs and are therefore massless. The three neutrinos interact weakly with the Higgs and have a very small mass.

top-quark, tau and tau-neutrino. Each generation is heavier than the last, with the top quark being the heaviest particle. Then we have the bosons, the carriers of the fundamental forces. Starting with the best known of four, the photon is the force-carrier of the electromagnetic force. The Z- and W-boson are force-carriers for the weak nuclear force. This force is responsible for the radioactive decay of some atoms, where weak refers to the relatively long time it takes for such a decay to actually happen. The last force is the strong nuclear force, which is passed on by gluons. The constant exchange of gluons between quarks is what glues them together in formations like a proton. The remaining particle is the Higgs, which is not a building block for matter, nor a force carrier. The Higgs is special as it is essential to the process through which the other particles acquire mass.

The existence of elementary particles and their interactions is tested by

experiments that let particles collide at very high energies. The world's largest and most powerful particle accelerator is the Large Hadron Collider (LHC) at CERN in Geneva. Here, protons are accelerated until almost the speed of light and are then violently collided. The experimental particle physicists make it their quest to reconstruct the details of the collision from the data collected by the detectors that are placed around the point of collision. All particles predicted by the SM are found, with the last one being the Higgs particle in 2012. Even more impressive is that no additional fundamental particles appeared at all. Besides the fact that it does not incorporate gravity, the SM fails to explain some of the biggest mysteries in the universe of our time. It does not explain the fact that there is almost no anti-matter in our universe, and neither the dark matter and dark energy which together seem to make up roughly 95% of the universe. The SM is therefore, in spite of its successes, incomplete and the field of particle physics is actively looking for answers.

Quantum Chromodynamics

The research conducted in this thesis focuses on the strong interactions between quarks and gluons. These interactions have a great imprint on the outcome of proton-proton collision at the LHC. The branch of the SM that describes the strong interactions is called Quantum Chromodynamics (QCD). Consider first the better known theory of Quantum Electrodynamics, which describes the interaction between electrically charged particles. Electrically charged particles interact with each other by exchanging photons. Two positively or two negatively charged particles repel and particles of opposite charge attract. The prefix 'Chromo' in QCD refers to the existence of three kinds of charges, referred to as colors. The quarks are the matter particles in the SM that carry color and they interact with each other by exchanging gluons. A large difference with QED is that the force carriers, the gluons, carry color themselves and they can therefore interact with themselves. The *color charge* of quarks and gluons is completely unrelated to the everyday meaning of color. The labels red, green, and blue simply got in fashion by the analogy to the primary colors. A striking characteristic of QCD is that it only allows color-neutral combinations at distances $> 10^{-15}$m. Due to this color confinement, particles that carry color are grouped into color neutral objects called hadrons and can only be studied indirectly. In particular, a quark and an anti-quark with opposite color charge combine into mesons, and three quarks with one red, one green and one blue combine into baryons. Here, we clearly see the reference to the primal colors: red, green and blue combine to white, which is considered neutral. A proton is a baryon that contains two up and one down

quark. However, due to the continuous interactions between quarks and gluons, hadrons are complicated objects that in reality are closer to a constantly changing soup of various quarks and gluons.

Effective theories, factorization and resummation

In any line of work one has to extend or refine the available set of tools to improve the product. In theoretical physics we need to extend our calculation techniques to increase the precision of our SM predictions. In particular we use so-called *effective theories* to circumvent complicated calculations.

To understand what an effective theory is, let us consider the theory invented by Enrico Fermi in the 30s. He was investigating beta decay: a type of radioactive decay in which an atom decays into another atom by emitting an electron or positron (the anti-particle of the electron). In particular, the beta decay of a neutron transforms it into a proton by the emission of an electron accompanied by an anti-electron neutrino. To explain this process he introduced the direct interaction between the four leptons. This four-point interaction is depicted on the left in figure 2. His explanation preceded the current theory of the weak nuclear force (part of the SM), in which the elementary W-boson is responsible for the decay. The weak force dictates that a down-quark can change into an up-quark by emitting a W-boson. The W-boson itself preferably decays into an electron and anti-electron neutrino. This decay process is schematically depicted on the right in figure 2.

Looking back, we now know that the decay is explained by the weak interaction, and we can interpret Fermi's theory as an effective theory. Predictions made with the four-point interaction are however much easier, and still give a reliable outcome. The predictive power relies on the separation of energy scales, which is the most important consideration when constructing an effective theory. In the case of Fermi's theory this means we have to avoid energies close to the mass of the W-boson; but for smaller energies Fermi's theory works excellently.

To predict the outcome of experiments at particle accelerators we can also use an effective theory. We use the separation of energy scales to distinguish particles with different energy and direction. To be more precise, we want to separate soft interactions (involving particles with little energy), collinear interactions (between particles that move in the same direction) and hard interactions (between particles that carry a lot of energy but do not move in the same direction). The effective theory that accomplishes this is Soft-Collinear Effective Theory (SCET). Theoretical uncertainties in this theory are a result of the separation between the energy at which the particles are

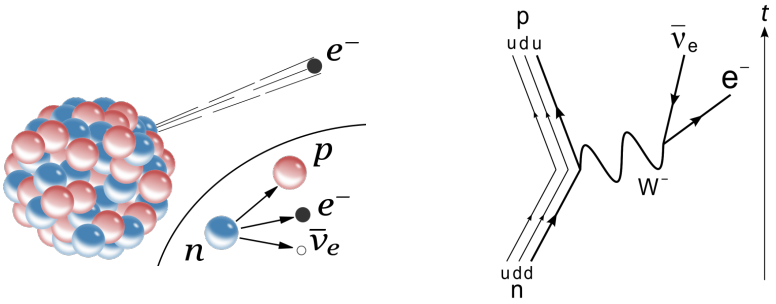

Figure 2 This figure presents two explanations of neutron decay: On the left we see the decay of an atom by means of a four point interaction between the neutron, the proton, the electron and the corresponding anti-neutrino. On the right the neutron decays through the weak force, as explained by the SM. The down-quark carries negative electric charge and the up-quark positive electric charge, the weak beta-decay is mediated by the W^--boson, such that the total charge is conserved. Source: Wikipedia.

collided and the energy at which the measurement is performed. These two factors are responsible for the validity of our effective theory, which can be quantified by looking at the corrections to the SCET approximation.

By using SCET we can calculate the contributions from collinear, soft and hard interactions separately. We call this factorization, as we have split the complete process into smaller (easier) pieces. We calculate each piece in an expansion, where we systematically include contributions that involve more interactions between particles when we go to higher orders. Going to higher orders is difficult, as one has to take an increasing number of interactions into account. However, contributions of soft and collinear radiation are enhanced and should be included to higher orders for precise predictions. This is remedied by factorization, which allows you to include the dominant effect of soft and collinear emissions at higher orders. Each ingredient in the factorization (soft, collinear, and hard contributions) depends on a specific energy scale. A circumstantial result of factorization is that each ingredient has an energy scale for which these dominant effects disappear, the so-called natural energy scale. We can thus calculate the soft, collinear and hard pieces at their natural energy scale, such that we do not have to worry about dominant higher order effects. Since the actual collision just involves one energy scale, we have to convert all contributions to the same energy afterwards. The procedure where all natural energy scales are evolved to a common energy scale is known as resummation. This resummation technique has the ability to predict the dominant contributions of collinear and soft radiation.

Research in this thesis

The research described in this thesis aims to increase the theoretical precision of SM predictions by using SCET. In chapter 2 we focus on jets, which are collimated sprays of hadrons that are often found in detectors at the LHC. They form whenever energetic quarks or gluons are produced in high-energy collisions. Jets thus contain important information about these fundamental particles and are therefore widely studied objects. In this chapter we provide an automated calculation technique to calculate the jet contribution to a measurement. In chapter 3 we use SCET to make a prediction for the process in which two protons collide and produce a boson and a jet. Specifically we consider the angle between a photon (or Z) and the jet. For situations where this angle almost becomes straight, i.e. when the photon and the jet are flying in the exact opposite direction, we find that SCET is particularly useful. In this limit the resummation is necessary to obtain reliable results, and SCET provides a framework in which this can be done. In chapter 4 we extend our set of tools with *track functions*. The data that experimentalists currently use from the LHC experiments to compare to theory is limited by the size of the calorimeter cells. The calorimeter is the part of the detector that measures the energy and direction of the particles produced in the proton-proton collision. It would be possible to improve the experimental accuracy by using data from the tracking system. The tracking system is a layer in the detector with the principle task to reconstruct the trajectory of electrically charged particles. The research described in this chapter focuses on the theoretical implementation of measurements solely based on electrically charged particles. We do this by using track functions, which describe the fraction of the produced particles that will leave tracks in the detectors.

The battle to find the first crack of the SM has begun, with the techniques described in this thesis playing an important part. Will precision physics beat the SM? Or will it hold its ground, giving us the immense task of explaining the open questions, related to e.g. dark matter and energy, for which we do not know where to start?

Acknowledgements

The work presented in this thesis could not have been accomplished without family, friends and colleagues. I would therefore like to dedicate the last pages to all those who helped me finish this thesis.

First and foremost, I would like to thank my supervisor Wouter for his invaluable supervision. Your advice, patience and understanding were crucial for me during the last couple of years. Your open mindset and pure intentions strengthened me and I could not have wished for a better supervisor. I will be forever grateful for your guidance, on both a professional and personal level. Lastly, I want to thank you for the critical and extensive feedback on this thesis.

To my co-promotor Eric, thank you for introducing me to the scientific world as a master student and for your words of wisdom throughout the years. To my independent supervisor Piet, thank you for your advice and for watching over me.

The research in this thesis resulted from collaboration with a number of other people. Besides the fact that none of the results presented in this thesis could have been obtained without any of you, I greatly enjoyed working together on a personal level. Franz, thank you for the countless blackboard sessions we shared. Your insights always helped me to tackle the problem. Ian, thank you for the enjoyable and educational discussions we had. You are a true inspiration. Rudi, thank you for always taking the time to sit down with me and explore new physics. Your enthusiasm is contagious. I am very grateful to have worked with each of you. Furthermore, I would like to thank the doctoral committee members for taking the time to read this thesis.

Nikhef has always felt like home to me. I want to thank the Nikhef theory group as a whole for being so welcoming. It was a pleasure to share lunch and coffee breaks with you. In particular, I want to thank my colleagues Avanish, Pedro, Jorinde, Darren, Melissa, Lorenzo, Michi, Rudi, Rhorry, Andreas and Rabbah for their advice and the fun times. I will never forget the moments we shared together. Avanish, I am thankful that we started our journey together and that we could confide in each other during the years.

I wish to extend my special thanks to Johan Veenstra. Your expertise literally saved my manuscript. Without your help in recovering the manuscript from a failing laptop, I would not have finished in time.

To all of my friends, for keeping me sane during the last years. Thank you for listening to whatever I had to say, ensuring me that I would be alright. Thank you for the fun distractions. I would like to thank the Roundnet community in Amsterdam. The pick-up games we played over the last year were a great outlet for me. Dora, for being a true friend. Your heart is pure, you're a pal and a confidant. Thank you for all the laughs we shared, especially during our amazing trip to Iceland. My roommates, Daitlin and Jip, you did not see me for days as I locked myself in my room to finish this thesis. Thank you for keeping up with my mood swings and absent behaviour. Maus, the burden I sometimes felt became your burden as well. Thank you for your patience and loving arms. You were there for me during the most crucial part of my PhD and I will always treasure the love and support I felt. Thank you for being you.

Finally, I would like to thank my parents for their unconditional support and belief in me. Neither this thesis, nor any of the steps that preceded it would have been possible without the loving environment that you have always provided. I am extremely grateful for everything you have done for me and for all the encouragement you gave me throughout the years.

Bibliography

[1] A. Basdew-Sharma, F. Herzog, S. S. van Velzen and W. J. Waalewijn, *One-loop jet functions by geometric subtraction*, *JHEP* **2020** (2020) 118.

[2] Y.-T. Chien, R. Rahn, S. Schrijnder van Velzen, D. Y. Shao, W. J. Waalewijn and B. Wu, *Recoil-free azimuthal angle for precision boson-jet correlation*, *Phys. Lett. B* **815** (2021) 136124 [2005.12279].

[3] Y. Li, I. Moult, S. S. van Velzen, W. J. Waalewijn and H. X. Zhu, *Extending precision perturbative qcd with track functions*, *Phys. Rev. Lett.* **128** (2022) 182001 [2108.01674].

[4] L. collaboration and R. A. et al, *Test of lepton universality in beauty-quark decays*, 2103.11769.

[5] A. Grozin, *Lectures on qed and qcd*, hep-ph/0508242.

[6] M. E. Peskin and D. V. Schroeder, *An Introduction to quantum field theory*. Addison-Wesley, Reading, USA, 1995.

[7] T. Gehrmann, *Introduction to QCD*, in *Theoretical Advanced Study Institute in Elementary Particle Physics: Journeys Through the Precision Frontier: Amplitudes for Colliders*, pp. 1–38, 2015, DOI.

[8] M. D. Schwartz, *Quantum Field Theory and the Standard Model*. Cambridge University Press, 3, 2014.

[9] H. Fritzsch, M. Gell-Mann and H. Leutwyler, *Advantages of the color octet gluon picture*, *Physics Letters B* **47** (1973) 365.

[10] C. G. Bollini and J. J. Giambiagi, *Dimensional Renormalization: The Number of Dimensions as a Regularizing Parameter*, *Nuovo Cim. B* **12** (1972) 20.

[11] G. 't Hooft and M. Veltman, *Regularization and renormalization of gauge fields*, *Nuclear Physics B* **44** (1972) 189.

[12] T. Cohen, *As scales become separated: Lectures on effective field theory*, 2019. 10.48550/ARXIV.1903.03622.

[13] G. 't Hooft, *Dimensional regularization and the renormalization group*, *Nuclear Physics B* **61** (1973) 455.

[14] S. Weinberg, *New approach to the renormalization group*, *Phys. Rev. D* **8** (1973) 3497.

[15] F. Herzog, B. Ruijl, T. Ueda, J. A. M. Vermaseren and A. Vogt, *The five-loop beta function of yang-mills theory with fermions*, *Journal of High Energy Physics* **2017** (2017) .

[16] M. T. e. a. Particle Data Group collabration, *Review of particle physics: Particle data group*, *Physical Review D* **98** (2018) .

[17] F. Bloch and A. Nordsieck, *Note on the radiation field of the electron*, *Phys. Rev.* **52** (1937) 54.

[18] T. Kinoshita, *Mass singularities of Feynman amplitudes*, *J. Math. Phys.* **3** (1962) 650.

[19] T. D. Lee and M. Nauenberg, *Degenerate Systems and Mass Singularities*, *Phys. Rev.* **133** (1964) B1549.

[20] V. N. Gribov and L. N. Lipatov, *Deep inelastic e p scattering in perturbation theory*, *Sov. J. Nucl. Phys.* **15** (1972) 438.

[21] Y. L. Dokshitzer, *Calculation of the Structure Functions for Deep Inelastic Scattering and e+ e- Annihilation by Perturbation Theory in Quantum Chromodynamics.*, *Sov. Phys. JETP* **46** (1977) 641.

[22] G. Altarelli and G. Parisi, *Asymptotic Freedom in Parton Language*, *Nucl. Phys. B* **126** (1977) 298.

[23] V. Antonelli, M. Dasgupta and G. P. Salam, *Resummation of thrust distributions in DIS*, *Journal of High Energy Physics* **2000** (2000) 001.

[24] D. G. Richards, W. J. Stirling and S. D. Ellis, *Second Order Corrections to the Energy-energy Correlation Function in Quantum Chromodynamics*, *Phys. Lett.* **119B** (1982) 193.

[25] R. Lefevre, *Inclusive jet cross section using the kt algorithm*, .

[26] L. G. Almeida, S. D. Ellis, C. Lee, G. Sterman, I. Sung and J. R. Walsh, *Comparing and counting logs in direct and effective methods of qcd resummation*, *Journal of High Energy Physics* **2014** (2014) .

[27] S. Catani, L. Trentadue, G. Turnock and B. Webber, *Resummation of large logarithms in e^+e^- event shape distributions*, *Nuclear Physics B* **407** (1993) 3.

[28] T. Cohen, *As scales become separated: Lectures on effective field theory*, 2019. 10.48550/ARXIV.1903.03622.

[29] A. V. Manohar, *Introduction to effective field theories*, 2018.

[30] I. W. Stewart, *Lectures on the Soft-Collinear Effective Theory*, *MIT Open Course Ware, Effective Field Theory (Spring 2013)* (2013) .

[31] T. Becher, A. Broggio and A. Ferroglia, *Introduction to Soft-Collinear Effective Theory*, vol. 896. Springer, 2015, 10.1007/978-3-319-14848-9, [1410.1892].

[32] C. W. Bauer, S. Fleming and M. E. Luke, *Summing Sudakov logarithms in $B \to X_s\gamma$ in effective field theory*, *Phys. Rev.* **D63** (2000) 014006 [hep-ph/0005275].

[33] C. W. Bauer, S. Fleming, D. Pirjol and I. W. Stewart, *An Effective field theory for collinear and soft gluons: Heavy to light decays*, *Phys. Rev.* **D63** (2001) 114020 [hep-ph/0011336].

[34] C. W. Bauer and I. W. Stewart, *Invariant operators in collinear effective theory*, *Phys. Lett.* **B516** (2001) 134 [hep-ph/0107001].

[35] C. W. Bauer, D. Pirjol and I. W. Stewart, *Soft collinear factorization in effective field theory*, *Phys. Rev.* **D65** (2002) 054022 [hep-ph/0109045].

[36] M. Beneke, A. P. Chapovsky, M. Diehl and T. Feldmann, *Soft collinear effective theory and heavy to light currents beyond leading power*, *Nucl. Phys.* **B643** (2002) 431 [hep-ph/0206152].

[37] T. Becher, A. Broggio and A. Ferroglia, *Introduction to soft-collinear effective theory*, *Lecture Notes in Physics* (2015) .

[38] C. W. Bauer, D. Pirjol and I. W. Stewart, *Power counting in the soft-collinear effective theory*, *Phys. Rev. D* **66** (2002) 054005.

[39] C. W. Bauer, D. Pirjol and I. W. Stewart, *On Power suppressed operators and gauge invariance in SCET*, *Phys. Rev.* **D68** (2003) 034021 [hep-ph/0303156].

[40] J. S. R. Chisholm, *Change of variables in quantum field theories*, *NNucl. Phys.* **26** (1961) 469.

[41] L. S. Kamefuchi and G. Salam, *Change of variables and equivalence theorems in quantum field theories*, *NNucl. Phys.* **28** (1961) 529.

[42] D. P. C.W. Bauer and I. Stewart, *Soft-collinear factorization in effective field theory*, *Physical Review D* **65** (2002) .

[43] K. S. Lee and I. W. Stewart, *Factorization for power corrections to $b \to xs$ and $b \to xue\nu$*, *Nuclear Physics B* **721** (2005) 325–406.

[44] C. C. Nishi, *Simple derivation of general fierz-type identities*, *American Journal of Physics* **73** (2005) 1160–1163.

[45] S. Fleming, A. H. Hoang, S. Mantry and I. W. Stewart, *Jets from massive unstable particles: Top-mass determination*, *Physical Review D* **77** (2008) .

[46] A. V. Manohar, *Deep inelastic scattering asx→1using soft-collinear effective theory*, *Physical Review D* **68** (2003) .

[47] J. C. Collins and D. E. Soper, *Parton Distribution and Decay Functions*, *Nucl. Phys.* **B194** (1982) 445.

[48] J. C. Collins, D. E. Soper and G. F. Sterman, *Transverse Momentum Distribution in Drell-Yan Pair and W and Z Boson Production*, *Nucl. Phys. B* **250** (1985) 199.

[49] T. Becher and M. Neubert, *Drell-Yan Production at Small q_T, Transverse Parton Distributions and the Collinear Anomaly*, *Eur. Phys. J. C* **71** (2011) 1665 [1007.4005].

[50] J.-Y. Chiu, A. Jain, D. Neill and I. Z. Rothstein, *A Formalism for the Systematic Treatment of Rapidity Logarithms in Quantum Field Theory*, *JHEP* **05** (2012) 084 [1202.0814].

[51] A. V. Manohar and I. W. Stewart, *The Zero-Bin and Mode Factorization in Quantum Field Theory*, *Phys. Rev. D* **76** (2007) 074002 [hep-ph/0605001].

[52] D. Y. Grigoriev, E. Jankowski and F. V. Tkachov, *Towards a standard jet definition*, *Phys. Rev. Lett.* **91** (2003) .

[53] S. Catani, Y. Dokshitzer, M. Seymour and B. Webber, *Longitudinally-invariant $k_\perp$-clustering algorithms for hadron-hadron collisions*, *Nuclear Physics B* **406** (1993) 187.

[54] S. D. Ellis and D. E. Soper, *Successive combination jet algorithm for hadron collisions*, *Physical Review D* **48** (1993) 3160–3166.

[55] Y. Dokshitzer, G. Leder, S. Moretti and B. Webber, *Better jet clustering algorithms*, *Journal of High Energy Physics* **1997** (1997) 001–001.

[56] M. Wobisch and T. Wengler, *Hadronization corrections to jet cross sections in deep-inelastic scattering*, 1999.

[57] A. J. Larkoski, S. Marzani, G. Soyez and J. Thaler, *Soft drop*, *Journal of High Energy Physics* **2014** (2014) .

[58] D. Krohn, J. Thaler and L.-T. Wang, *Jet trimming*, *Journal of High Energy Physics* **2010** (2010) .

[59] C. Frye, A. J. Larkoski, J. Thaler and K. Zhou, *Casimir meets poisson: improved quark/gluon discrimination with counting observables*, *Journal of High Energy Physics* **2017** (2017) .

[60] M. Cacciari, G. P. Salam and G. Soyez, *The anti-k_t jet clustering algorithm*, *JHEP* **04** (2008) 063 [0802.1189].

[61] M. Cacciari, G. P. Salam and G. Soyez, *Fastjet user manual*, *The European Physical Journal C* **72** (2012) .

[62] M. Cacciari and G. P. Salam, *Dispelling the n^3 myth for the kt jet-finder*, *Physics Letters B* **641** (2006) 57–61.

[63] W. M.-Y. Cheung, M. Luke and S. Zuberi, *Phase space and jet definitions in soft-collinear effective theory*, *Physical Review D* **80** (2009) .

[64] S. D. Ellis, C. K. Vermilion, J. R. Walsh, A. Hornig and C. Lee, *Jet Shapes and Jet Algorithms in SCET*, *JHEP* **11** (2010) 101 [1001.0014].

[65] C. W. Bauer and A. V. Manohar, *Shape function effects in $B \to X_s\gamma$ and $B \to X_u\ell\bar{\nu}$ decays*, *Phys. Rev.* **D70** (2004) 034024 [hep-ph/0312109].

[66] T. Becher and M. Neubert, *Toward a NNLO calculation of the $\bar{B} \to X_s\gamma$ decay rate with a cut on photon energy. II. Two-loop result for the jet function*, *Phys. Lett. B* **637** (2006) 251 [hep-ph/0603140].

[67] T. Becher and M. D. Schwartz, *Direct photon production with effective field theory*, *JHEP* **02** (2010) 040 [0911.0681].

[68] T. Becher and G. Bell, *The gluon jet function at two-loop order*, *Phys. Lett. B* **695** (2011) 252 [1008.1936].

[69] R. Brüser, Z. L. Liu and M. Stahlhofen, *Three-Loop Quark Jet Function*, *Phys. Rev. Lett.* **121** (2018) 072003 [1804.09722].

[70] P. Banerjee, P. K. Dhani and V. Ravindran, *Gluon jet function at three loops in QCD*, *Phys. Rev.* **D98** (2018) 094016 [1805.02637].

[71] A. Hornig, C. Lee and G. Ovanesyan, *Effective Predictions of Event Shapes: Factorized, Resummed, and Gapped Angularity Distributions*, *JHEP* **05** (2009) 122 [0901.3780].

[72] T. Becher and G. Bell, *NNLL Resummation for Jet Broadening*, *JHEP* **11** (2012) 126 [1210.0580].

[73] G. Bell, A. Hornig, C. Lee and J. Talbert, e^+e^- *angularity distributions at NNLL′ accuracy*, *JHEP* **01** (2019) 147 [1808.07867].

[74] A. J. Larkoski, D. Neill and J. Thaler, *Jet Shapes with the Broadening Axis*, *JHEP* **04** (2014) 017 [1401.2158].

[75] M. Procura, W. J. Waalewijn and L. Zeune, *Joint resummation of two angularities at next-to-next-to-leading logarithmic order*, *JHEP* **10** (2018) 098 [1806.10622].

[76] T. T. Jouttenus, *Jet Function with a Jet Algorithm in SCET*, *Phys. Rev. D* **81** (2010) 094017 [0912.5509].

[77] J. Chay, C. Kim and I. Kim, *Factorization of the dijet cross section in electron-positron annihilation with jet algorithms*, *Phys. Rev.* **D92** (2015) 034012 [1505.00121].

[78] Z.-B. Kang, F. Ringer and I. Vitev, *The semi-inclusive jet function in SCET and small radius resummation for inclusive jet production*, *JHEP* **10** (2016) 125 [1606.06732].

[79] L. Dai, C. Kim and A. K. Leibovich, *Fragmentation of a Jet with Small Radius*, *Phys. Rev. D* **94** (2016) 114023 [1606.07411].

[80] H.-n. Li, Z. Li and C.-P. Yuan, *QCD resummation for jet substructures*, *Phys. Rev. Lett.* **107** (2011) 152001 [1107.4535].

[81] Y.-T. Chien and I. Vitev, *Jet Shape Resummation Using Soft-Collinear Effective Theory*, *JHEP* **12** (2014) 061 [1405.4293].

[82] P. Cal, F. Ringer and W. J. Waalewijn, *The jet shape at NLL′*, *JHEP* **05** (2019) 143 [1901.06389].

[83] S. Fleming, A. H. Hoang, S. Mantry and I. W. Stewart, *Top Jets in the Peak Region: Factorization Analysis with NLL Resummation*, *Phys. Rev.* **D77** (2008) 114003 [0711.2079].

[84] A. H. Hoang, C. Lepenik and M. Stahlhofen, *Two-Loop Massive Quark Jet Functions in SCET*, *JHEP* **08** (2019) 112 [1904.12839].

[85] D. Krohn, M. D. Schwartz, T. Lin and W. J. Waalewijn, *Jet Charge at the LHC*, *Phys. Rev. Lett.* **110** (2013) 212001 [1209.2421].

[86] W. J. Waalewijn, *Calculating the Charge of a Jet*, *Phys. Rev.* **D86** (2012) 094030 [1209.3019].

[87] T. Kasemets, W. J. Waalewijn and L. Zeune, *Calculating Soft Radiation at One Loop*, *JHEP* **03** (2016) 153 [1512.00857].

[88] G. Bell, R. Rahn and J. Talbert, *Automated Calculation of Dijet Soft Functions in Soft-Collinear Effective Theory*, *PoS* **RADCOR2015** (2016) 052 [1512.06100].

[89] G. Bell, R. Rahn and J. Talbert, *Generic dijet soft functions at two-loop order: correlated emissions*, *JHEP* **07** (2019) 101 [1812.08690].

[90] G. Bell, R. Rahn and J. Talbert, *Generic dijet soft functions at two-loop order: uncorrelated emissions*, 2004.08396.

[91] G. Bell, B. Dehnadi, T. Mohrmann and R. Rahn, *Automated Calculation of $\boldsymbol{N}$-jet Soft Functions*, *PoS* **LL2018** (2018) 044 [1808.07427].

[92] I. Moult, I. W. Stewart, F. J. Tackmann and W. J. Waalewijn, *Employing Helicity Amplitudes for Resummation*, *Phys. Rev.* **D93** (2016) 094003 [1508.02397].

[93] A. Budhraja, A. Jain and M. Procura, *One-loop angularity distributions with recoil using Soft-Collinear Effective Theory*, *JHEP* **08** (2019) 144 [1903.11087].

[94] J.-y. Chiu, A. Jain, D. Neill and I. Z. Rothstein, *The Rapidity Renormalization Group*, *Phys. Rev. Lett.* **108** (2012) 151601 [1104.0881].

[95] J. Collins, *Foundations of perturbative QCD*, vol. 32. Cambridge University Press, 11, 2013.

[96] M. G. Echevarria, A. Idilbi and I. Scimemi, *Factorization Theorem For Drell-Yan At Low q_T And Transverse Momentum Distributions On-The-Light-Cone*, *JHEP* **07** (2012) 002 [1111.4996].

[97] T. Becher and G. Bell, *Analytic Regularization in Soft-Collinear Effective Theory*, *Phys. Lett. B* **713** (2012) 41 [1112.3907].

[98] M. Ritzmann and W. J. Waalewijn, *Fragmentation in Jets at NNLO*, *Phys. Rev. D* **90** (2014) 054029 [1407.3272].

[99] F. Herzog, *Geometric IR subtraction for final state real radiation*, *JHEP* **08** (2018) 006 [1804.07949].

[100] T. Hahn, *CUBA: A Library for multidimensional numerical integration*, *Comput. Phys. Commun.* **168** (2005) 78 [hep-ph/0404043].

[101] C. F. Berger, T. Kucs and G. F. Sterman, *Event shape / energy flow correlations*, *Phys. Rev.* **D68** (2003) 014012 [hep-ph/0303051].

[102] I. W. Stewart, F. J. Tackmann and W. J. Waalewijn, *Factorization at the LHC: From PDFs to Initial State Jets*, *Phys. Rev. D* **81** (2010) 094035 [0910.0467].

[103] E. Panzer, *Algorithms for the symbolic integration of hyperlogarithms with applications to Feynman integrals*, *Comput. Phys. Commun.* **188** (2015) 148 [1403.3385].

[104] A. I. Davydychev and M. Kalmykov, *New results for the epsilon expansion of certain one, two and three loop Feynman diagrams*, *Nucl. Phys. B* **605** (2001) 266 [hep-th/0012189].

[105] A. I. Davydychev and M. Kalmykov, *Some remarks on the epsilon expansion of dimensionally regulated Feynman diagrams*, *Nucl. Phys. B Proc. Suppl.* **89** (2000) 283 [hep-th/0005287].

[106] M. Kalmykov and A. Sheplyakov, *lsjk - a C++ library for arbitrary-precision numeric evaluation of the generalized log-sine functions*, *Comput. Phys. Commun.* **172** (2005) 45 [hep-ph/0411100].

[107] CDF collaboration, F. Abe et al., *Observation of top quark production in $\bar{p}p$ collisions*, *Phys. Rev. Lett.* **74** (1995) 2626 [hep-ex/9503002].

[108] U. Blumenschein et al., *Pushing the precision frontier at the LHC with V+jets*, 2, 2018, 1802.02100.

[109] V. Kartvelishvili, R. Kvatadze and R. Shanidze, *On Z and Z + jet production in heavy ion collisions*, *Phys. Lett. B* **356** (1995) 589 [hep-ph/9505418].

[110] CMS collaboration, A. M. Sirunyan et al., *Study of Jet Quenching with $Z+jet$ Correlations in Pb-Pb and pp Collisions at $\sqrt{s}_{NN} = 5.02$ TeV*, *Phys. Rev. Lett.* **119** (2017) 082301 [1702.01060].

[111] S. Cao and X.-N. Wang, *Jet quenching and medium response in high-energy heavy-ion collisions: a review*, 2002.04028.

[112] A. Gehrmann-De Ridder, T. Gehrmann, E. W. N. Glover, A. Huss and T. A. Morgan, *Precise QCD predictions for the production of a Z boson in association with a hadronic jet*, *Phys. Rev. Lett.* **117** (2016) 022001 [1507.02850].

[113] R. Boughezal, C. Focke, X. Liu and F. Petriello, *W-boson production in association with a jet at next-to-next-to-leading order in perturbative QCD*, *Phys. Rev. Lett.* **115** (2015) 062002 [1504.02131].

[114] R. Boughezal, J. M. Campbell, R. K. Ellis, C. Focke, W. T. Giele, X. Liu et al., *Z-boson production in association with a jet at next-to-next-to-leading order in perturbative QCD*, *Phys. Rev. Lett.* **116** (2016) 152001 [1512.01291].

[115] J. M. Campbell, R. K. Ellis and C. Williams, *Direct Photon Production at Next-to–Next-to-Leading Order*, *Phys. Rev. Lett.* **118** (2017) 222001 [1612.04333].

[116] A. Gehrmann-De Ridder, T. Gehrmann, E. W. N. Glover, A. Huss and D. M. Walker, *Next-to-Next-to-Leading-Order QCD Corrections to the Transverse Momentum Distribution of Weak Gauge Bosons*, *Phys. Rev. Lett.* **120** (2018) 122001 [1712.07543].

[117] X. Chen, T. Gehrmann, N. Glover, M. Höfer and A. Huss, *Isolated photon and photon+jet production at NNLO QCD accuracy*, *JHEP* **04** (2020) 166 [1904.01044].

[118] L. Chen, G.-Y. Qin, L. Wang, S.-Y. Wei, B.-W. Xiao, H.-Z. Zhang et al., *Study of Isolated-photon and Jet Momentum Imbalance in pp and PbPb collisions*, *Nucl. Phys. B* **933** (2018) 306 [1803.10533].

[119] P. Sun, B. Yan, C. P. Yuan and F. Yuan, *Resummation of High Order Corrections in Z Boson Plus Jet Production at the LHC*, *Phys. Rev. D* **100** (2019) 054032 [1810.03804].

[120] Y.-T. Chien, D. Y. Shao and B. Wu, *Resummation of Boson-Jet Correlation at Hadron Colliders*, *JHEP* **11** (2019) 025 [1905.01335].

[121] M. Dasgupta and G. P. Salam, *Resummation of nonglobal QCD observables*, *Phys. Lett. B* **512** (2001) 323 [hep-ph/0104277].

[122] Y.-T. Chien, D. Y. Shao and B. Wu, *Resummation of boson-jet correlation at hadron colliders*, *Journal of High Energy Physics* **2019** (2019) .

[123] G. Salam, "E_t^{∞} Scheme." Unpublished.

[124] D. Bertolini, T. Chan and J. Thaler, *Jet Observables Without Jet Algorithms*, *JHEP* **04** (2014) 013 [1310.7584].

[125] C. W. Bauer, S. Fleming, D. Pirjol, I. Z. Rothstein and I. W. Stewart, *Hard scattering factorization from effective field theory*, *Phys. Rev.* **D66** (2002) 014017 [hep-ph/0202088].

[126] CMS collaboration, S. Chatrchyan et al., *Event Shapes and Azimuthal Correlations in Z + Jets Events in pp Collisions at $\sqrt{s} = 7$ TeV*, *Phys. Lett.* **B722** (2013) 238 [1301.1646].

[127] CMS collaboration, V. Khachatryan et al., *Measurements of differential production cross sections for a Z boson in association with jets in pp collisions at $\sqrt{s} = 8$ TeV*, *JHEP* **04** (2017) 022 [1611.03844].

[128] ATLAS collaboration, M. Aaboud et al., *Measurement of the cross section for isolated-photon plus jet production in pp collisions at $\sqrt{s} = 13$ TeV using the ATLAS detector*, *Phys. Lett.* **B780** (2018) 578 [1801.00112].

[129] D. Boer, P. J. Mulders and C. Pisano, *Dijet imbalance in hadronic collisions*, *Phys. Rev. D* **80** (2009) 094017 [0909.4652].

[130] S. Catani and M. Grazzini, *QCD transverse-momentum resummation in gluon fusion processes*, *Nucl. Phys.* **B845** (2011) 297 [1011.3918].

[131] M. Arratia, Y. Song, F. Ringer and B. V. Jacak, *Jets as precision probes in electron-nucleus collisions at the future Electron-Ion Collider*, *Phys. Rev. C* **101** (2020) 065204 [1912.05931].

[132] Y.-T. Chien, R. Rahn, D. Y. Shao, W. J. Waalewijn and B. Wu, *Precision boson-jet azimuthal decorrelation at hadron colliders*, .

[133] M. A. Ebert and F. J. Tackmann, *Resummation of Transverse Momentum Distributions in Distribution Space*, *JHEP* **02** (2017) 110 [1611.08610].

[134] S. Mantry and F. Petriello, *Factorization and Resummation of Higgs Boson Differential Distributions in Soft-Collinear Effective Theory*, *Phys. Rev.* **D81** (2010) 093007 [0911.4135].

[135] M.-X. Luo, T.-Z. Yang, H. X. Zhu and Y. J. Zhu, *Transverse Parton Distribution and Fragmentation Functions at NNLO: the Gluon Case*, *JHEP* **01** (2020) 040 [1909.13820].

[136] D. Gutierrez-Reyes, S. Leal-Gomez, I. Scimemi and A. Vladimirov, *Linearly polarized gluons at next-to-next-to leading order and the Higgs transverse momentum distribution*, *JHEP* **11** (2019) 121 [1907.03780].

[137] S. Moch, J. A. M. Vermaseren and A. Vogt, *Three-loop results for quark and gluon form-factors*, *Phys. Lett. B* **625** (2005) 245 [hep-ph/0508055].

[138] S. Moch, J. Vermaseren and A. Vogt, *The Quark form-factor at higher orders*, *JHEP* **08** (2005) 049 [hep-ph/0507039].

[139] T. Becher and M. Neubert, *Infrared singularities of scattering amplitudes in perturbative QCD*, *Phys. Rev. Lett.* **102** (2009) 162001 [0901.0722].

[140] T. Gehrmann, T. Luebbert and L. L. Yang, *Calculation of the transverse parton distribution functions at next-to-next-to-leading order*, *JHEP* **06** (2014) 155 [1403.6451].

[141] M. G. Echevarria, I. Scimemi and A. Vladimirov, *Universal transverse momentum dependent soft function at NNLO*, *Phys. Rev. D* **93** (2016) 054004 [1511.05590].

[142] T. Lübbert, J. Oredsson and M. Stahlhofen, *Rapidity renormalized TMD soft and beam functions at two loops*, *JHEP* **03** (2016) 168 [1602.01829].

[143] S. Moch, J. A. M. Vermaseren and A. Vogt, *The Three loop splitting functions in QCD: The Nonsinglet case*, *Nucl. Phys.* **B688** (2004) 101 [hep-ph/0403192].

[144] O. V. Tarasov, A. A. Vladimirov and A. Y. Zharkov, *The Gell-Mann-Low Function of QCD in the Three Loop Approximation*, *Phys. Lett. B* **93** (1980) 429.

[145] S. A. Larin and J. A. M. Vermaseren, *The Three loop QCD Beta function and anomalous dimensions*, *Phys. Lett. B* **303** (1993) 334 [hep-ph/9302208].

[146] P. B. Arnold and M. H. Reno, *The Complete Computation of High p_T W and Z Production in 2nd Order QCD*, *Nucl. Phys.* **B319** (1989) 37.

[147] T. Becher, C. Lorentzen and M. D. Schwartz, *Precision Direct Photon and W-Boson Spectra at High p_T and Comparison to LHC Data*, *Phys. Rev.* **D86** (2012) 054026 [1206.6115].

[148] F. Tackmann. Private Communication.

[149] Y. Li and H. X. Zhu, *Bootstrapping Rapidity Anomalous Dimensions for Transverse-Momentum Resummation*, *Phys. Rev. Lett.* **118** (2017) 022004 [1604.01404].

[150] A. Gao, H. T. Li, I. Moult and H. X. Zhu, *Precision QCD Event Shapes at Hadron Colliders: The Transverse Energy-Energy Correlator in the Back-to-Back Limit*, *Phys. Rev. Lett.* **123** (2019) 062001 [1901.04497].

[151] T. Becher, G. Bell and S. Marti, *NNLO soft function for electroweak boson production at large transverse momentum*, *JHEP* **04** (2012) 034 [1201.5572].

[152] S. Catani and M. Grazzini, *Higgs Boson Production at Hadron Colliders: Hard-Collinear Coefficients at the NNLO*, *Eur. Phys. J. C* **72** (2012) 2013 [1106.4652].

[153] S. Catani, L. Cieri, D. de Florian, G. Ferrera and M. Grazzini, *Vector boson production at hadron colliders: hard-collinear coefficients at the NNLO*, *Eur. Phys. J. C* **72** (2012) 2195 [1209.0158].

[154] T. Gehrmann, T. Lubbert and L. L. Yang, *Transverse parton distribution functions at next-to-next-to-leading order: the quark-to-quark case*, *Phys. Rev. Lett.* **109** (2012) 242003 [1209.0682].

[155] M. G. Echevarria, I. Scimemi and A. Vladimirov, *Unpolarized Transverse Momentum Dependent Parton Distribution and Fragmentation Functions at next-to-next-to-leading order*, *JHEP* **09** (2016) 004 [1604.07869].

[156] M.-X. Luo, X. Wang, X. Xu, L. L. Yang, T.-Z. Yang and H. X. Zhu, *Transverse Parton Distribution and Fragmentation Functions at NNLO: the Quark Case*, *JHEP* **10** (2019) 083 [1908.03831].

[157] A. Behring, K. Melnikov, R. Rietkerk, L. Tancredi and C. Wever, *Quark beam function at next-to-next-to-next-to-leading order in perturbative QCD in the generalized large-N_c approximation*, *Phys. Rev. D* **100** (2019) 114034 [1910.10059].

[158] M.-x. Luo, T.-Z. Yang, H. X. Zhu and Y. J. Zhu, *Quark Transverse Parton Distribution at the Next-to-Next-to-Next-to-Leading Order*, *Phys. Rev. Lett.* **124** (2020) 092001 [1912.05778].

[159] M. A. Ebert, B. Mistlberger and G. Vita, *Transverse momentum dependent PDFs at N^3LO*, *JHEP* **09** (2020) 146 [2006.05329].

[160] D. Gutierrez-Reyes, I. Scimemi, W. J. Waalewijn and L. Zoppi, *Transverse momentum dependent distributions with jets*, *Phys. Rev. Lett.* **121** (2018) 162001 [1807.07573].

[161] D. Gutierrez-Reyes, I. Scimemi, W. J. Waalewijn and L. Zoppi, *Transverse momentum dependent distributions in e^+e^- and semi-inclusive deep-inelastic scattering using jets*, *JHEP* **10** (2019) 031 [1904.04259].

[162] J. M. Campbell and R. K. Ellis, *Next-to-leading order corrections to $W + 2$ jet and $Z + 2$ jet production at hadron colliders*, *Phys. Rev.* **D65** (2002) 113007 [hep-ph/0202176].

[163] J. M. Campbell, R. K. Ellis and D. L. Rainwater, *Next-to-leading order QCD predictions for $W + 2$ jet and $Z + 2$ jet production at the CERN LHC*, *Phys. Rev.* **D68** (2003) 094021 [hep-ph/0308195].

[164] T. Becher and M. Hager, *Event-Based Transverse Momentum Resummation*, *Eur. Phys. J. C* **79** (2019) 665 [1904.08325].

[165] S. Dulat, T.-J. Hou, J. Gao, M. Guzzi, J. Huston, P. Nadolsky et al., *New parton distribution functions from a global analysis of quantum chromodynamics*, *Phys. Rev.* **D93** (2016) 033006 [1506.07443].

[166] T. Sjostrand, S. Ask, J. R. Christiansen, R. Corke, N. Desai, P. Ilten et al., *An Introduction to PYTHIA 8.2*, *Comput. Phys. Commun.* **191** (2015) 159 [1410.3012].

[167] H.-M. Chang, M. Procura, J. Thaler and W. J. Waalewijn, *Calculating Track-Based Observables for the LHC*, *Phys. Rev. Lett.* **111** (2013) 102002 [1303.6637].

[168] H.-M. Chang, M. Procura, J. Thaler and W. J. Waalewijn, *Calculating Track Thrust with Track Functions*, *Phys. Rev. D* **88** (2013) 034030 [1306.6630].

[169] G. P. Korchemsky and A. V. Radyushkin, *Renormalization of the Wilson Loops Beyond the Leading Order*, *Nucl. Phys. B* **283** (1987) 342.

[170] A. Idilbi, X.-d. Ji and F. Yuan, *Resummation of threshold logarithms in effective field theory for DIS, Drell-Yan and Higgs production*, *Nucl. Phys. B* **753** (2006) 42 [hep-ph/0605068].

[171] T. Becher, M. Neubert and B. D. Pecjak, *Factorization and Momentum-Space Resummation in Deep-Inelastic Scattering*, *JHEP* **01** (2007) 076 [hep-ph/0607228].

[172] T. Becher and M. Neubert, *On the Structure of Infrared Singularities of Gauge-Theory Amplitudes*, *JHEP* **06** (2009) 081 [0903.1126].

[173] A. J. Larkoski, I. Moult and B. Nachman, *Jet Substructure at the Large Hadron Collider: A Review of Recent Advances in Theory and Machine Learning*, *Phys. Rept.* **841** (2020) 1 [1709.04464].

[174] R. Kogler et al., *Jet Substructure at the Large Hadron Collider: Experimental Review*, *Rev. Mod. Phys.* **91** (2019) 045003 [1803.06991].

[175] S. Marzani, G. Soyez and M. Spannowsky, *Looking inside jets: an introduction to jet substructure and boosted-object phenomenology*, vol. 958. Springer, 2019, 10.1007/978-3-030-15709-8, [1901.10342].

[176] ATLAS collaboration, G. Aad et al., *Measurement of colour flow with the jet pull angle in $t\bar{t}$ events using the ATLAS detector at $\sqrt{s} = 8$ TeV*, *Phys. Lett. B* **750** (2015) 475 [1506.05629].

[177] CMS collaboration, A. M. Sirunyan et al., *Measurement of jet substructure observables in $\mathrm{t\bar{t}}$ events from proton-proton collisions at $\sqrt{s} = 13$TeV*, *Phys. Rev. D* **98** (2018) 092014 [1808.07340].

[178] ATLAS collaboration, G. Aad et al., *Measurement of soft-drop jet observables in pp collisions with the ATLAS detector at $\sqrt{s}$ =13 TeV*, *Phys. Rev. D* **101** (2020) 052007 [1912.09837].

[179] ATLAS collaboration, G. Aad et al., *Measurement of the Lund Jet Plane Using Charged Particles in 13 TeV Proton-Proton Collisions with the ATLAS Detector*, *Phys. Rev. Lett.* **124** (2020) 222002 [2004.03540].

[180] ALICE collaboration, S. Acharya et al., *Measurements of the groomed and ungroomed jet angularities in pp collisions at* $\sqrt{s} = 5.02$ *TeV*, 2107.11303.

[181] S. Marzani, G. Soyez and M. Spannowsky, *Looking inside jets*, *Lecture Notes in Physics* (2019) .

[182] T. Kinoshita, *Mass singularities of feynman amplitudes*, *Journal of Mathematical Physics* **3** (1962) 650.

[183] T. D. Lee and M. Nauenberg, *Degenerate systems and mass singularities*, *Phys. Rev.* **133** (1964) B1549.

[184] H. Chen, I. Moult, X. Zhang and H. X. Zhu, *Rethinking Jets with Energy Correlators: Tracks, Resummation and Analytic Continuation*, 2004.11381.

[185] B. T. Elder, M. Procura, J. Thaler, W. J. Waalewijn and K. Zhou, *Generalized Fragmentation Functions for Fractal Jet Observables*, *JHEP* **06** (2017) 085 [1704.05456].

[186] N. Sveshnikov and F. Tkachov, *Jets and quantum field theory*, *Phys. Lett. B* **382** (1996) 403 [hep-ph/9512370].

[187] F. V. Tkachov, *Measuring multi - jet structure of hadronic energy flow or What is a jet?*, *Int. J. Mod. Phys. A* **12** (1997) 5411 [hep-ph/9601308].

[188] G. P. Korchemsky and G. F. Sterman, *Power corrections to event shapes and factorization*, *Nucl. Phys. B* **555** (1999) 335 [hep-ph/9902341].

[189] C. W. Bauer, S. P. Fleming, C. Lee and G. F. Sterman, *Factorization of* e^+e^- *Event Shape Distributions with Hadronic Final States in Soft Collinear Effective Theory*, *Phys. Rev. D* **78** (2008) 034027 [0801.4569].

[190] D. M. Hofman and J. Maldacena, *Conformal collider physics: Energy and charge correlations*, *JHEP* **05** (2008) 012 [0803.1467].

[191] A. Belitsky, S. Hohenegger, G. Korchemsky, E. Sokatchev and A. Zhiboedov, *From correlation functions to event shapes*, *Nucl. Phys. B* **884** (2014) 305 [1309.0769].

[192] A. Belitsky, S. Hohenegger, G. Korchemsky, E. Sokatchev and A. Zhiboedov, *Event shapes in $\mathcal{N} = 4$ super-Yang-Mills theory*, *Nucl. Phys. B* **884** (2014) 206 [1309.1424].

[193] P. Kravchuk and D. Simmons-Duffin, *Light-ray operators in conformal field theory*, *JHEP* **11** (2018) 102 [1805.00098].

[194] C. Basham, L. S. Brown, S. D. Ellis and S. T. Love, *Energy Correlations in electron - Positron Annihilation: Testing QCD*, *Phys. Rev. Lett.* **41** (1978) 1585.

[195] C. Basham, L. Brown, S. Ellis and S. Love, *Energy Correlations in electron-Positron Annihilation in Quantum Chromodynamics: Asymptotically Free Perturbation Theory*, *Phys. Rev. D* **19** (1979) 2018.

[196] L. J. Dixon, M.-X. Luo, V. Shtabovenko, T.-Z. Yang and H. X. Zhu, *Analytical Computation of Energy-Energy Correlation at Next-to-Leading Order in QCD*, *Phys. Rev. Lett.* **120** (2018) 102001 [1801.03219].

[197] M.-X. Luo, V. Shtabovenko, T.-Z. Yang and H. X. Zhu, *Analytic Next-To-Leading Order Calculation of Energy-Energy Correlation in Gluon-Initiated Higgs Decays*, *JHEP* **06** (2019) 037 [1903.07277].

[198] J. Henn, E. Sokatchev, K. Yan and A. Zhiboedov, *Energy-energy correlation in N=4 super Yang-Mills theory at next-to-next-to-leading order*, *Phys. Rev. D* **100** (2019) 036010 [1903.05314].

[199] H. Chen, M.-X. Luo, I. Moult, T.-Z. Yang, X. Zhang and H. X. Zhu, *Three point energy correlators in the collinear limit: symmetries, dualities and analytic results*, *JHEP* **08** (2020) 028 [1912.11050].

[200] A. Belitsky, S. Hohenegger, G. Korchemsky, E. Sokatchev and A. Zhiboedov, *Energy-Energy Correlations in N=4 Supersymmetric Yang-Mills Theory*, *Phys. Rev. Lett.* **112** (2014) 071601 [1311.6800].

[201] G. Korchemsky and E. Sokatchev, *Four-point correlation function of stress-energy tensors in $\mathcal{N} = 4$ superconformal theories*, *JHEP* **12** (2015) 133 [1504.07904].

[202] A. Belitsky, S. Hohenegger, G. Korchemsky and E. Sokatchev, *N=4 superconformal Ward identities for correlation functions*, *Nucl. Phys. B* **904** (2016) 176 [1409.2502].

[203] I. Moult and H. X. Zhu, *Simplicity from Recoil: The Three-Loop Soft Function and Factorization for the Energy-Energy Correlation*, *JHEP* **08** (2018) 160 [1801.02627].

[204] D. Chicherin, J. Henn, E. Sokatchev and K. Yan, *From correlation functions to event shapes in QCD*, 2001.10806.

[205] M. Kologlu, P. Kravchuk, D. Simmons-Duffin and A. Zhiboedov, *Shocks, Superconvergence, and a Stringy Equivalence Principle*, 1904.05905.

[206] M. Kologlu, P. Kravchuk, D. Simmons-Duffin and A. Zhiboedov, *The light-ray OPE and conformal colliders*, 1905.01311.

[207] C.-H. Chang, M. Kologlu, P. Kravchuk, D. Simmons-Duffin and A. Zhiboedov, *Transverse spin in the light-ray OPE*, 2010.04726.

[208] L. J. Dixon, I. Moult and H. X. Zhu, *Collinear limit of the energy-energy correlator*, *Phys. Rev. D* **100** (2019) 014009 [1905.01310].

[209] I. Moult, G. Vita and K. Yan, *Subleading power resummation of rapidity logarithms: the energy-energy correlator in $\mathcal{N} = 4$ SYM*, *JHEP* **07** (2020) 005 [1912.02188].

[210] H. Chen, T.-Z. Yang, H. X. Zhu and Y. J. Zhu, *Analytic Continuation and Reciprocity Relation for Collinear Splitting in QCD*, 2006.10534.

[211] H. Chen, I. Moult and H. X. Zhu, *Quantum Interference in Jet Substructure from Spinning Gluons*, 2011.02492.

[212] M. A. Ebert, B. Mistlberger and G. Vita, *The Energy-Energy Correlation in the back-to-back limit at N^3LO and N^3LL'*, 2012.07859.

[213] H. Chen, I. Moult and H. X. Zhu, *Spinning Gluons from the QCD Light-Ray OPE*, 2104.00009.

[214] G. Korchemsky, E. Sokatchev and A. Zhiboedov, *Generalizing event shapes: In search of lost collider time*, 2106.14899.

[215] J. C. Collins and D. E. Soper, *Back-To-Back Jets in QCD*, *Nucl. Phys. B* **193** (1981) 381.

[216] K. Konishi, A. Ukawa and G. Veneziano, *Jet Calculus: A Simple Algorithm for Resolving QCD Jets*, *Nucl. Phys.* **B157** (1979) 45.

[217] U. P. Sukhatme and K. E. Lassila, *Q^2 Evolution of Multi - Hadron Fragmentation Functions*, *Phys. Rev. D* **22** (1980) 1184.

[218] A. Majumder and X.-N. Wang, *The Dihadron fragmentation function and its evolution*, *Phys. Rev. D* **70** (2004) 014007 [hep-ph/0402245].

[219] D. J. Gross and F. Wilczek, *ASYMPTOTICALLY FREE GAUGE THEORIES. 2.*, *Phys. Rev. D* **9** (1974) 980.

[220] S. Ferrara, R. Gatto and A. F. Grillo, *Positivity Restrictions on Anomalous Dimensions*, *Phys. Rev.* **D9** (1974) 3564.

[221] G. Mack, *All unitary ray representations of the conformal group SU(2,2) with positive energy*, *Commun. Math. Phys.* **55** (1977) 1.

[222] J. M. Campbell and E. W. N. Glover, *Double unresolved approximations to multiparton scattering amplitudes*, *Nucl. Phys. B* **527** (1998) 264 [hep-ph/9710255].

[223] S. Catani and M. Grazzini, *Collinear factorization and splitting functions for next-to-next-to-leading order QCD calculations*, *Phys. Lett. B* **446** (1999) 143 [hep-ph/9810389].

[224] D. A. Kosower and P. Uwer, *Evolution kernels from splitting amplitudes*, *Nucl. Phys. B* **674** (2003) 365 [hep-ph/0307031].

[225] W. T. Giele and E. W. N. Glover, *Higher-order corrections to jet cross sections in e^+e^- annihilation*, *Phys. Rev. D* **46** (1992) 1980.

[226] G. F. R. Sborlini, D. de Florian and G. Rodrigo, *Double collinear splitting amplitudes at next-to-leading order*, *JHEP* **01** (2014) 018 [1310.6841].

[227] A. Gehrmann-De Ridder and E. Glover, *A complete ($\mathcal{O}(\alpha\alpha_s)$) calculation of the photon + 1 jet rate in e^+e^- annihilation*, *Nuclear Physics B* **517** (1998) 269–323.

[228] J. Gao, V. Shtabovenko and T.-Z. Yang, *Energy-energy correlation in hadronic Higgs decays: analytic results and phenomenology at NLO*, *JHEP* **02** (2021) 210 [2012.14188].

[229] C. Anastasiou and K. Melnikov, *Higgs boson production at hadron colliders in NNLO QCD*, *Nucl. Phys. B* **646** (2002) 220 [hep-ph/0207004].

[230] R. N. Lee, *Presenting LiteRed: a tool for the Loop InTEgrals REDuction*, 1212.2685.

[231] R. N. Lee, *LiteRed 1.4: a powerful tool for reduction of multiloop integrals*, *J. Phys. Conf. Ser.* **523** (2014) 012059 [1310.1145].

[232] A. V. Smirnov and F. S. Chuharev, *FIRE6: Feynman Integral REduction with Modular Arithmetic*, *Comput. Phys. Commun.* **247** (2020) 106877 [1901.07808].

[233] C. Meyer, *Algorithmic transformation of multi-loop master integrals to a canonical basis with CANONICA*, *Comput. Phys. Commun.* **222** (2018) 295 [1705.06252].

[234] J. M. Henn, *Multiloop integrals in dimensional regularization made simple*, *Phys. Rev. Lett.* **110** (2013) 251601 [1304.1806].

[235] A. Gehrmann-De Ridder, T. Gehrmann and G. Heinrich, *Four particle phase space integrals in massless QCD*, *Nucl. Phys. B* **682** (2004) 265 [hep-ph/0311276].

[236] V. Magerya and A. Pikelner, *Cutting massless four-loop propagators*, *JHEP* **12** (2019) 026 [1910.07522].

[237] D. Maitre, *HPL, a mathematica implementation of the harmonic polylogarithms*, *Comput. Phys. Commun.* **174** (2006) 222 [hep-ph/0507152].

[238] DELPHI collaboration, P. Abreu et al., *Tuning and test of fragmentation models based on identified particles and precision event shape data*, *Z. Phys. C* **73** (1996) 11.

[239] L. J. Dixon, I. Moult and H. X. Zhu, *Collinear limit of the energy-energy correlator*, *Physical Review D* **100** (2019) .

[240] Y.-T. Chien, R. Rahn, D. Y. Shao, W. J. Waalewijn and B. Wu. To appear.